THE ELECTROCHEMISTRY OF LEAD DIOXIDE FORMED ON LEAD AND LEAD ALLOYS IN SULPHURIC ACID

by

Sheila Karen Marie Kelly

A Doctoral thesis submitted in partial fulfilment of the requirements for the award of Doctor of Philosophy of Loughborough University of Technology.

April 1981

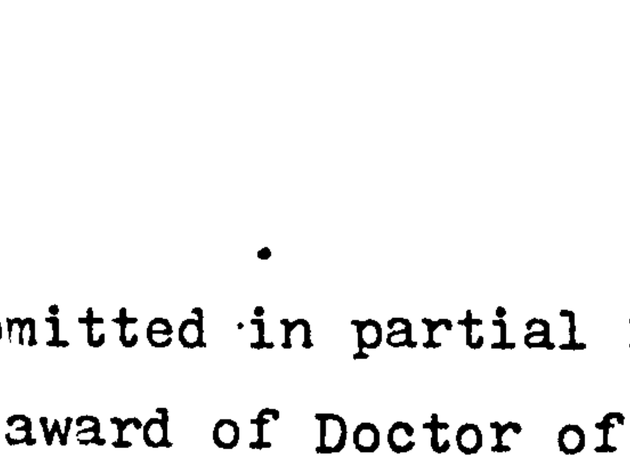

ACKNOWLEDGEMENTS

I would like to express my gratitude to my supervisor, Prof. N.A. Hampson, for his constant help and encouragement throughout this project. Financial support from Chloride Technical Ltd. is acknowledged and in particular the interest and guidance of Mr. Kenneth Peters. Finally, my thanks are also due to my fellow research students for their many hours of stimulating discussion.

The work in this thesis has not been submitted, in full or in part, to this or any other institution for a higher degree.

LIST OF SYMBOLS

A	electrode area
A'	nucleation rate constant
A_1	actual area of an isolated nucleus
A_{1ex}	top area of an isolated nucleus
b	Tafel slope
C	total differential capacitance
C_G	differential capacitance of the diffuse double layer
C_H	differential capacitance of the compact double layer
C_o	concentration of oxidised species (O)
C_o^s	Surface concentration of oxidised species(O)
C_o^b	bulk concentration of oxidised species (O)
C_p	concentration of electrolyte at a pore mouth
C_R^s	surface concentration of reduced species (R)
C_R	concentration of reduced species (R)
C_o^b	bulk concentration of reduced species (R)
C_{DL}	double layer capacitance
D_o	Fick's diffusion coefficient
E	electrode potential on a suitable reference scale
E^o	standard electrode potential
E_p	potential of peak current
E_{pzc}	potential of zero charge
E_r	reversible electrode potential (at i = 0)
$E_{\frac{1}{2}}$	polarographic half wave potential
F	Faraday's constant

h	height of a nucleus
i	current, current density
ia, ic	partial anodic and cathodic current densities
im, ip	peak current, peak current density
i_o	exchange current density
i_{res}	residual oxygen evolution current
j	$(-1)^{\frac{1}{2}}$
k	potential dependent reaction rate constant
ka,kc	potential dependent rate constants for the anodic and cathodic reactions
k^o	apparent standard rate constant
k_s	specific rate constant at E
k_{sh}	standard heterogeneous rate constant
M	molar mass
n,z	number of electrons
N	number of nuclei, number of moles of reactant
No	initial number of nuclei
O	oxidised species
q	charge on electrode, flux of diffusing species
p	penetration ('length') depth of a porous electrode
Q_m	charge
r	radius of nucleus, radius of an electrode
R	gas constant, reduced species
R_{CT}, R_D	charge transfer resistance
R_{sol}	ohmic resistance of electrolyte
t	time

t_m	time at maximum current
T	temperature
u	age of a nucleus
V_1, V_2, V_3	rates of advance of a nucleus
V	volume of electrode
W	Warburg impedance
x	distance from electrode
Z	total cell impedance
Z'	real part of electrode impedance
Z''	imaginary part of electrode impedance
(z)	net distributed charge acting at a mean distance (z) from the electrode
α	charge transfer coefficient
β	symmetry factor
δ	diffusion boundary layer thickness
δ_o	hydronamic boundary layer thickness
η_D	charge transfer overpotential
θ	surface coverage, charge transfer resistance, nucleation constant (controlled by potential)
ν	kinematic viscosity, potential sweep rate
ρ	density of deposit
σ	Warburg coefficient
$\phi_m, \phi_2, \phi_1, \phi_s$	potentials at various points within the double layer as shown in Figs. 2.1 - 2.4.
ω	angular velocity, angular frequency
ε	interfacial permittivity
$\rightarrow$	direction of a given reaction

CONTENTS

SUMMARY

The electrochemistry of lead dioxide has been studied using the techniques of linear sweep voltammetry, potentiostatic pulse experiments and a.c. impedance measurements. A morphological examination was also carried out using the technique of scanning electron microscopy. The formation of lead dioxide was investigated on both the flat lead/lead alloy electrode and the porous electrode which was produced by oxidation of a standard automotive positive paste on a lead/lead alloy base. The electrochemistry of the pure lead electrode (both flat and porous) was investigated and the effect on this of various alloy additions was observed. The alloys used, all of potential industrial importance, were lead-antimony, lead-bismuth, lead-calcium-tin and lead-calcium-tin-bismuth at various levels of bismuth addition. An a.c. study of Pb-Ca-Sn-Mg-Al is also included.

The effect of antimony addition to lead has been isolated as the production of a secondary oxidation layer. This provides an explanation for the superior active material retention of antimony containing grids in the lead-acid battery, the relatively large material development with the antimonial alloy giving rise to a more mechanically sound function between grid and paste. The formation of this extra corrosion layer on antimonial lead may also explain the high degree of top bar corrosion which occurs in the oxygen region of the battery.

The commercial significance of bismuth as a grid alloying ingredient has been highlighted and a useful bismuth concentration range determined for both lead and lead-calcium-tin alloys.

CHAPTER 1

INTRODUCTION

Despite recent concentrated efforts toward the development of small, light-weight secondary electrochemical power sources, the lead-acid battery, first introduced in 1859, remains unsurpassed at the forefront of major battery systems today. Numerous attempts have been made, however, to replace antimony as the grid alloying ingredient. Lead-antimony alloys have been used as support grids for lead-acid positive and negative battery plates for a considerable number of years. The alloying antimony is added to improve castability and subsequent handleability. It is widely known that antimony in automotive positive grids extends the service life by improving the capability to resist deep cycling and extensive overcharge. This effect is believed to be due to the lead-antimony alloy providing a corrosion layer which has good adhesion to the active material and a corrosion product which does not penetrate inbetween the crystallites of the grid alloy producing an intergranular attack. A Pronounced disadvantage, however, is that the presence of antimony in the cell lowers the potential of hydrogen evolution due to the deposition of antimony on the negative plate with a consequent lowering of the hydrogen overvoltage at that electrode.

Attempts to substitute other materials for antimony have been fairly successful and materials suggested as replacements include

alloys of calcium, tin, magnesium, aluminium, titanium and bismuth. There is no doubt that improvements in the suppression of the hydrogen evolution reaction have resulted from these substitutions but unfortunately the removal of antimony from the positive grids has resulted in rather inferior cycle lives.

The modern trend towards the development of low cost, low maintenance batteries of high capacity has led to the introduction of alloys based on calcium-lead; this alloy has already proved itself, in principle, in standby and telephone batteries[1] but there are some indications that the use of calcium in place of antimony introduces service difficulties.

Several workers have considered the effect of alloying lead with various amounts of bismuth[2-7]. Small quantities of bismuth (< 0.3%) do not seem to have any significant effect on the metallurgical properties of lead; as the quantity of bismuth is increased the lead is found to harden, its bending strength being considerably reduced. A detailed study of the effect of bismuth on battery performance[8] has shown that the presence of bismuth results in an increase in the amount of positive shedding (i.e. loss of active material as sludge in the cell case) and promoted grid growth. These increases, however, do not appear to be linear with increasing bismuth content.

This thesis investigates the electrochemistry of pure lead electrodes and examines the effect on this of antimony addition. A specific 'antimony effect' is isolated. Various alloy substitutions

are made and the electrochemistry of lead-bismuth binarys, lead-calcium-tin alloys and lead-calcium tin-bismuth electrodes is studied. The suitability of these alloys as replacements for antimony in the lead-acid battery positive plate is discussed.

CHAPTER 2

THEORETICAL PRINCIPLES

2.1. The Electrode-Electrolyte Interphase

An understanding of the composition of the electrode-electrolyte interphase is of paramount importance in an investigation of electrode kinetics since the reactions occur within this region. When a metal is placed in an electrolyte an electrical double layer exists at the metal-solution interphase; Two layers of electrical charge (of equal magnitude and opposite sign) are separated by a distance of the order of tenths of nanometers so producing a potential difference across the interfacial region. The results obtained from different experimental methods of examining the interphase have led to various theories and models for the metal-solution interphase.

The simplest model for the distribution of ions at the interphase was proposed by Helmholtz[9] in 1879; He regarded the interphase as consisting of two rigidly held planes of equal and opposite charge, one on the metal surface and the other on the solution side of the interphase at a fixed distance away from the electrode. This arrangement approximates to a parallel-plate capacitor and the following assumptions are inherent in the model:

(a) the separated charges at the interphase are in electrostatic equilibrium

(b) there is no transfer of charge in either direction across the interphase with changes in electrode potential.

(c) the charge in the solution near to the electrode interphase changes with changes in electrode potential.

These assumptions imply that the electrical double layer is purely capacitive and has no parallel resistive components. The Helmholtz model of the double layer is shown diagrammatically in Fig. 2.1. Electrodes which closely obey these conditions are termed "ideally polarisable" and in practice metal-solution interphases only approximate to the ideal situation.

The simple model was improved by Gouy[10] who pointed out that the electrostatic interaction between the field and charges on the ions is counteracted by random thermal motion which would cause a degree of diffuseness on the charge on the solution side of the interphase. A similar theory was proposed independently by Chapman[11]. The Gouy-Chapman diffuse double-layer model as it came to be known is shown in Fig. 2.2 and represents a substantial improvement over the Helmholtz model in that a dependence of differential capacity on both potential and concentration is predicted. A major cause for the discrepancies between theoretical prediction from the Gouy-Chapman model and experimental results was that the compact part of the interphase had been overlooked. The theory was further modified by Stern[12] who combined the two previous models to give a model consisting of a monolayer of ions on the electrode with the remaining ions in a diffuse layer as with the Gouy-Chapman model. He took into account the finite size of the ions (up to then they had been considered as point charges only) by postulating that they could only approach the electrode to within a certain distance (the plane of closest approach). He further postulated that some ions could undergo adsorption by means other

purely electrostatic attraction. Stern's model of the double layer is shown diagramatically in Fig. 2.3 and is effectively two capacitors acting in series to determine the total differential capacity of the interphase. The total capacitance of the double layer, C, is given by

$$\frac{1}{C} = \frac{1}{C_H} + \frac{1}{C_G} \qquad (2.1)$$

where C_{II} denotes the capacity due to the compact layer and C_G the capacity due to the diffuse layer which extends from the plane of closest approach to the bulk solution. Although this model was an improvement on previous ones there still remained discrepancies between theoretical predictions and experimental results.

The Stern model was modified further by Grahame[13] who suggested that the interphase consisted of three layers; the first layer extends from the electrode to a plane passing through the centres of the adsorbed anions, which are not likely to be hydrated, and is called the inner Helmholtz plane. The second layer consists of the hydrated cations at their distance of closest approach with the plane through their centres being known as the outer Helmholtz plane. The final layer between the outer Helmholtz plane and the bulk solution is the diffuse layer of Gouy-Chapman. This model is shown in Fig. 2.4. The predicted variation of potential with distance for the various models are also shown in Figs. 2.1 - 2.4.

Fig. 2.1 Helmholtz Model of the Double Layer.

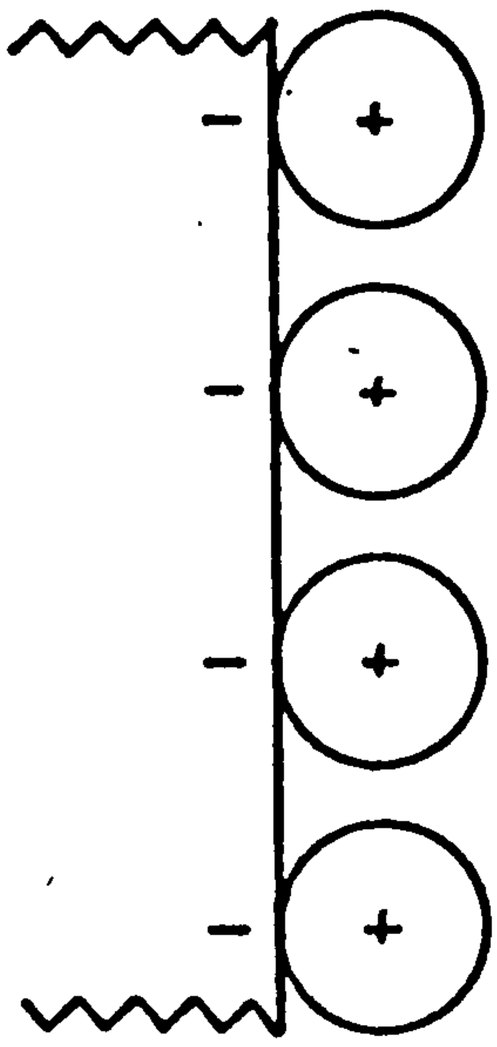

Variation of Potential with Distance through the Interface predicted by the Helmholtz Model.

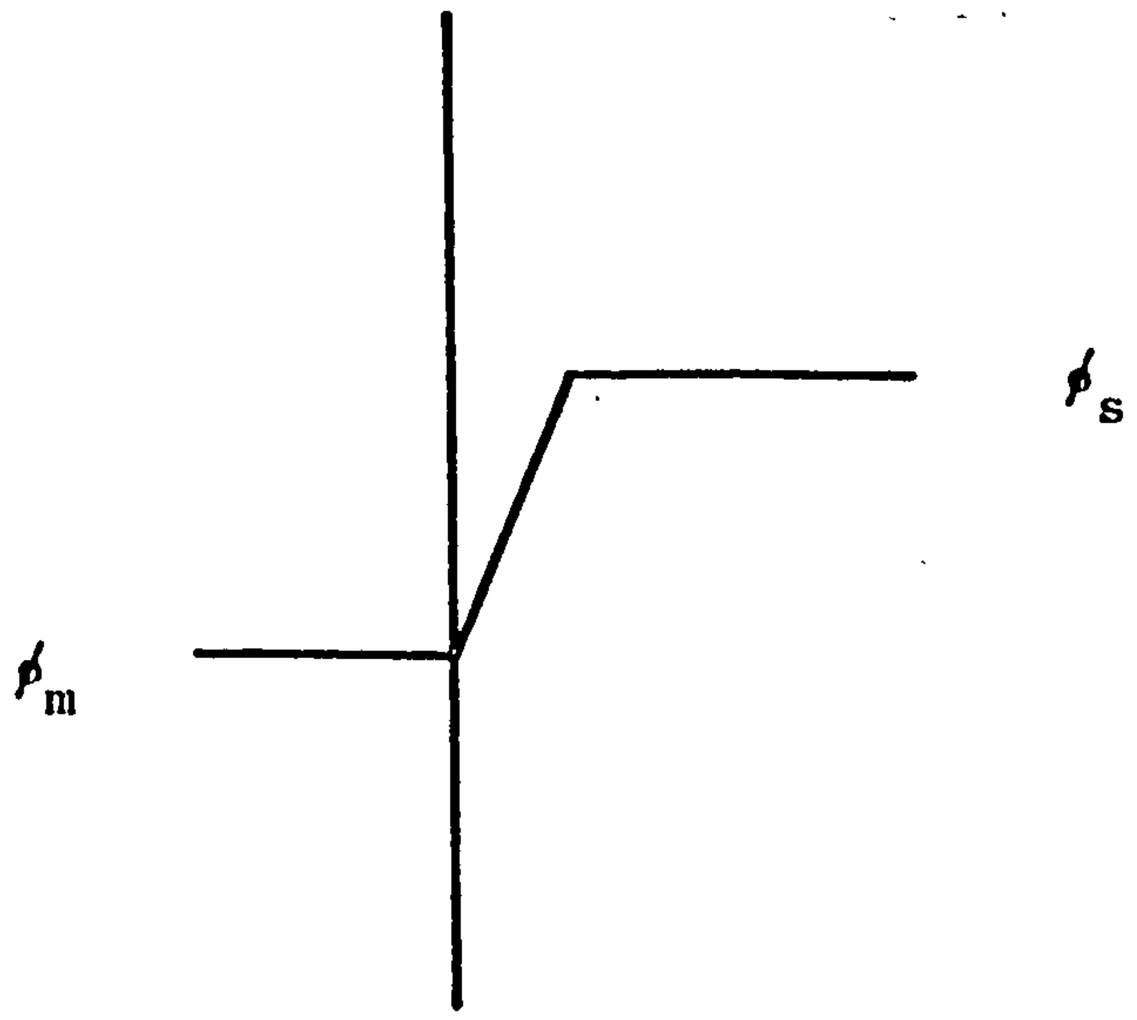

Fig.2.2 Gouy - Chapman Model of the Double Layer.

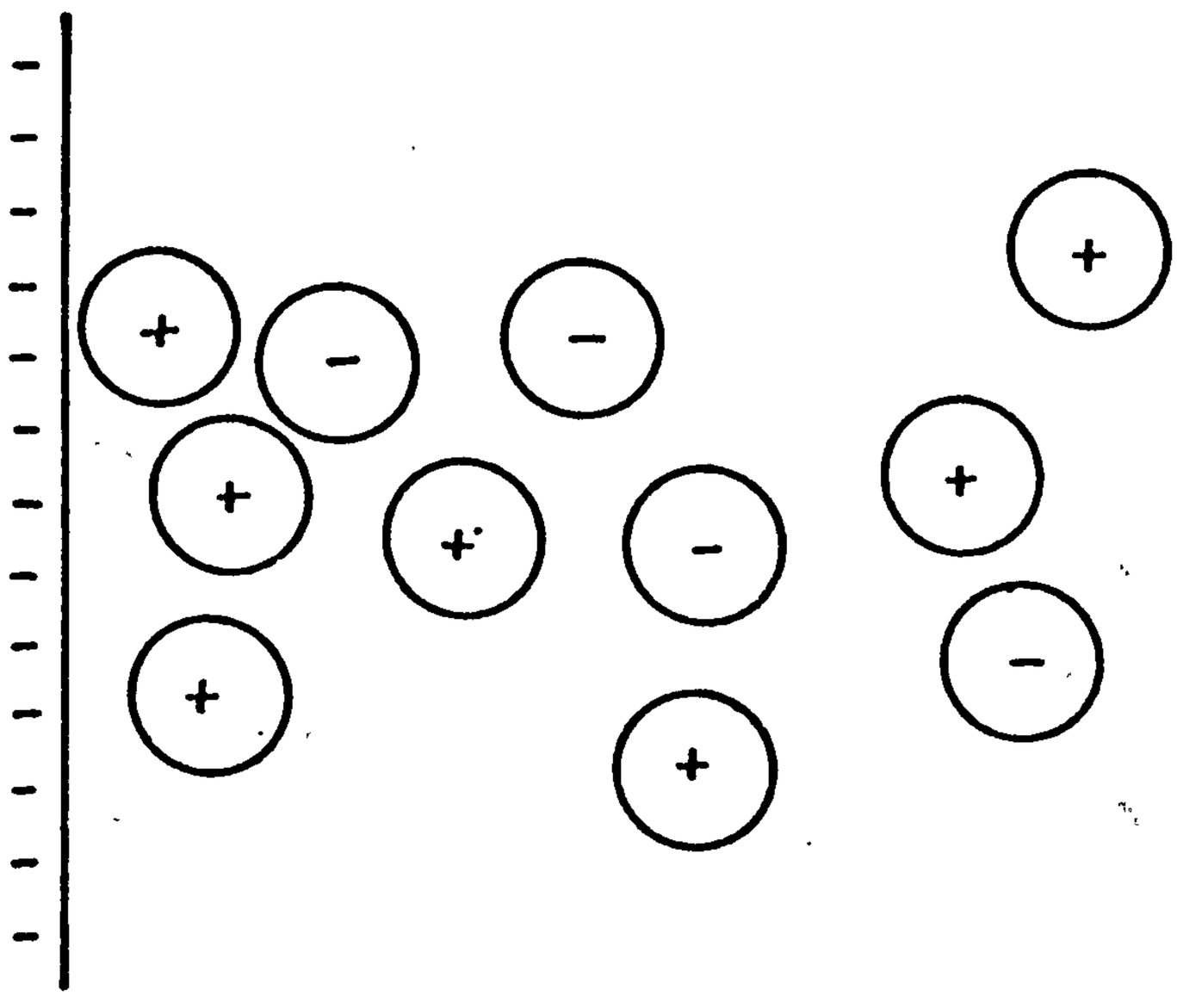

Variation of Potential with Distance through the Interface predicted by the Gouy - Chapman Model.

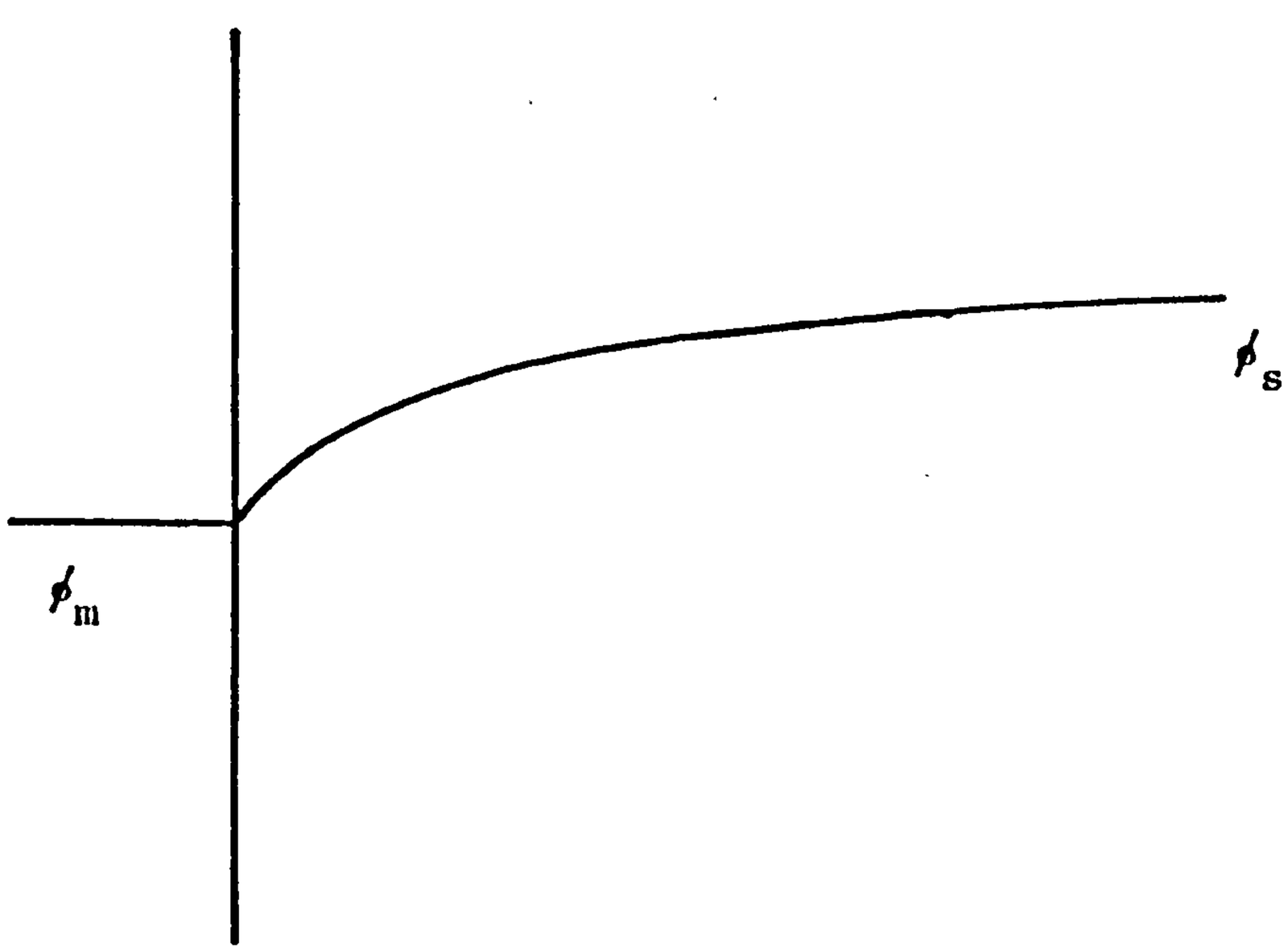

Fig.2.3 Stern Model of the Double Layer.

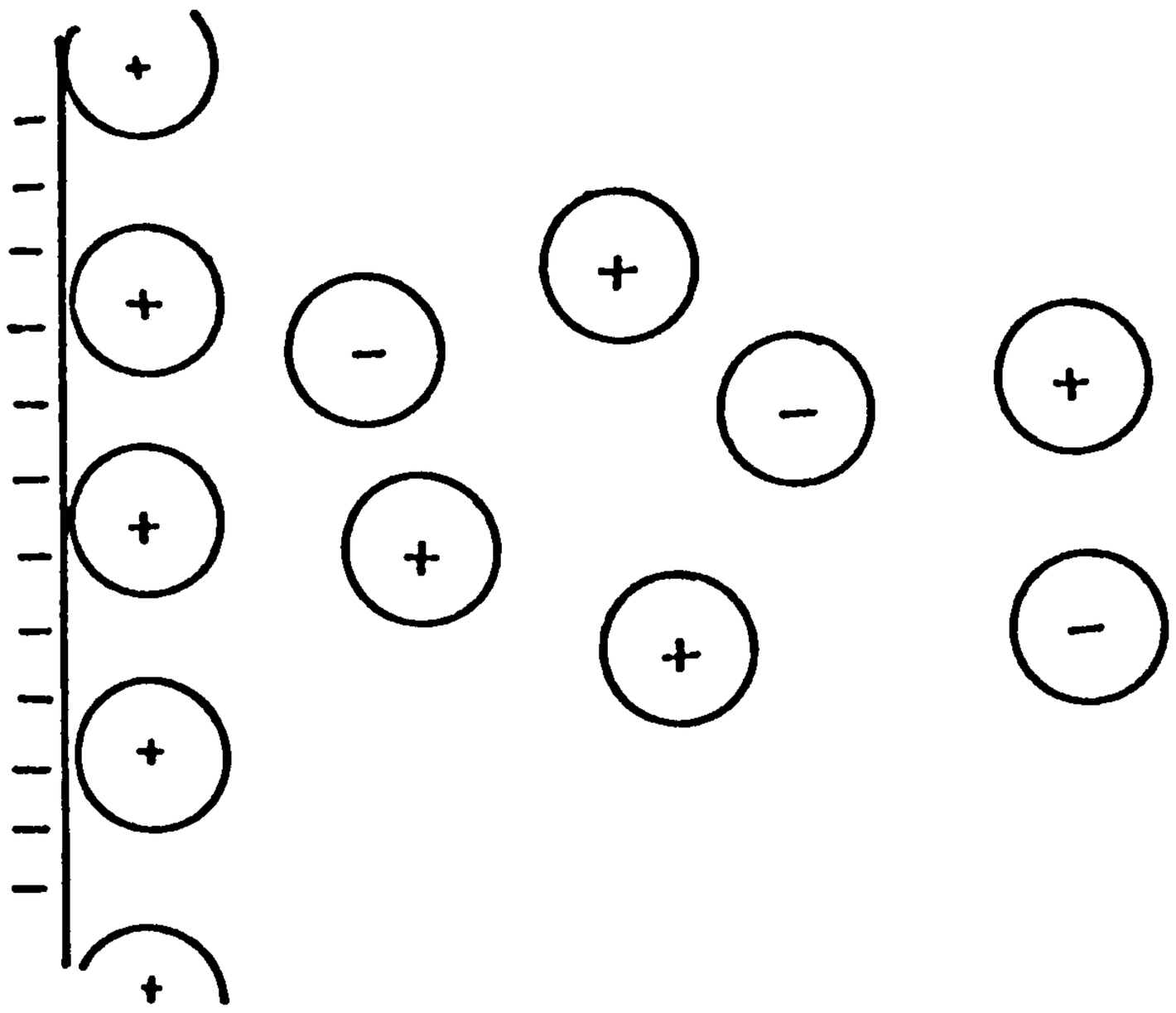

Variation of Potential with Distance through the Interface predicted by the Stern Model.

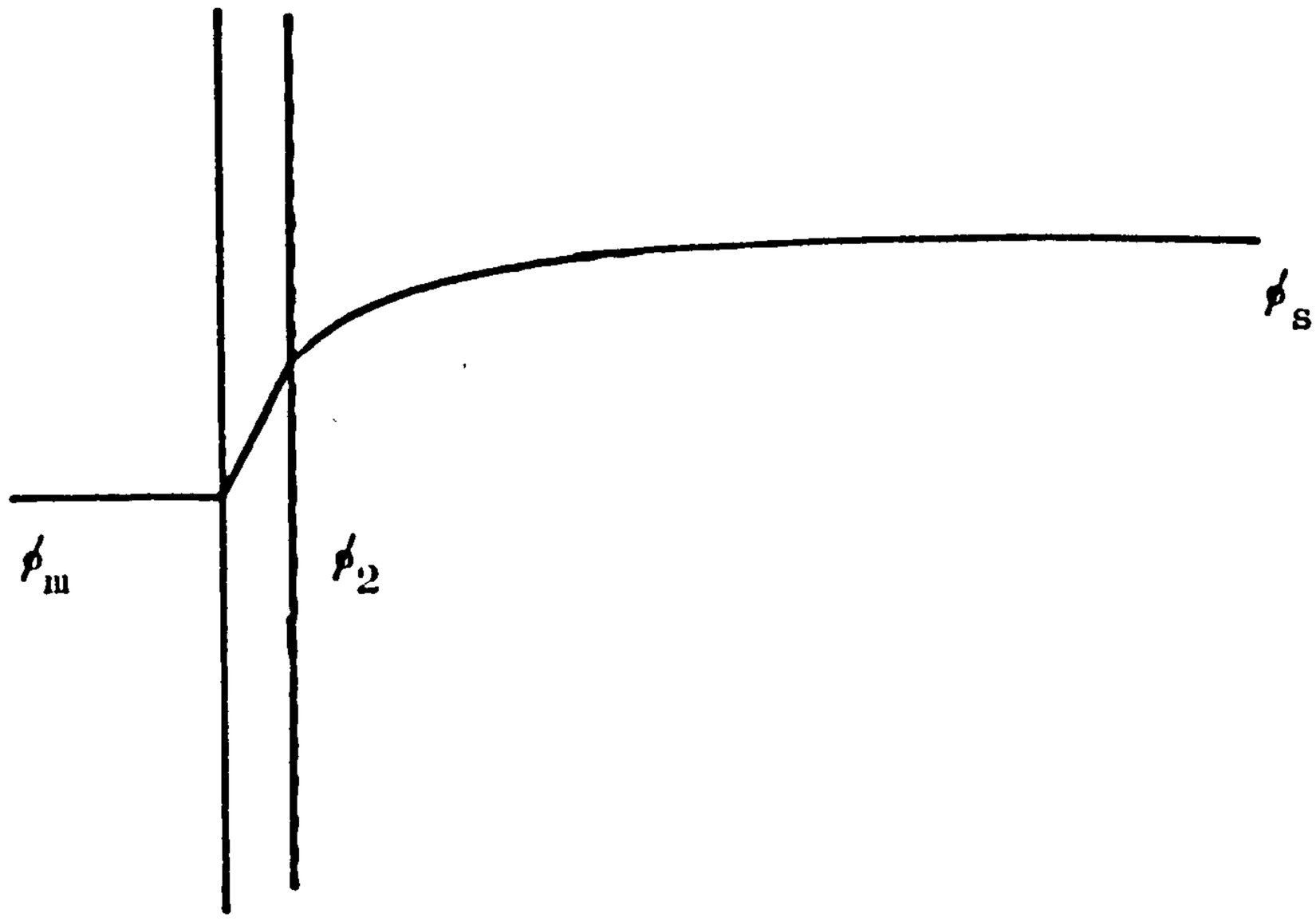

Fig. 2.4 Grahame Model of the Double Layer.

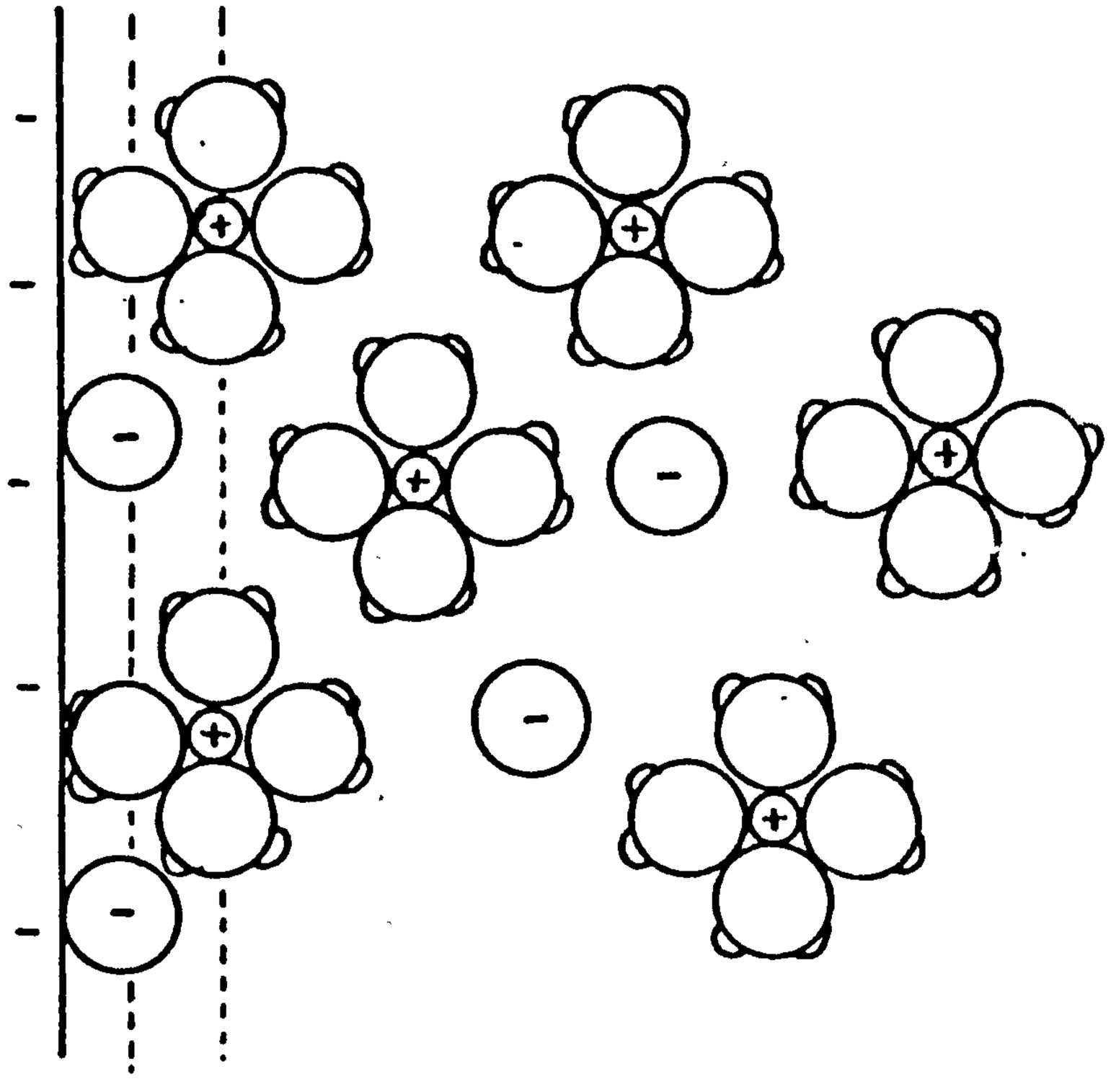

Variation of Potential with Distance through the Interface predicted by the Grahame Model.

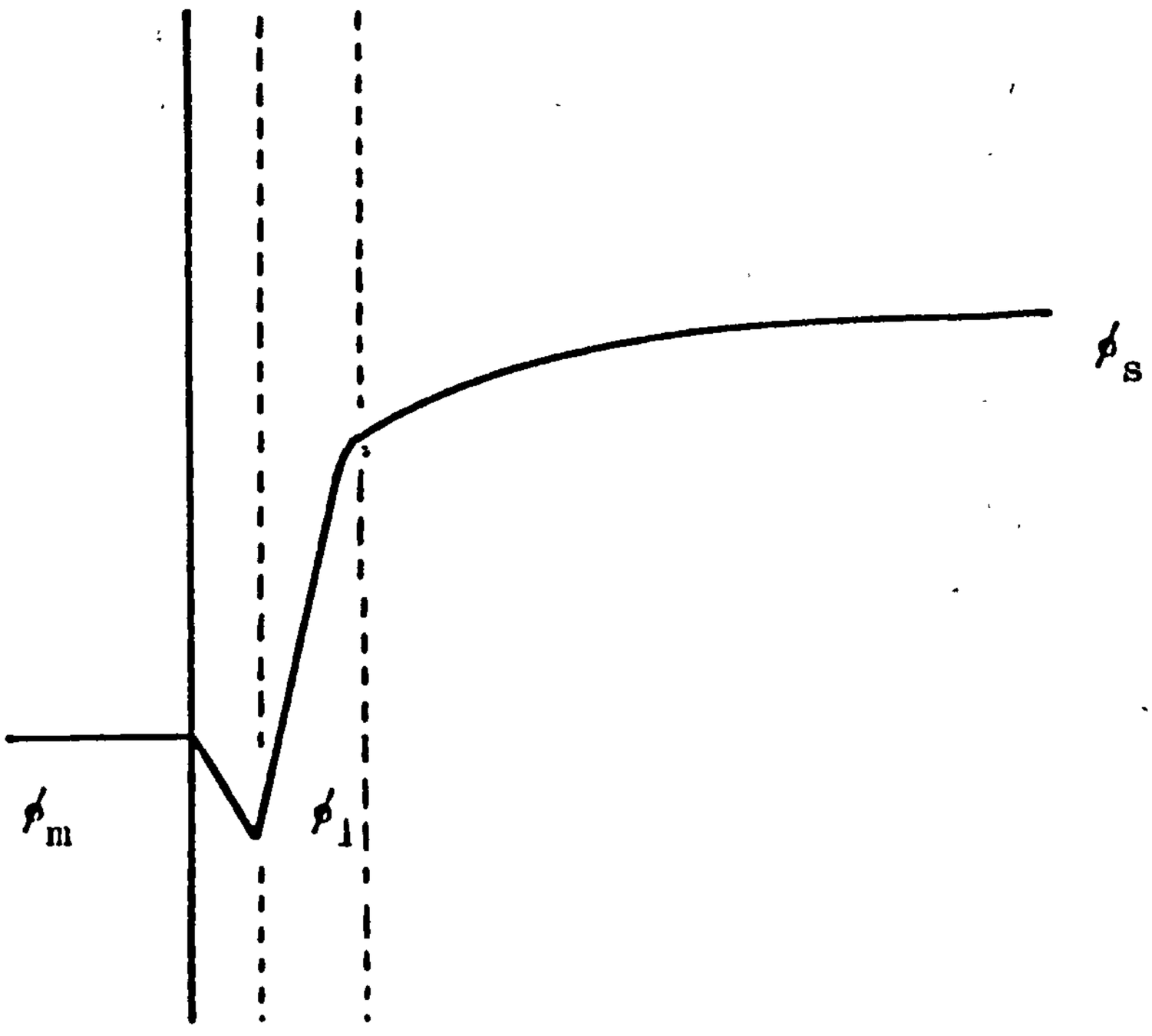

TEXT CUT OFF IN ORIGINAL

Fig. 2.5 Bockris et al. Model of the Double Layer

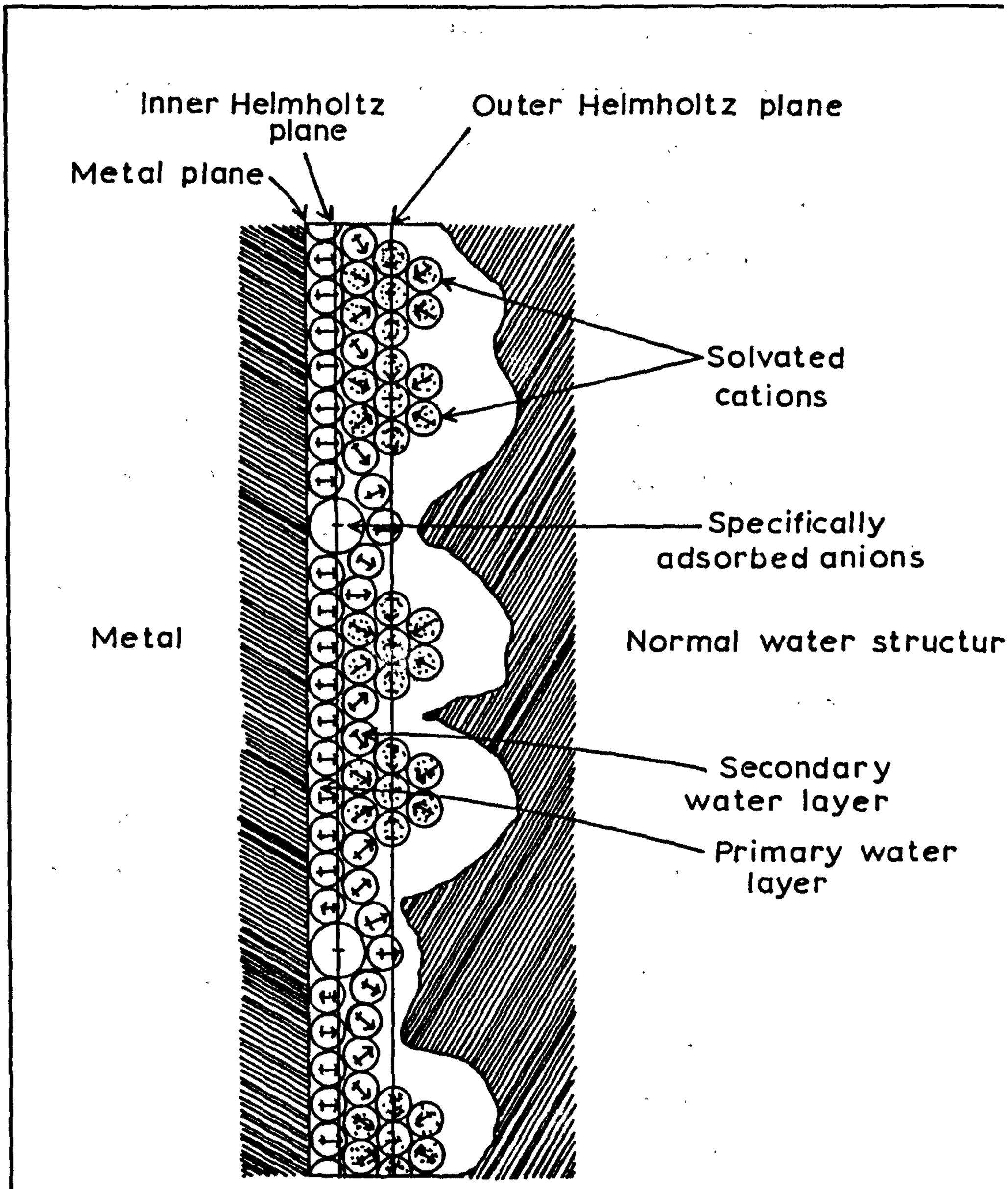

A more recent theory for the distribution of ions in the double layer which takes into account the predominant existance of the solvent in the interphase has been proposed by Bockris, Devanathan and Muller[14]. They suggest that the surface of the electrode is covered with an orientated layer of water molecules, but on certain sites, these water molecules are replaced by specifically adsorbed ions which do not carry a hydration shell. The plane passing through the centres of these specifically adsorbed ions is the inner Helmholtz plane (Fig. 2.5). Next are the ions which retain their hydration shell and are situated outside the primary layer of water molecules adsorbed on the electrode surface; the plane passing through their centres is the outer Helmholtz plane.

Most of the work on the theory of the double layer since 1963 has been concerned with the compact layer and has concentrated on the orientated behaviour of the layer of water molecules within this layer e.g. Levine et al[15], Damaskin and Frumkin[16] and Parsons[17].

Cooper and Harrison[18-22] have questioned this subdivision of the double layer into a concentration independent compact layer and a diffuse region and particularly with regard to the structure and properties of individual solvent molecules within the compact layer. They proposed a new approach to the double layer in which it is treated as a single entity with no basis on the concepts of compact layer, inner or outer Helmholtz planes, or contact adsorption. The structure of the double layer is considered to arise specifically from the known differences between anions and cations in aqueous solution. The essential points of the model are:

1. The net distributed charge $\rho(z)$ acts at a mean distance (z) from the electrode.

2. The differential capacity C is given by:

$$C = \frac{dq}{d(\Delta E)} = \frac{\mathcal{E}}{(z) + q(d(z)/dq) - q((z)/\mathcal{E})(d\mathcal{E}/dq)} \quad (2.2)$$

where q is the surface charge density

ΔE is the potential drop between the electrode and bulk electrolyte

$\mathcal{E}$ is the appropriate interfacial permittivity.

In conclusion, a study of the differential capacitance is crucial in establishing conditions under which the exchange reaction at an electrode-electrolyte interphase may be studied in the absence of adsorption and film formation at the electrode surface[23,24]

2.2. The Charge Transfer Process

Electrode processes are heterogeneous reactions which occur at the metal-electrolyte interphase and are accompanied by the transfer of electric charge through this interphasial region. Since the electrode process involves the transfer of electrons from one substance to another it is therefore a redox-type reaction and may be represented by the overall equation:

$$O + ze \underset{k_a}{\overset{k_c}{\rightleftharpoons}} R \quad (2.3)$$

The overall current (per unit electrode area) flowing at a given potential can be expressed as

$$i = zF(k_c C_o^s - k_a C_R^s) \qquad (2.4)$$

i.e. the difference between the forward and reverse rates;

C_o^s and C_R^s are the surface concentrations of O and R, whilst k_c and k_a are the potential dependent rate constants given by

$$k_c = k_c^o \exp\left(\frac{-\alpha zFE}{RT}\right) \qquad (2.5)$$

and

$$k_a = k_a^o \exp\frac{(1-\alpha)zFE}{RT} \qquad (2.6)$$

where α is the charge transfer coefficient

E is the electrode potential

and k_c^o is the value of k_c at the reference potential

k_a^o is the value of k_a at the reference potential

By substitution of equations (2.5) and (2.6) into equation (2.4) we obtain

$$i = zF\left[k_c^o C_o^s \exp\left(\frac{-\alpha zFE}{RT}\right) - k_a^o C_R^s \exp\left(\frac{(1-\alpha)zFE}{RT}\right)\right] \qquad (2.7)$$

At the reversible potential (Er) we have a situation where the net current is zero and

$$i_c = i_a = i_o \qquad (2.8)$$

i_o is defined as the exchange current density and it follows from (2.8) that

$$i_o = zFk_c^o C_o^s \exp\left(\frac{-\alpha zFEr}{RT}\right)$$

$$= zFk_a^o C_R^s \exp\left(\frac{(1-\alpha)\, zFEr}{RT}\right) \qquad (2.9)$$

By solving (2.9) for $zFk_c^o C_o^s$ and $zFk_a^o C_R^s$ and substituting into (2.7) we obtain

$$i = i_o \left[\exp\frac{(-\alpha zF(E-Er))}{RT} - \exp\frac{(1-\alpha)zF(E-Er)}{RT} \right] \qquad (2.10)$$

where (E-Er) is defined as the charge transfer overpotential[25] (η_D). Equation (2.10) describes the current density-overpotential relationship for an electrode-electrolyte system (in the presence of excess supporting electrolyte) and was first derived by Erdey-Gruz and Volmer[26].

1) <u>For low overpotentials</u>

$$|\eta_D| \ll \frac{RT}{zF} \quad \text{or} \quad |\eta_D| \ll \frac{RT}{(1-\alpha)zF}$$

The overpotential-current curve is linear and differentiation of equation (2.10) with $\eta_D = 0$ gives

$$-\left(\frac{di}{d\eta_D}\right)_{\eta_D \to 0} = \frac{zF}{RT} \cdot i_o \qquad (2.11)$$

Since the current-overpotential relationship is of the form of Ohm's law, the reciprocal of the left-hand side of (2.11) is defined as the charge transfer resistance R_{CT}[27,28] so that

$$R_{CT} = \frac{RT}{zF} \cdot \frac{1}{i_o} \qquad (2.12)$$

ii) <u>At high overpotentials</u>

We have $|\eta_D| \gg \frac{RT}{zF}$ or $|\eta_D| \gg \frac{RT}{(1-\alpha)zF}$

and one of the exponents in equation (10) can be dropped. At high cathodic overpotentials $\eta_D = \frac{RT}{\alpha zF} \log i_o - \frac{RT}{\alpha zF} \log i$ (2.13)

At high anodic overpotentials: $\eta_D = \frac{RT}{(1-\alpha)zF} \log i_o + \frac{RT}{(1-\alpha)zF} \log i$ (2.14)

Equations (2.13) and (2.14) are the Tafel relationships[29].

The exchange current density can be obtained from the values of charge transfer resistance at low overpotentials, and by extrapolating η_D vs. log i plots back to the equilibrium potential from measurements taken at high overpotentials. The concept of exchange current was introduced by Butler[30] in 1936 and its dependence on reactant concentration is given by[31]

$$i_o = zFk^o (C_o)^{1-\alpha} (C_R)^{\alpha} \qquad (2.15)$$

where k^o is the apparent standard rate constant first introduced by Randles.[32]

This theory of the charge transfer process applies only to the simple electrode reaction for which all of the electrons are transferred simultaneously. Electrode reactions in which a number of electrons are transferred successively have been comprehensively reviewed by Losev[33] who has considered processes with a single limiting step and others with comparable rate constants for successive steps.

The most recent developments to the theory for simple electrode reactions has been derived from quantum mechanics concepts, and have largely been the work of Levich[34], Marcus[35], and Dogonadse[36]. The reaction does not occur in one smooth step over a single energy barrier but proceeds in various stage. The reactant must first diffuse to the electrode and then the ionic atmosphere arrange and solvent orientate to form a transition state. Finally the electron is transferred and only this step has to be treated kinetically. The first stages of the reaction are all in equilibrium and can be treated by thermodynamics. Following electron transfer, the ligand bond distances are altered and the solvent dipoles and ion atmosphere reorientated. When an electron is transferred there is no change in energy. That radiationless isoenergetic electron transfer can take place is a central feature of the Marcus and Levich theories. A detailed theory for the process of solvent reorganisation has been worked out by Levich and Dogonadse[37].

2.3. Mass Transport Processes

The electrode process, which can be represented by equation (2.3)

$$O + ze \rightleftharpoons R$$

may be considered to be composed of three individual processes:

$$O_{bulk} \longrightarrow O_{electrode} \qquad (2.16)$$

$$O_{electrode} + ze \longrightarrow R_{electrode} \qquad (2.17)$$

$$R_{electrode} \longrightarrow R_{bulk} \qquad (2.18)$$

The overall flow of electrons can be limited by either process (2.16) or process (2.17). If the first step, given by equation (2.16), is the slowest then the overall reaction is said to be mass transfer controlled since the process is limited by mass transfer of the oxidised species (O) to the electrode. If, however, (2.17) has a slower rate than (2.16) the process is limited by the rate of electron transfer and the reaction is charge transfer controlled. In some instances neither of the above processes are as slow as a chemical transformation involving the electroactive species, in which case the chemical transformation is the rate determining process.

The three modes of mass transfer which are normally encountered are migration, convection and diffusion.

i) Migration

Mass transfer by migration is the result of the forces exerted on charged particles by an electric field. In the presence of a large

excess of support electrolyte the migration of electroactive material is minimised to such an extent that it may be neglected.

ii) Convection

Natural or free convection will always develop spontaneously in any solution undergoing electrolysis; this arises as a result of density differences which develop near the electrode and may also originate from thermal or mechanical disturbances. Forced convection may be effected from many sources of external turbulence e.g. stirring the solution, rotating the electrode, bubbling gas close to the electrode etc.

iii) Diffusion

Whenever concentration differences are established diffusion will exist. Since a concentration gradient develops as soon as electrolysis is initiated, diffusion occurs to some extent in every electrode reaction. If we consider a planar electrode immersed in an electrolyte solution containing O, which is reduced according to equation (2.3) then the number of moles of O which diffuse past a given area (A/cm^2) in a time dt, is proportional to the concentration gradient of the diffusing species:

$$\frac{dN}{A.dt} = Do \quad \frac{\partial Co}{\partial x} \qquad (2.19)$$

This is Fick's first law, relating diffusion rates to concentration. The left-hand side of equation (2.19) is known as the flux (q) and is the number of moles diffusing through unit area per unit time.

Do is the diffusion coefficient, defined as the number of molecules per second crossing unit area under unit concentration gradient. As electrolysis continues, C_o and hence $\frac{\partial C_o}{\partial x}$ decrease with time since O is being consumed at the electrode.

Fick's second law describes the variation of Co with time and may be summarised as

$$\frac{\partial C_o}{\partial t} = Do \frac{\partial^2 C_o}{\partial x^2} \qquad (2.20)$$

The solution of equation (20) in terms of $C_o(x,t)$ is given by equation (21):-

$$C_o(x,t) = C_o^b \frac{2}{\pi^{\frac{1}{2}}} \int_0^{x/2} D^{\frac{1}{2}} t^{\frac{1}{2}} e^{-y^2} dy \qquad (2.21)$$

with the conditions for the solution of equation (2.20) being:

$$\text{at } t = 0 \qquad C_o^s = C_o^b$$

$$\text{at } t > 0 \qquad C_o^s = 0$$

also $C_o \longrightarrow C_o^b$ as $x \longrightarrow \infty$

where C_o^s and C_o^b correspond to the concentrations of O at the electrode surface and in the bulk solution. The instantaneous current, i_t, is proportional to the flux at x = 0, so

$$i_t = zFAq(O,t) = zFAD_o \left(\frac{\partial C_o}{\partial x} \right)_{o,t} \qquad (2.22)$$

The value of $\left(\frac{\partial C_o}{\partial x} \right)_{o,t}$ is obtained by differentiating equation (21) and evaluating at x = 0.

The final expression for the instantaneous current at a planar electrode under diffusion control becomes

$$i_t = \frac{zFAD_o^{\frac{1}{2}} C_o^b}{\pi^{\frac{1}{2}} t^{\frac{1}{2}}} \qquad (2.23)$$

2.4. The Rotating Disc Electrode

The rotating disc electrode (RDE) gives rise to the phenomenon of forced convection. The fundamental mathematical problem associated with this technique is in solving the equations related to a fluid moving past a solid surface. At the surface the fluid flow velocity is zero. At some distance away, measured in the x direction normal to the surface, the flow velocity has a value characteristic of the bulk solution unaffected by the solid body. Between these extremes there exists a region in which there is a substantial velocity gradient. This layer is known as the hydronamic boundary layer (δ_o). Reacting species will be transported to a rotating electrode physically by the moving fluid. In addition to this forced convection, there will be diffusion when concentration gradients exist.

From a detailed consideration of the hydrodynamics in an experiment with the rotating disc electrode, Levich[29] has shown that

$$i = \frac{nF \vec{k} C_o^{\infty}}{1 + 1.61 \vec{k} \omega^{-\frac{1}{2}} \nu^{1/6} D_o^{-\frac{2}{3}}} \qquad (2.24)$$

where $\vec{k}$ is the potential dependant rate constant for the forward electrode reaction, ω is the rotation speed in radians s^{-1}, ν is the kinematic viscosity (viscosity/density), D_o is the diffusion coefficient of the oxidised species and C_o^{∞} is the bulk concentration of the oxidised species.

At large overpotentials, $\vec{k}$ will be large and the electron transfer is fast compared to mass transfer i.e. the electrode process is mass transfer controlled. For large k, equation (2.24) reduces to

$$i = 0.621\ nFD_o^{\frac{2}{3}}\ \nu^{-1/6}\ C_o^{\infty} \omega^{\frac{1}{2}} \qquad (2.25)$$

and a plot of i vs. $\omega^{\frac{1}{2}}$ will be linear.

Conversely for small values of $\vec{k}$, the situation when working at low overpotentials, the electron transfer is slow compared with mass transfer and equation (2.24) becomes

$$i = nF\vec{k}\ C_o^{\infty} \qquad (2.26)$$

and the current does not depend on the rotation rate.

For intermediate values of $\vec{k}$, mass transfer and electron transfer are of comparable rates and equation (2.24) must be used in full and is usually rewritten as

$$\frac{1}{i} = \frac{1}{nF\vec{k}C_o^{\infty}} + \frac{1.61\ v^{1/6}}{nFD_o^{\frac{2}{3}}\ C_o^{\infty}} \cdot \frac{1}{\omega^{\frac{1}{2}}} \qquad (2.27)$$

A plot of $\frac{1}{i}$ vs.. $\frac{1}{\omega^{\frac{1}{2}}}$ is linear and the value of $\vec{k}$ may be obtained from the intercept.

For some electrode reactions the reverse reaction must also be considered

$$O + ne \underset{\overleftarrow{k}}{\overset{\vec{k}}{\rightleftharpoons}} R \qquad (2.28)$$

and the solution of the rotating disc problem is

$$\frac{1}{i} = \frac{1}{nF(\vec{k}\ C_o^{\infty} - \overleftarrow{k}\ C_R^{\infty})} + \frac{1.61\ v^{1/6}\ (\vec{k}D_o^{\frac{1}{3}} + \overleftarrow{k}\ D_o/D_R^{\frac{2}{3}})}{nF\ D_o(\ \vec{k}C_o^{\infty} - \overleftarrow{k}C_R^{\infty})\ \omega^{\frac{1}{2}}} \qquad (2.29)$$

A plot of $1/i$ vs $1/\omega^{\frac{1}{2}}$ will still be linear and both $\vec{k}$ and $\overleftarrow{k}$ can be obtained from the slope and intercept.

2.5. Faradaic Impedance Measurements

The faradaic impedance at the working electrode arises from the electrochemical reaction taking place there. Randles[38,39] proposed that the electrode impedance could be represented by the equivalent circuit shown in Fig. 2.6 where R_{sol} is the ohmic resistance of the electrolyte, and C_{DL} is the double layer capacitance (which varies with d.c. potential depending on the concentration and nature of the electrolyte). Θ is the charge transfer resistance and is related to the exchange current density by equation (2.12). The Warburg Impedance[40] is the a.c. impedance due to charged species diffusing to and from the electrode. Randles derived the following expressions for Θ and W:

$$\Theta = \frac{RT}{z^2F^2k_{sh}} \cdot (C_o^s)^{\alpha} \; (C_R^s)^{1-\alpha} \qquad (2.30)$$

and

$$W = \sigma \omega^{-\frac{1}{2}} (1-j) \qquad (2.31)$$

where σ is the Warburg coefficient, ω the angular frequency and $j = (-1)^{\frac{1}{2}}$.

The Warburg coefficient can be expressed as

$$\sigma = \frac{RT}{z^2F^2 2^{\frac{1}{2}}} \left(\frac{1}{C_o^s D_o^{\frac{1}{2}}} + \frac{1}{C_R^s D_R^{\frac{1}{2}}} \right) \qquad (2.32)$$

In (2.31) and (2.32), C_o^s and C_R^s can be replaced by C_o^b and C_R^b if measurements are made at the equilibrium potential. At potentials away from this value σ and Θ can be expressed in terms of bulk

concentrations provided that (2.31) and (2.32) are suitably modified[41]

Various methods have been proposed for the determination of Θ and σ from impedance measurements. Vector methods were used by Randles[38] and Delahay[42]. Gerischer[43] has presented a treatment in which he neglected the imaginary part of the Warburg impedance and Vetter[44] has corrected the cell impedance for the double layer capacitance and solution ohmic resistance. In the present studies the "complex plane" technique devised by Sluyters[45] was used. This method involves plotting the real component (Z') and the imaginary component (Z'') of the cell impedance against each other as a function of some varied parameter (usually frequency).

The cell impedance is given by

$$Z = R_{sol} + \frac{1}{j\omega C_L + \frac{1}{\Theta + \sigma\omega^{\frac{1}{2}} - j\sigma\omega^{\frac{1}{2}}}} \qquad (2.33)$$

After separation of the r eal and imaginary parts of Z we obtain

$$z = Z' - jZ'' \qquad (2.34)$$

where Z' and Z'' are given by

$$Z' = R_{sol} + \frac{\Theta + \sigma\omega^{-\frac{1}{2}}}{(\sigma\omega^{\frac{1}{2}}C_L+1)^2+\omega^2 C_L(\Theta+\sigma\omega^{-\frac{1}{2}})^2} \qquad (2.35)$$

and

$$Z'' = \frac{\omega C_L(\Theta+\sigma\omega^{-\frac{1}{2}})^2 + \sigma\omega^{-\frac{1}{2}}(\sigma\omega^{-\frac{1}{2}}C_L+1)}{(\sigma\omega^{\frac{1}{2}}C_L+1)^2+\omega^2 C_L(\Theta+\sigma\omega^{-\frac{1}{2}})^2} \qquad (2.36)$$

FIG.2.6. Electrical analogue of the electrode interphase.

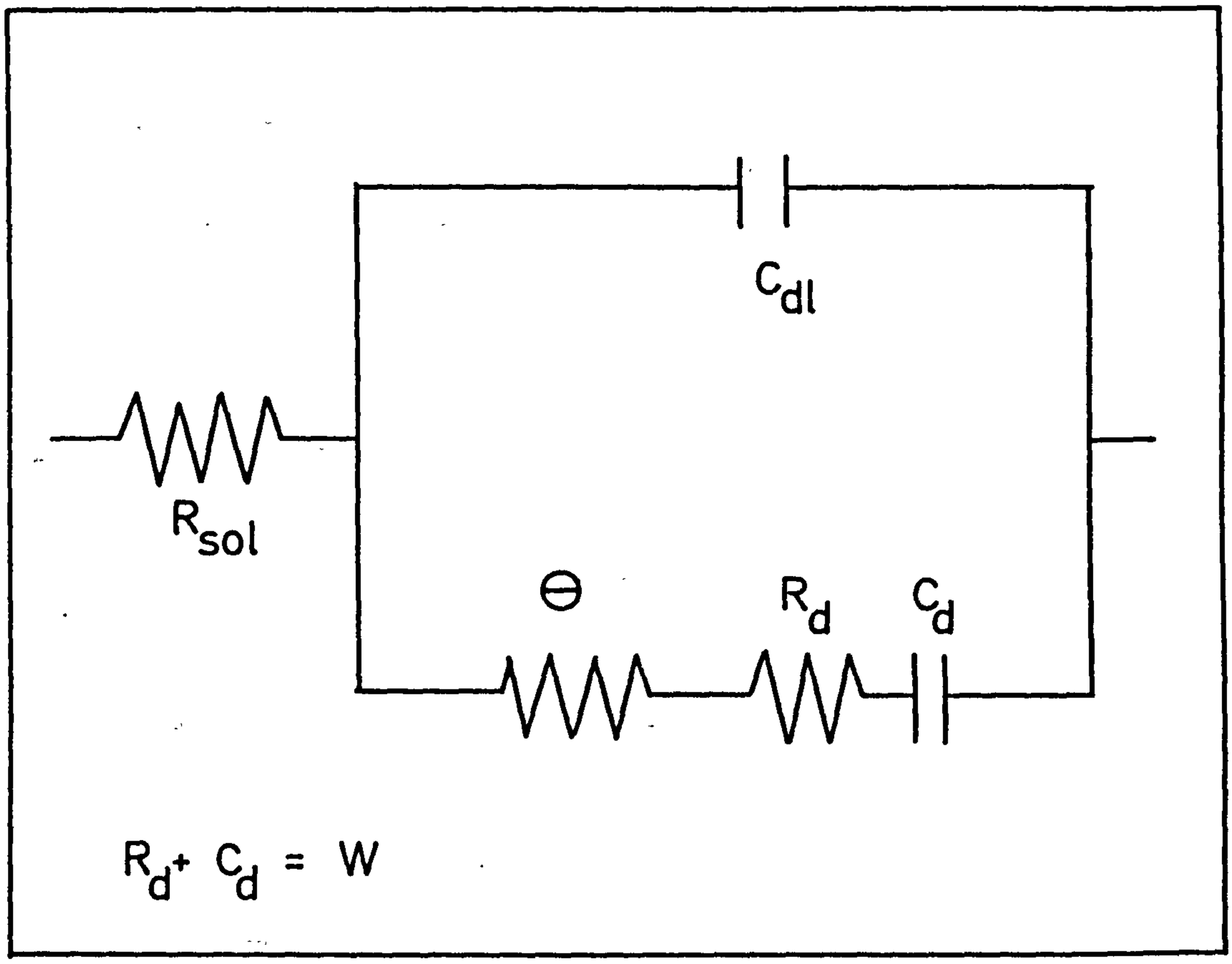

Although equation(2.34)is complex, its two limiting frequencies yield important results:

a) <u>At low frequencies</u>

Equation (2.34) reduces to

$$Z = R_{sol} + \Theta + 6\omega^{-\frac{1}{2}} - j\,(6\omega^{-\frac{1}{2}} + 2\theta^2 C_L) \qquad (2.47)$$

When the real and imaginary parts are plotted against each other we obtain a straight line of unit slope.

b) <u>At high frequencies</u>

The concentration polarisation (W) can be neglected for a fairly irreversible reaction and (2.34) reduces to

$$z = R_{sol} + \frac{\Theta}{1 + \omega^2 C_L^2 \Theta^2} - j\,\frac{\omega\, C_L \Theta^2}{1 + \omega^2 C_L^2 \Theta^2} \qquad (2.38)$$

In this case, if the real and imaginary parts are plotted against each other, a semi-circle is obtained (Fig. 2.7). At lower frequencies, diffusion polarisation will give rise to a distortion of the semi-circle, as illustrated in Fig. 2.8, eventually leading to a line of 45° slope.

The simple process has been extended to incorporate the effects of surface processes by Grahame[47] and more recently by Sluyters[48]. The incorporation of extra resistances and capacitances in the simple electrode analogue are used to represent the adsorption of species. If the adsorbate is not electroactive then the effect is to modify the double layer capacitance. If, however, the adsorbed species are able to undergo a redox reaction then the effect is an

FIG. 2.7 Complex plane display - charge transfer control.

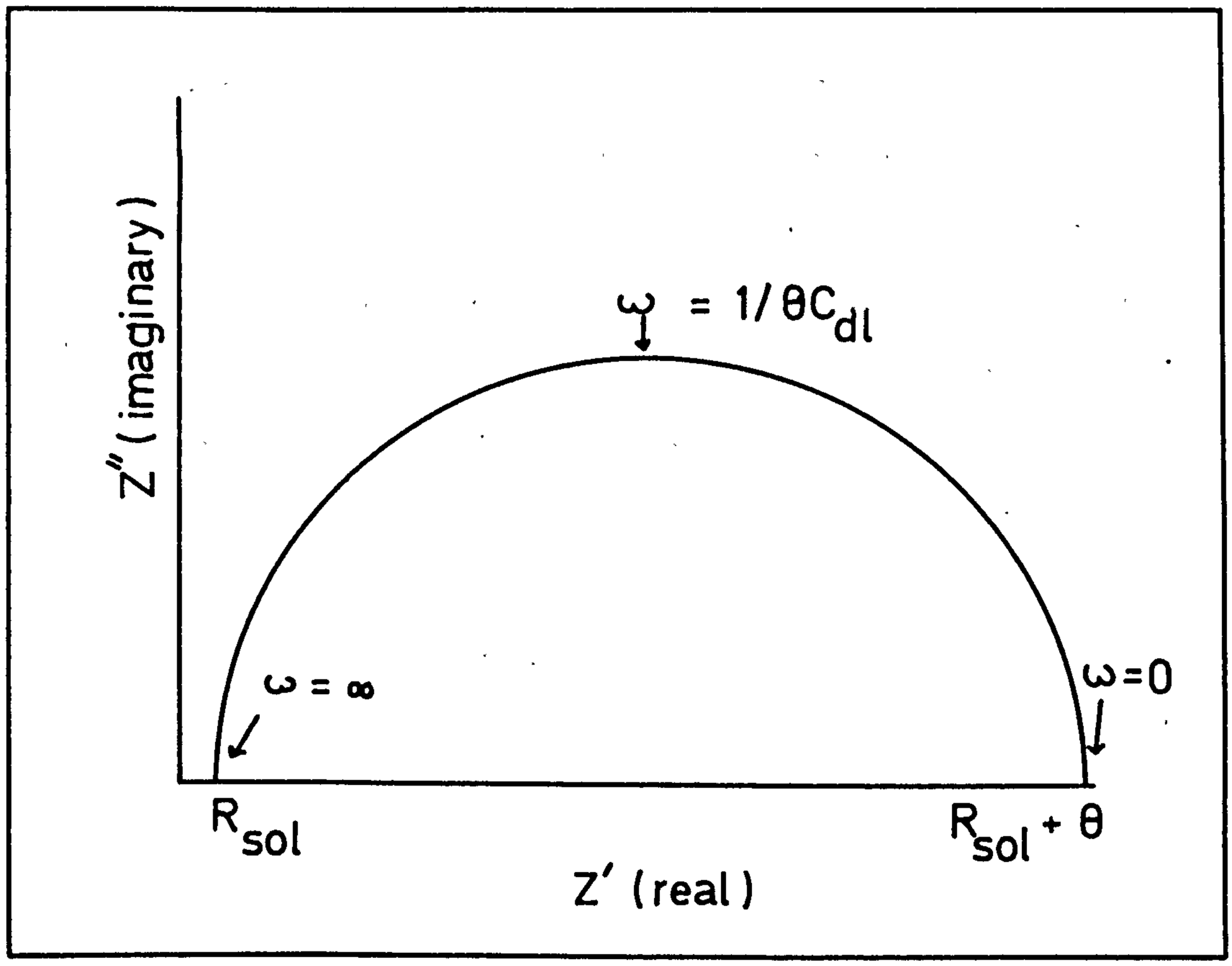

FIG. 2.8 . Complex plane display - mixed control.

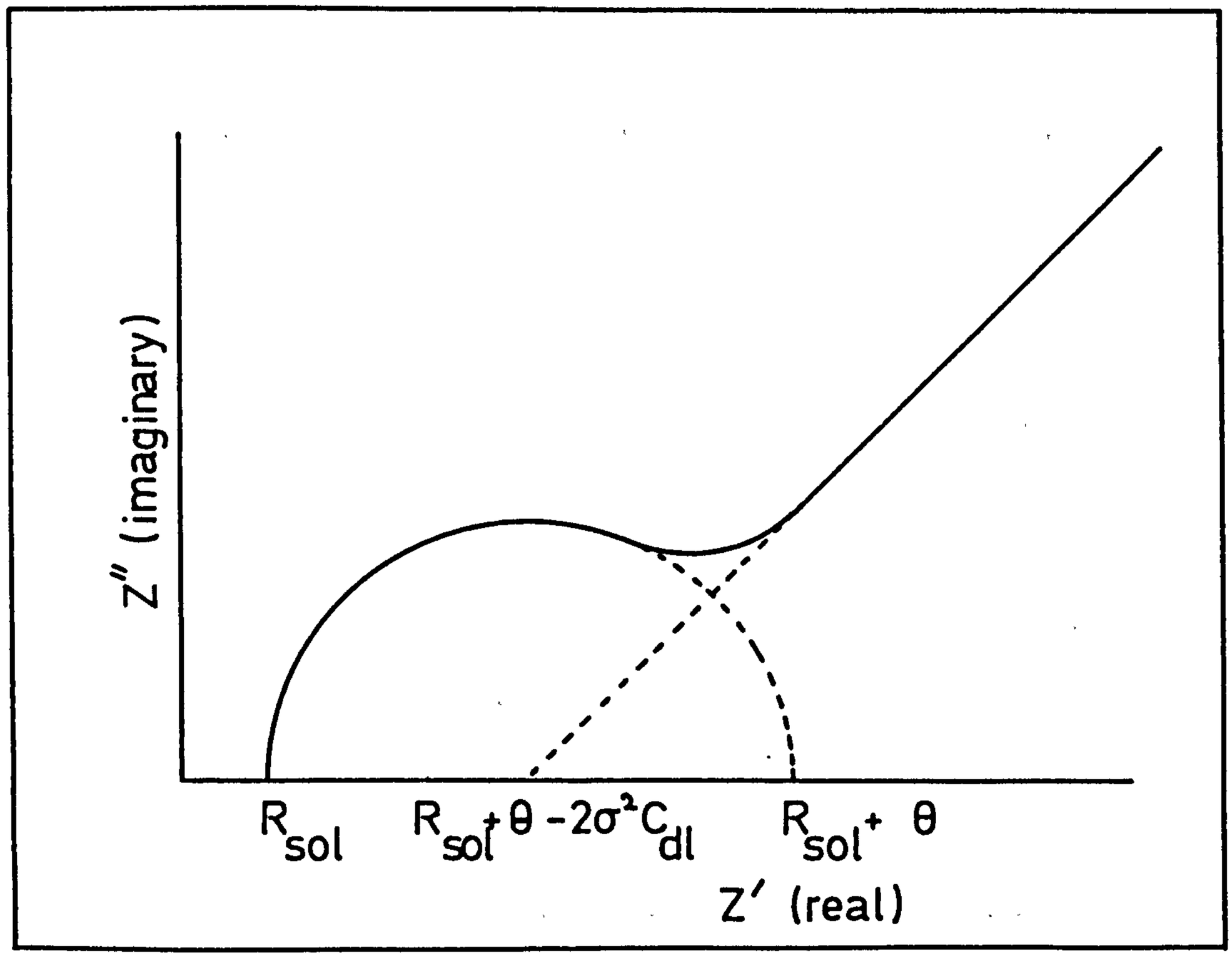

extra resistance and capacitance shunting the double layer. The first example of this was described by Laitinen and Randles[49]. The review by Armstrong et al[50] extends the discussion of complex reactions to passivity and nucleation and growth processes. Here the impedance spectra due to 2-dimensional nucleation and growth have been calculated. It was demonstrated that extremely distorted semicircles are to be expected as distinct from ones found for the adsorbed intermediate case (adatom model). A recent review of the impedance of electrical storage cells has been made by Hampson et al[51]. which includes a discussion of the use of the impedance of cells as in 'in situ' test of energy availability.

2.6. Cyclic Voltammetry

In cyclic voltammetry the potential applied to an electrode is changed linearly with time in a repetitive manner and the current is measured as a function of potential or time. If only a single sweep (anodic or cathodic) is performed then the technique is known as the linear potential sweep method.

The fundamental equations for sweeping voltammetry have been developed by Delahay[44], Shain[52,53] and others[54-57]. The basic feature of a voltammogram (i.e. a current-potential plot during the sweep) is the appearance of a current peak at a potential characteristic of the electrode reaction taking place. The position and shape of this current peak depend on many factors including sweep-rate, electrode material, solution composition and the concentration of the reactants. Only the linear potential sweep can provide accurate

kinetic parameters, since the equations derived apply only if there are no concentration gradients in solution just before the sweep is started. Cycling the potential several times creates complex concentration gradients near to the electrode surface and the boundary-layer problem has not been solved. Thus, cyclic voltammetry is better suited to the identification of steps in the overall reaction and of new species which appear in solution during electrolysis as a result of combined electrochemical and chemical steps. Nevertheless, an approximate value of the rate constant can be derived from the separation of the anodic and cathodic peak potentials at a given sweep rate for irreversible reactions.

The mechanisms indicated by cyclic voltammetry alone are relevant only to the specific experimental conditions chosen, and may not be applicable to steady-state electrolysis of the same systems in well stirred solutions. Kinetic parameters can only be evaluated correctly if the reaction mechanism is known and the equations relevant to this mechanism employed. In spite of these limitations, cyclic voltammetry has found widespread usage in the study of organic electrode reactions and is particularly valuable for the qualitative detection of intermediates formed in complex reaction sequences.

The basic equations of linear potential sweep relate the peak current density (i_p), and the corresponding potential (E_p) to k_s, the electrochemical specific rate constant at the standard potential E^o, the Tafel slope (b), the concentration in solution (C^o), and the sweep rate (ν), which is equivalent to $\frac{dE}{dt}$. For a simple charge transfer process under reversible conditions, where both reactant and

product are soluble, i_p (in A cm^{-2} at 25°C) is given by

$$|i_p| = 2.72 \times 10^5 \, n^{3/2} \, D^{\frac{1}{2}} \, C^o \nu^{\frac{1}{2}} \qquad (2.39)$$

where D is in $cm^2 \, s^{-1}$, C^o in mol cm^{-3} and ν in V s^{-1}. E_p is related to the polarographic half-wave potential ($E_{\frac{1}{2}}$) by

$$E_p = E_{\frac{1}{2}} - 1.1 \frac{RT}{nF} \qquad (2.40)$$

Under totally irreversible conditions, i.e. when the rate of the reverse reaction is negligible throughout the potential region studied, the following equations apply:

$$i_p = 3.01 \times 10^5 \, n \left(\frac{2.3RT}{bF}\right)^{\frac{1}{2}} \, D^{\frac{1}{2}} \nu^{\frac{1}{2}} \, C^o \qquad (2.41)$$

where all of the units are as in equation 2.39 and b is in volts. The peak potential is given under these conditions by

$$E_p = E_{\frac{1}{2}} - b \left(0.52 - \tfrac{1}{2} \log \frac{b}{D} - \log k_s + \tfrac{1}{2} \log \nu \right) \qquad (2.42)$$

The variation of E_p with sweep rate is an indication of the departure of the system from equilibrium. The specific rate constant (k_s) at the standard potential and the Tafel slope can be calculated from a plot of E_p vs $\log \nu$ according to (2.42) provided that the diffusion coefficient is known.

At sufficiently slow sweep rates a system will behave reversibly, whilst at high sweep rates it will behave irreversibly. From the characteristic sweep rate at which this transformation occurs it is possible to determine k_s.

The equations above apply quantitatively only to first order charge transfer reactions with no kinetic or catalytic complications.

2.7. The Potential-Step Method

In the potential-step method, the potential of the working electrode is instantaneously changed from a potential at which the state is well defined and static to a new potential where the reaction of interest takes place; the current-time response is monitored as the system relaxes to the steady state. The transient takes the form of an initial current spike, which can be attributed mainly to the charging of the double layer, followed by a current decay as a result of depletion of the reactant near the electrode surface.

The time dependence of measured currents when falling transients are solely a consequence of diffusion have been discussed in section 2.3

The other limiting case occurs when the rate of diffusion is much faster than the electron transfer process or any other reaction in the overall sequence. The current, in this case, will be independent of time except for a charging current at very short times.

In the intermediate situation, the difference in rates between diffusion and the other processes will be minimal and a falling i-t transient will again be observed since diffusion is partially determining the rate of the electrode process. The decay curve will fall less steeply however, than when diffusion is solely rate determining. Mass transfer will be fastest at short times (i.e. when the concentration gradient is steepest), and at long times the current will tend to become

diffusion controlled.

It has been shown (equation (2.23)) that at high overpotentials when the electron transfer is fast, The current was always determined by the rate of diffusion, the whole transient yields a linear plot of i vs $t^{-\frac{1}{2}}$. At lower overpotentials where, in the steady state, electron transfer and diffusion occur at similar rates it is possible to show that

$$i = nF\, k_c C_o^b \exp\left(\frac{k_c + k_a}{D}\right)^2 t \;\text{erfc.}\; \frac{(k_c + k_a)t^{\frac{1}{2}}}{D^{\frac{1}{2}}} \qquad (2.43)$$

and that this expression has the limiting forms

$$i = \frac{nFk_c C_o^b\, D^{\frac{1}{2}}.t^{\frac{1}{2}}}{\pi^{\frac{1}{2}}(k_c + k_a)} \quad \text{at long times} \qquad (2.44)$$

and

$$i = nFk_c C_o^b \left(1 - \frac{(k_c+k_a)}{\pi^{\frac{1}{2}} D^{\frac{1}{2}}} .t^{\frac{1}{2}}\right) \text{ at short times} \qquad (2.45)$$

Hence at short times the i-t transient contains kinetic data which may be obtained by extrapolation of a linear i vs. $t^{\frac{1}{2}}$ plot to t=0, while at long times a plot of i vs. $t^{-\frac{1}{2}}$ should be linear.

2.8. Electrocrystallisation

The formation of a crystalline deposit on an electrode can be considered to consist of two main stages:

(i) The initial stages of growth which produce a very thin layer of product

(ii) Subsequent thickening of the layer to form a macro-deposit

One of the essential prerequisites for crystal growth is the generation of an edge at which growth can proceed. In general, the formation of nuclei is required so that growth can occur at their peripheries. This section is restricted solely to the potentiostatic response of the nucleation and growth model(without edge effects).

A. Two Dimensional Nucleation and Growth

i) Without Diffusion

When a pulse is started nuclei form as discrete centres, either instantaneously or progressively with time, and grow[58].

If the transport of material to a growing centre is not rate determining, then its rate of growth depends only upon geometric factors. Expressed as a current this rate is

$$i = nFkA \tag{2.46}$$

where

$$nFkA \quad \rho\frac{nF}{M}\cdot\frac{\partial V}{\partial r}\cdot\frac{\partial r}{\partial t} \tag{2.47}$$

where A is the area on which material is deposited, V is the volume and k is the rate constant for the electrochemical equation for growth around the periphery. Once A and dV/dr are known (by taking a particular geometry) then integration of (2.47) give r as a function of t. This enables the calculation of an expression for the

current flow and hence the characteristic current-time curves in the early stages (before nuclei overlap) can be deduced.

These calculations can be extended to progressive nucleation where the number of nuclei at any one time (N) is given by

$$N = No(1-(\exp-A't) \tag{2.48}$$

where A' is the nucleation rate constant and No is the initial number of nuclei. The processes of nucleation and growth occur simultaneously and the resulting current is given by

$$i = \int_0^t i(u) \left(\frac{dN}{dt}\right)_{t=u} du \tag{2.49}$$

where u is the age of a nucleus. The value of i(u) can be found by integration of (2.47) and expressing A in terms of the radius of the surface. If i(u) is represented in this manner and t is replaced by u and dN/dt by

$$\frac{dN}{dt} = NoA' \exp(-A't) \tag{2.50}$$

or in particular simply by the approximationi

$$\frac{dN}{dt} = NoA' = A' \tag{2.51}$$

then i can be estimated as a function of t.

A summary of the expressions for an unbound electrode, calculated on this basis, have been given previously[59]. These dependencies are all

of the form $i \propto t^{\beta}$ and are rising transients with β depending primarily on the geometry and type of nucleation.

When nuclei overlap the form of the current-time curve can still be calculated provided that the overlapping is random, the growth outwards is uniform and the boundaries of the electrode do not interfere. For random overlap Avrami[60] has shown that:

$$A_1 = 1 - \exp(-A_{1\,ex}) \tag{2.52}$$

where A_{1ex} is the top area of an isolated nucleous and A_1 is the actual area. Combining this with equation (2.47) allows i to be determined. The results(for the growth of cylinders of height h) are:

$$i = \frac{nF\pi M}{\rho} h A' k^2 t^2 \exp \frac{-\pi M^2 A' k^2 t^2}{3\rho^2} \tag{2.53}$$

for progressive and

$$i = \frac{nF\pi M}{\rho} Nok^2 t \exp \frac{-\pi M^2 Nok^2 t^2}{\rho^2} \tag{2.54}$$

for instantaneous nucleation.

Equations (2.53) and (2.54) have the characteristic shape shown in Fig. 2.9 when plotted in the non-dimensional form. The experimental i-t plots have a similar shape. The maximum current (im) and time (tm) are obtained by differentiation of (2.53) and (2.54) The arguments used to derive equations (2.53) and (2.54) have been

extended to "layer-by-layer" growth[61] and Fig. 2.10 displays the i-t transient.

ii) <u>With Diffusion</u>

The i-t relationship can be estimated when the nuclei are surrounded by a fixed diffusion zone. For the previous case, i.e. without diffusion, the value of $(i_m t_m/Q_m)$ is constant and has a theoretical value of 1.0 for progressive and 0.6 for instantaneous nucleation, where Q_m is the maximum charge. When, however, 2-D nucleation and growth occurs with diffusion, a simulation shows that the $(i_m t_m/Q_m)$ value is no longer a fixed constant but is less than the values for progressive nucleation and for instantaneous nucleation. The chemistry and electrochemistry of the system will determine how the apparent fixed diffusion zone arises[62].

The problem of a diffusion zone which increases with time without overlap has been considered[63] for the growth of one 2-D nucleus expanding at a rate determined by the flux; the diffusion zone is concentric to the nucleus. The radius at time t is considered to obey:

$$r(t) = \theta (Dt)^{\frac{1}{2}} \qquad (2.55)$$

where r(t) is the radius of the nucleus at time t and θ is a constant controlled by the potential, M and ρ. For instantaneous nucleation, the Avrami[52] treatment gives:

$$i = q_m \pi \theta^2 D \exp -\pi \theta^2 D N_o t \qquad (2.56)$$

and for progressive nucleation gives:

$$i = q_m \pi \theta^2 D A' t \exp. \quad -\pi \frac{\theta^2 D A' t^2}{2} \qquad (2.57)$$

B. Three Dimensional Nucleation and Growth

In principle, three-dimensional deposits can always be formed by the "layer-by-layer" growth mentioned earlier. It is more useful, however, to consider a model[64] which ignores the finite size of atoms. The problem has been attacked in the manner of Fig. 2.11 where the rates of advance V_1, V_2 and V_3 are defined. The calculations are performed on a slice of a cone (of height dx) a distance x from the metal surface. It is assumed that the nuclei are distributed at random on the surface and the interaction of slices at a height x can be described by the Avrami equation. A number of models for three-dimensional growth are shown in Fig. 2.11 and the corresponding i-t curves in Figs. 2.12.

Fig 2.9 Theoretical current time curves according to

(a) equation (2.53)

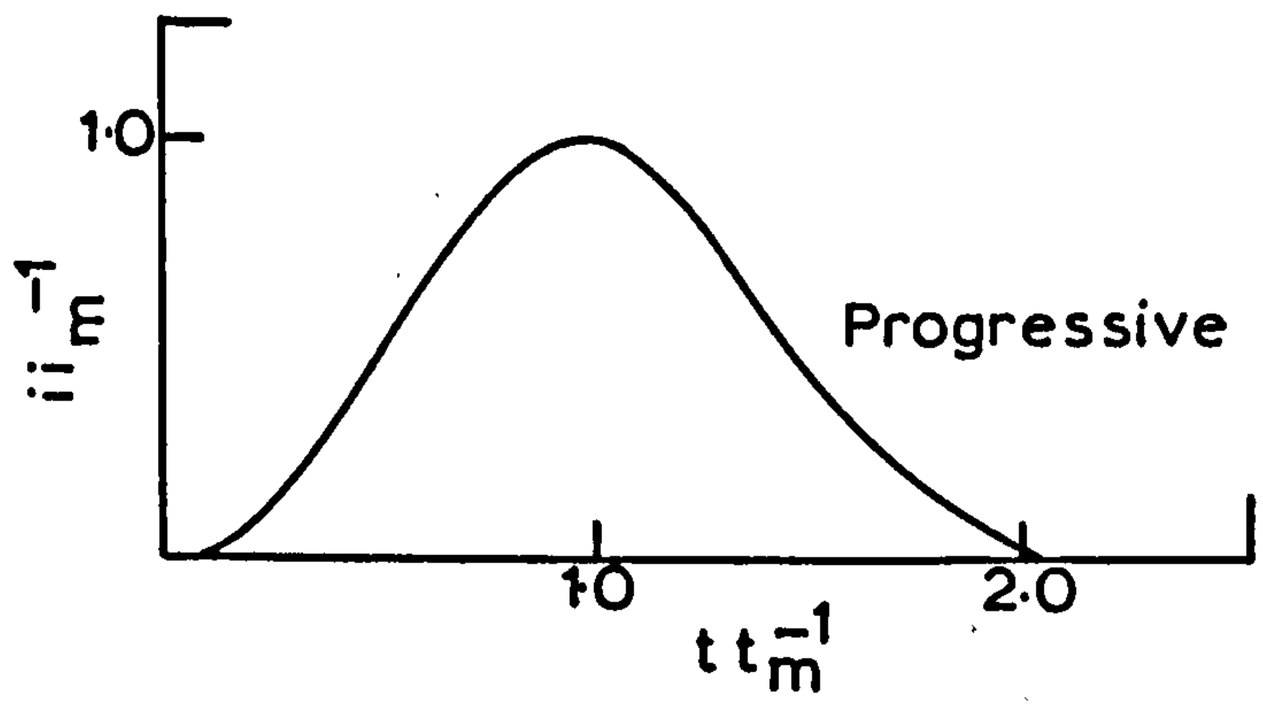

(b) equation (2.54)

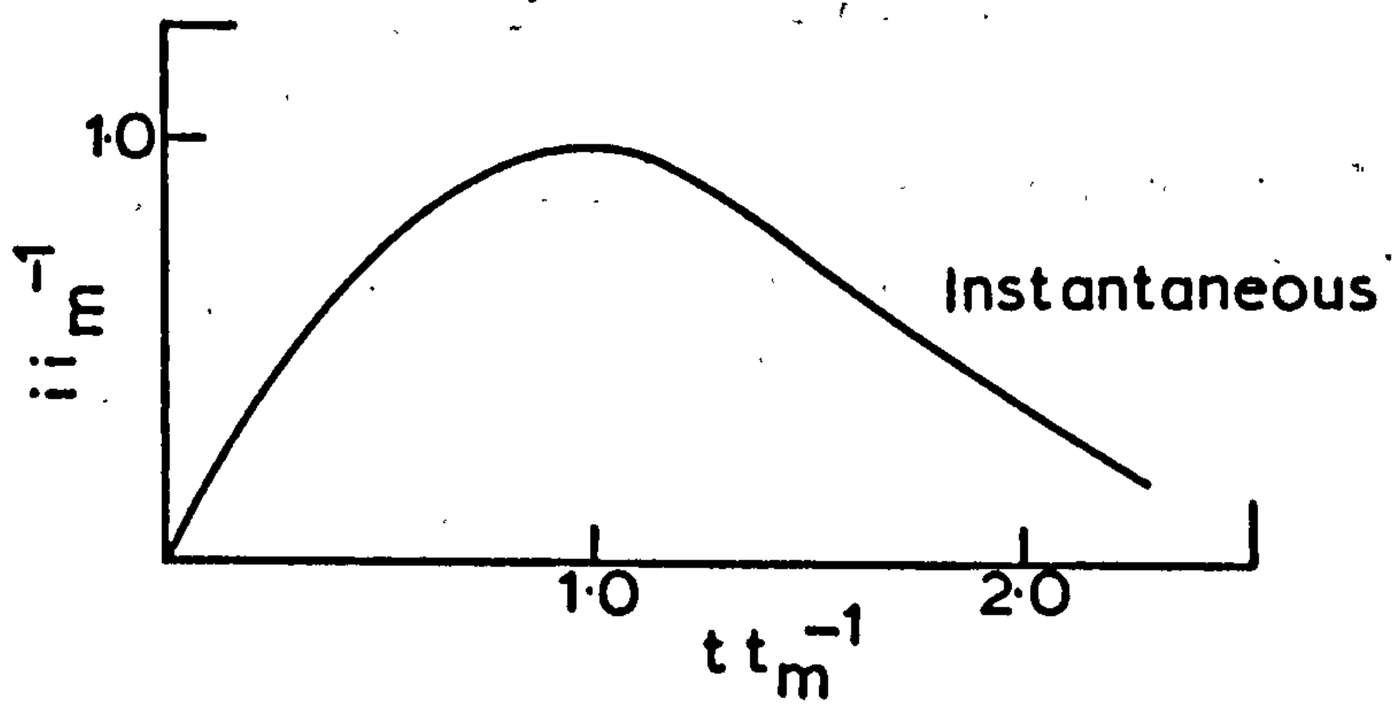

Fig. 2.10 Total current transient for layer by layer growth showing contribution from individual layers

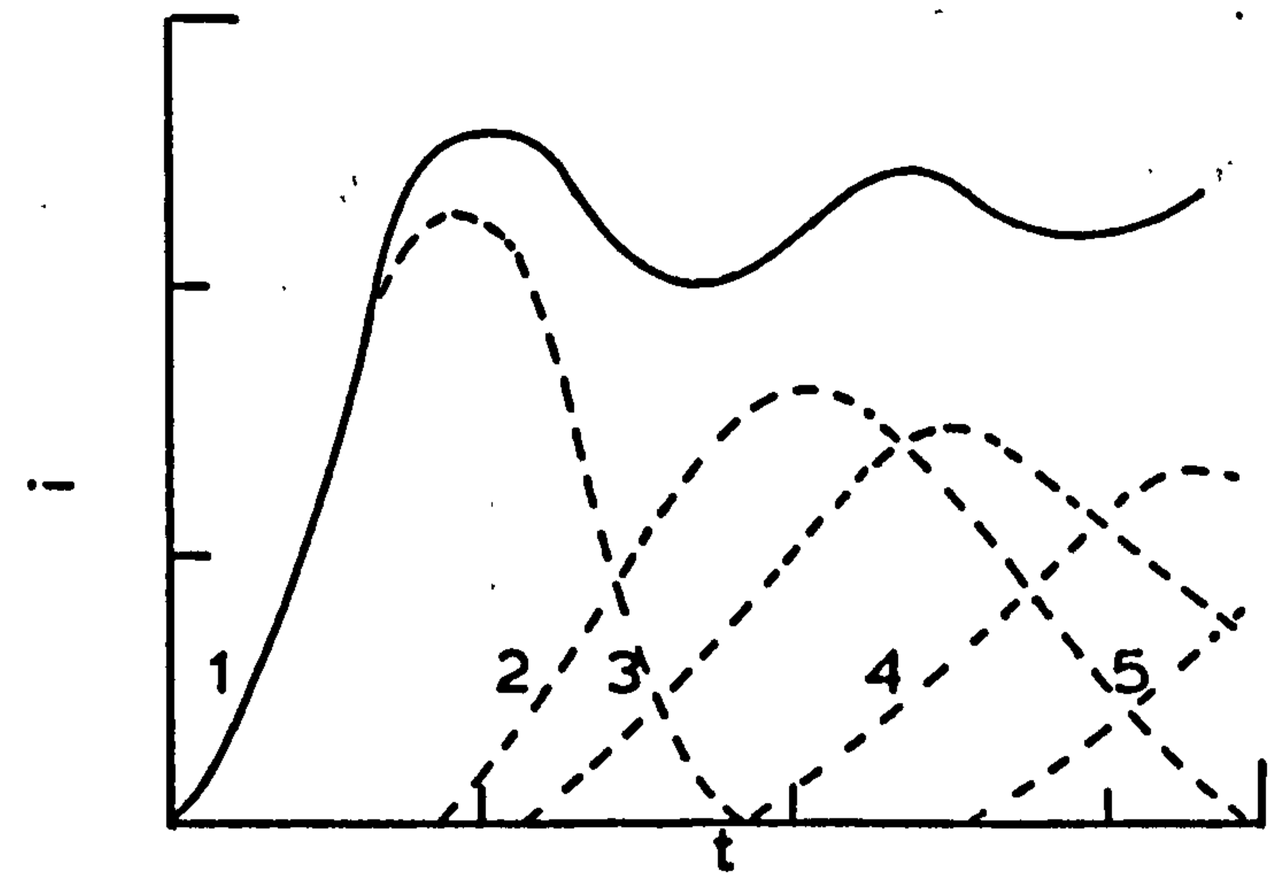

Fig 2.11 Three dimensional models

(a) growth of circular cones on an inert substrate (metal deposition)

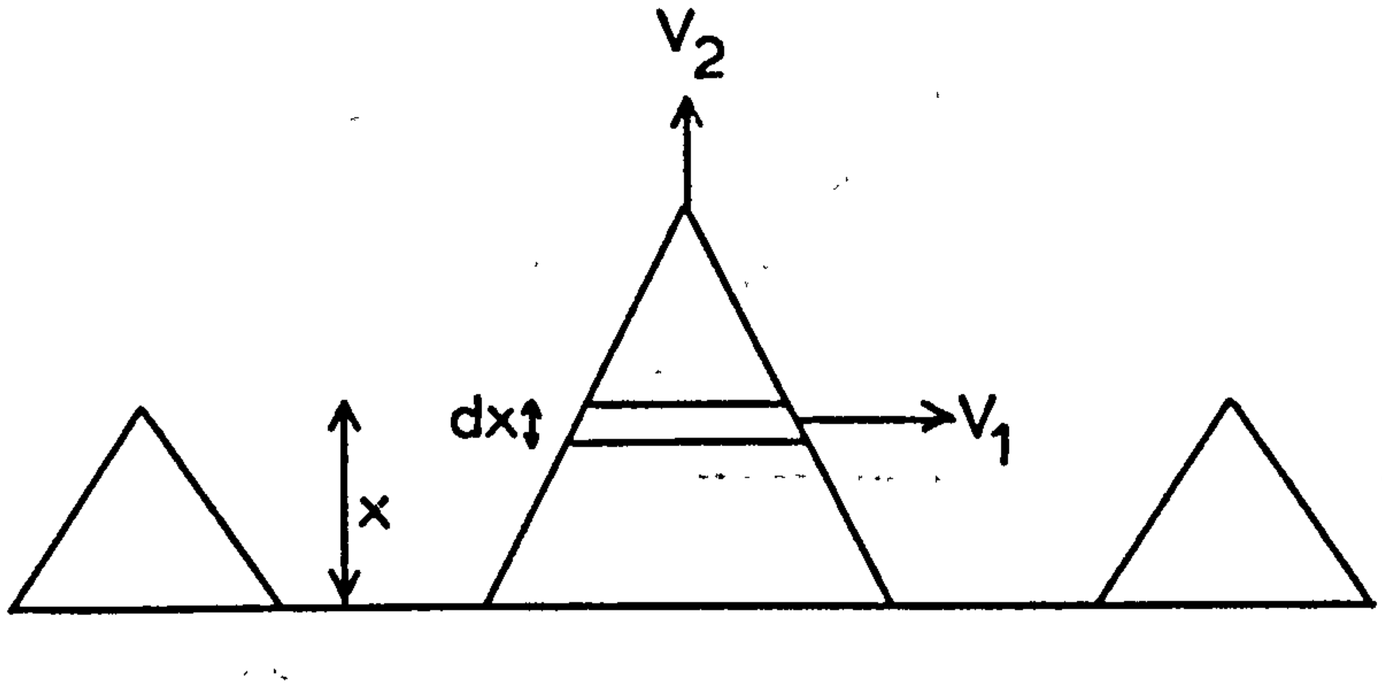

(b) growth of circular cones on a substrate of the same material, the base plane moves with velocity V_3 (metal deposition)

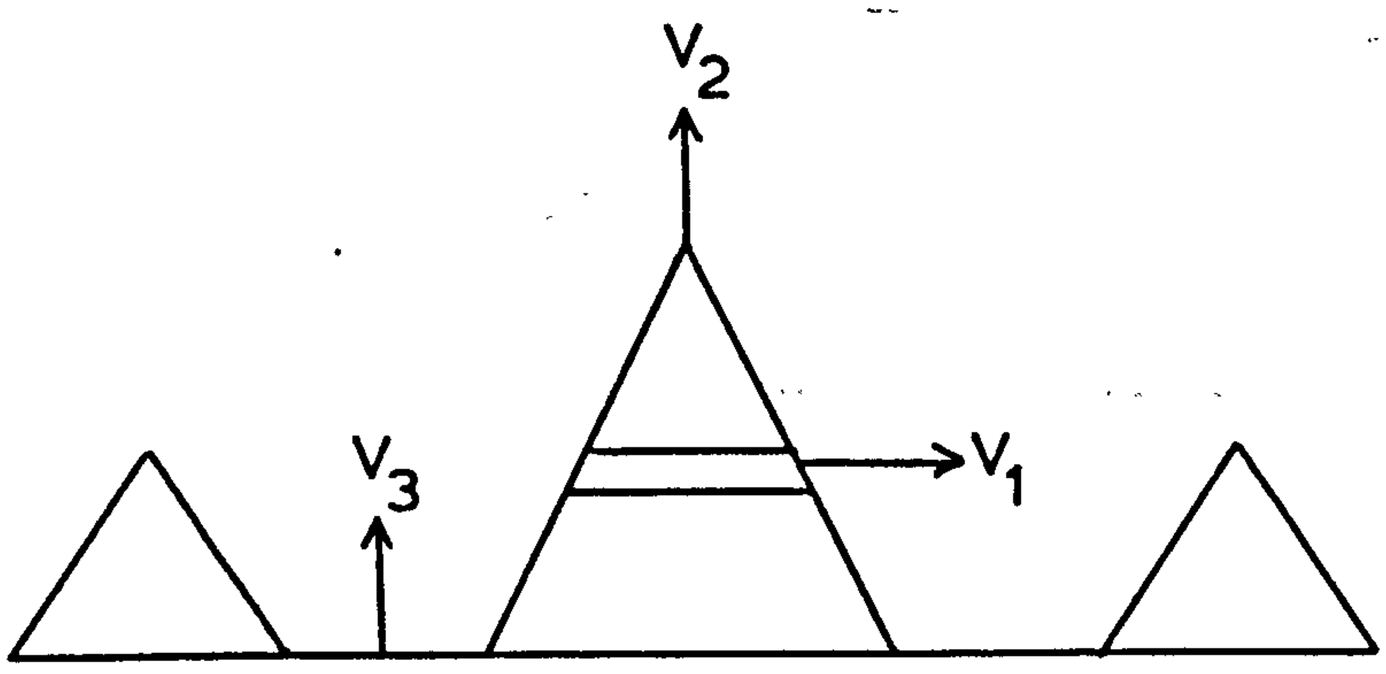

(c) current only flows into the uncovered area (passivation)

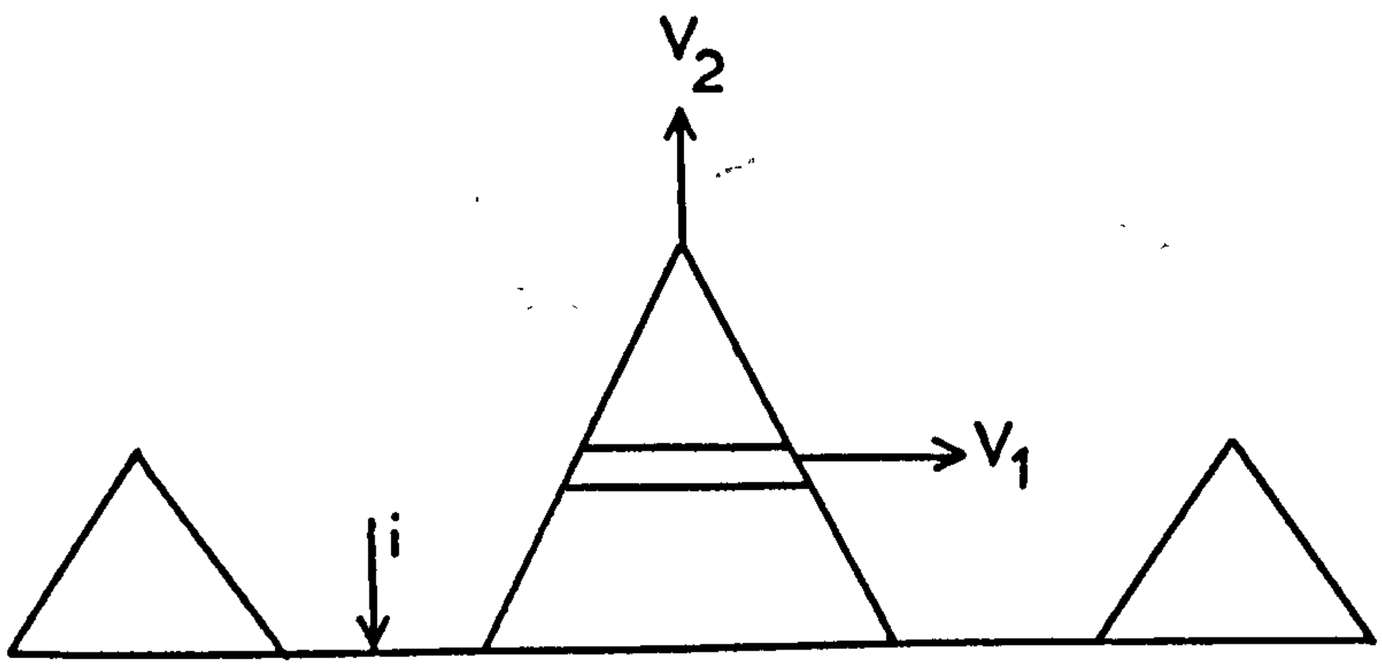

Fig 2.12 The form of current time transients for the models of Figure 2.11

(a)

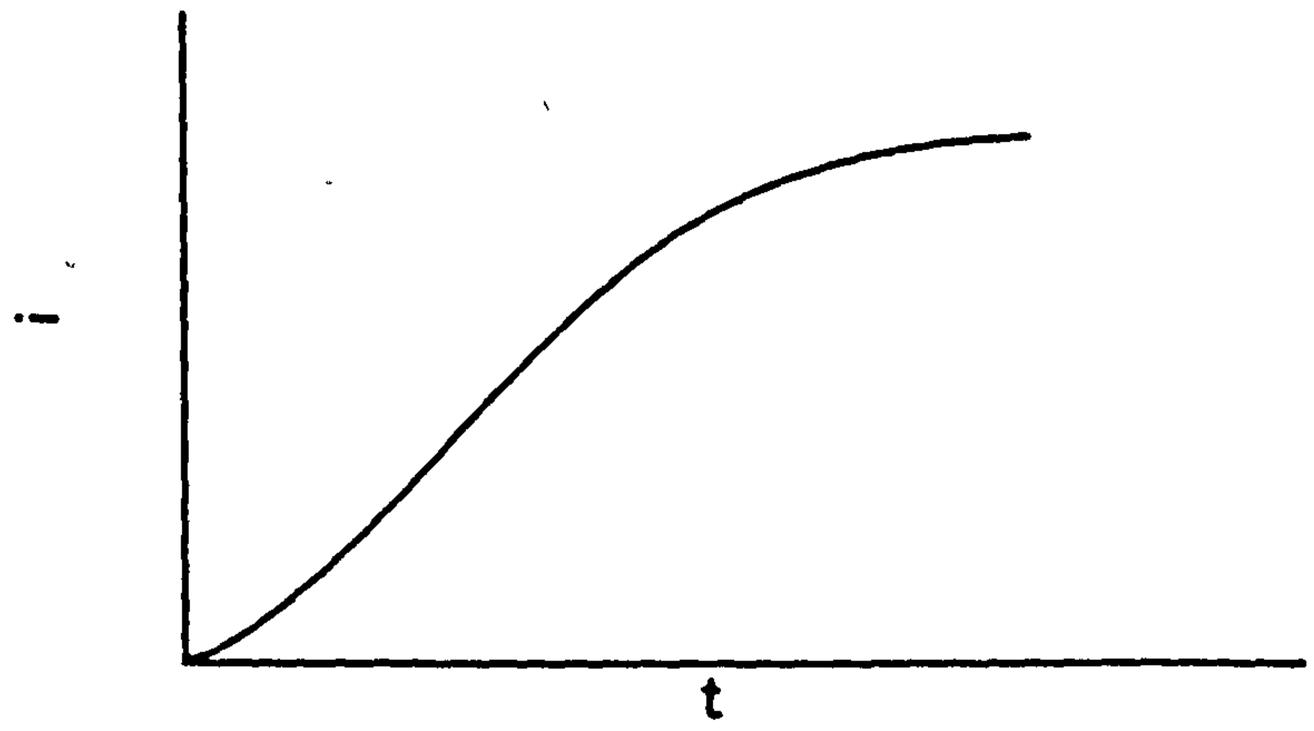

(b)

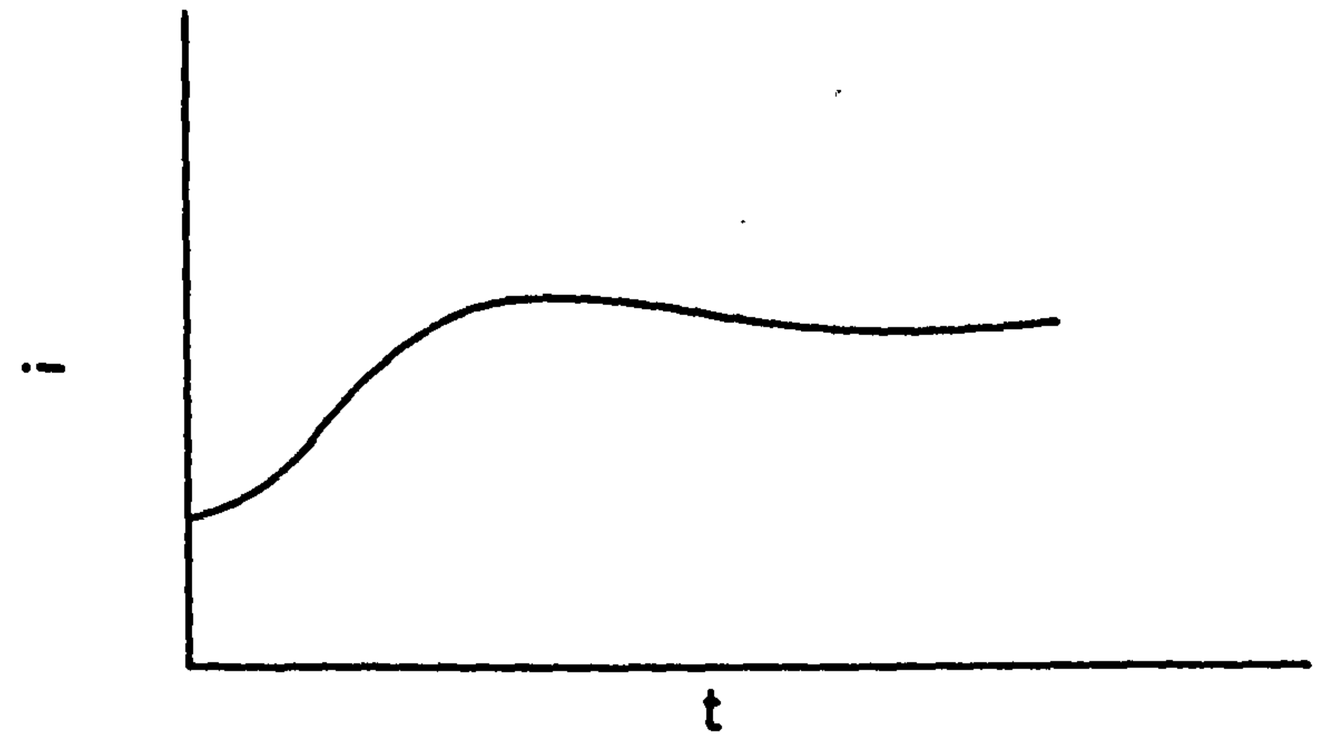

(c)

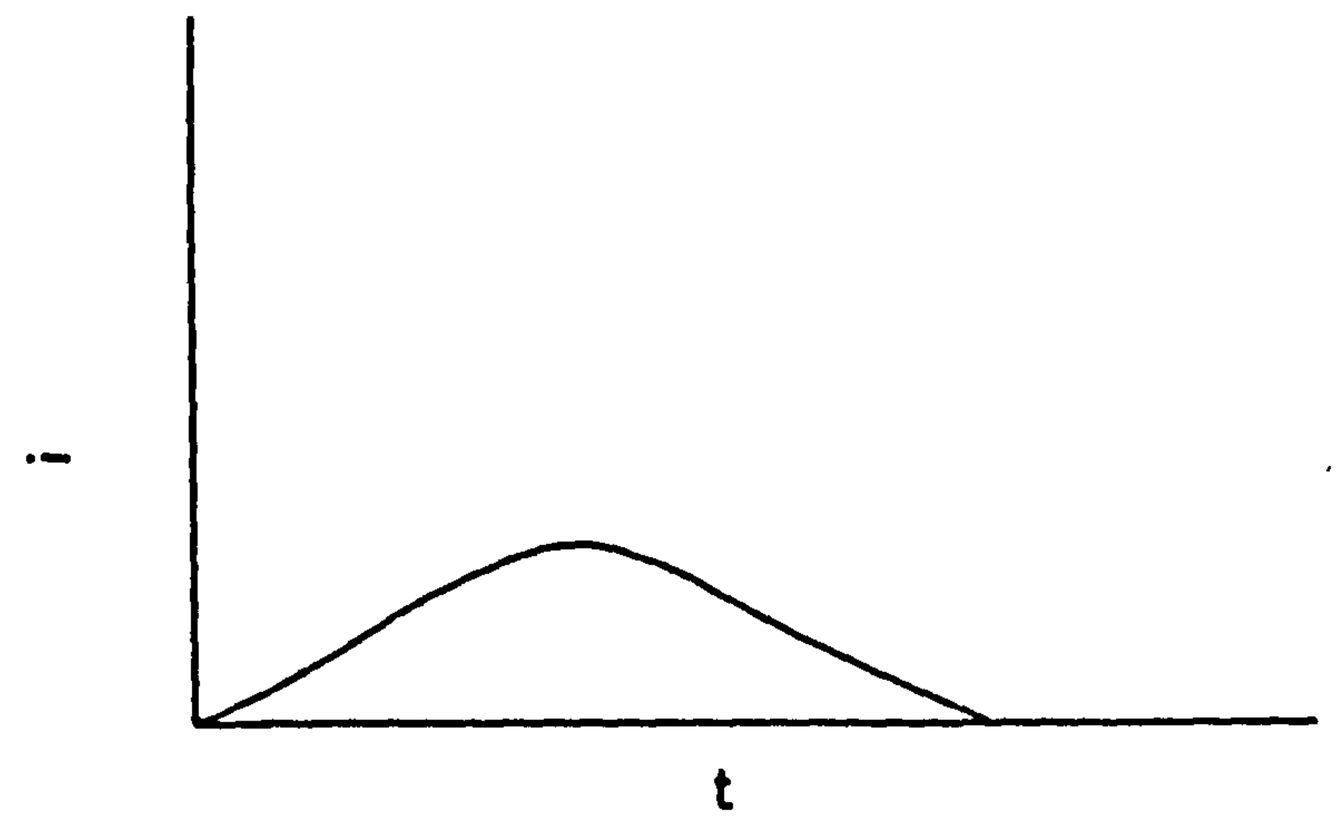

2.9. Porous Electrode Theory

The performance of porous lead electrodes is a function of many parameters which include:

(a) temperature
(b) rate of discharge
(c) quantity of active material present
(d) electrode thickness
(e) porosity of electrode
(f) concentration of electrolyte
(g) quantity of electrolyte
(h) electrode design

The task of modelling the porous electrode to account for all these factors is enormous and at best the model is a simplified mathematical expression for the transport and kinetic phenomena occurring at the electrode. Work on mathematical modelling has been reviewed by a number of authors[65-68]. The majority of models use a one-dimensional approach, where the pore geometry is ignored. This representation is valid when the distances over which there is significant variation in concentration and potential are large compared with the characteristic dimensions of the pore system. The models of flooded porous electrodes may be divided into three categories[69]:

(a) The pore model
(b) The analogue model
(c) The macrohomogeneous model

(a) The Pore model

The work on this model up to 1966 has been well reviewed by de Levie[65]. The electrode is represented by a parallel cyclindrical pore of constant radius perpendicular to the outer surface[70]. This

representation is difficult to apply to electrodes which must be considered as two-dimensional since questions would arise concerning the direction of the pores. The pore is considered to be homogeneously filled with electrolyte and the matrix resistance is assumed to be negligible. An important concept to arise from this theory is that of the penetration depth which characterises the distance to which a reaction can penetrate a porous electrode[70,71]. This length indicates the optimum thickness for a porous electrode and has considerable significance since electrodes much thinner than the penetration depth behave like planar electrodes of enhanced surface while those much thicker than the penetration depth are highly inefficient. De Levie has shown[65] that this characteristic length varies with the mechanism of current control. For a reaction-controlled porous electrode

$$1/p = \left(\frac{RTrk}{2nFi_o}\right)^{\frac{1}{2}} \qquad (2.58)$$

and for diffusion control, Bode[72] has shown that

$$1/p = \frac{C_p DnF}{i(1-p)} \qquad (2.59)$$

Bode has calculated a value for the penetration depth of 1mm for the lead-acid battery. In equation (2.59) C_p represents the concentration of electrolyte at the pore mouth so we can see that p varies with reactant concentration and hence the rate of discharge.

(b) The analogue model

This model makes use of equivalent circuits with the resistance of carrier materials and electrolytes in conjunction with polarisation resistance[73,74]. There are several drawbacks to this representation

e.g. non-linear resistances must be used when the overvoltage does not vary linearly with the current density and the influence of diffusion - cannot be satisfactorily modelled.

(c) The Macrohomogeneous Model

This model views the electrode on a macroscopic scale and disregards the geometric detail of its structure. The whole electrode-electrolyte system is regarded as the superposition of two continua: the electrode matrix and the electrolyte which fills the voids within the matrix. Variables in the two phases, such as potential and current are regarded as continuous functions of time and space[75]. The model is based on equations describing mass transfer, ionic and electric currents, electrode kinetics, conservation equations for each dissolved species and, more recently, structural changes of the electrode occurring during cycling.

At a given time, there will be a large range of reaction rates within the pores, the distribution of which will be determined by physical structure, conductivities of electrode and electrolyte, and by parameters that characterise the rate of reaction. This rate distribution directly influences the net power available from a battery and will change during the course of charge/discharge reactions. These microsocpic variations are averaged over the dimensions of the porous electrode into continuously varying functions. The parallel plate configuration, together with the high conductivity current collectors in most batteries, means that quantities such as potentials, current densities and concentrations vary only with depth into the electrode, and the problem becomes one-dimensional. These variables can be

inter-related by several equations to describe the behaviour of the porous electrode. The structural changes occurring during discharge of porous electrodes (such as the lead electrode) need to be considered. One of the first contributions in this field was made by Alkire et al[76] who investigated flooded porous metal electrodes undergoing structural change by anodic dissolution. Alkire and Place[77] later used the steady-state approach again to examine the transient behaviour of porous electrodes during depletion of a limited quantity of solid reactant.

One of the most comprehensive models has been described by Bennion and co-workers[78,79] for porous electrodes with sparingly soluble reactants (as in the porous lead electrode). The model is based on the solution of a set of coupled partial differential equations representing the various applicable laws of transport and conservation. The authors allowed for non-uniform current distributions, and also for significant changes in the relative distribution of reactants and products, but not the effect of pore-plugging.

Specific applications of the macrohomogeneous model to the lead-acid cell have been made by Micka and Rousar[80-82], Simonsson [70,83-86] and others[87-89], using the steady-state approach to predict current distributions, discharge profiles and acid depletion profiles.

CHAPTER 3

EXPERIMENTAL TECHNIQUES

3.1. Electrolytic Systems

3.1.1. Electrolyte Solutions

Elcctrolyte solutions were prepared from AnalaR grade chemicals and water tridistilled from dionised stock. Dissolved oxygen was removed from solutions by the passage of white spot nitrogen, deoxygenated by passing over copper at 400°C and prehumidified for at least three days prior to measurement.

3.1.2. Electrolytic Cells

All cells were made from borosilicate glass and cell fittings were attached via lubrication-free ground glass joints. These cells, together with all glassware, were cleaned by steeping for a week in a 50:50 mixture of nitric acid and sulphuric acid. The acid was removed by thoroughly washing with tri-distilled water.

Fig. 3.14 shows a diagramatic sketch of the cell used for both L.S.V. and potentiostatic pulse experiments. For the a.c. impedance measurements, a smaller two-compartment cell was employed with both the working and the counter electrode being in the same compartment with the large surface area counter electrode being parallel to the working electrode.. Galvanostatic charging was carried out in the upward-facing position to prevent oxygen gas retention in the porous matrix. This was achieved by using the cell depicted in Fig. 3.15.

Fig. 3.14 L.S.V. Cell

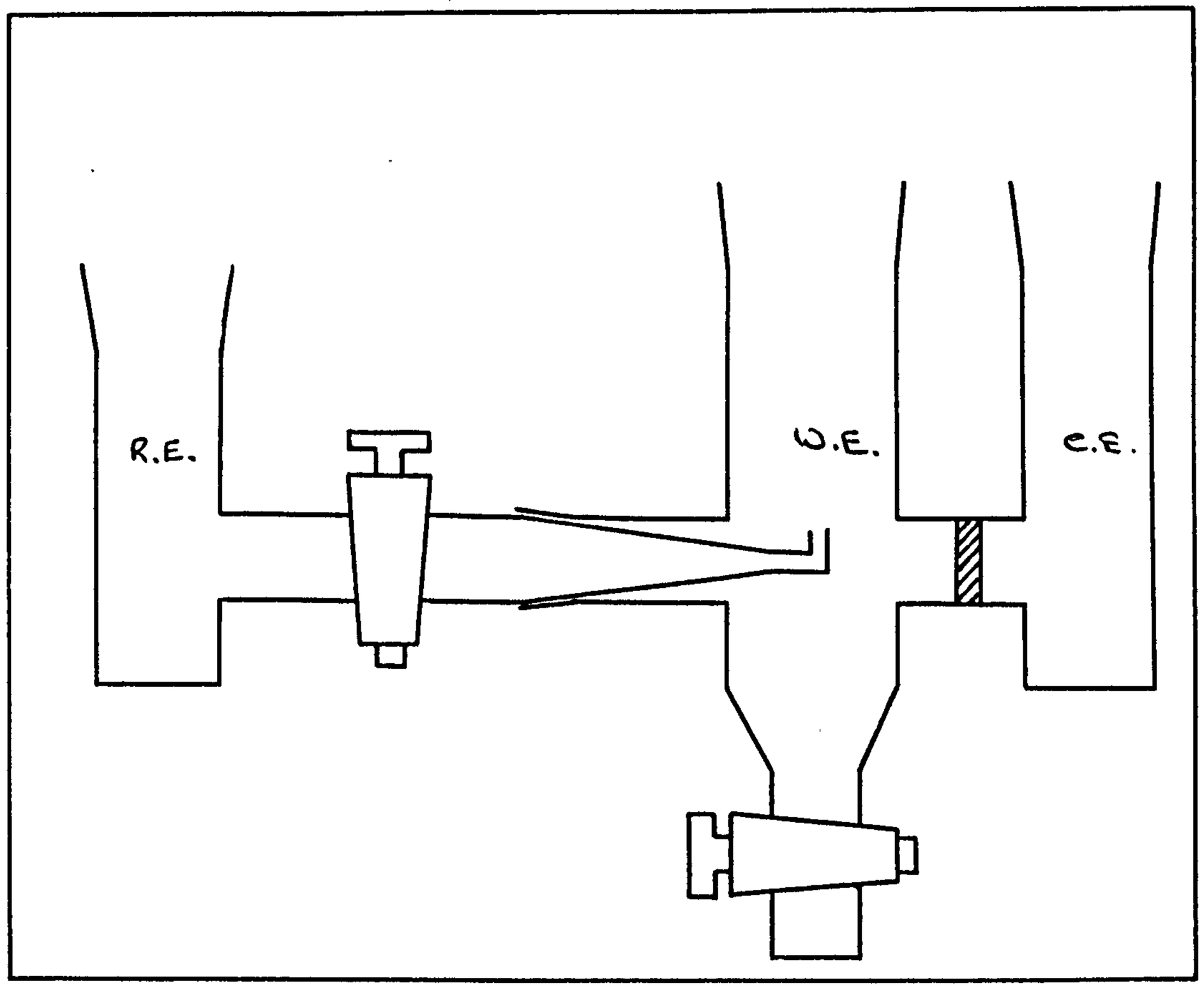

Fig. 3.15
Galvanostatic polarisation cell

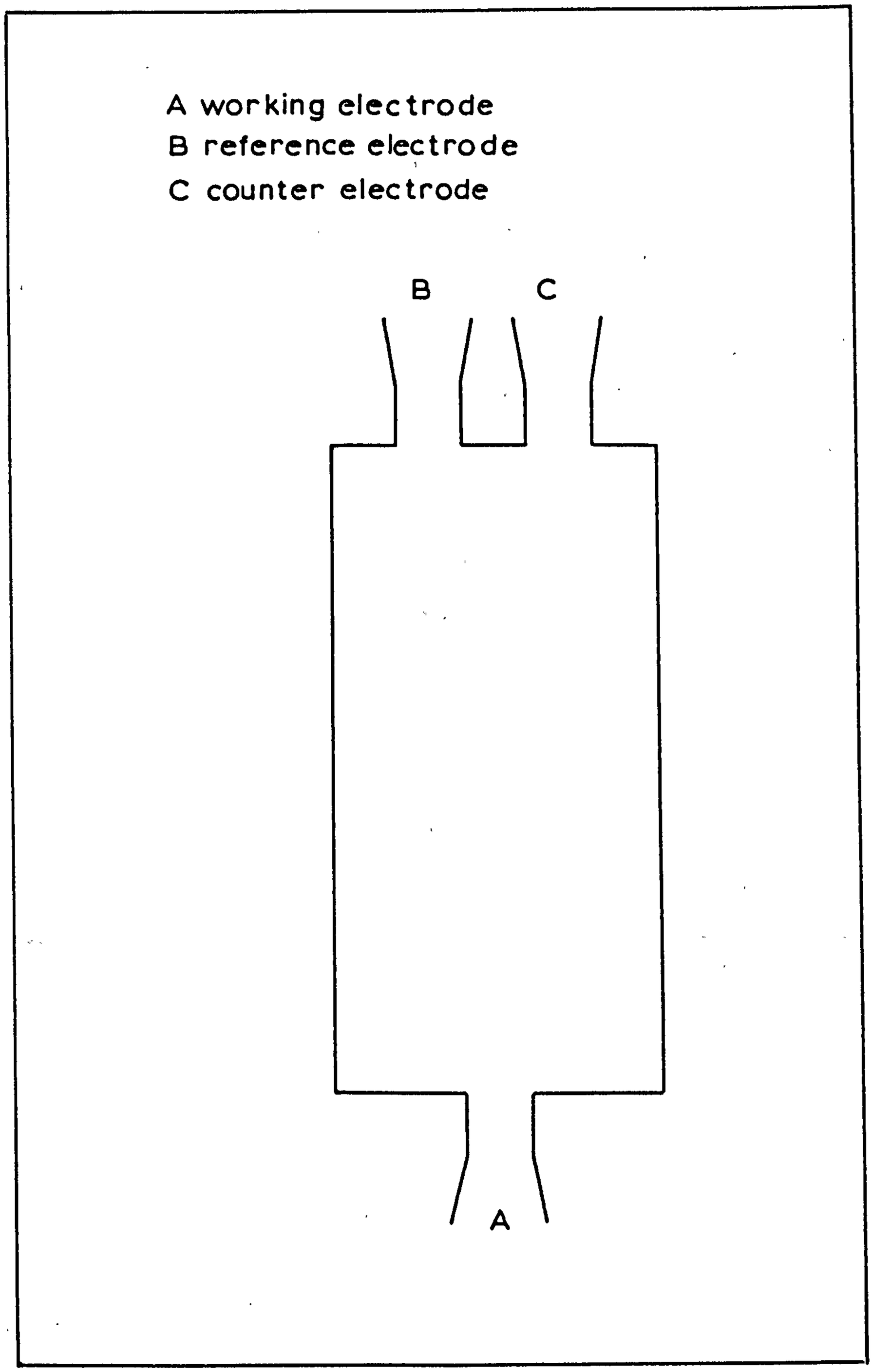

3.1.3. Planar electrodes

Test electrodes were always manufactured as rotating disc electrodes as shown in Fig. 3.16. Lead and Pb-alloy electrodes of cross-sectional area 0.071cm^2 were manufactured by machining rods and setting in a Telfon shroud. Pre-cast rods aged for at least a month were always used in an attempt to simulate the industrial situation as far as possible. The shape and dimensions of the electrode were in accordance with hydronamic requirements[90]. Electrical contact between the electrode and the shaft of the R.D.E. assembly was effected by using a stout steel spring (soldered at the electrode end). A mercury pool provided the contact between the rotating electrode and the external circuit.

The electrode preparation consisted of a polish on roughened glass followed by a chemical etch (10% HNO_3, 10s) and a thorough rinse with tri-distilled water, For Scanning Electron Microscope studies, experiments were made on specially constructed stubs. These consisted of a Teflon shrouded electrode which screwed into the end of a R.D.E. assembly with liquid tight seal.

3.1.4. Porous Electrodes

The electrode is shown in Fig. 3.17 and is basically a R.D.E. with a solid support (pure lead or various lead alloys) lying beneath the level of the Teflon shrouding so that pasting the electrode flush with the Teflon produced a porous layer of leady-oxide (0.76 mm in depth, 3mm diameter). Following the pasting of the recess, the electrode was allowed to stand in a humid atmosphere for three days and then oven-dried at 45°C overnight.

Fig. 3.16
Rotating disc electrode

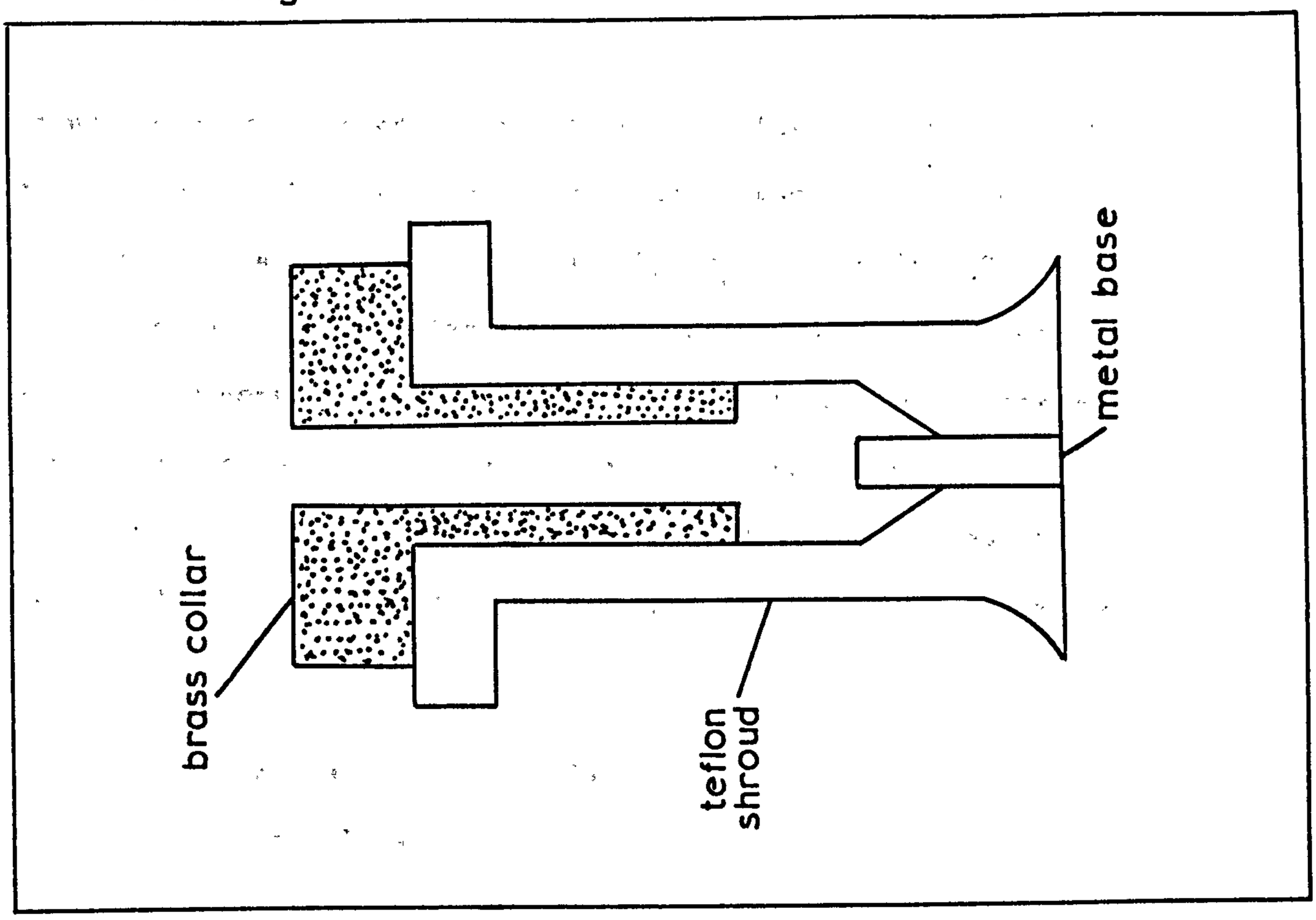

Fig. 3.17
Porous electrode construction

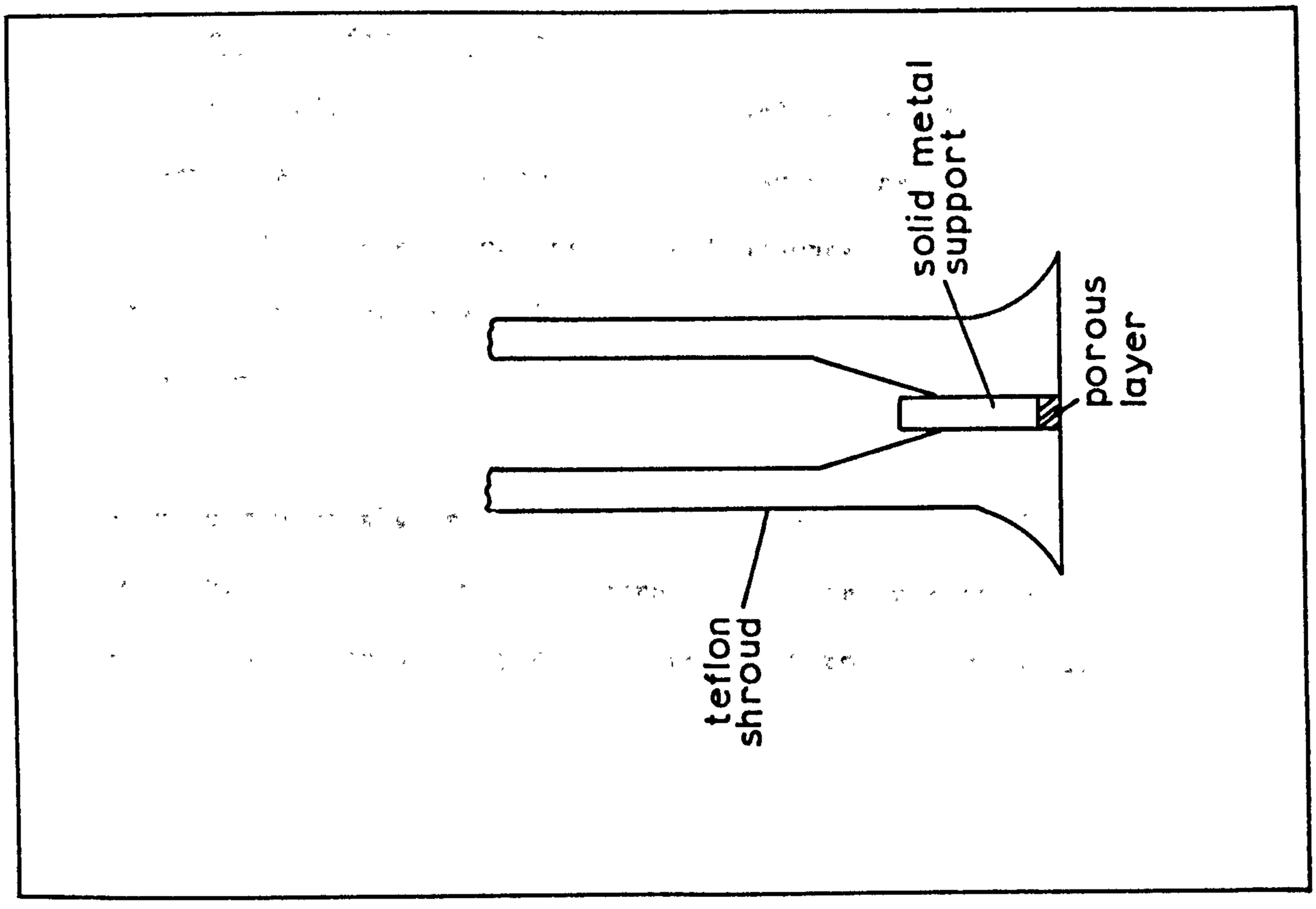

The porous matrix was converted to lead dioxide by galvanostatic polarisation (0.3MH_2SO_4; $\sim$25 mAcm^{-2}) which was continued until the potential was steady (1250mV vs. Hg/Hg_2SO_4 in 0.3M H_2SO_4), and oxygen was freely evolved from the porous matrix. It was necessary to convert the electrode to lead dioxide in the upward facing position otherwise oxygen gas saturating the matrix interfered with the oxidation. The standard automotive positive paste used has a density of 4.10 g/ml and its production consisted of

1080 Kg grey oxide (60% PbO)

0.9 Kg Silica

78 litres 1.4 s.g. H_2SO_4

138 litres water

3.1.5. Counter and Reference Electrodes

For the L.S.V., potentiostatic pulse and galvanostatic oxidation experiments the counter electrode was a pure lead (99.99%) coil. A large surface area pure lead-sheet parallel to, and underneath, the working electrode was employed in a.c. impedance experiments.

Potentials were always measured with reference to a Hg/Hg_2SO_4 electrode in H_2SO_4 of the same concentration as the working solution. The construction of the wick-type reference electrode is shown in Fig. 3.18.

Fig. 3.18 Reference Electrode

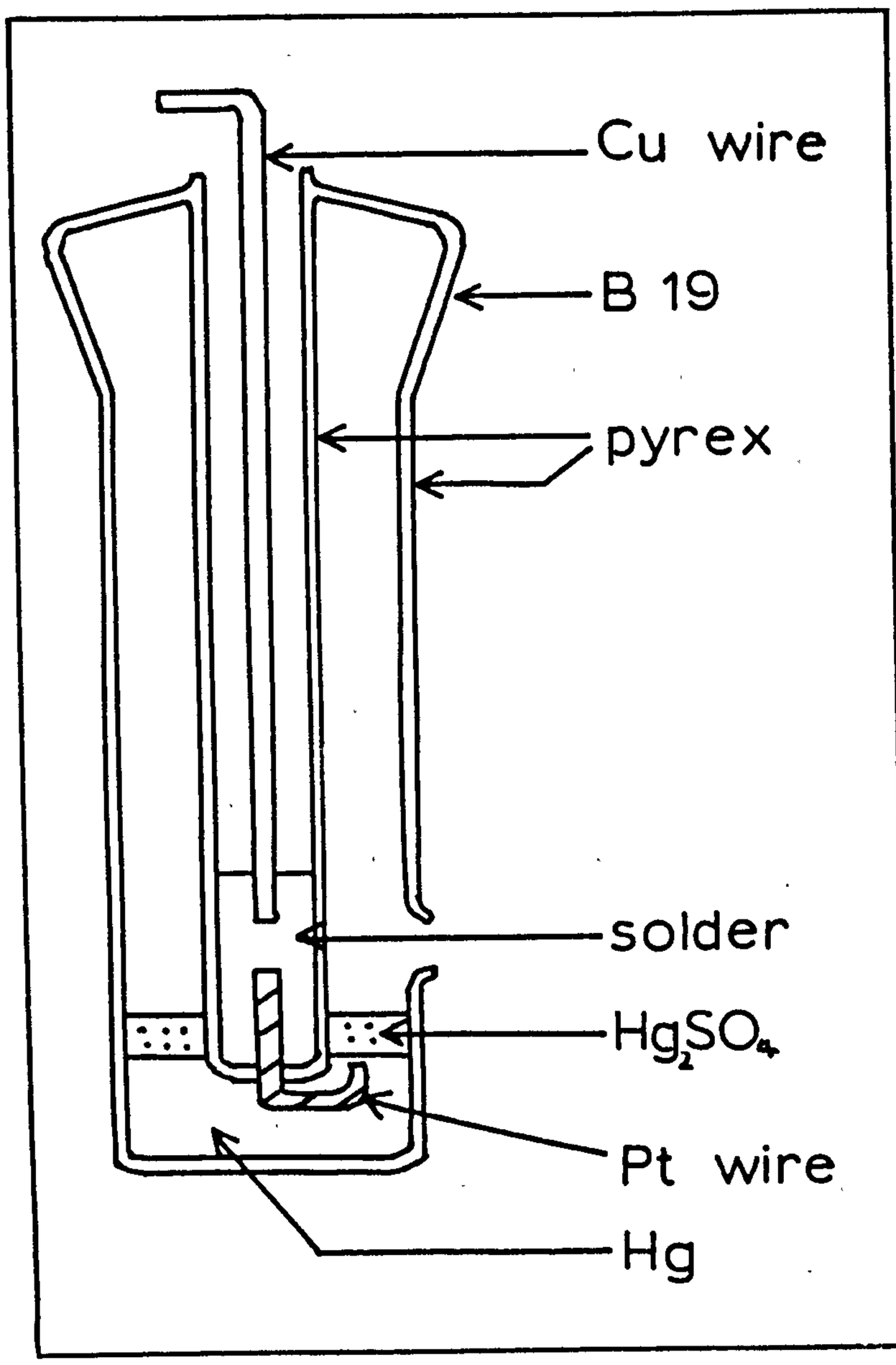

3.2. Electrical Circuits

3.2.1. Cyclic Sweep Voltammetry and Potentiostatic Step Experiments

A block diagram of the circuit used is given in Fig. 3.19. Potentials were fixed across the cell by a Kemitron potentiostat with an inbuilt liquid crystal voltmeter. A function generator (Kemitron) was used in conjunction with an X-Y-t recorder (Bryans 26000 A4)

3.2.2. Faradaic Impedance Measurements

A microprocessor-based system was employed which could measure cell impedances in a programmed sequence[91].

The frequency response analyser (Solartron 1172) is now an established instrument for the determination of electrochemical impedance data[92]. It essentially consists of a programmable generator that provides the perturbing sinusoidal signal, a correlator to analyse the response of the system, and a display to present the results. The fundamental response of a system to a sinusoidal perturbation of the form, $\Delta E \sin \omega t$, will be of the form A sin $(\omega t + \Theta)$. The FRA has the advantage of rejecting all harmonics present in the output of the system and minimises the effect of random noise. A single measurement at a particular frequency can be made by programming the generator with the required frequency and signal amplitude. More usually, however, the generator is programmed to sweep through a large frequency range by choosing suitable values of the maximum frequency (up to 10 kHz), the minimum frequency (down to 0.1mHz), and the number of points per frequency decade at which measurements are to be taken. The instrument will then take measurements sequentially

in either direction at equally spaced intervals (either on a logarithmic or a linear scale) over the designated range. The response is given once a measurement has been completed and can be displayed in one of three possible notations: amplitude (A) and phase angle (Θ) relative to the output signal, log (A) and Θ, or the real and imaginary parts of the impedance. The results together with the measurement frequency are then transferred to a tele-type printer and tape-punch. (The tape-punch facility is particularly useful as it allows the results to be fed directly into a computer for subsequent analysis). Simultaneously the results can be plotted on an X-Y recorder to give the impedance spectrum directly.

The time required for the FRA to make a single measurement is equal to the period of the signal (i.e. 1 second at 1Hz) and this becomes a major contribution to the total experimental time at low frequencies. In most practical applications a certain amount of random noise is invariably superimposed on the signal to be analysed and this may be significantly affect the measurement accuracy. Since this is essentially an averaging instrument, when noise is troublesome greater accuracy can be achieved by increasing the integration (averaging) time.

Fig. 3.19 L.S.V and potentiostatic pulse circuit

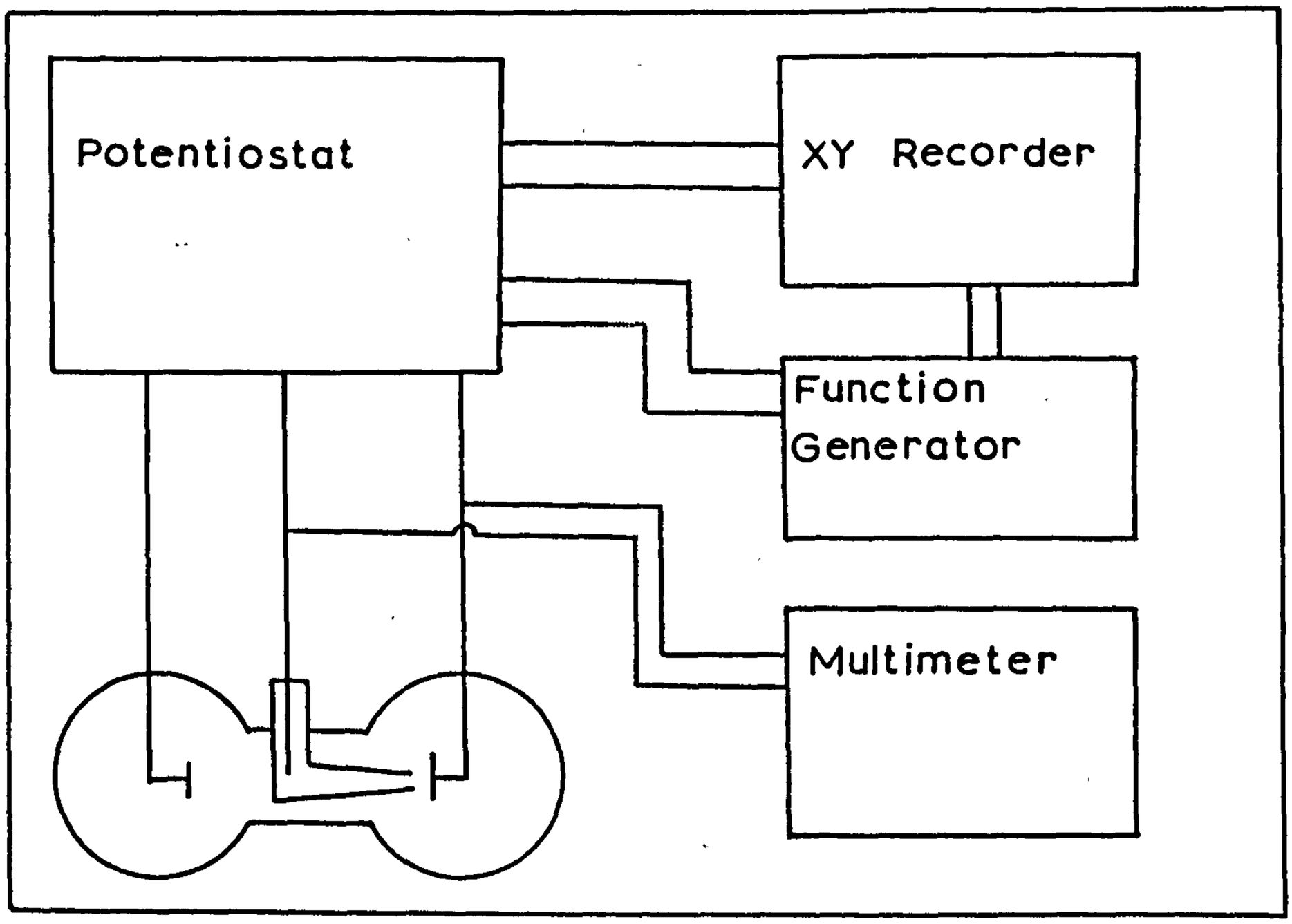

CHAPTER 4

THE EFFECT OF ALLOYING WITH ANTIMONY ON THE ELECTROCHEMICAL PROPERTIES OF SOLID LEAD

4.1. Linear Sweep Voltammetry Studies

Experimental

The experiments consisted of cycling to a constant response between 400mV and 1520mV. The time taken for constancy was approximately 1.5h. It was found necessary to 'initiate' the reaction by sweeping up to 2000mV in the first cycle otherwise no product lead dioxide was formed under the cycling conditions ($7mVs^{-1}$ to $100mVs^{-1}$) with the positive limit at 1520mV. Once the reaction had been initiated it proceeded normally. The need for this procedure was expected in view of the early observations of Fleischmann et al[93] who emphasised the need for a considerable initial overpotential.

Results and Discussion

4.1a) Early cycle history

A feature of the early cycle pattern is the small anodic current which flows during the netative-going sweep in the region 1000-1200 mV. This was obtained with both antimonial and pure lead electrodes provided that the positive limit of the sweep was ~2000 mV; the shape was, however, much less well defined with the alloy (Fig. 4.20). This suggests that the response is not only connected with the metal itself but because of the limit required is also connected with oxygen or related species. The charge of ~270 μCcm^{-2} contained in the integrated anodic area of the peaks suggests the formation of a monolayer of species equivalent to Pb^{2+}.

Similar peaks have previously been reported. The curve obtained by Panesar[92] shows a cathodic peak immediately preceeding the anodic one. This cathodic signal can be explained if a certain amount of lead dioxide had been produced during the anodic excursion into the oxygen region. The cathodic charge represents the extent of this PbO_2 formation. The absence of a cathodic region in Fig. 4.20, however, indicates that no highly oxidised species of Pb are present in these experiments (in which the anodic excursion is not as large) and this throws doubt on the anodic peak being due to α-PbO_2 formation as suggested by Panesar[92].

Sunderland[93] also studied these small peaks using 0.5M H_2SO_4 and observed a reversal in the peak order. He interpreted the anodic peak as an oxidation of water by an intermediate Pb^{3+} species. The

Fig. 4.20 Early cycle L.S.V. - Lead ($v = 50 mV s^{-1}$)

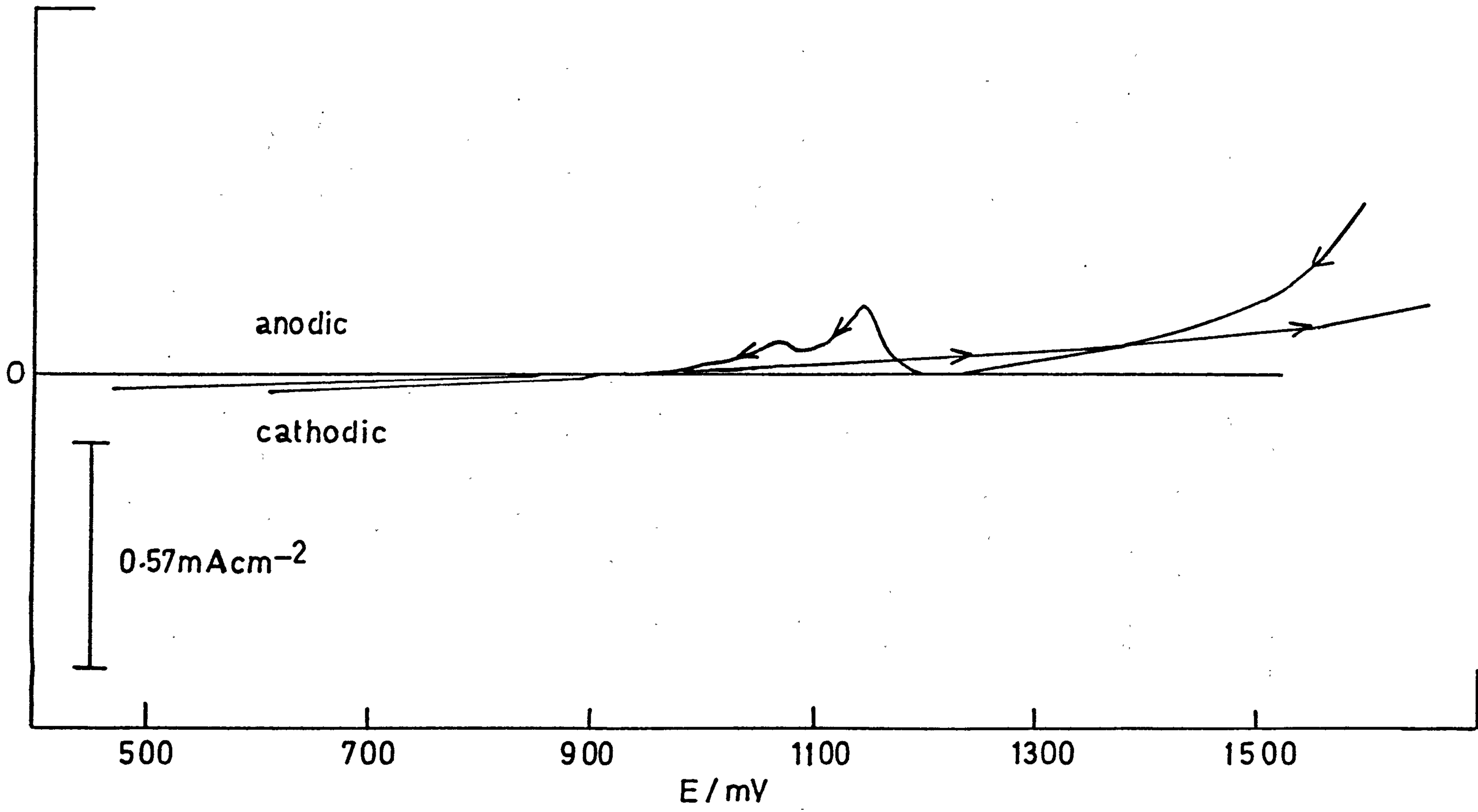

displacement of the cathodic peak (PbO_2 reduction) from the potential noted by Panesar is readily explicable by the decade difference in acid concentration between Sunderlands' experiments and the others, however, his explanation seems to be inadequate in the present case because of the non-appearance of a cathodic signal.

A more reasonable explanation can be given in terms of the production of a layer of O_2 or related absorbed species during the potential excursion into the oxygen region which disrupts the $PbSO_4$ layer. On sweeping back, the desorption of O_2 exposes parts of the Pb surface which can undergo attack by the electrolyte requiring an anodic current flow to produce a passivating film.

The observed double peak can be interpreted if the surface is initially covered by O atoms (or OH radicals) produced by the high positive potential which remain at the electrode in the adsorbed state and which ultimately combine to form O_2ads. and finally being evolved as gaseous O_2. These adsorption reactions will be dependent on the potential so that as the potential moves negatively from the positive limit the formation of $O_{2_{ads}}$ from O_{ads} renders a portion of the initially covered surface available for attack and conversion to a passivating film of $PbSO_4$. At somewhat lower potentials as O_2 is evolved the remainder can be oxidised giving a double peak. Thus the two peaks are produced as a result of depassivation of the electrode by oxygen species[96-98] and should be equivalent to a monolayer of $PbSO_4$ as observed.

The early cycle patterns also show that the alloy takes longer to give a constant response than the pure Pb electrode. PbO_2 formation is somewhat more developed on the pure Pb electrode after cycling for only a short while.

Another interesting feature of the early potentiodynamic curves is that the anodic current due to the formation of PbO_2 occurs at a more negative potential on antimonial lead than on pure lead suggesting that the kinetic barrier to the oxidation of Pb^{2+} to Pb^{4+} is lowered in the case of the alloy. This may be due to the effect of antimony on the grain structure of the lead producing a more attackable form or the production of a more conducting layer of $PbSO_4$ by the incorporation of antimonial species into the $PbSO_4$ layer.

4.1b) Constant response curves

Fig. 4.21 shows stabilised potential curves for both lead and antimonial lead. These curves show much broader peaks than those obtained by Casson et al[99]. This difference arises from the mode of electrode pre-treatment; Casson et al following Fleischmann etal[93] used lead freshly electroplated onto massive lead. Since it was the intention to follow established industrial practice, pre-cast lead rods, aged for at least one month, were used. With the more reactive freshly plated electrode a thick deposit of compact PbO_2 is readily formed. With the electrode used here the deposit is more porous with a consequent broadening of the peaks as the reaction is driven through the porous layer by the increasing overpotential.

Fig. 4.21 Stabalised L.S.V. curves

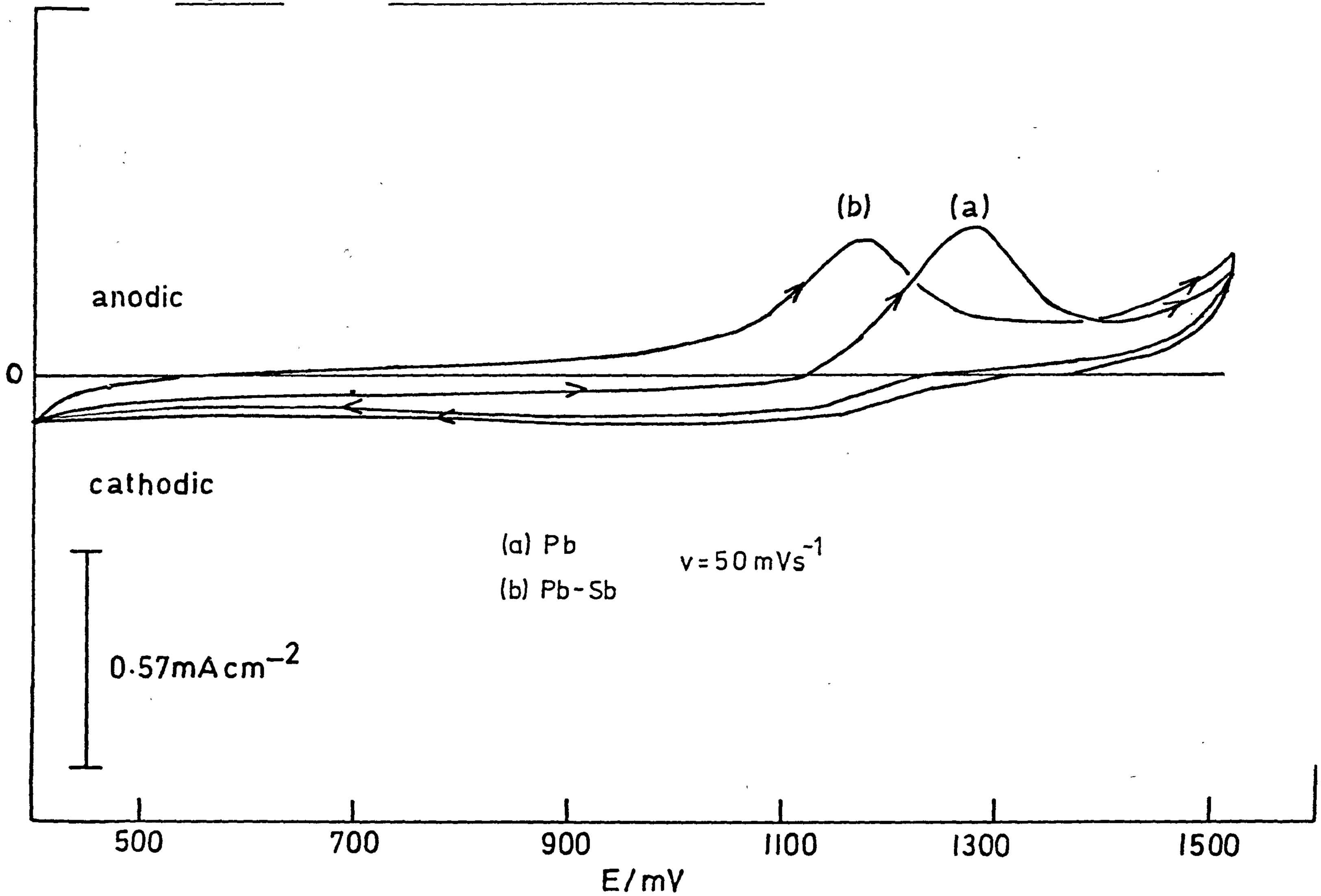

A well defined anodic current is observed during the positive-going sweep on the alloy whereas the current remains cathodic up to 1100 mV (40 mVs^{-1}) in the case of pure Pb after which PbO_2 formation rapidly occurs confirming that corrosion begins at a lower potential with the alloy.

Fig. 4.22 shows the relationship between Ep the peak potential in the oxidation of $PbSO_4$ to PbO_2 and sweep rate in the form of Ep versus log sweep rate. This follows the expected equation developed by Canagaratna et al[100] for the development of a single layer on an electrode. It is clear from the lines in those figures that formation of PbO_2 occurs at a much less positive potential on the alloy than on the pure metal.

Fig. 4.23 shows the relationship between ip and the peak current and sweep rate as plots of ip versus $\sqrt{\text{sweep rate}}$. Similar straight line plots are obtained with both the pure lead and the Pb/Sb in the range 7 - 100 mVs^{-1}. Here we are apparently dealing with a process in which the current is controlled by diffusion in the solid state. This is supported by the fact that the current flowing in the peak was not dependent on the rotation speed of the electrode, the diffusion of oxygen species through the electrode taking place via a solid state process. The correspondence of the data for the alloy and single metal systems indicate that the kinetics of the transport of mass and charge through the electrodes are the same.

The charge contained in the positive-going sweep was calculated by dividing the integrated area under the peaks by the sweep rate,

Fig. 4.22 Dependence of sweep-rate on potential

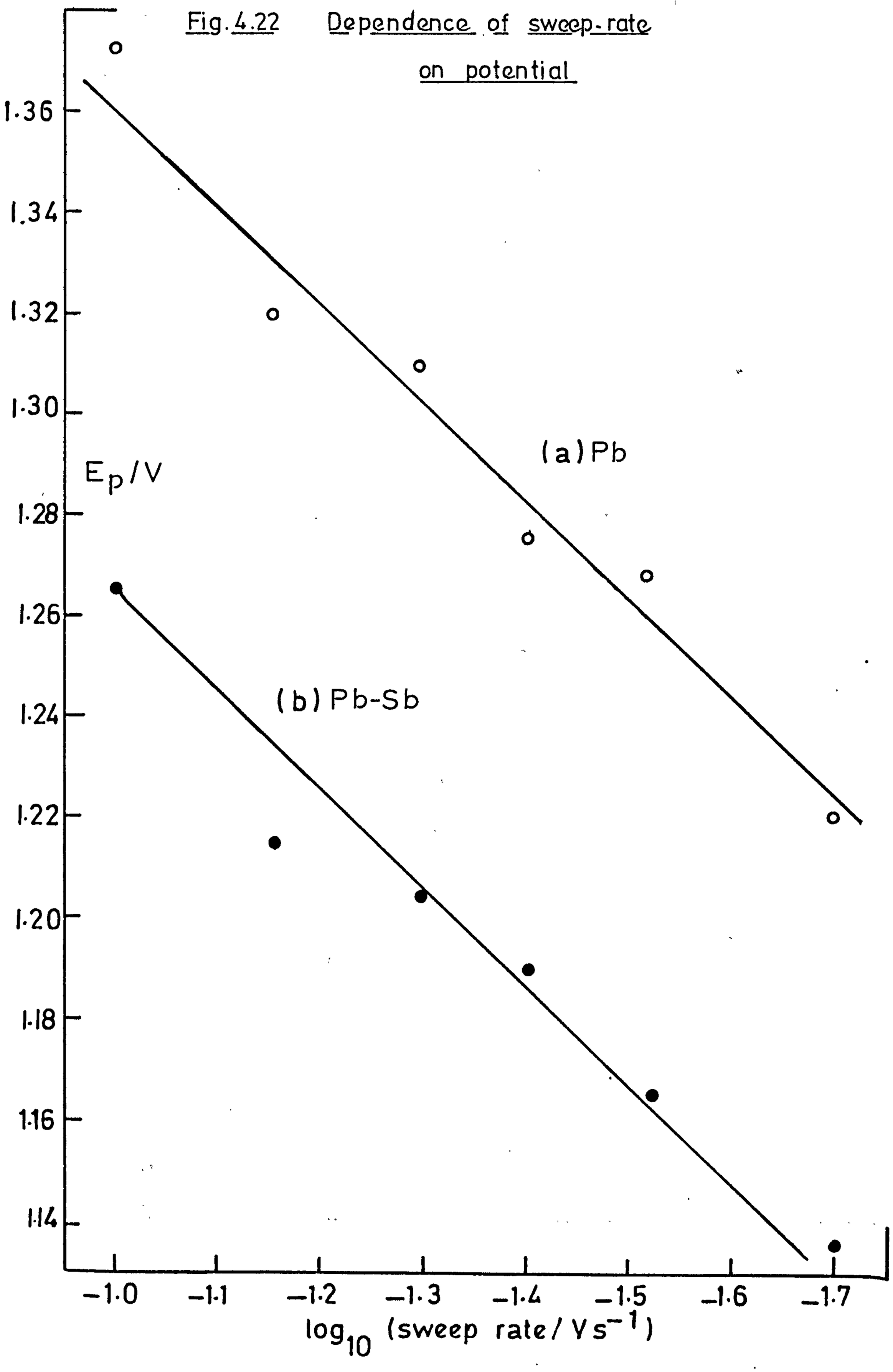

Fig. 4.23 Dependence of i_p on sweep-rate

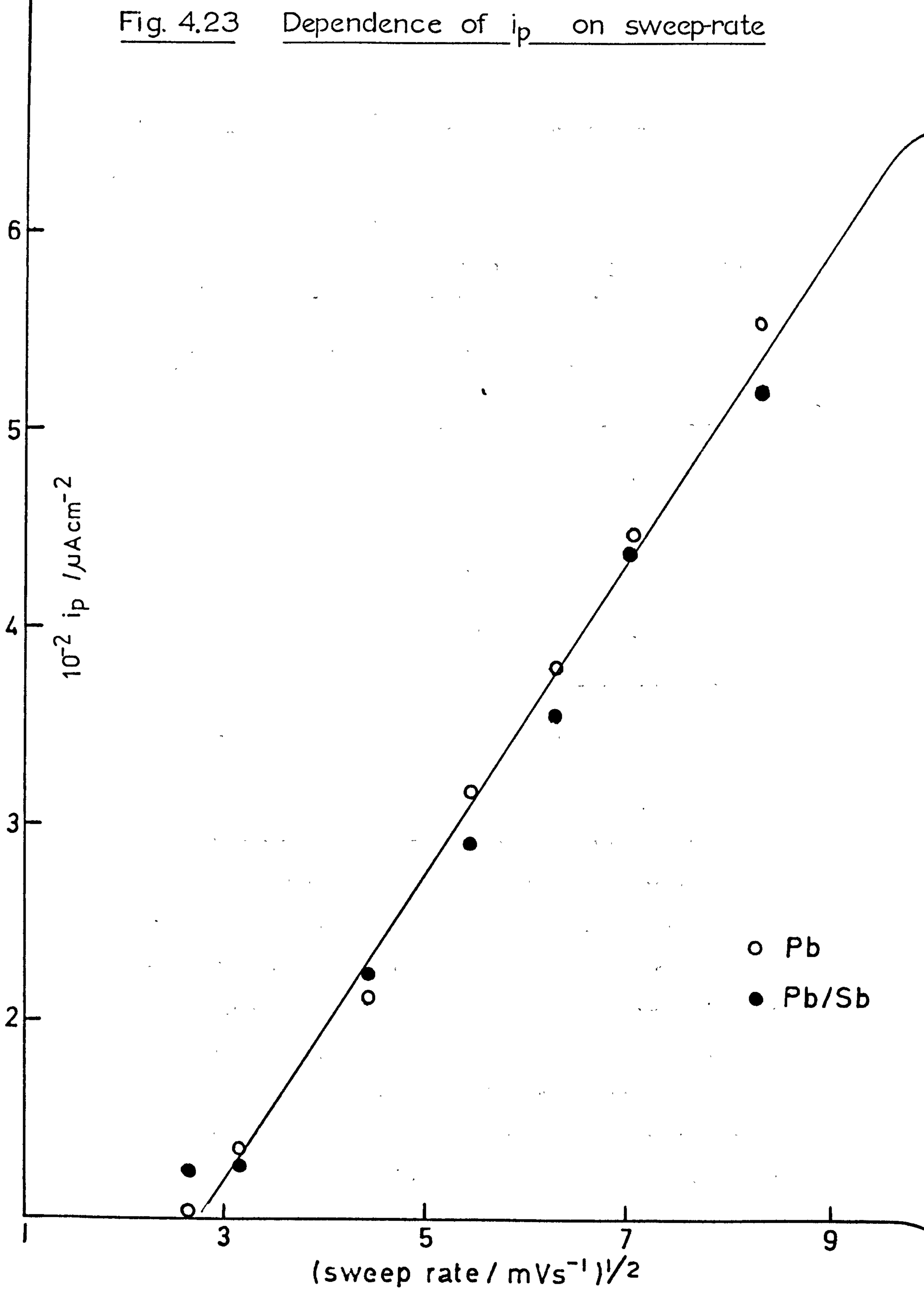

following Canagaratna et al[100]. This data is summarised in the table below.

A comparison of the cha rge contained in the positive-going sweep and its dependency on the sweep rate

ν (mVs^{-1})	Charge ($mC\ cm^{-2}$)	
	Pure Pb	Pb/Sb
7	- 2.233*	7.332
10	- 0.785	5.545
20	0.721	3.822
30	0.780	3.260
40	0.946	2.815
50	1.010	2.731
70	1.021	2.236
100	0.988	2.075

* The minus sign denotes a cathodic charge

The data summarised in the table above shows several differences between pure lead and the alloy. First is the much greater quantity of charge obtained with the alloy. This indicates that the extent of attack occurring in the electrochemical cycling is much greater for the alloy than the pure metal. This may be the reason for the superior active material retention of Sb containing grids than pure Pb grids. The relatively large material development with the antimonial alloy giving rise to a more mechanically sound junction between grid and paste in the battery. This fact may also explain the known behaviour of antimonial lead in the oxygen region where certain stationary batteries

have exhibited a high degree of top bar corrosion. The conclusion must be drawn that the passivating layer on Pb forms more rapidly, is tighter and more mechanically sound than antimonial lead. This observation is confirmed by calculation of the charge in the negative going sweep which again is considerably greater in the case of the alloy. Secondly, the alloy exhibits a larger sweep-rate dependency of charge than pure Pb. This indicates that the oxidised layer on pure Pb is of fairly constant thickness and discharges to about the same extent throughout all the experimental conditions. The alloy on the other hand reacts in a way more typical of a porous layer in which the reaction is driven further into the porous mass at lower sweep rates, i.e. a more efficient electrochemical process when more time is available for this to occur.

CONCLUSIONS

1. The L.S.V. curves for pure lead and antimonial lead show considerable differences.
2. The antimonial lead was initially less reactive than the pure lead as indicated by the current response in the early cycles of the potentiodynamic curve.
3. The ultimate net charges in the potentiodynamic curves were considerably greater in the case of the alloy.
4. The peak current dependencies on the rate of potential sweeping for both pure Pb and the alloy were similar and in agreement with data obtained from similar systems.
5. A small anodic current flowing in the early cycle history seems to have been previously misassigned; it is probably due to lead sulphate formation at a surface previously passivated by oxygen.
6. Active material retention can be usefully discussed within the framework of the differences in the electrochemical behaviour of lead and antimonial lead.

4.2. Potentiostatic step experiments

4.2(i) Experimental

Prior to potentiostatic step experiments all electrodes were cycled to a constant response between the limits 400mV-1520mV ($50mVs^{-1}$). The pulse experiments were made from 400mV after completion of the cyclic preparation and a stabilising period ('hold') at 400mV. The current in this 'hold' period was quite small ($\sim 1 \mu A$) and was generally less than observed in earlier experiments on electrodeposited lead[93,101] There was no apparent reduction of the current with time during the hold period.

4.2(ii) Results and discussion

a) Pure lead electrodes

Figure 4.24 shows the results of a potential step on a film of $PbSO_4$ formed on pure lead. The behaviour is quite typical of all the results on pure lead and indicates a nucleation and growth process.

In all the potential step experiments, at the front of every rising transient a current "spike" was observed which is mainly due to double layer charging. Although the lack of any rotation speed dependence of the "spike" (or the subsequent current) indicates that lead ions do not leave the electrode via the agency of the solution, it was difficult to obtain any quantitatively useful information regarding the electrode/electrolyte interphase. The complication was the very high initial current in the transient itself. It was interesting to note, however, that in experiments with 'hold' periods in excess of 15min. the "spike" was relatively small and constant. A further point of interest is that a larger "spike" was observed with the alloy than with pure lead.

Fig. 4.24 i-t transient for potentiostatic pulse from 400mV to 1250mV

(pure Pb)

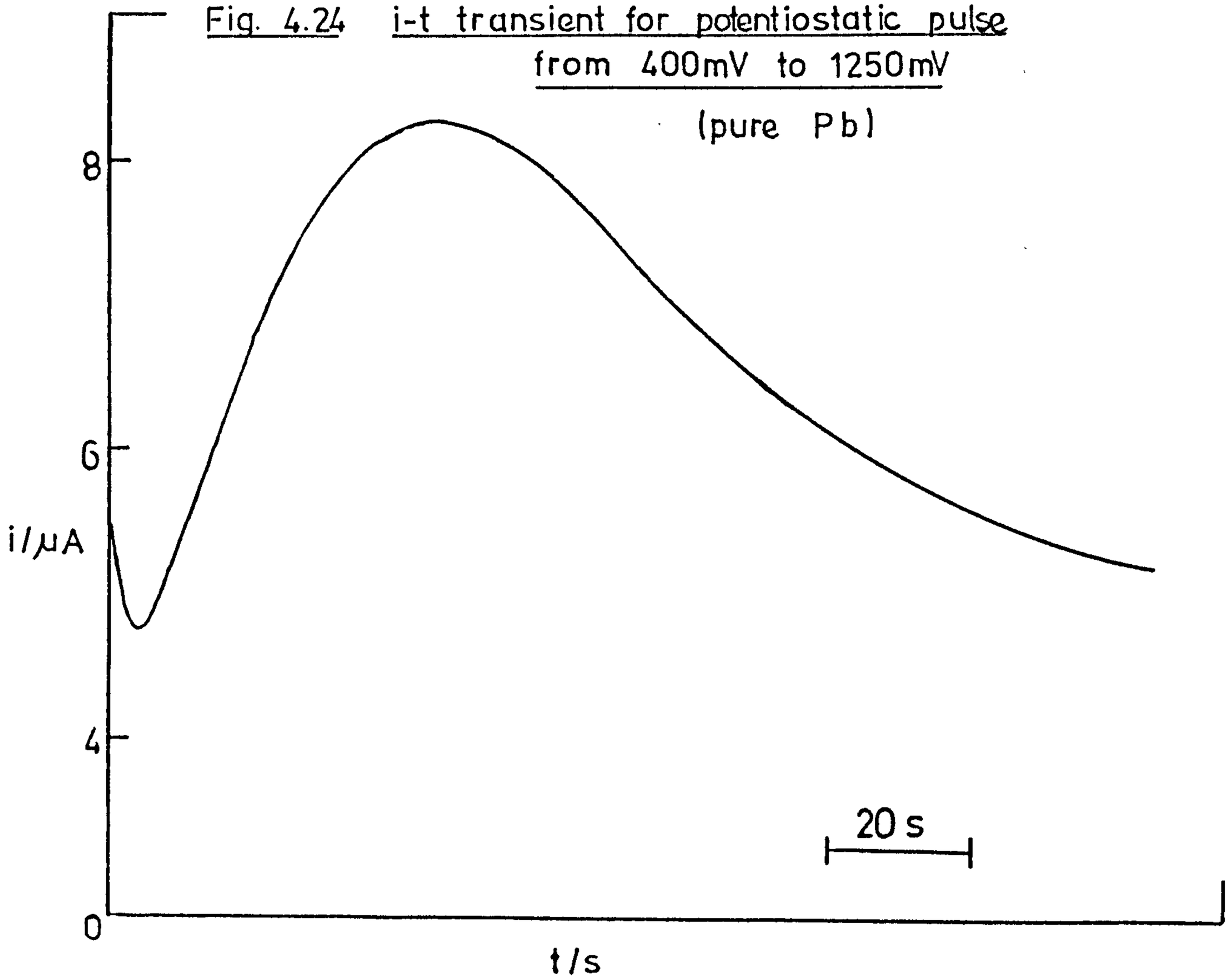

Although the current after the "spike" did not rise from zero it was possible to identify the form of the current increase. It was in this case, however, different from the previously reported data obtained by Flieschmann and Thirsk[93] using potentiostatically formed $PbSO_4$ from freshly electrodeposited lead. In those cases the $i-t^3$ relationship observed at the beginning of the current increase was indicative of a three dimensional progressive nucleation process with ultimate current limitation due to overlap of growing centres. It was crucial for this experimental process that the excursion into the PbO_2 region be the first otherwise there is a great deal of evidence to show that the electrocrystallisation process responsible for the first current rise is a two dimensional instantaneous nucleation and growth[101,102].

In these experiments the part of the initial rising currents which can be analysed conforms to a linear i vs. t relationship characteristic of a 2-dimensional growth process. This is shown clearly in Fig. 4.25.

A further difference is the attainment of the peak current maximum at a time very much less than observed under corresponding conditions in the earlier experiments on uncycled electrodes[93,101]. For example times of $\sim$ 10min. were quite typical of the Casson work which is $\sim$ 10 times that of similar experiments here. It can be concluded from these results that the cycled electrode contains sufficient nuclei for the electrocryatallisation to proceed at a speed sufficient to change the process from the relatively slow 3-dimensional one observed with uncycled electrodes to the 2-dimensional faster process.

Fig. 4.25 i-t relationship for series of pulse expts.
(400-1250mV, Pb)
Rise in transient

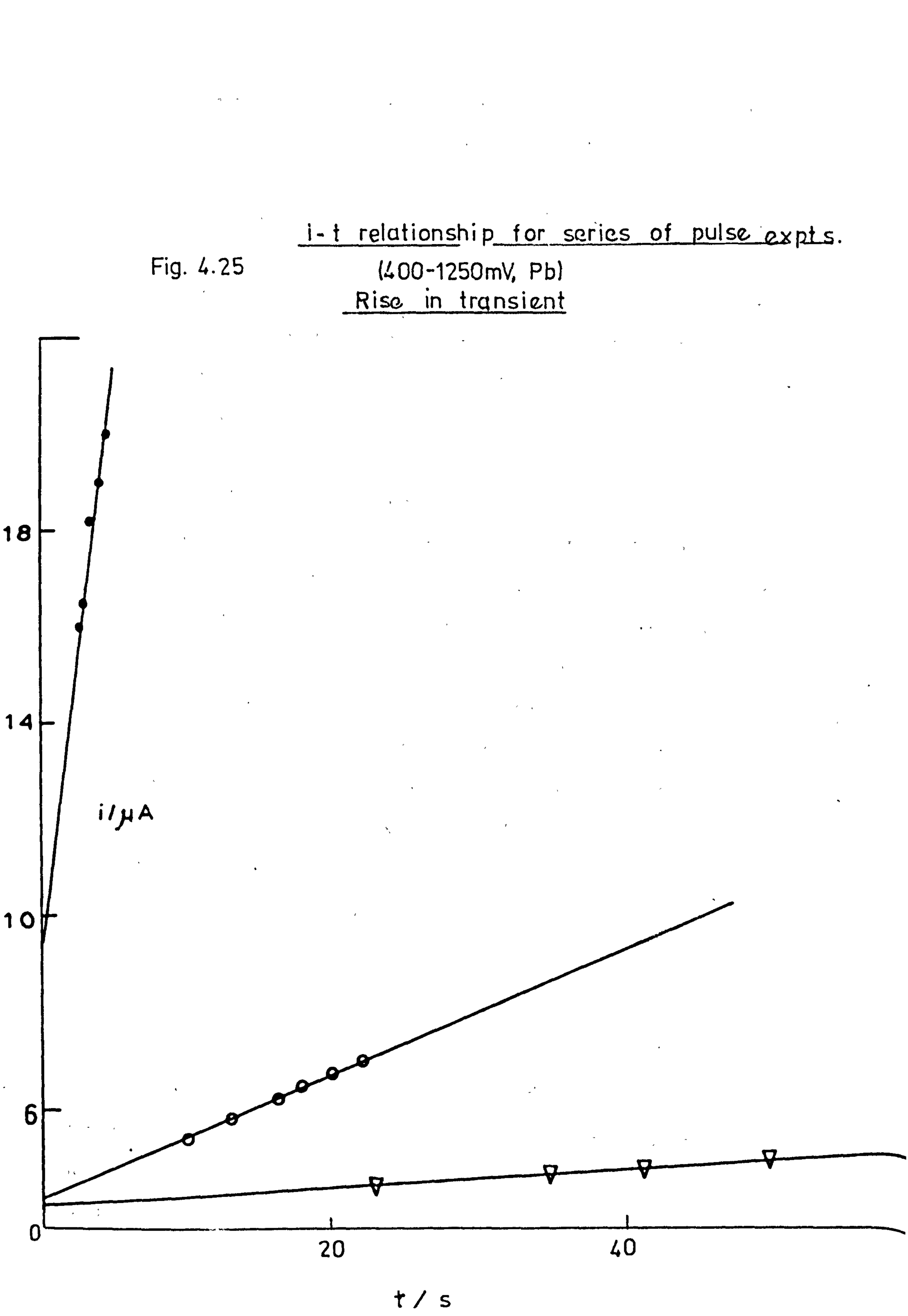

The equation for the 2-dimensional process previously found for the conversion of lead sulphate to lead dioxide[93] is

$$i = (zF\pi M/\rho)N_o k^2 t \exp(-\pi M^2 N_o k^2 t^2/\rho^2) \qquad (60)$$

A further proof that equation (60) applies in this case is clear from Figure 4.26 where a plot of $\ln((i-i_r)/t)$ versus t^2 shows a rectilinear relationship, here the current is corrected for the oxygen evolution process.

Figure 4.27 contains data corresponding to a number of experiments in which, after cycling, the electrode was "held" for different times potentiostatted in the lead sulphate region. It can be seen that the rising slopes di/dt are quite sensitive to the "hold" period which from equation (60) indicates that the effect of the prolonged time in the PbO_2 reduction region is to remove nucleation centres. The same conclusion is obtained by considering the position in time of the current maximum which is displaced to longer times by prolonging the preoxidation "hold" period. From equation (60) by differentiation and setting $di/dt = 0$ it is found that t_m is related to N_o and k by

$$t_m^2 = \rho^2/2\pi M^2 N_o k^2 \qquad (61)$$

The increase in t_m with "hold" time confirms that nucleation centres have been removed by the prolonged "hold" period. It should be noted that it is unlikely that the "hold" has any effect upon k since this is generally only dependent on potential; it is possible, however, that a small amount of recrystallisation of the $PbSO_4$ layer occurs during the potential "hold" - this is likely to be small. It

Fig. 4.26 Data for falling transient (Pb)

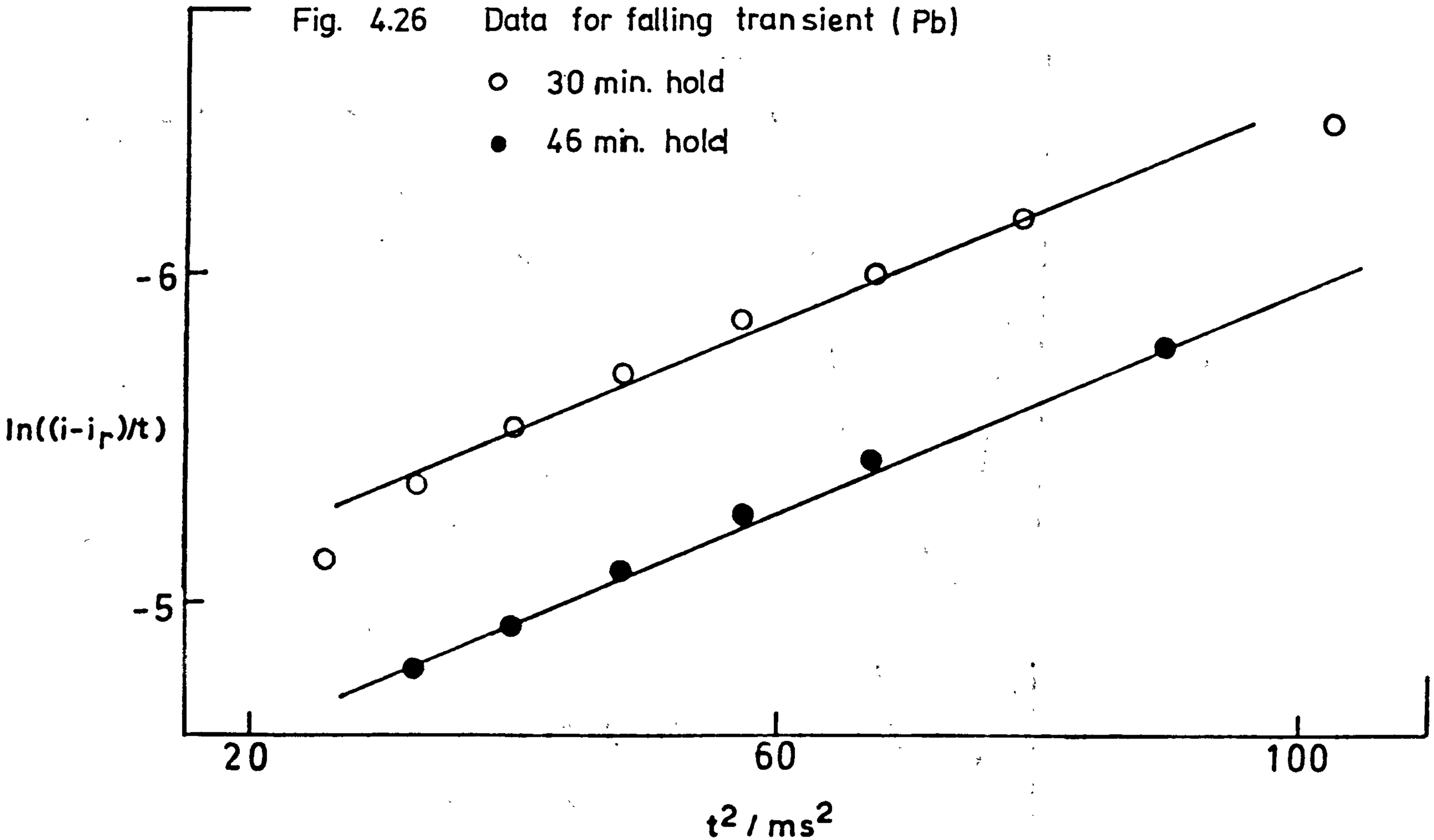

Fig. 4.27

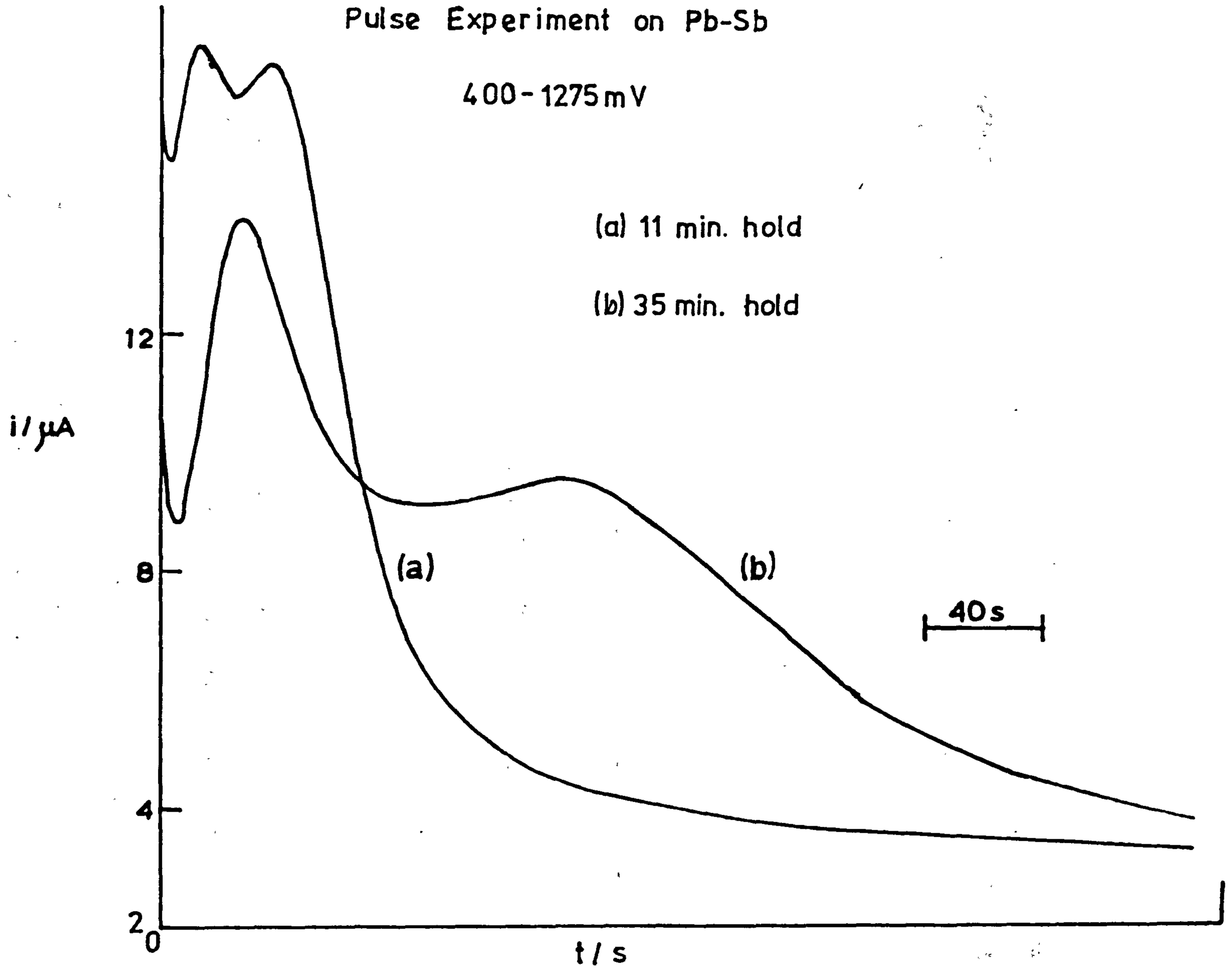
Pulse Experiment on Pb-Sb
400 - 1275 mV
(a) 11 min. hold
(b) 35 min. hold
12
i/μA
8
4
2
0
(a)
(b)
40s
t / s

is possible therefore to ascribe the effect of "hold" time to the nucleation site density.

At long times the oxidation process is complicated by the intruding oxygen evolution reaction. This is well known[101], however, it is nevertheless very surprising that the intrusion of the oxygen evolution reaction could be detected so early on in the oxidation. In earlier experiments oxygen intrusion was observed only after 15 min at 1350mV, here at 1275 mV clear evidence for oxygen was obtained after a few minutes. The effect of the intrusion of the gaseous evolution can be observed by considering the charge (corrected for the apparent steady state oxygen current) in the rising and falling transient before an experimental steady state current is observed. This is shown in the Table below.

The charge contained under the transient curve (corrected for oxygen evolution) and the residual oxygen current (pure Pb)

'Hold' time (min)	i_r (μA)	Charge contained in peak (mC cm^{-2})
6	6.0	17.3
14	4.4	11.6
15	4.5	8.3
25	4.0	3.1
30	4.2	5.0
46	6.5	6.2

The charge under the peak decreases with hold time to a fairly steady value.

It can be concluded that considerably more oxidation (of $PbSO_4$ to PbO_2) occurs with parallel oxygen evolution if the number of nucleation centres in the lead sulphate are reduced by holding in the PbO_2 reduction region. This parallel oxidation must be small for the level of current in the quasi-steady-state response at long times was found to be independent of the "hold" time eventhough considerable amounts of $PbSO_4$ must be still available for reduction after the termination of the peak. The $PbSO_4$ oxidation process is rendered relatively inefficient by the removal of PbO_2 nucleation centres since the vast majority of the current passing after the peak is going into the oxygen reaction.

A further confirmation of the slow annihilation of nucleation centres with "hold" time arises from the intercepts at t = 0 in Figure 4.25. The longer the "hold" the less the initial current which indicates that the extent of the growth points as well as the number are modified by the reduction.

A final interesting point requiring comment is that previous work on cycled electrodeposited lead[101] has shown that a very shallow secondary peak was present. It has not been possible to discover such a response in these experiments even though the current responses were monitored for considerable times. It may be that in this system the peak was obscured by oxygen evolution rather than being absent; in any case it seems that this difference is an electrometallurgical effect.

b) Antimonial lead electrodes

Figure 4.27 shows the current response transient of the antimonial lead alloy (Pb-Sb (5%)). It is seen that it differs considerably from that of pure lead. The most significant difference is the appearance of a second peak. This feature was observed in every experiment with the alloy. Fig .4.28 shows the first available slopes of the rising portions of the transients. These compare in both magnitude and dependence on the "hold" time with the single peak observed with the pure lead. The table below contains the charge in the first peak of the alloy response as a function of hold time and these data are within 20% of corresponding ones for the pure lead. The effect of the "hold" time on t_m for the first peak is in agreement with the single peak on pure lead. It can be concluded from this that the electrocrystallisation reaction in the first peak for the alloy is identical with the single electrocrystallisation process on pure lead.

The Charge Contained under the transient curve (corrected for oxygen evolution) and the residual oxygen current (Pb-Sb(5%))

'Hold' time (min)	i_r (μA)	Charge contained in 1st peak (mC cm^{-2})
11	3.5	12.2
35	2.5	12.2
46	4.0	11.9
60	3.6	9.2
103	3.0	5.5

Fig. 4.28 i-t relationship for rising transient

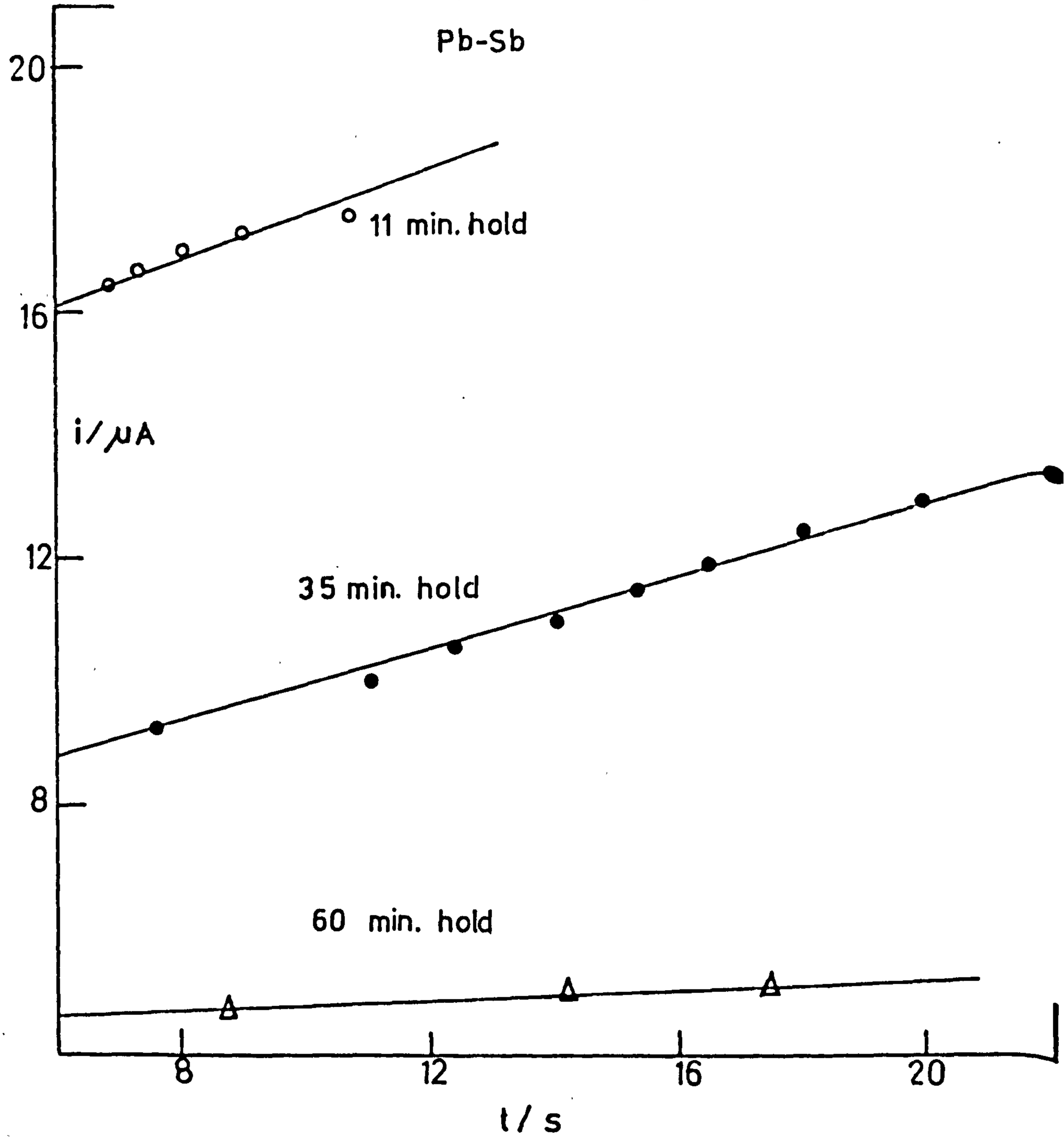

The second peak observed with the alloy is difficult to analyse due to the convolution with the first process and the evolution of oxygen. The most convenient way to proceed is to investigate the falling part of the second transient. A correction was made for the oxygen current and the falling parts of the second peak are represented in Figure 4.29 by plotting ln $(^{(i-i_r)}/_t)$ vs t^2. Satisfactory straight lines confirm that the process follows equation (60). Moreover it can be concluded from this that since no correction in t is required the process starts at time t = 0. The position in time of the maximum for the second process is dependent upon the "hold" and the dependency is linear as shown in Figure 4.30.

Equation (61) can be rewritten with this in mind to predict the effect of "holding" as

$$t^2_{hold} \propto \rho^2 / 2\pi M^2 N_o' k_2^2 \qquad (62)$$

i.e. when no holding time is allowed the second peak is observed at a very short time and the current falls from an initially high value. This trend is clearly discernable from the transients of Figure 4.27.

The observed differences in behaviour of the alloy and pure lead are important for they are of immediate application to lead cell technology. The development of the extra 2-dimensional oxidation peak in the case of the alloy reinforces the view that the film on antimonial lead in sulphuric acid is not completely passivating and that a thickening occurs. The results here indicate that a further layer is produced in addition to that on pure lead. Moreover this secondary layer contains at least as much charge as the primary layer. Holding the electrode

Fig. 4.29 Falling Transient

Pb-Sb

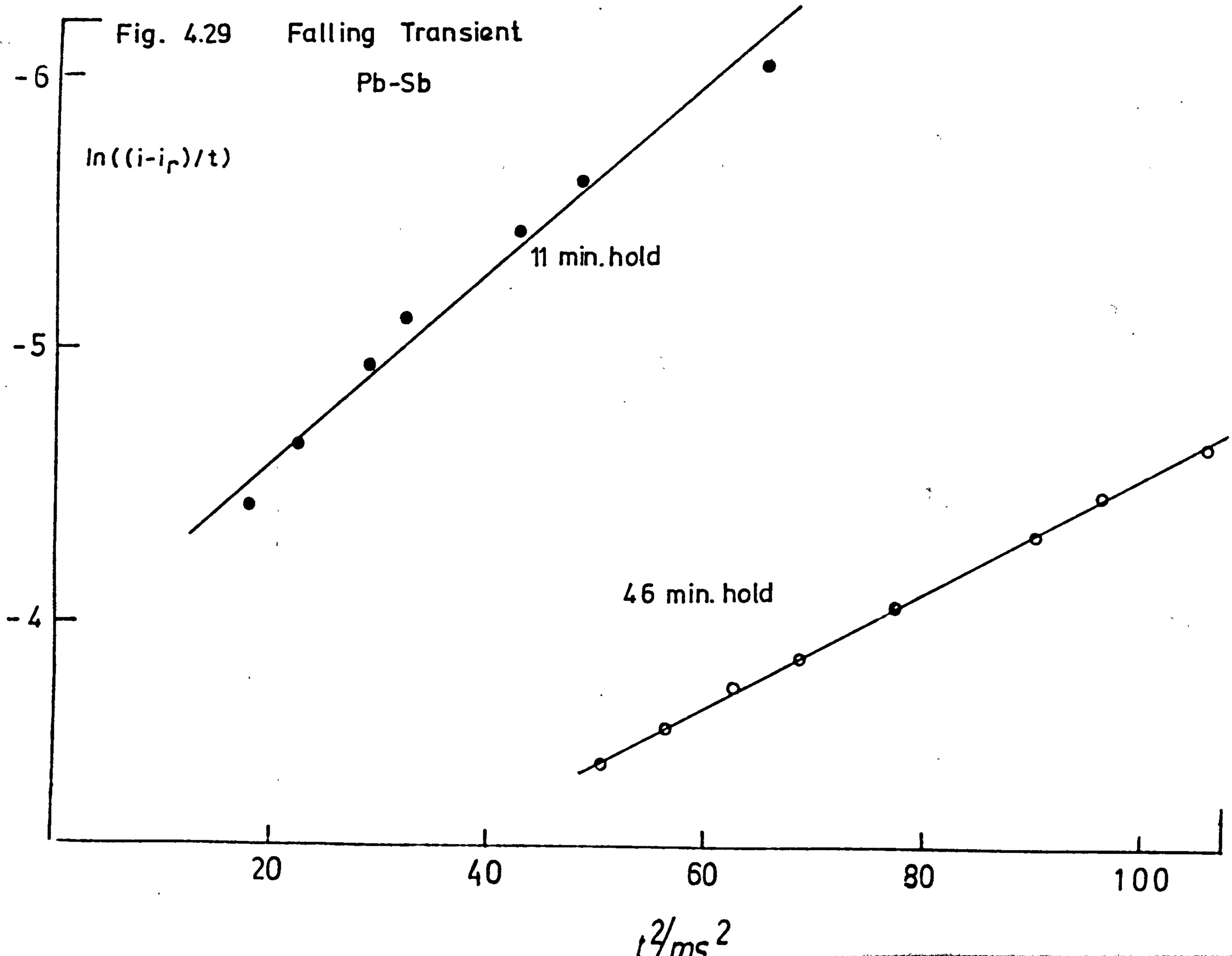

Fig. 4.30 The Effect of hold time on appearance of 2nd peak

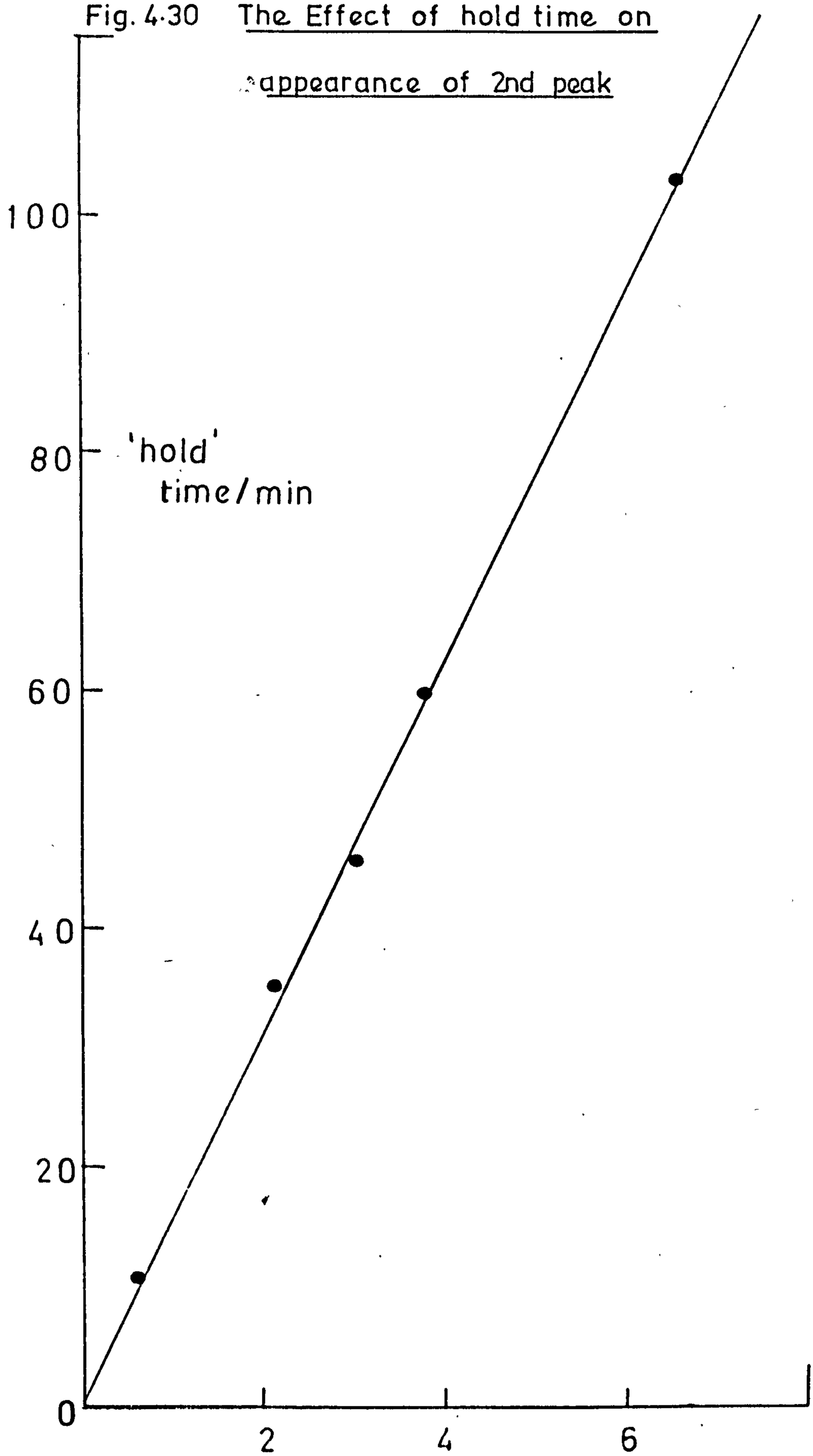

in the reduction region annihilates the nucleation centres in both of the layers, this observation has implications in the charging behaviour of the lead-acid cell where it is clearly disadvantageous to delay recharge. With the antimonial alloy the extent of the removal of the nucleation centres in the secondary layer appears less than that in the primary layer and answers the perplexing question of why antimony is beneficial in the grid for the recharge characteristics. The presence of nucleation sites in the secondary layer being an additional threshold pathway to faster rates of recharging.

It is interesting that the only two electrocrystallisation processes observed with the more corrodible antimonial lead are similar to the first two processes observed in the commercial ("porous") electrode. It should be noted in this connection that the currents involved here are only a fraction of that observed in the earlier work of Casson[99] nevertheless, a similar layered growth is indicated.

CONCLUSIONS

1. On lead cycled between the $PbSO_4$ and the PbO_2 regions and then stepped from $PbSO_4$ the oxidation transient indicates the conversion to PbO_2 as a 2-dimensional instantaneous nucleation process with subsequent overlap of growing centres.

2. "Holding" the $PbSO_4$ filmed electrode in the $PbSO_4$ potential region removes nucleation centres and reduces the extent of the remaining ones.

3. Removal of nucleation centres renders low the ultimate efficiency of the oxidation process, considerable oxygen being evolved before the oxidation is complete.

4. On antimonial lead the oxidation of (cyclically) grown lead sulphate is complicated and two current peaks in the transient reveal two 2-dimensional instantaneous nucleation and growth processes.

5. The analysis of the charge in the transients and the shape indicates that the single layer of lead sulphate on lead is probably identical with the primary layer on antimonial lead.

6. The presence of the secondary layer on antimonial lead assists the efficiency of oxidation of the $PbSO_4$ deposit.

4.3. A morphological examination of the effect of antimony on the electrochemistry of lead.

4.3.1. Experimental

Electrodes were cycled to constant response as before (400-1520mV, 50 mVs^{-1}) and held in the $PbSO_4$ reduction region for a period prior to the potentiostatic pulse experiments. The potentiostatic oxidations were performed exactly as in 4.2 with the electrodes being removed from the cell after various oxidation times. After completion of the electrochemical experiments, samples were washed with tri-distilled water, rinsed with acetone and stored in a vacuum dessicator. For microscopic study samples were coated with a thin layer of gold (10-20 nm) by diode sputtering and examination was carried out using a Jeol JSM 35 scanning electron microscope (tube voltage of 20 kV). Imaging was by secondary electron emission.

4.3.2. Results and Discussion

Fig. 4.32 shows the surface morphology of a pure lead electrode following a short oxidative period in the PbO_2 region (1275mV). The lead dioxide matrix consists of crystallites which conglomerate into small spherical groups interspersed with well-defined prismatic crystals which are readily identifiable as residual lead sulphate still available for oxidation. The sulphate crystals are several orders of magnitude larger than the groups of PbO_2. Figs 4.33-4.35 show that as the length of time the electrode is held in the PbO_2 region is increased the oxidation of residual $PbSO_4$ to PbO_2 is accomplished and complete surface coverage with PbO_2 is attained.

TOP

2 μm

magnification=5,000

BOTTOM

0.5μm

magnification = 20,000

Fig. 4.32 Growth of PbO_2 from $PbSO_4$ on flat Pb electrode after 10 s

TOP

2 μm

magnification=5,000

BOTTOM

0.5μm

magnification = 20,000

Fig. 4·33 Growth of PbO_2 from $PbSO_4$ on flat Pb electrode after 20 s

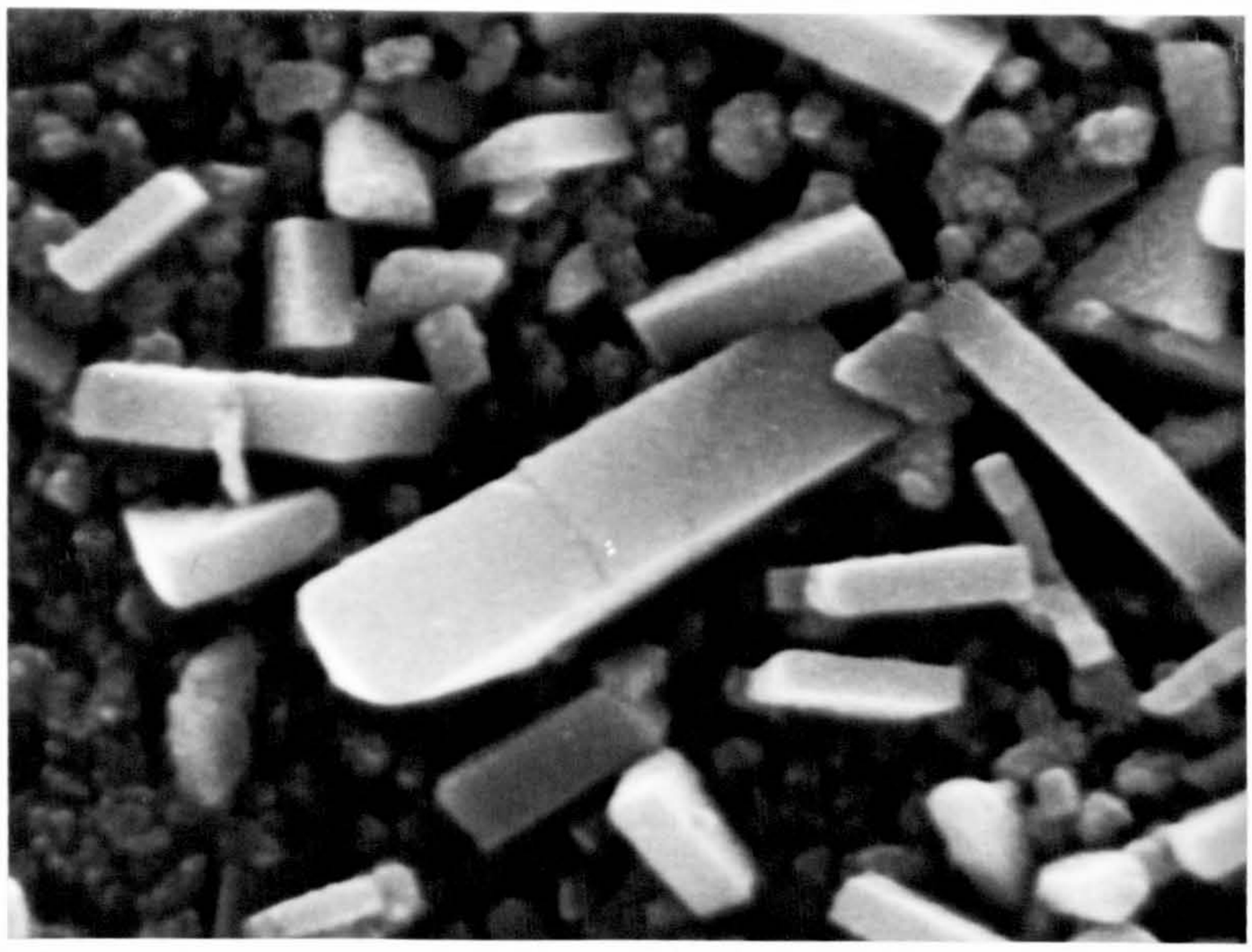

TOP

2 μm

magnification=5,000

BOTTOM

0.5μm

magnification = 20,000

Fig. 4.34 Growth of PbO_2 from $PbSO_4$ on flat Pb electrode after 30s

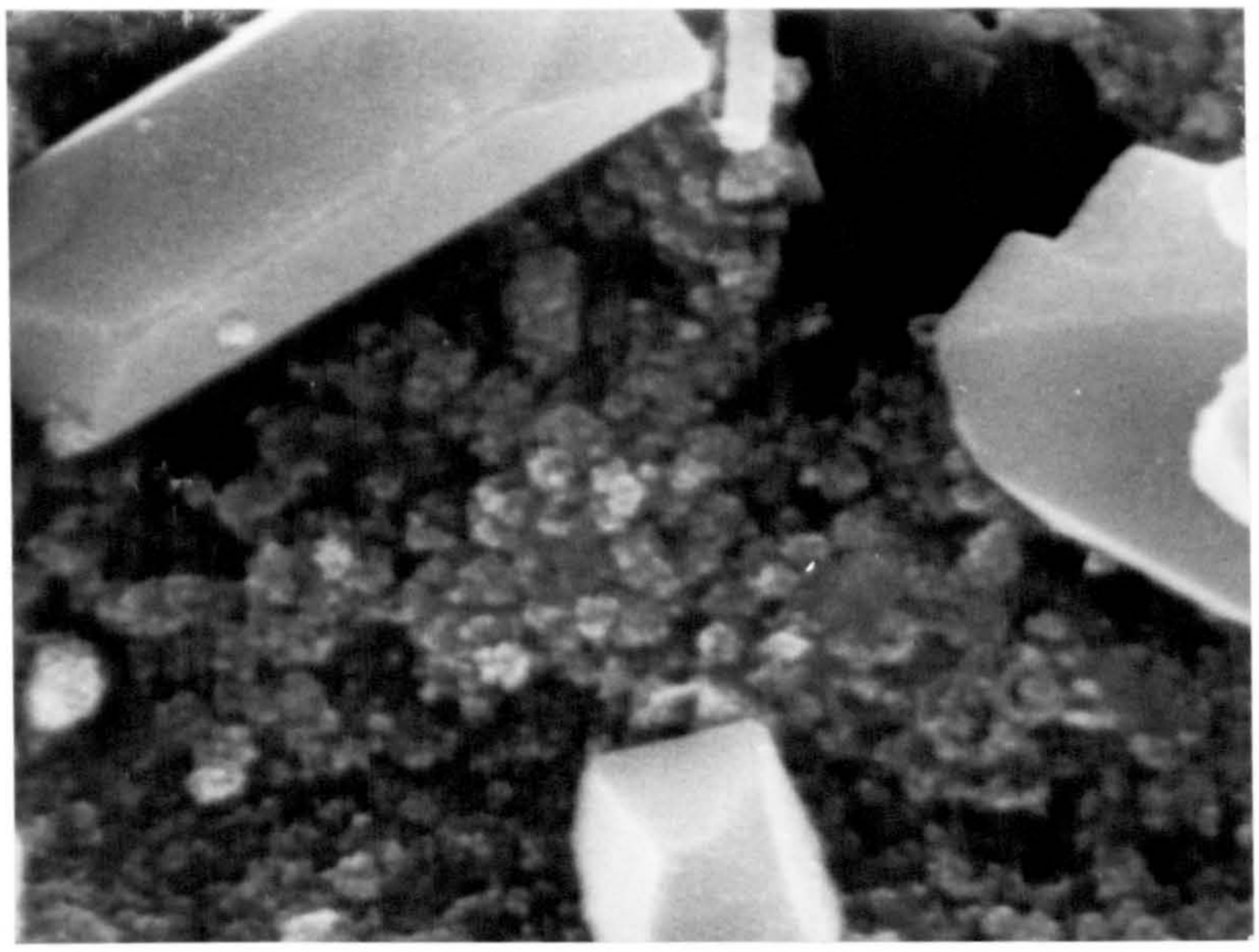

TOP

2 μm

magnification=5,000

BOTTOM

0.5μm

magnification = 20,000

Fig. 4.35 Growth of PbO_2 from $PbSO_4$ on flat Pb electrode after 50 s

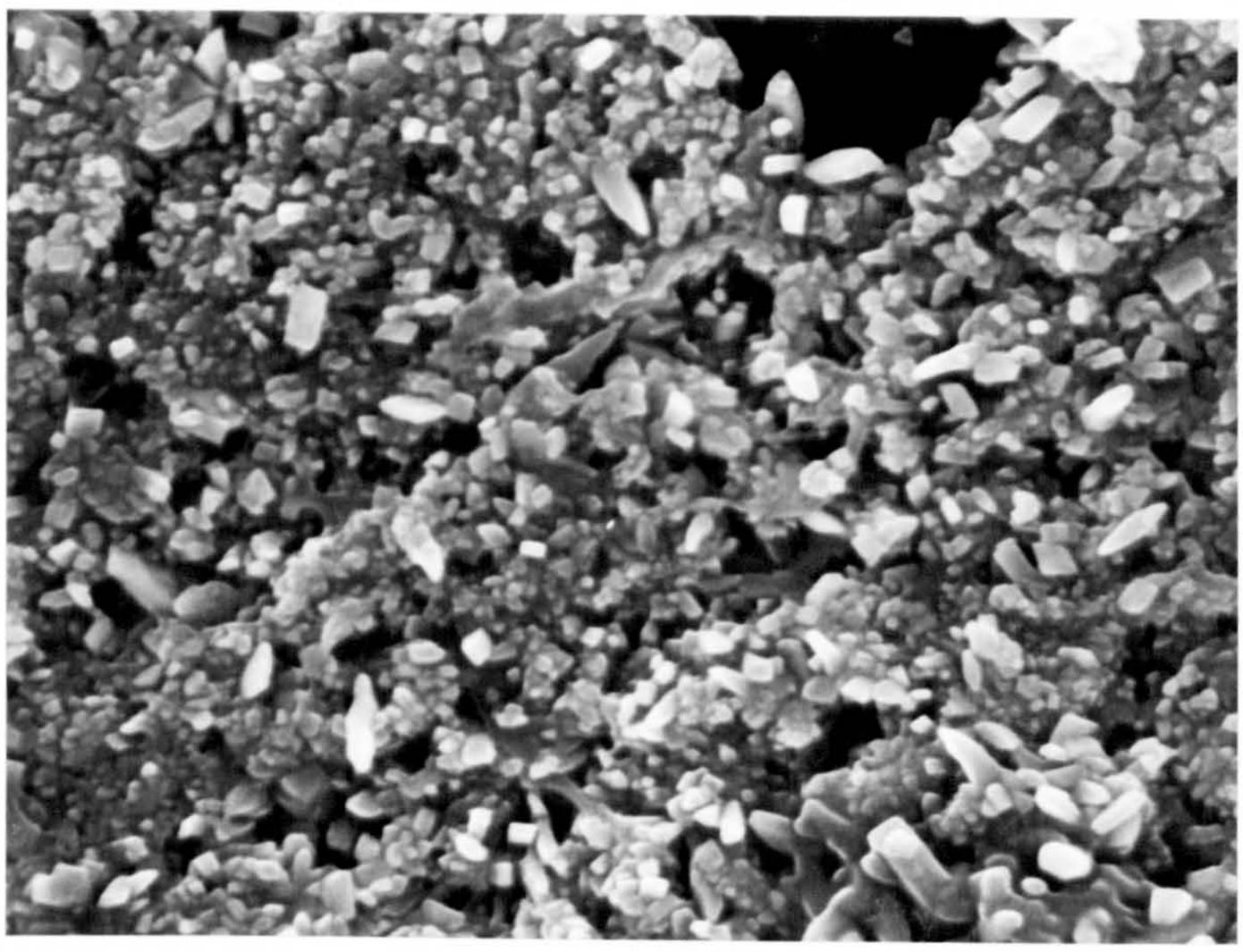

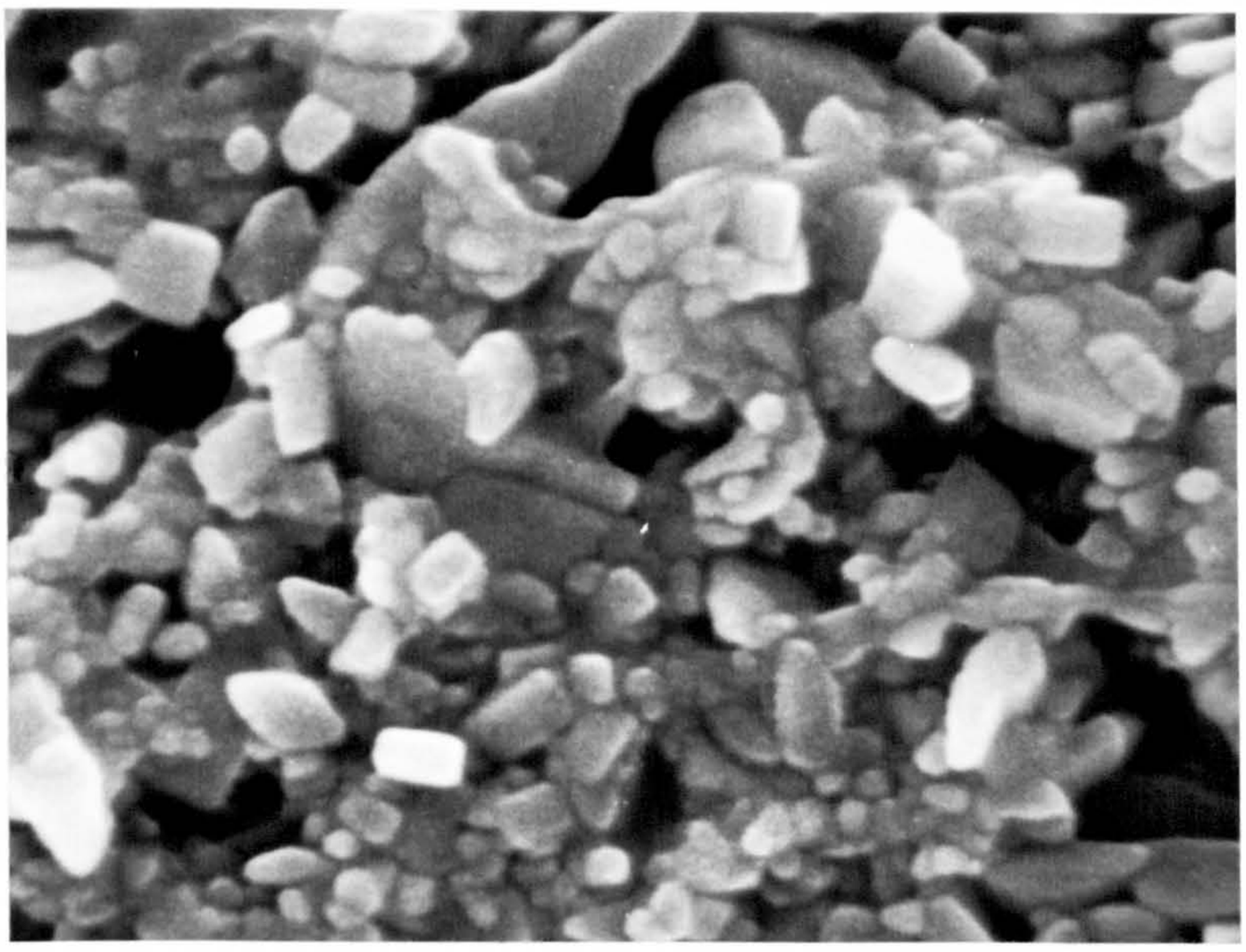

TOP

2 μm

magnification=5,000

BOTTOM

0.5μm

magnification = 20,000

Fig. 4.36 Growth of PbO_2 from $PbSO_4$ on flat Pb-Sb electrode after 10s

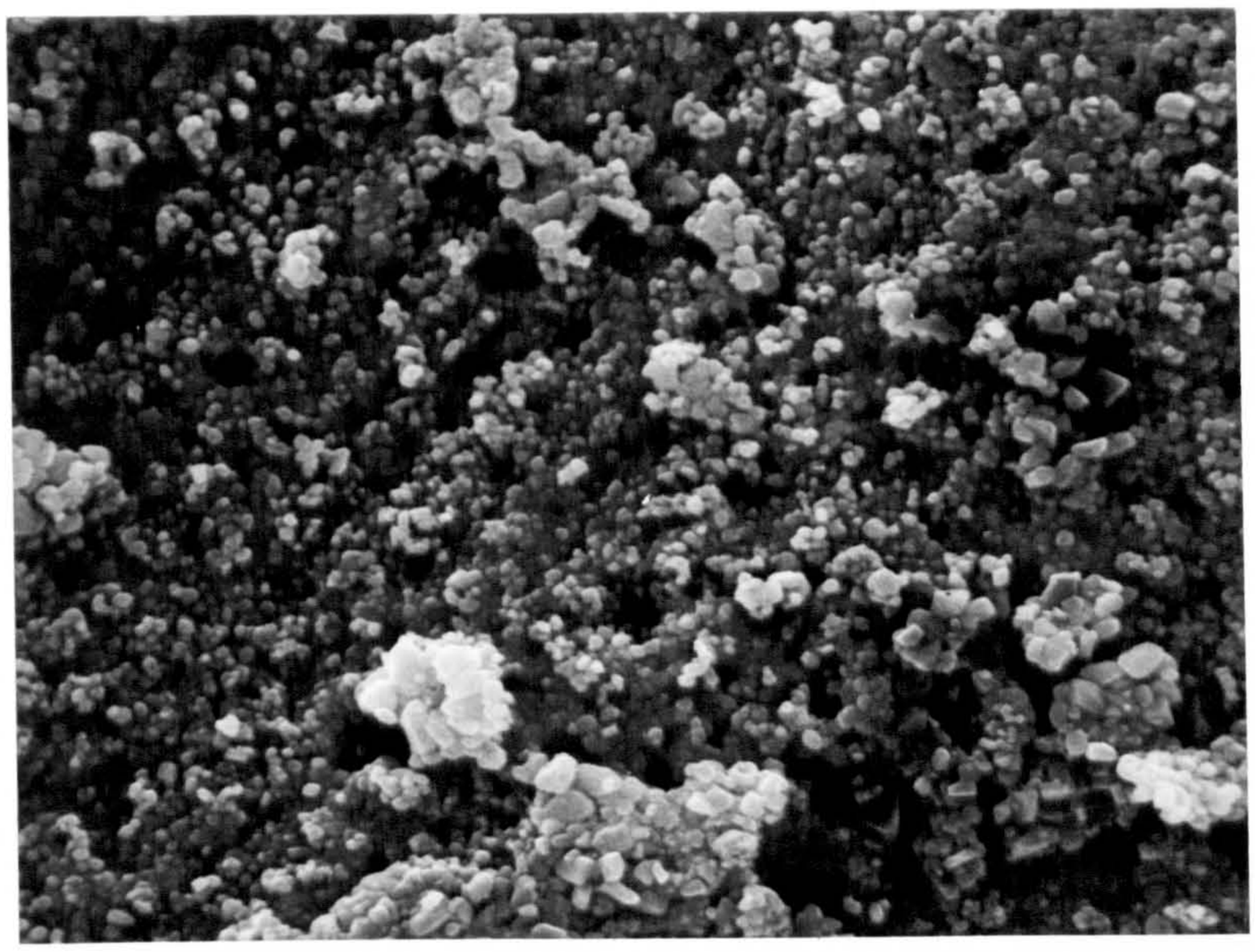

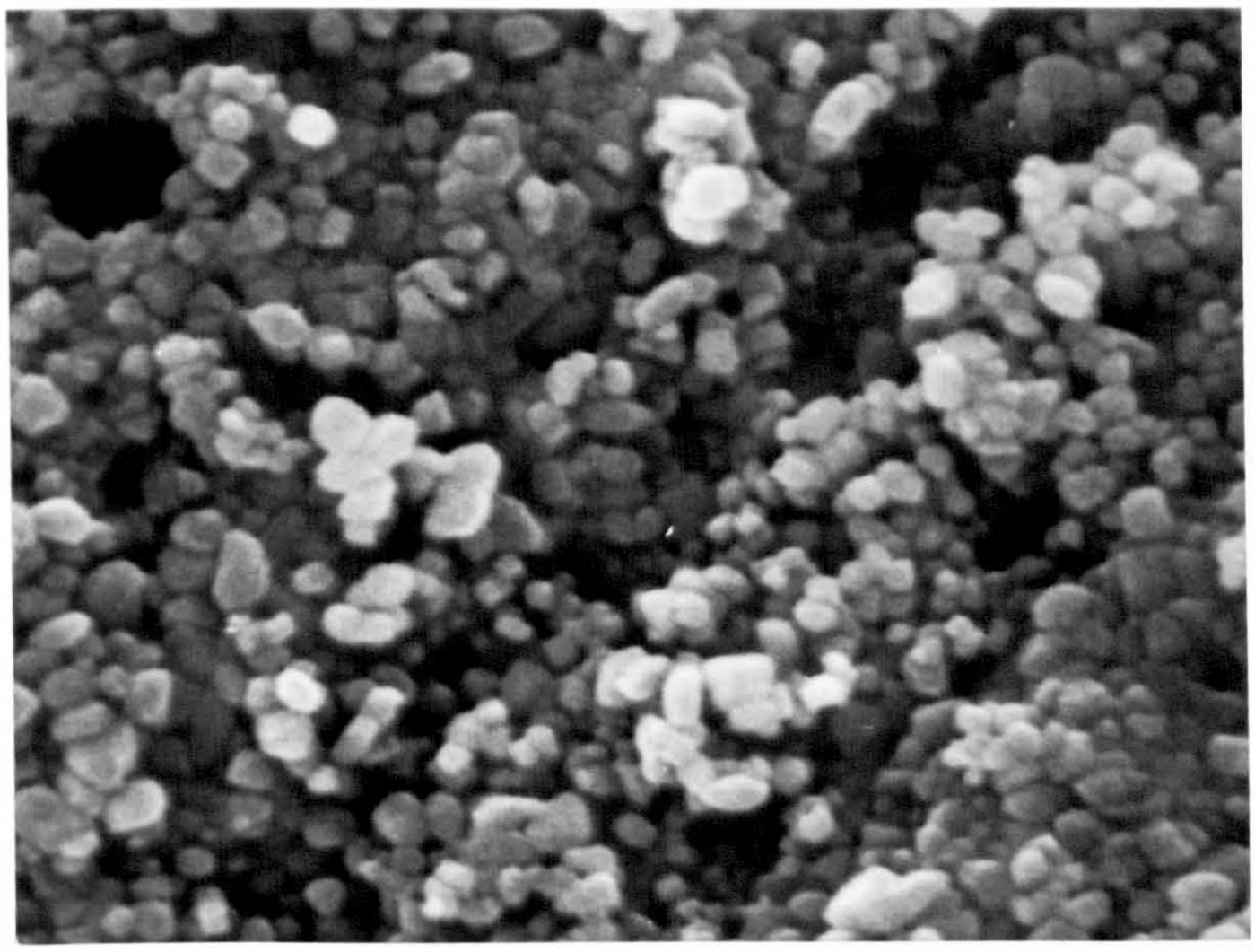

TOP

2 μm

magnification=5,000

BOTTOM

0.5μm

magnification = 20,000

Fig. 4.37 Growth of PbO_2 from $PbSO_4$ on flat Pb-Sb after 20 s

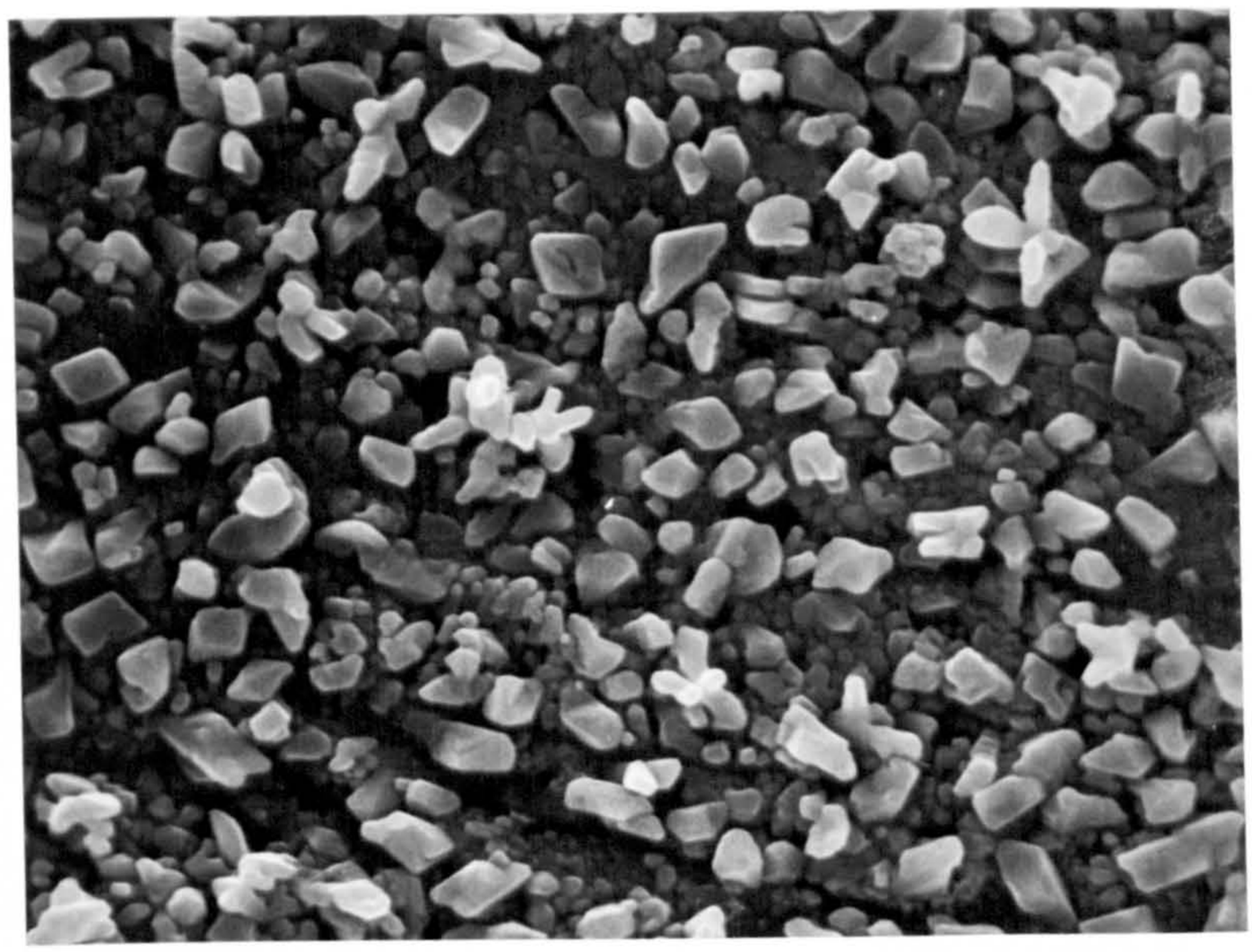

TOP

2 μm

magnification=5,000

BOTTOM

0.5μm

magnification = 20,000

Fig. 4.38 Growth of PbO_2 from $PbSO_4$ on flat Pb-Sb after 30 s

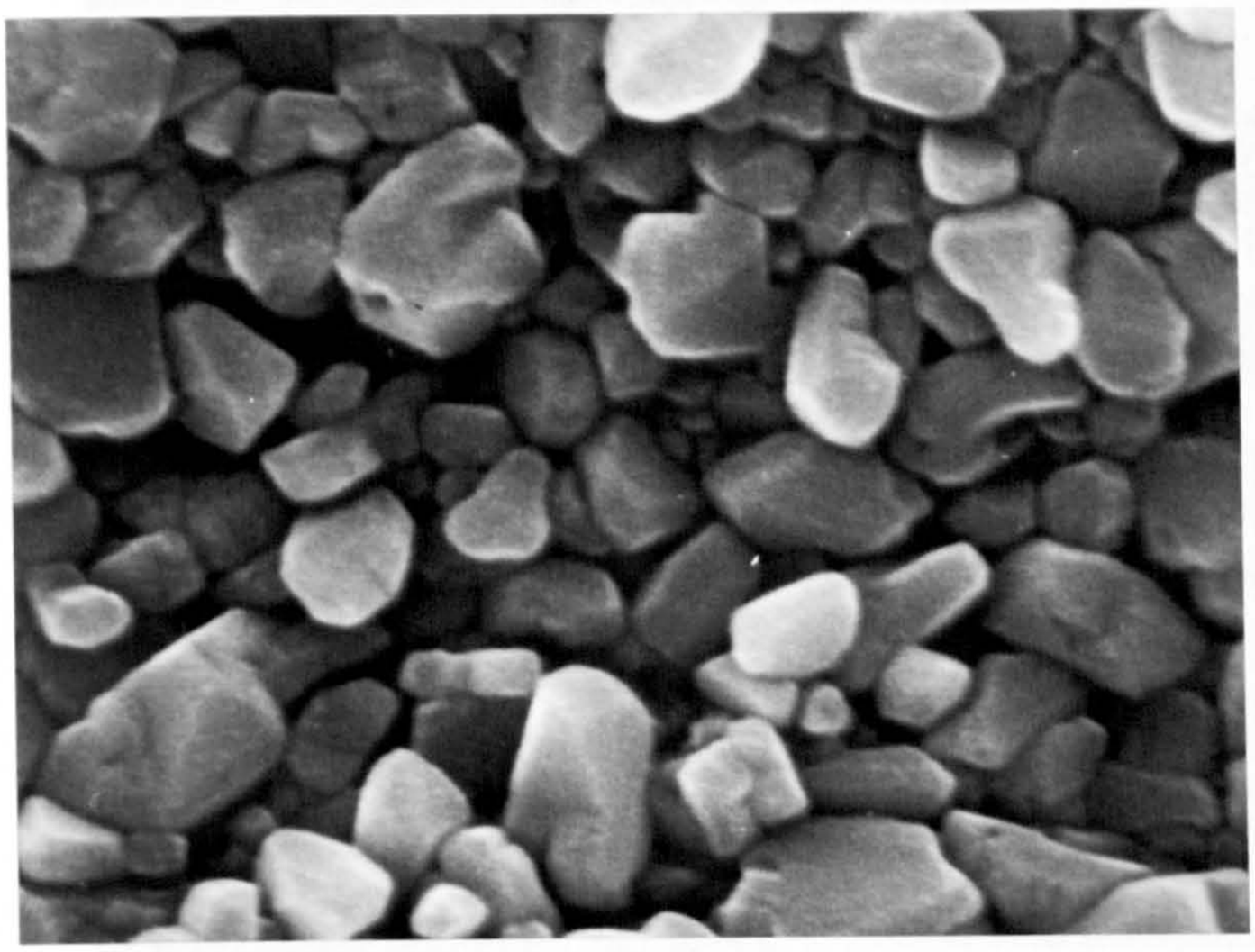

Fig. 4·39 Growth of PbO_2 from $PbSO_4$ on flat Pb-Sb after 90 s

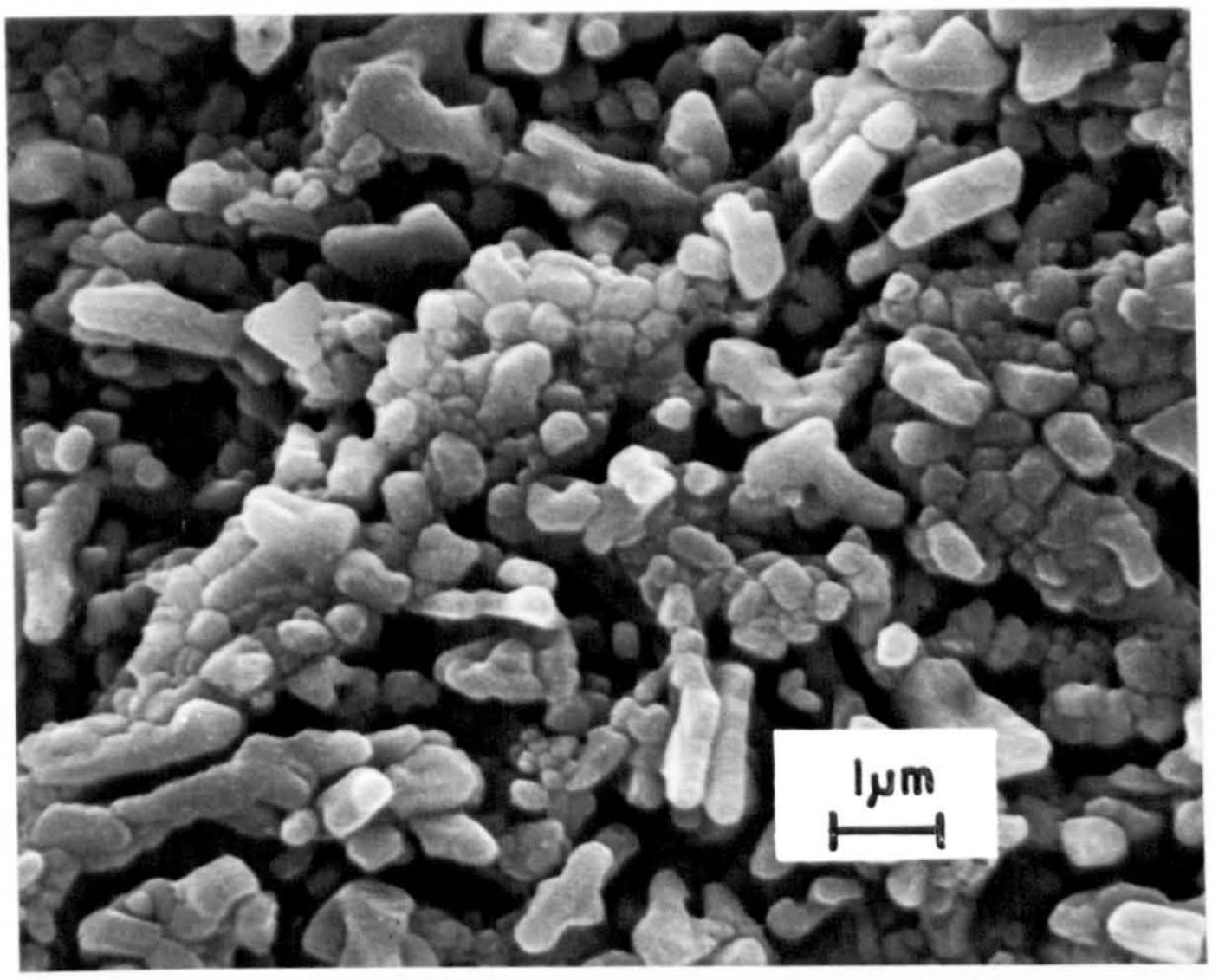

×10⁴

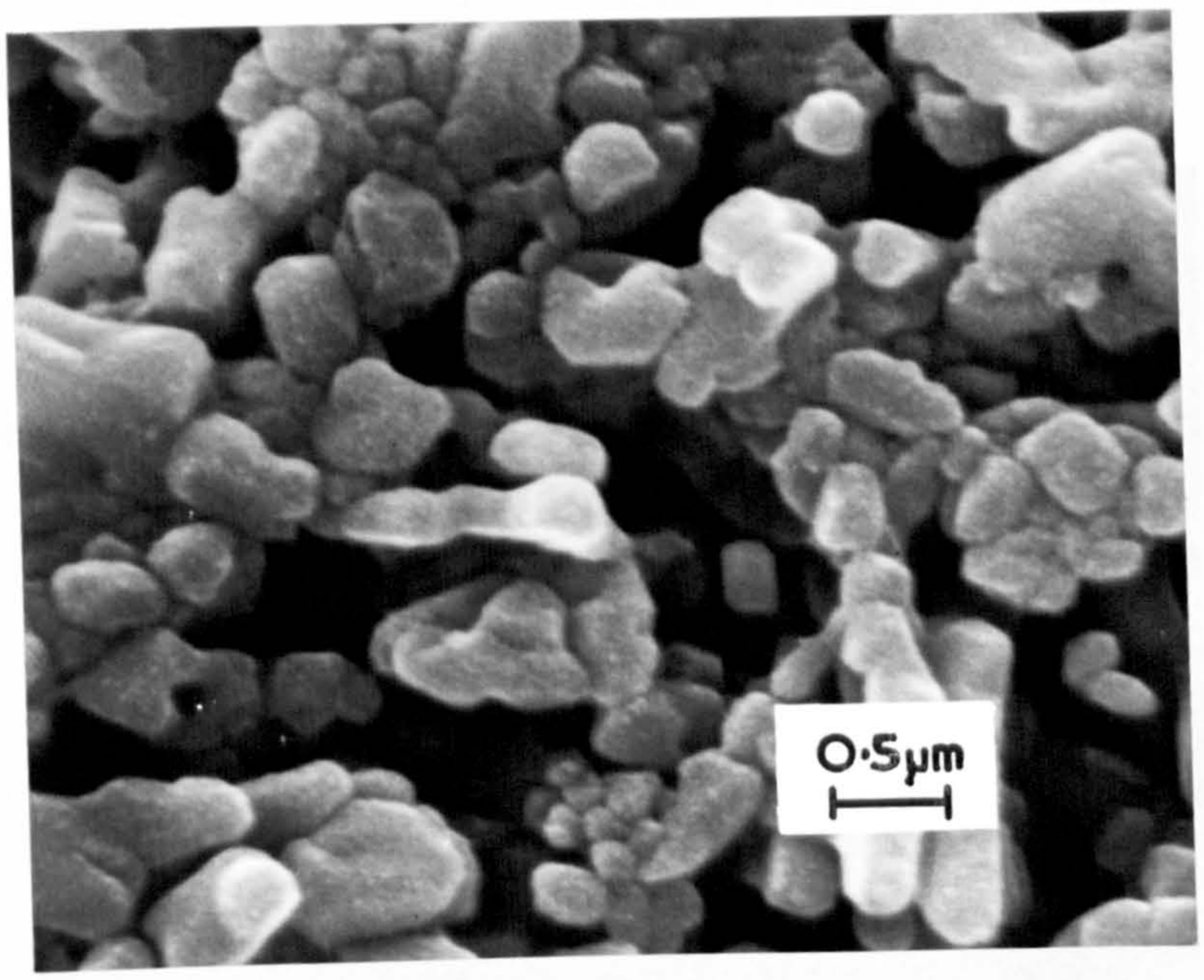

x 20,000

Fig. 4.40 Growth of PbO_2 from $PbSO_4$ on flat Pb-Sb after 150 s

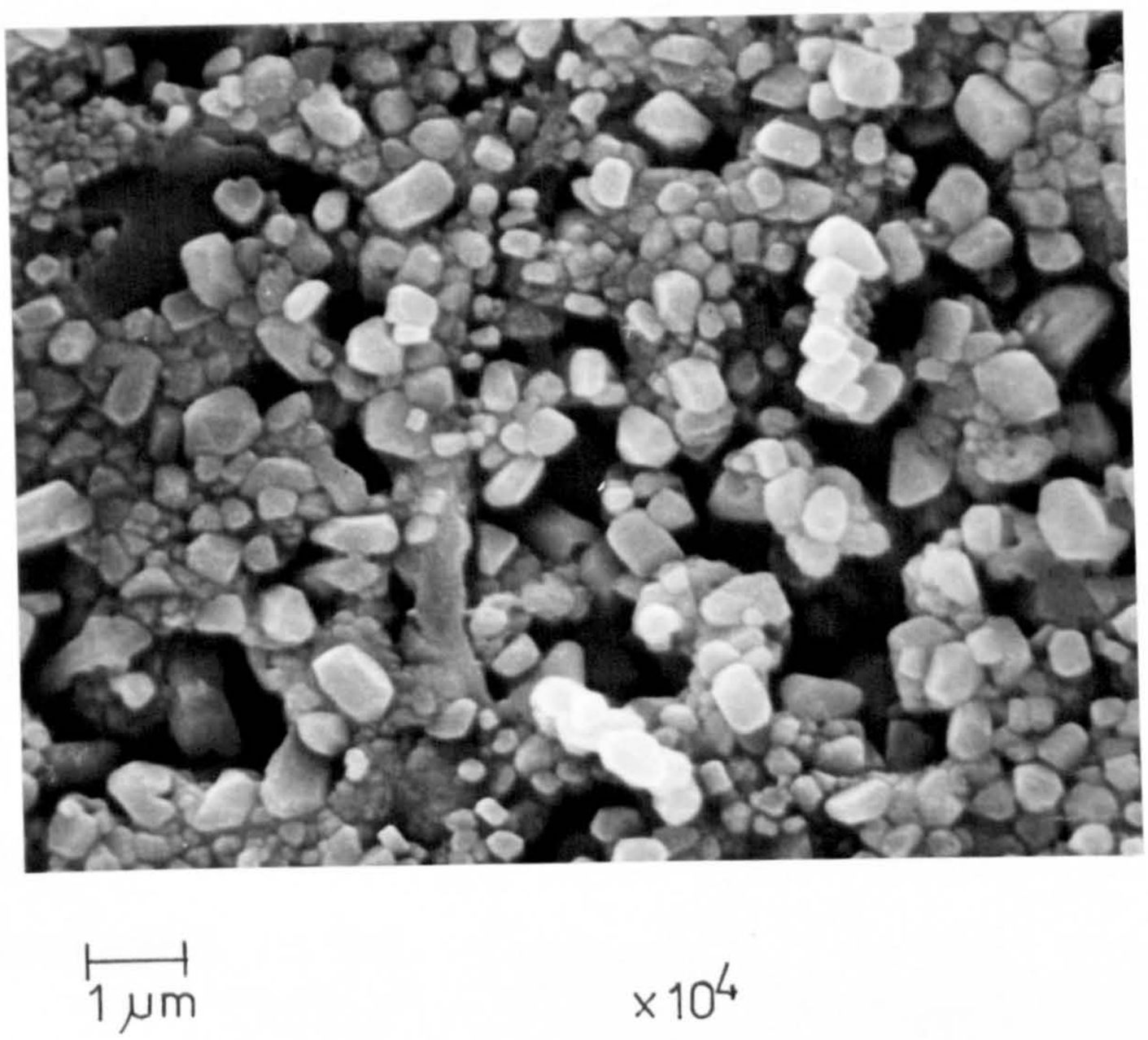

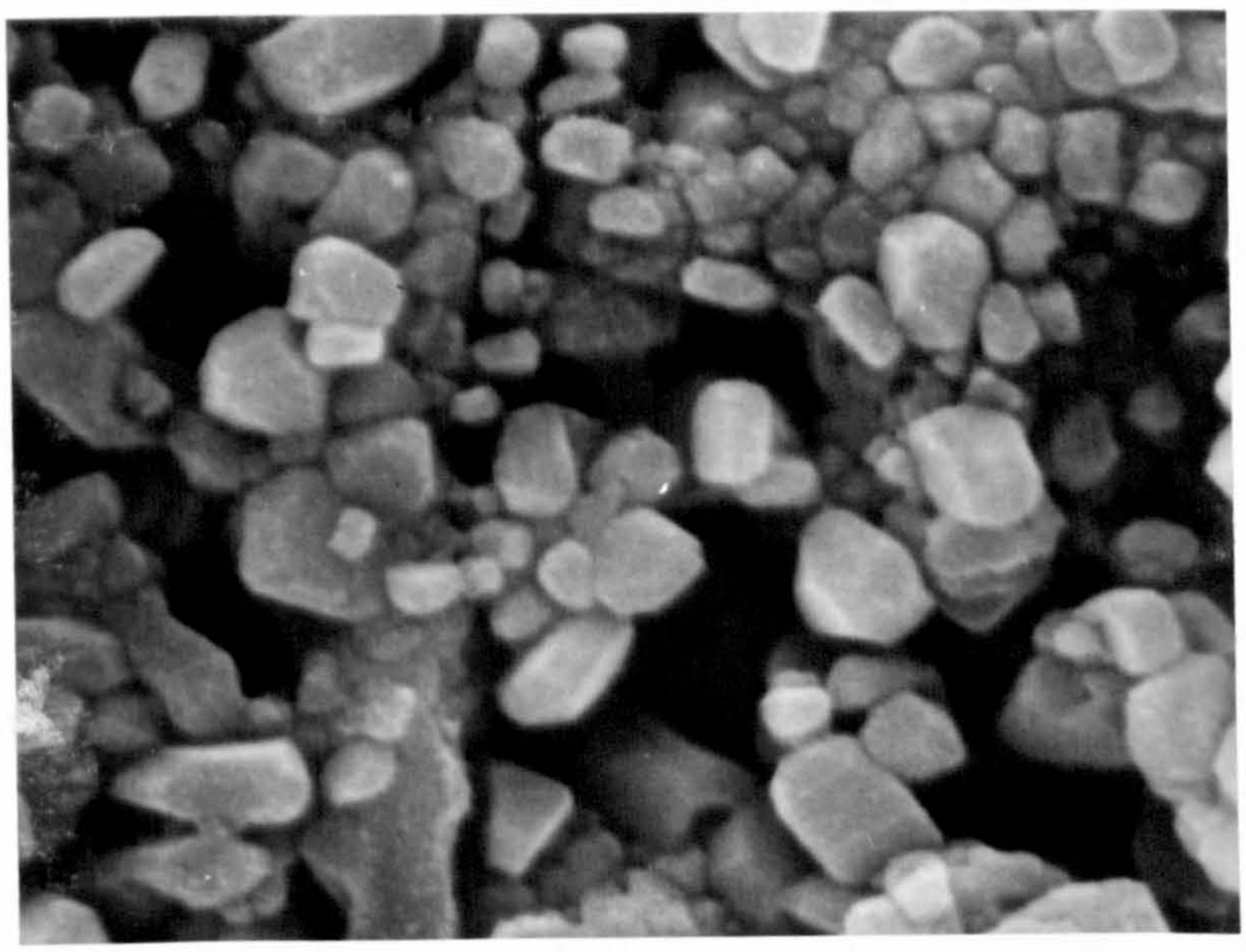

Similar experiments were performed on the electrode containing 5.15% Sb and the corresponding surface morphologies are shown in Figs. 4.36-4.39. Several differences between the pure lead and the antimonial alloy are immediately apparent; the first of these is the absence of unoxidised lead sulphate crystals on the surface which is completely covered with the finer grained PbO_2 structure (compare Figs. 4.32 and 4.36). This observation is significant since it suggests that the presence of antimony serves to somehow activate the surface of the electrode so enabling the product PbO_2 to form more quickly than on an unactivated pure Pb surface. In 4.1 it was concluded that one of the beneficial effects of antimony addition to lead is that it assists the efficiency of oxidation of the $PbSO_4$ deposit; this conclusion is confirmed by the morphological evidence presented below.

A second interesting comparison between PbO_2 formation on pure and antimonial lead is the gradual development of a secondary layer of PbO_2 in the presence of antimony. This is in excellent agreement with the electrometric data given previously (4.2) from which the existence of this duplex layer had been predicted. Figs. 4.36-4.38 show the primary layer of spongy PbO_2 (dia $\sim 0.1\mu m$) being covered with a further layer of much larger, well-defined crystals (dia $\sim 0.5\mu m$) which do not appear to bond to each other. In 4.2 it was shown that both processes (i.e. formation of the primary and secondary layers on antimonial lead) start from zero time since no time correction was necessary when analysing the second peak obtained in the potential step experiments. As the oxidation time is increased this secondary layer of PbO_2 is seen to form voids which multiply until eventually the layer

breaks up (Figs. 4.39 and 4.40). Burbank[103] has observed a similar phenomenon during deep cycling experiments on antimonial alloys, the reason given being the extreme stress caused as the larger crystals grow in size resulting in the fracture of mechanical bonds between the larger and smaller crystals.

Further comparison of Figs. 4.32 and 4.36 shows that the structure of PbO_2 on the pure lead electrode is similar to the primary layer formed on antimonial lead; this is once again in good agreement with our previous electrometric data when analysis of the charge in the transients and the shape came to the same conclusion.

Many workers have attempted to explain the mechanism of the action of antimony on lead dioxide formation. Anodic dissolution of Sb from the electrode has been recognised for many years[104,105] and subsequent behaviour of the dissolved antimony has been studied by tracer techniques[106,107] and S.I.M.S. studies[108,109]. It is also acknowledged that the presence of antimony in the electrolyte has an effect on the surface morphology of the oxidation product[110,111] and Arifuku et al[108] have shown that the distribution profile of Sb in oxide films on Pb-Sb is virtually independent of the final polarisation potential. X-ray diffraction techniques have been used[103] to examine the structure of Pb and antimonial lead alloys during cycling experiments; the author has reported the major presence of β-PbO_2 in the outer layer of the cycled oxidation film on Pb-Sb while beneath a mixture of α and β-PbO_2 formed a microcrystalline coating firmly attached to the metal surface. The absence of a firmly-

bound secondary layer of β-PbO_2 on the pure lead surface was explained in terms of the ability of Sb to nucleate the β-PbO_2 in the primary corrosion layer which bonds with β-PbO_2 produced on further cycling[103]. A probable explanation for our observations can be given along these lin es; the formation of α-PbO_2 in the corrosion film can be explained in terms of acid depletion within the pores of the film as the oxidation proceeds resulting in the formation of a medium which is effectively alkaline in nature. The presence of Sb in the oxidation layer effects the formation of nucleation centres for β-PbO_2 which is present in far greater quantities than on a pure Pb surface. The β-PbO_2 so formed bonds to β-PbO_2 already present in the corrosion layer to form a secondary corrosion film.

CHAPTER 5

THE ELECTROCHEMICAL BEHAVIOUR OF SIMPLE LEAD-BISMUTH BINARY ALLOYS

5.1. Experimental

"Stabilized" electrodes were obtained by cycling to a constant response between the limits 400mV and 1520mV for approximately 1½ hours as previously described in Chapter 4 for pure Pb and Pb-Sb alloys. As before it was found necessary to 'initiate' the reaction by sweeping to a positive limit of 2000mV in the first cycle. The three levels of bismuth used were

wt.%	
0.063 ±	0.002
0.127 ±	0.01
0.267 ±	0.04 (95% confidence limits)

The initial lead sample from which the alloys were made was found to have the following impurities:

0.0025% Ag, 0.0026% Cu, 0.0025% Ti, 0.01% Bi

5.2. Results and Discussion

5.2(i) Linear Sweep Experiments

a) Rate of Attainment of Constant Response

The two anodic current peaks obtained with Pb and Pb-Sb alloys (Chapter 4) were also noticeable in the early cycle pattern of the Pb-Bi binary electrodes (with the positive potential limit set at 2000mV). The quantity of charge contained in the integrated anodic area of these peaks was independent of bismuth concentration in the range studied confirming the finding that the response is due to the base metal (Pb) itself and is also connected with oxygen and other related species because of the upper limit required.

The extent of formation of product lead dioxide showed a large variation with bismuth content such that as the Bi level was increased the corresponding alloy required a large number of cycles to give a constant response (negligible change in peak current values).

b) Constant Response Curves

Stabilised potential curves for each alloy under test are shown in Figure 5.42. The intermediate Bi concentration (0.127 wt %) appears to produce the most stable alloy with peak current values (i_p in PbO_2 formation peak) appreciably less than those for electrodes containing higher (0.267 wt %) and lower (0.063 wt %) levels of bismuth. The position of this current maximum also changes with varying Bi content - the intermediate alloy having an i_p value at the more negative potential. This suggests that the kinetic barrier to the oxidation of $PbSO_4$ varies with the quantity of Bi in the test electrode.

Fig. 5.42 Stabilized L.S.V. Curves ($50\,mV\,s^{-1}$)

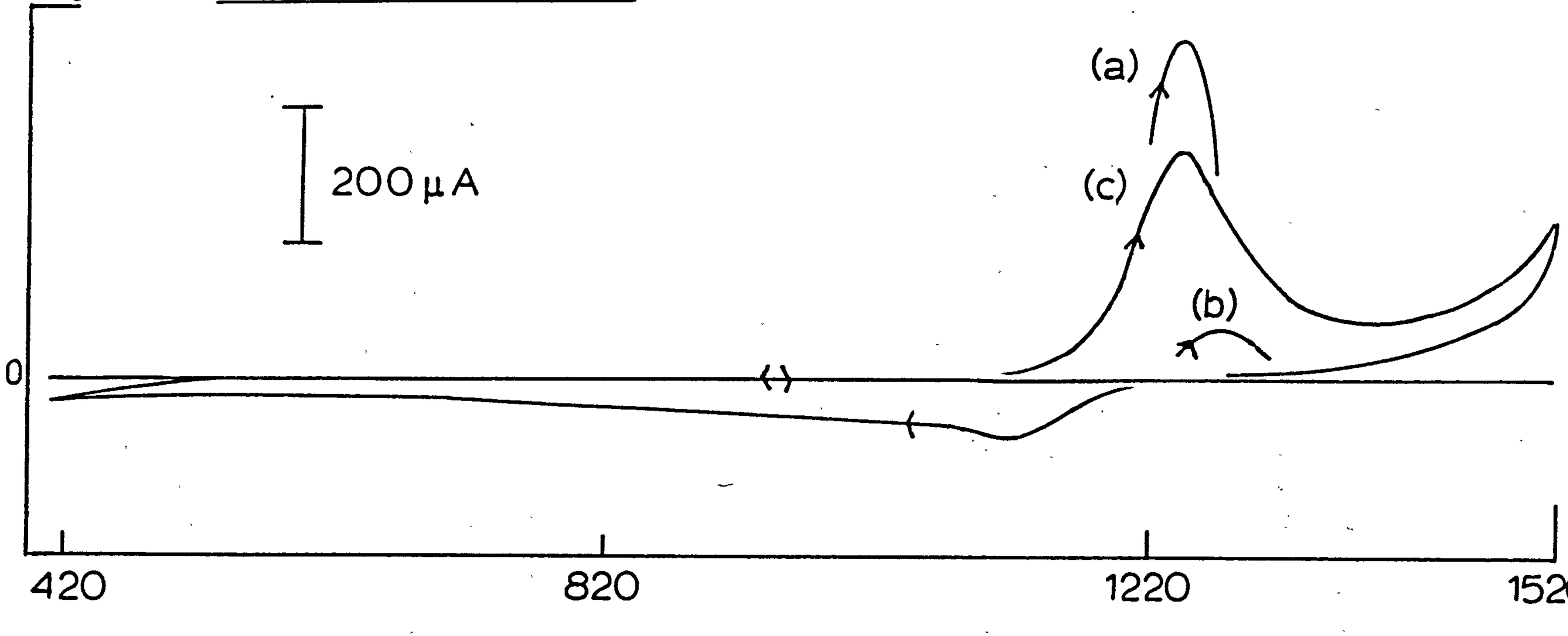

(a) 0·063% Bi
(b) 0·127% Bi
(c) 0·267% Bi

The form of the maximum current (corrodibility) and peak potential variation with bismuth concentration is interesting; a maximum stability to anodic attack occurs within the range studied here. Figure 5.43 depicts this trend as a plot of i_p vs Bi content for stabilised electrodes. A possible explanation for this can be given in terms of grain refinement caused by the incorporation of Bi into the lead lattice. As the amount of Bi is increased, the quantity of lead available for surface reaction is depleted, hence the stability of the alloy initially rises with increasing Bi levels. Zener[112] has shown that grain growth should cease when the average grain size Dm is given by equation (62a).

$$Dm = \frac{d}{F} \qquad (62a)$$

where d signifies the average diameter of an inclusion and F the fraction of the volume in the alloy. It is possible that this condition applies when the concentration of Bi in the alloy lies between 0.14 - 0.19 wt % and so accounts for the minimum in Fig. 5.43. These results contrast with those of Bryntseva[113] and Gonzales[114]: Bryntseva has reported an increase in the electrochemical corrosion of lead anodes containing concentration of Bi up to 2% and Gonzales has claimed that the corrosion rate can be doubled by increasing the Bi content from 0.01 to 0.1%. The latter author emphasised that the precise increase depended on the conditions of the test which greatly differ from those used here and probably account for the difference between their results and ours.

The relationship between peak potential (E_p) and sweep rate (v) is shown in Fig. 5.44 as a plot of E_p vs $\log_{10}$ v for each alloy

Fig. 5.43 i_p vs. Bi content

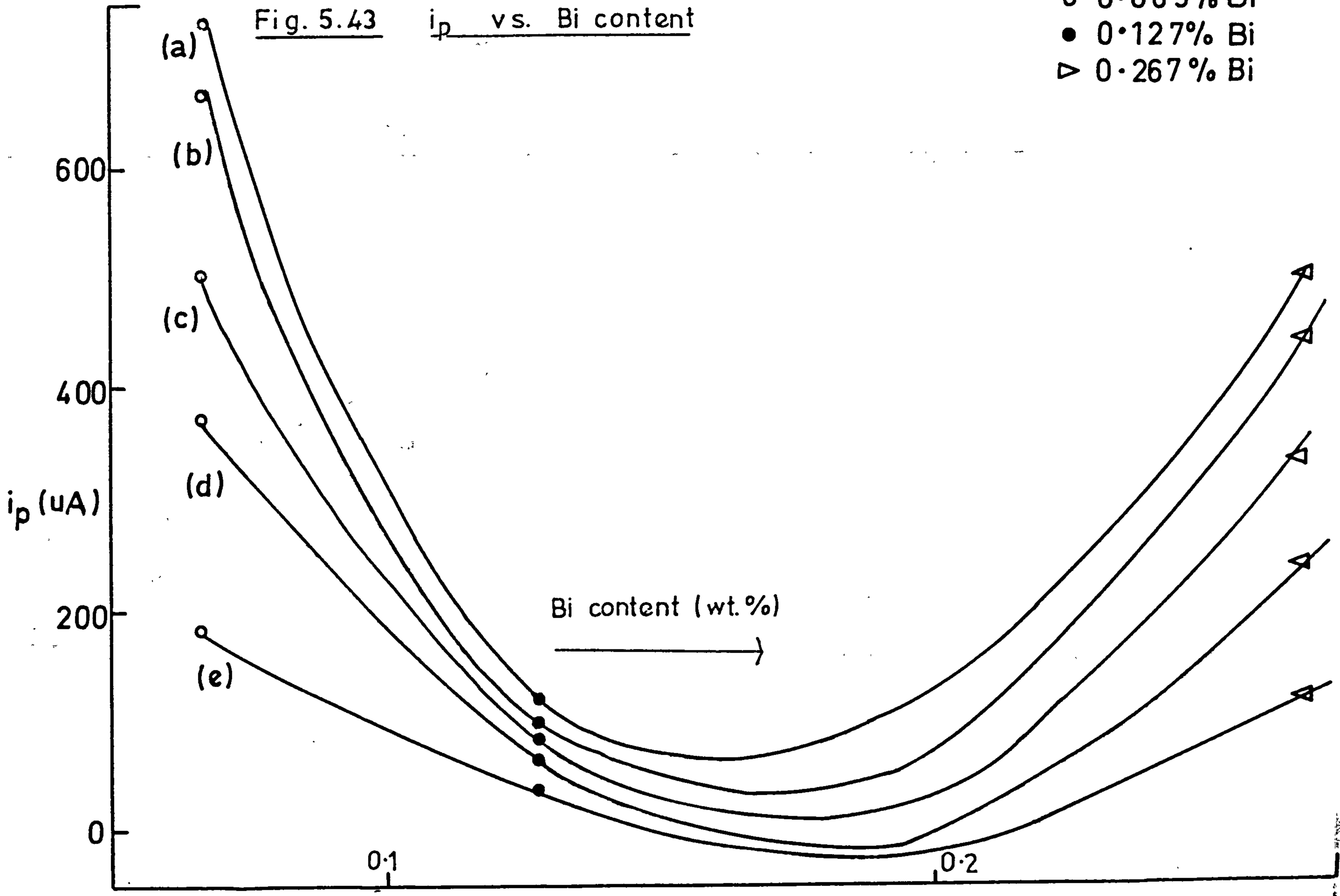

Fig. 5.44 Relationship between E_p and sweep rate

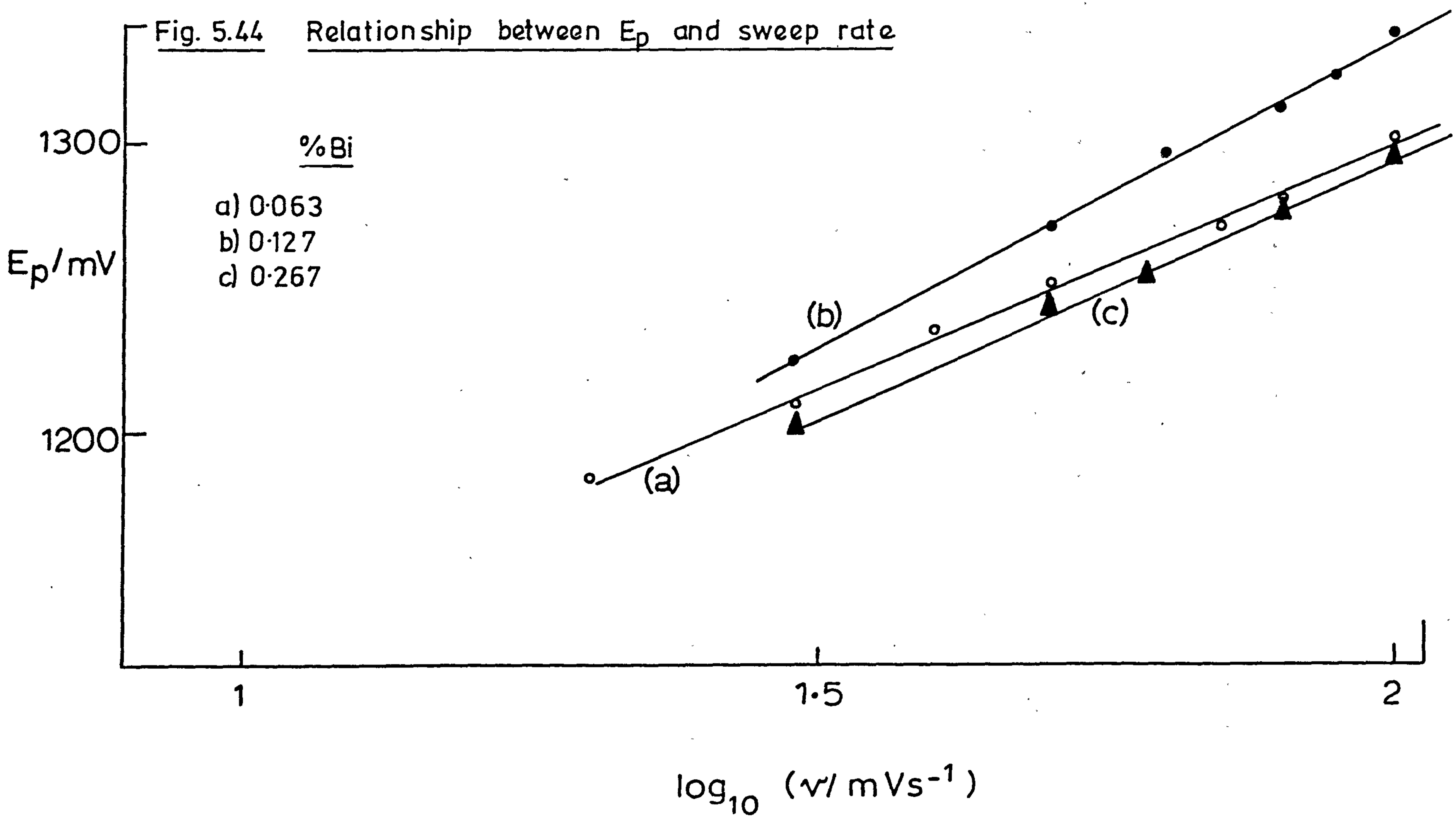

under test. This data is in agreement with that obtained by Canagaratna et al[100] and with the data given in Chapter 4 (for both pure and antimonial lead) for the growth of a single layer on an electrode surface. Fig. 5.45 shows the relationship between the peak current (i_p) and sweep rate (v) in the form of a plot of i_p against $\sqrt{v}$. In each case (three bismuth concentrations) the peak current values are much larger than corresponding data on Pb and Pb-Sb (5%) electrodes indicating that concentrations as low as 0.06% Bi in lead result in the formation of an alloy which is much more susceptible to anodic attack than one containing a relatively high proportion of antimony.

A summary of the integrated anodic charge for stabilised Pb-Bi electrodes is given in the table below:-

Calculated anodic charge during positive-going sweep (400-1520mV) for stabilised electrodes

Sweep rate (mVs^{-1})	Anodic charge ($mC\ cm^{-2}$)		
	0.063 % Bi	0.127 % Bi	0.267 % Bi
10	35.4	6.2	32.2
30	23.0	4.9	20.5
50	18.0	3.9	16.0
60	16.7	3.2	14.5
80	15.3	2.9	12.7
100	14.1	2.9	11.7

An interesting feature here is the similarity between Pb-Sb and Pb-Bi electrodes, both exhibiting a much larger sweep-rate dependency of charge than pure lead . As already discussed in Chapter 4, this can be attributed to the constant thickness of the oxidised layer on pure lead which discharges to approximately the same extent throughout. The Pb-Sb and Pb-Bi alloys on the other hand form a layer which is more porous than that on pure lead and so the reaction is driven deeper into the spongey mass at lower rates of sweeping. The lack of any rotation speed dependence during the electrochemical cycling indicates that the diffusion of species through the electrode occurs via a solid state process similar to that for Pb and Pb-Sb electrodes.

Potential Sweep Experiments

These were performed after formation of $PbSO_4$ by cyclic potential sweeping and a stabilising period at 400mV when the current became negligible ($\lesssim 1 \mu A$). It has already been shown in the previous chapter that the length of time the electrodes are held in the sulphate region has a significant effect on the oxidative behaviour of the lead sulphate deposit and has suggested this is due to the removal of nucleation sites formed during the stabilising sweep; for this reason the reductive period prior to potential stepping was kept constant at approx. 20 mins.

Fig. 5.46 shows a typical current response curve when a lead sulphate deposit (formed by continuous cycling on a Pb-Bi base) is stepped into the lead dioxide region. The form of the transient is similar to that for pure lead where the initial double layer charging spike is followed by an increase in current due to the formation and

Fig. 5.45 i_p vs. $v^{1/2}$

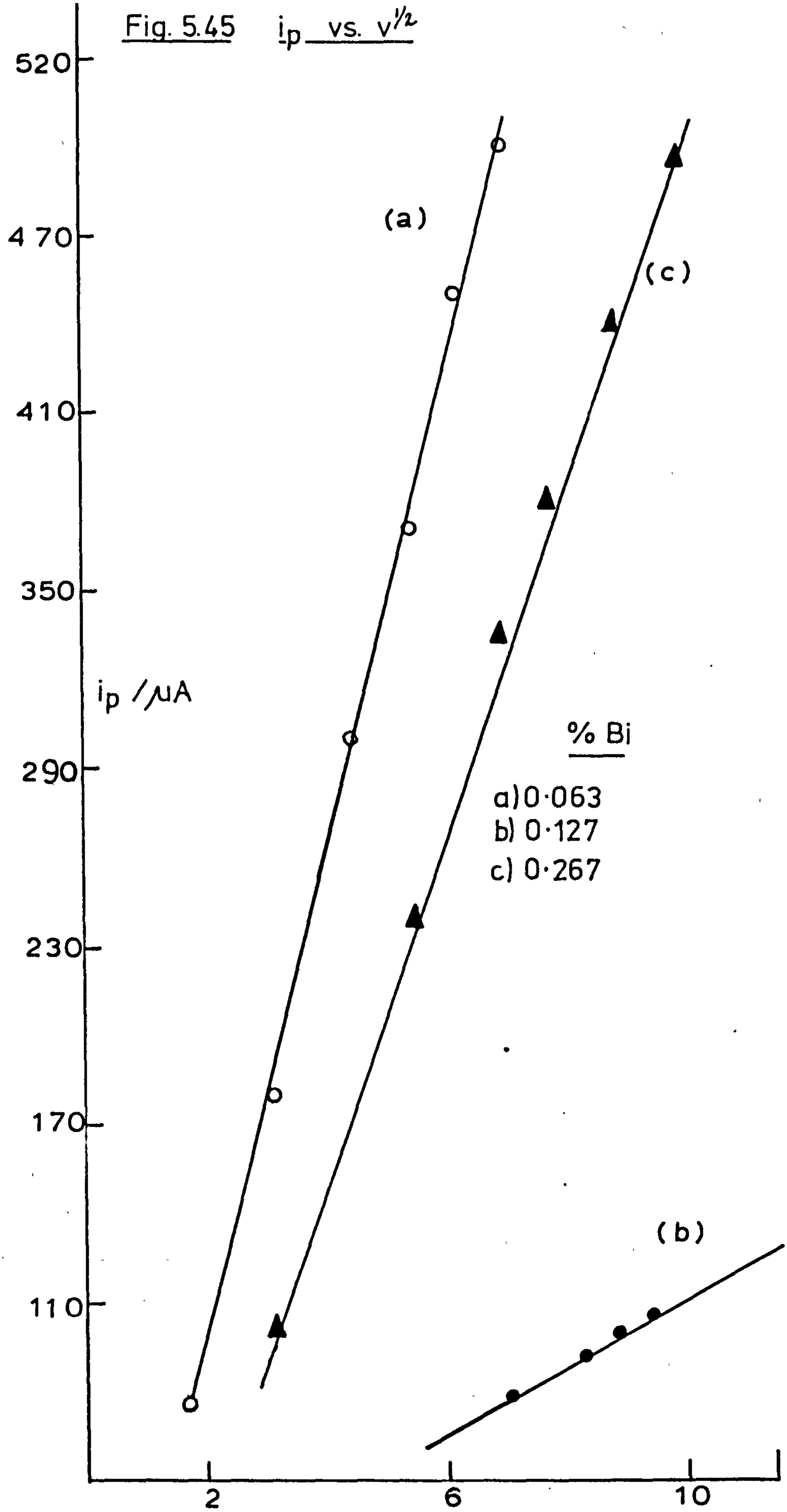

Fig 5.46 i-t transient for potential step from 400mV to 1100mV

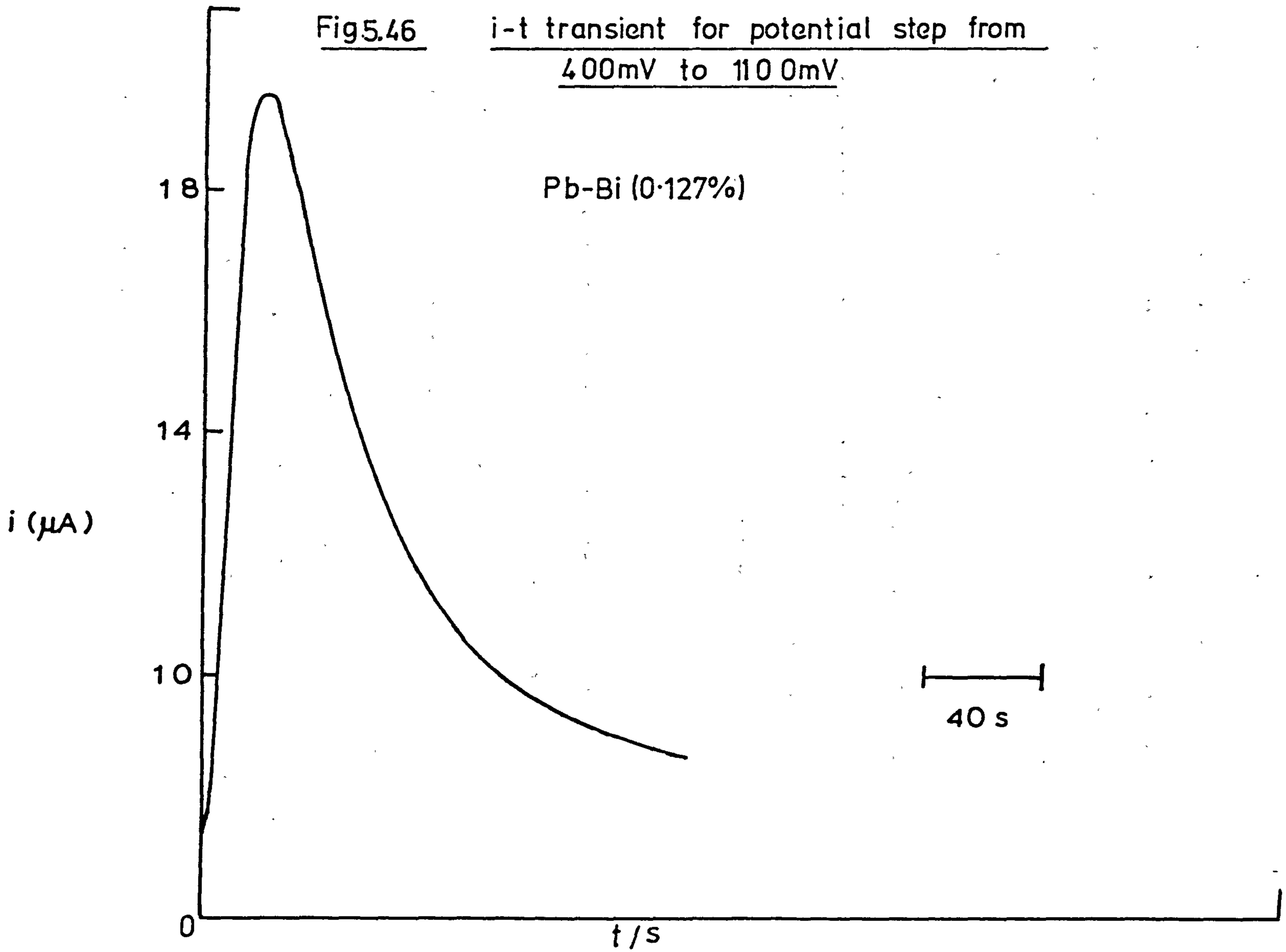

growth of nucleation centres. The presence of a single oxidation peak is indicative of a completely passivated film (PbO_2) with most of the residual current flow due to the oxygen evolution reaction because of the high overpotential used. These observations contrast with the data given for Pb-Sb in Chapter 4. when a thickening of the oxidised deposit does occur and a second rise in transient is obtained as a further layer of product PbO_2 is formed.

Although at the start of the transient response (Pb/Bi) the current did not rise from zero (indicating the presence of some growth centres) we were able to identify a two-dimensional growth process similar to that for Pb and Pb-Sb (Chapter 4) by the residual linear i-t correlation represented by equation (60).

Fig.5.47 shows a typical series of current-time curves for the rise in transient as a cyclically-formed $PbSO_4$ deposit on a Pb-Bi base is stepped to various overpotentials in the PbO_2 region. The slopes of these lines are seen to increase with increasing overpotential which is to be expected from equation (60) ($di/dt \propto k^2No$ at short times). The potential dependency of k^2No is shown in Fig. 5.48 as a plot of overpotential vs $\log_{10}$ (di/dt). It is interesting to note that as the electrodes are stepped to a series of increasing overpotentials the peak current values rise to a limiting value then start to fall.

It can be shown[115] that for instantaneous nucleation

$$i_m = (2\pi No)^{\frac{1}{2}} n F k h e^{-\frac{1}{2}} \qquad (63)$$

which when compared with the data in Fig. 5.48 shows that for a simple dimensional process the value of i_m should not decrease. This fall-off

in peak current values is accompanied by a corresponding fall in the charge contained in the oxidation peak (calculated by a simple integration process). A possible explanation for this can be given in terms of a reduction in effective surface area of the electrode due to partial coverage of the surface by gaseous oxygen (again because of the high overpotentials used):

Surface area before potential step = A_s

Surface area after potential step = $A_s(1-\theta)$

where θ represents the area of the electrode covered with oxygen. (As the overpotential is increased the value of θ will also increase and i_m subsequently falls). Fig. 5.49 confirms the presence of oxygen on the electrode surface with a reduced plot of i/i_m vs t/t_m; the current values at the tail-end of the curve ($t/t_m > 1.5$) are larger than expected due to the contribution of the oxygen evolution current.

A further proof that the reaction studied here follows a simple 2-dimensional growth mechanism is provided in Fig. 5.50 with a typical plot of $\ln \frac{i-i_r}{t}$ vs t^2 with a correction for the oxygen evolution current being made. The straight lines obtained are in good agreement with equation (60).

These results are of great importance to industry and battery manufacturers in particular since they give the optimum level of bismuth for use as a grid alloying ingredient in the lead-acid battery system. They do not however provide any information concerning the recharge characteristics of such an alloy. Dewitt and Myers[116] found Bi to have a less harmful effect than Sb on self-discharge and gassing rates. These beneficial properties of bismuth if combined with the

optimum level of the alloy (minimum anodic corrosion) in the positive battery grid could go a long way in promoting Bi as a replacement for Sb in the lead-acid system today.

Fig. 5.47

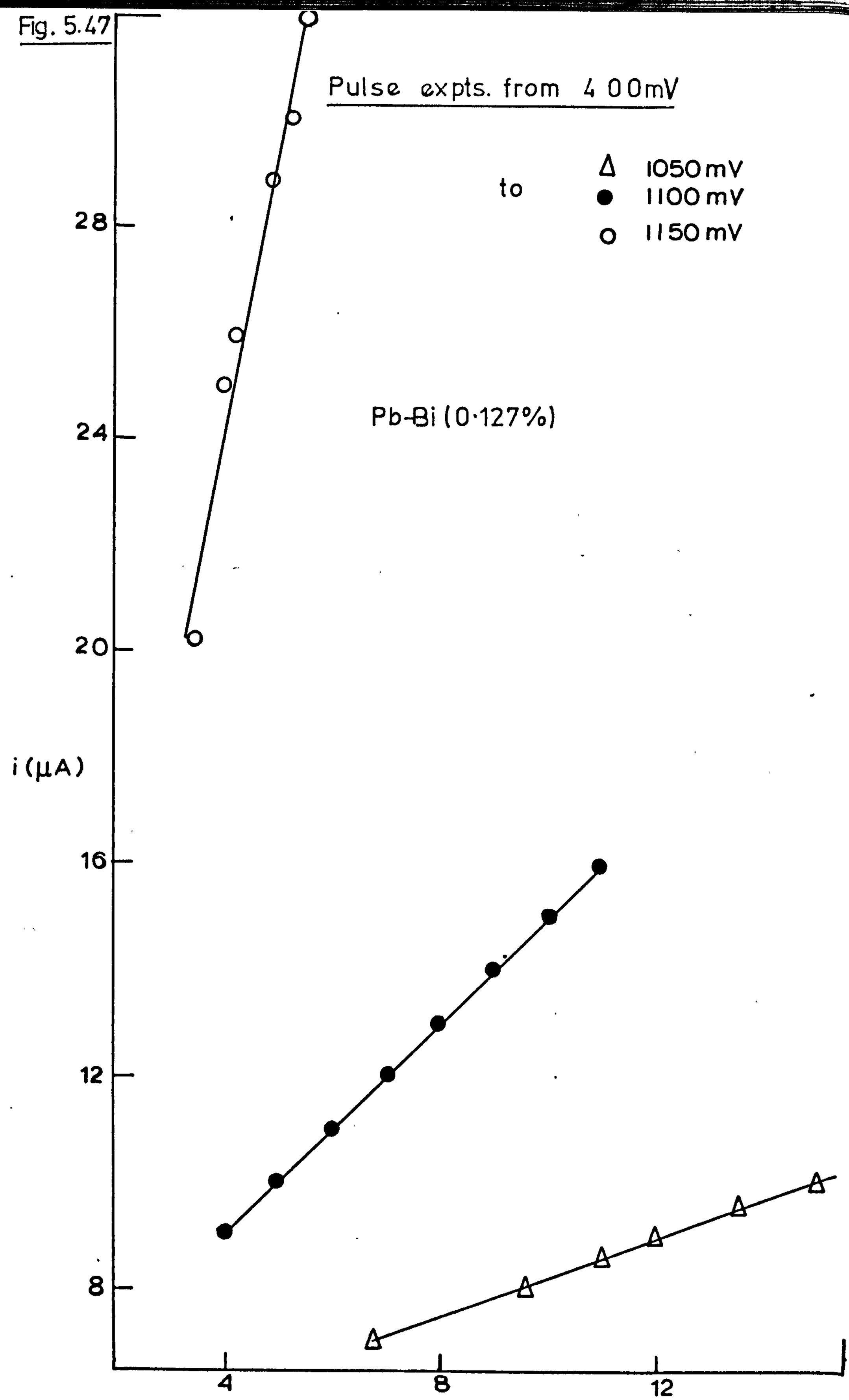
Pulse expts. from 400mV
to
Δ 1050mV
● 1100mV
○ 1150mV
Pb-Bi (0·127%)
i (μA)
28
24
20
16
12
8
4
8
12
t (s)

Fig. 5.48 Plot of η vs. log (di/dt)

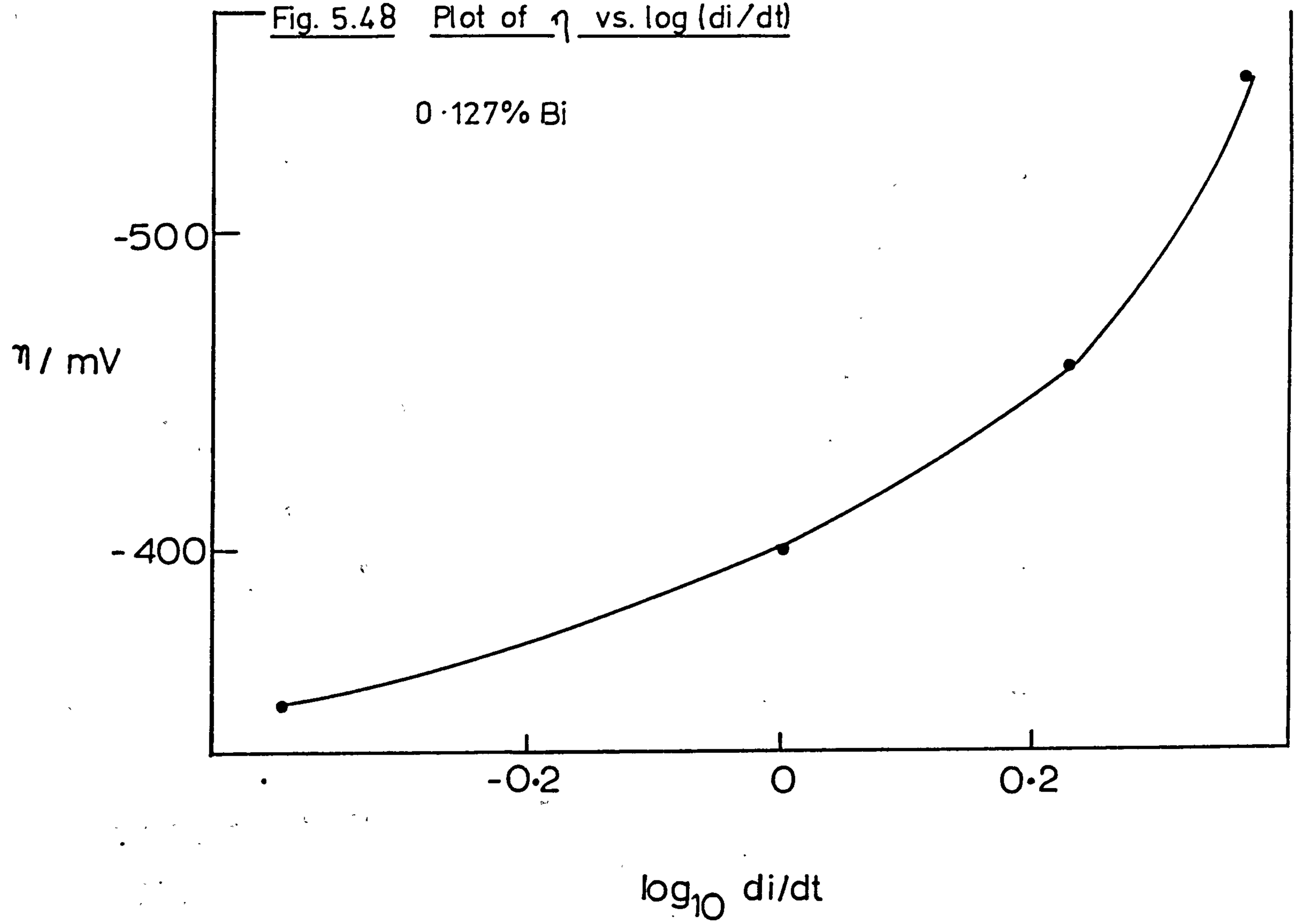

Fig. 5.49 Dimensionless Plot for potential step transient

0·127% Bi, 400-1100 mV

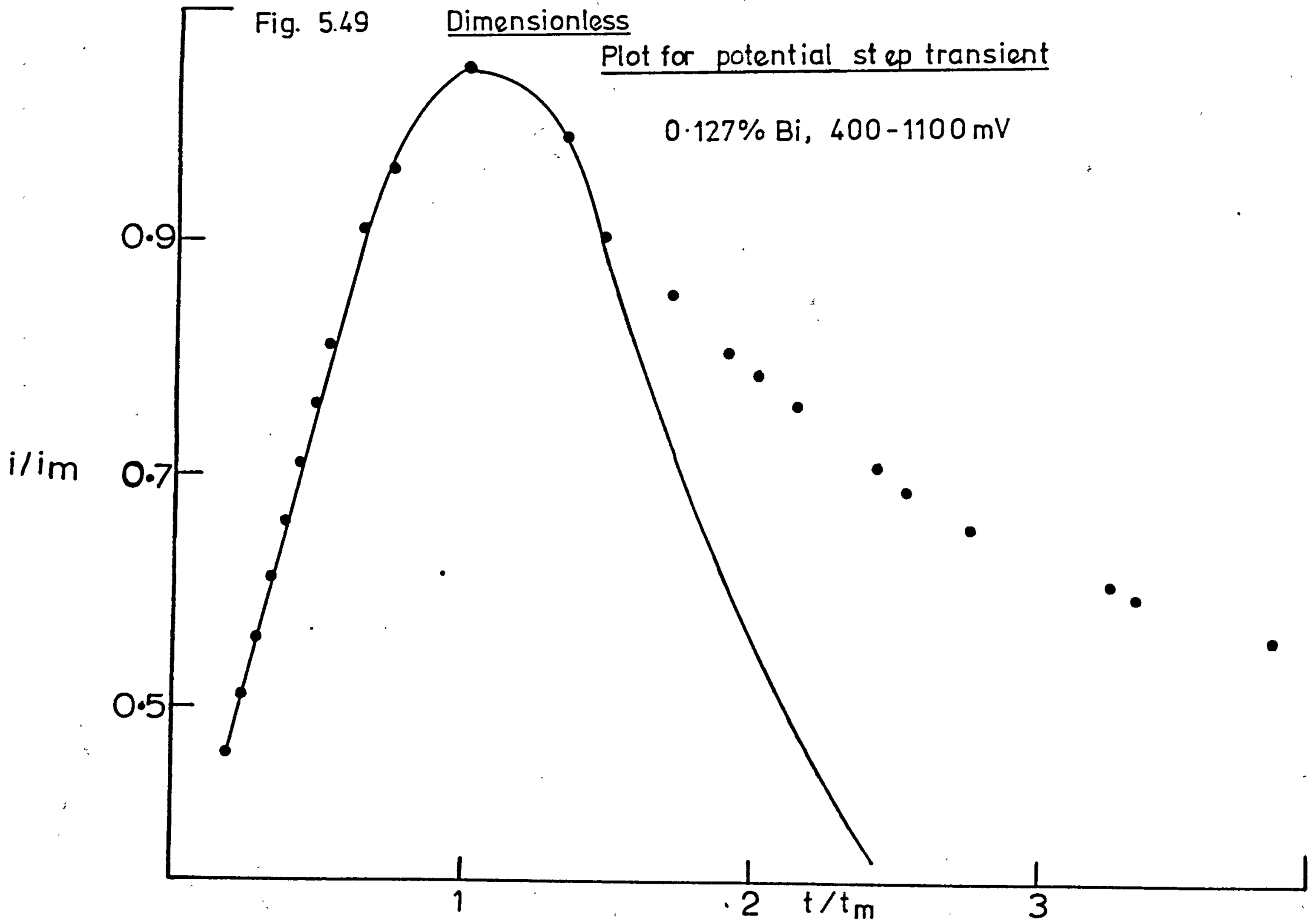

Fig. 5.50 Analysis of falling transient

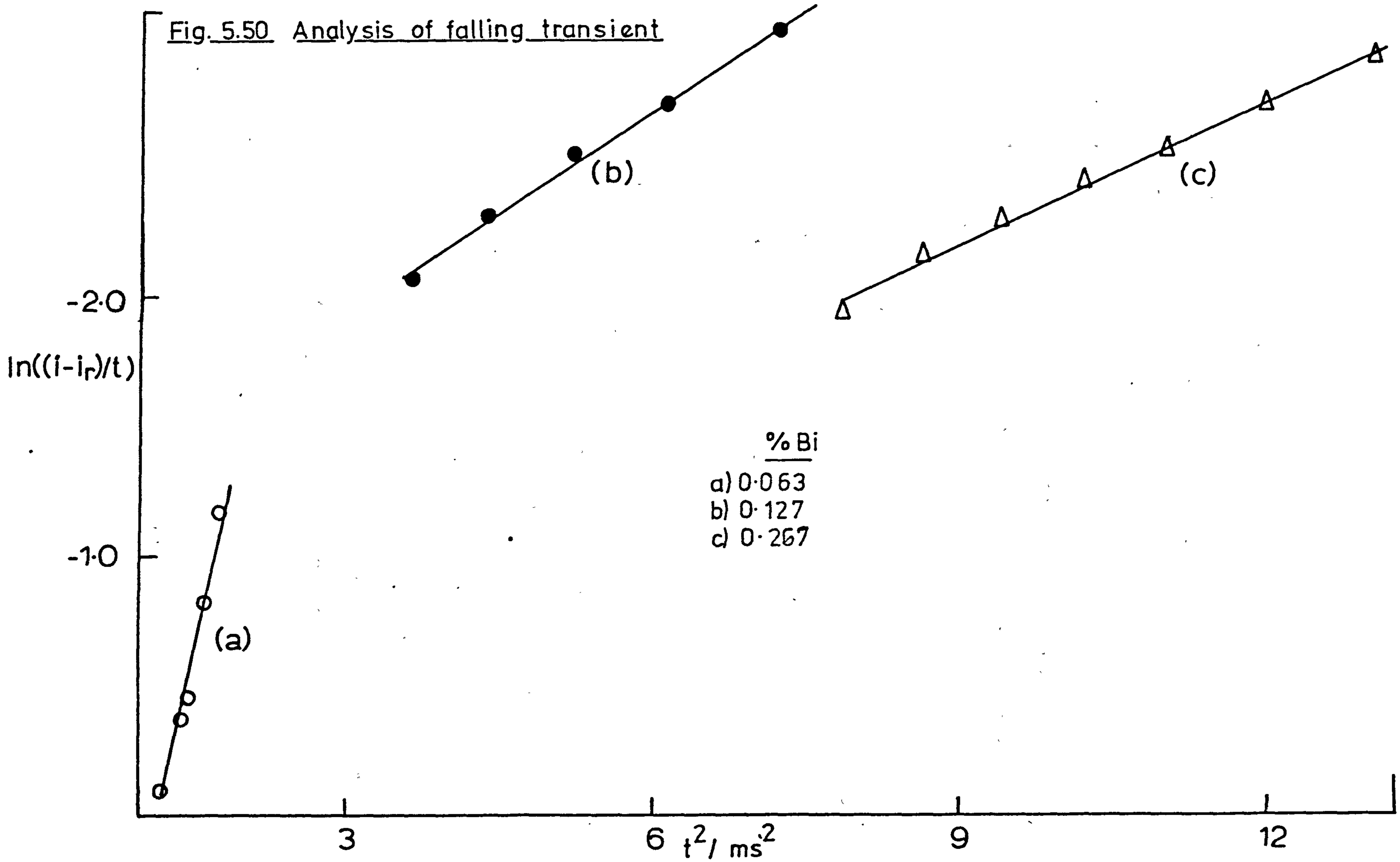

CHAPTER 6

THE ELECTROCHEMISTRY OF FLAT Pb-Ca- Sn AND VARIOUS FLAT Pb-Ca-Sn-Bi ALLOYS

6.1. Experimental

The electrode pre-treatment and experimental set-up were identical to those already described for Pb, Pb-Sb and Pb-Bi (Chapters 4 and 5). The alloys used contained

(a)	0.090% Ca	0.65% Sn	0.0061% Al	
(b)	0.092% Ca	0.67% Sn	0.0070% Al	0.084% Bi
(c)	0.088% Ca	0.66% Sn	0.0056% Al	0.151% Bi
(d)	0.083% Ca	0.67% Sn	0.0053% Al	0.281% Bi

6.2 Results and Discussion

6.2 (i) Linear Sweep Voltammetry

The rate of attainment of constant response was studied by following changes in peak current values (i_p) as the electrode was cycled continuously between the limits 400 mV and 1520 mV. As before, it was found necessary to raise the upper limit to 2000 mV otherwise negligible product PbO_2 was formed. Peak current values for the Pb/Ca/Sn alloy are shown in the table below together with the percentage increase in peak current ($i_p/i_{p\ max} \times 100$) and the potentials at which these occur.

Rate of Attainment of Constant Response during cycling operations -

Pb/Ca/Sn

No of Cycles	i_p(A)	Ep(mV)	$i_{p/i_{p\ max}}$ x 100
5	16	1140	8.2%
9	18.5	1140	9.5%
13	20	1150	10.3%
20	68	1238	35%
40	151	1255	78%
60	194	1265	100%

It was thought worthwhile to investigate more closely the early cycle pattern and subsequent behaviour as various levels of Bi are added to the alloy. The results are shown in Fig. 6.51 as a plot of percentage increase in peak current vs. cycle number. The form of these curves is interesting; an initial lag in current during the early cycles is followed by a sudden increase in current flow which becomes directly proportional to the cycling time. These observations lead to a new mechanism for the formation of PbO_2 from $PbSO_4$ which is shown diagrammatically in Fig. 6.52.

At significant rates of potential sweep since the $PbSO_4 \longrightarrow PbO_2$ reaction is slow due to the need for nucleation and growth to occur the conversion of $PbSO_4$ on the surface is incomplete. During the initial cycles the surface undergoes oxidation at isolated sites which grow as the amount of cycling increases. This growth accelerates as further conversion occurs since the attack occurs at pits in the surface so

Fig. 6.51

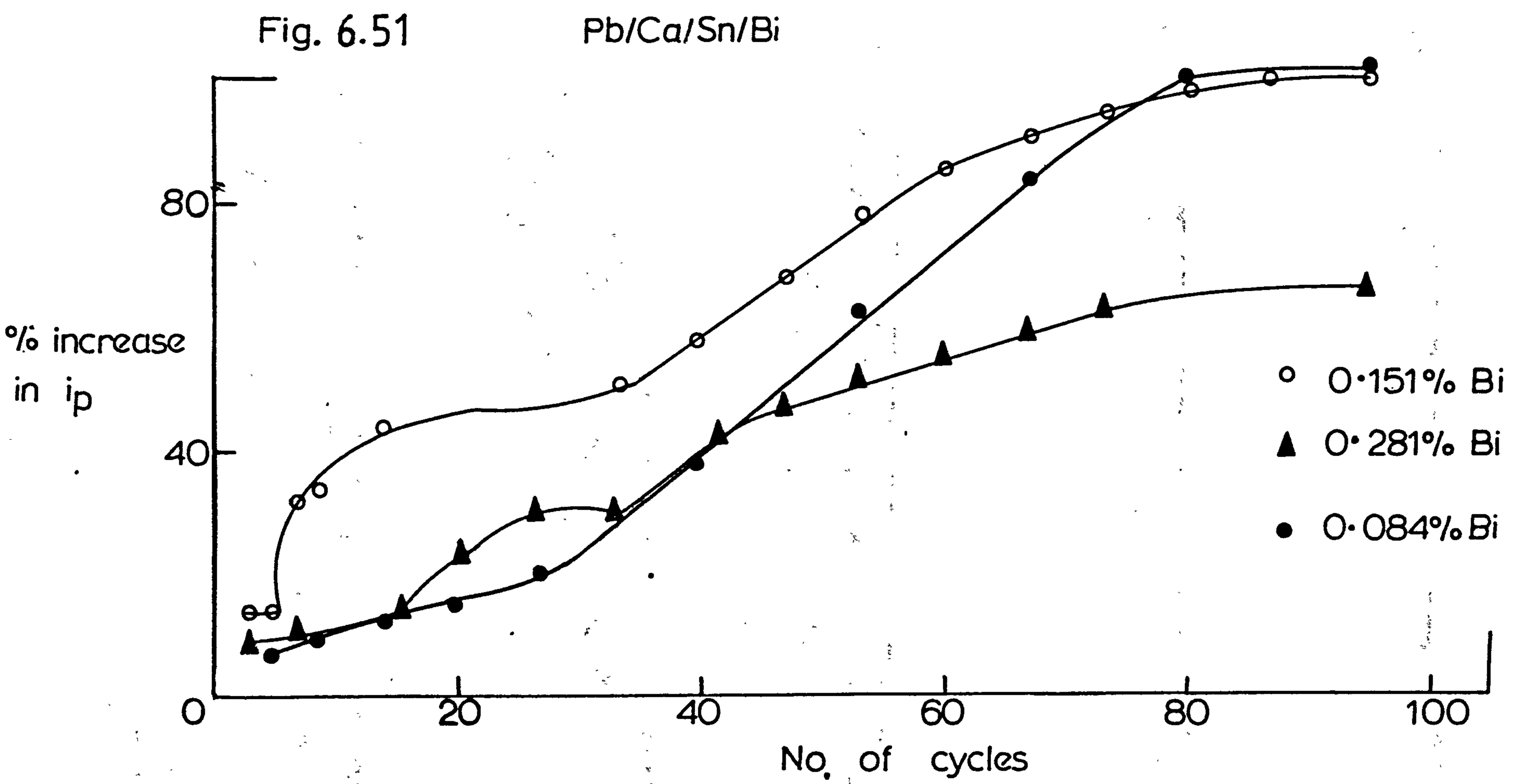
Pb/Ca/Sn/Bi
% increase in i_p
80
40
0
20
40
60
80
100
No. of cycles
○ 0·151% Bi
▲ 0·281% Bi
● 0·084% Bi

(a) Pb-alloy surface

(b) formation of nucleation centres

(c) attack occurs at pit in the surface

(d) accessible area increases with time

(e) amount of PbO_2 produced $\propto$ cycling time

(f) electrode blocking (i_p constant)

Fig. 6.52

that the accessible area increases with time. As cycling continues these pits increase until they form a single advancing front. At this point the amount of PbO_2 produced is linear with time. This rectilinearity, however, comes to a limit when the extent of the electrode blocking process due to the formation of PbO_2 excludes the reactant H_2SO_4 molecules from the surface and the charge in the peak ($\propto i_p$) becomes a constant value; this is confirmed in Fig. 6.51.

An alternative mechanism is the formation of PbO_2 from $PbSO_4$ on the surface followed by a diffusion mechanism to build up a spongey deposit extending into the solution. This diffusion cannot be a solution mechanism since the current is not rotation speed dependent. If it exists the diffusion is surface diffusion which occurs to preferred growth points on the PbO_2 lattice. A similar process to the corrosion mechanism described above occurs with the active area of dissolution being defined by the area of $PbSO_4$/Pb which is oxidised. The shortcoming here is that there is no apparent reason for the linear region at intermediate cycling times. A 2-D process would give a linear region as $t \longrightarrow 0$.

Electrodes were considered to have reached a constant response when changes in i_p values during successive cycling operations were negligible ($< 0.05 \mu A$).

A typical stabilized potential curve for Pb-Ca-Sn is shown in Fig. 6.53. The form of the curve is similar to those previously obtained with pure lead and the antimonial lead alloy (Chapter 4). Several differences however are apparent between the various alloy responses. The most obvious of these are the much larger $i_{pmax.}$ values (for PbO_2 formation from $PbSO_4$) obtained with the Pb-Ca-Sn alloy showing this to be more susceptible to anodic attack than a pure lead electrode or one containing antimony as the grid alloying ingredient. Another interesting feature of the potentiodynamic curves is the much more pronounced reduction peak ($PbO_2 \longrightarrow PbSO_4$) obtained with Pb-Ca-Sn; the work on Pb and Pb-Sb (Chapter 4) has shown much broader reduction peaks and this was attributed to the mode of electrode pretreatment. The addition of Ca/Sn to pure Pb produces a PbO_2 deposit which is more analogous to that of a freshly plated, more reactive electrode more akin to that described by Fleischmann[93] than to the deposit produced on flat lead and Pb/Sb electrodes.

Fig. 6.53

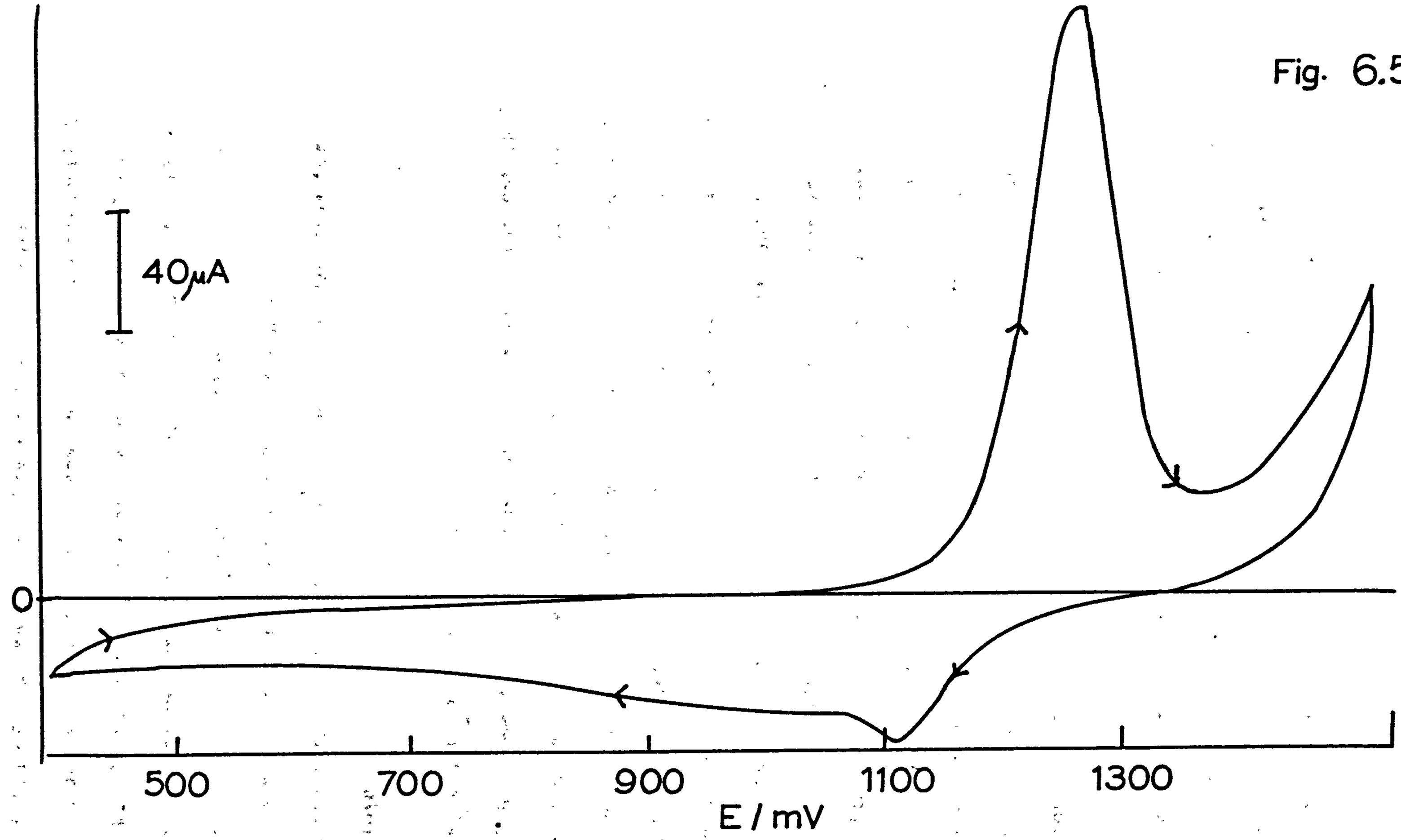

The addition of bismuth to the alloy results in an overall decrease in i_p values as the additive renders the alloy less susceptible to anodic attack. Of the three levels of bismuth added to the alloy, the intermediate concentration (0.151%) rendered the alloy most stable to anodic corrosion (i.e. lowest i_p values). In Chapter 5 it has been shown that the most stable concentration of Bi in the simple Pb-Bi binary lies in the range 0.14-0.19%; this also seems to hold true for Pb-Ca-Sn-Bi alloys.

6.2ii) Potentiostatic Pulse Measurements

Fig. 6.54 shows the typical rise and fall in transient obtained when the Pb/Ca/Sn alloy was pulsed from 400mV ($PbSO_4$ region) into the PbO_2 region. The initial double-layer charging spike is followed by an increase in current which has the i - t relationship indicative of a fast 2-dimensional process. This is in good agreement with similar data obtained for each of the Pb-Ca-Sn-Bi alloys under test and has been attributed to the pre-existence of nuclei on the alloy surface prior to potentiostatic pulse experiments as a result of the extensive cycling during the electrode preparation. A further proof that this mechanism is indeed two-dimensional, similar to that for Pb, Pb-Sb and Pb-Bi (Chapters 4 and 5), is given in Fig. 6.55 as a plot of ln $(\frac{i-ir}{t})$ vs. t^2 for long times ($t/tm > 1$).

A series of experiments were performed in which the alloy (Pb/Ca/Sn) was pulsed to a series of potentials each in the PbO_2/O_2 region. The peak current value (i_m) and the area under the curve for each potentiostatic pulse are summarised in the table overleaf.

Fig. 6.54

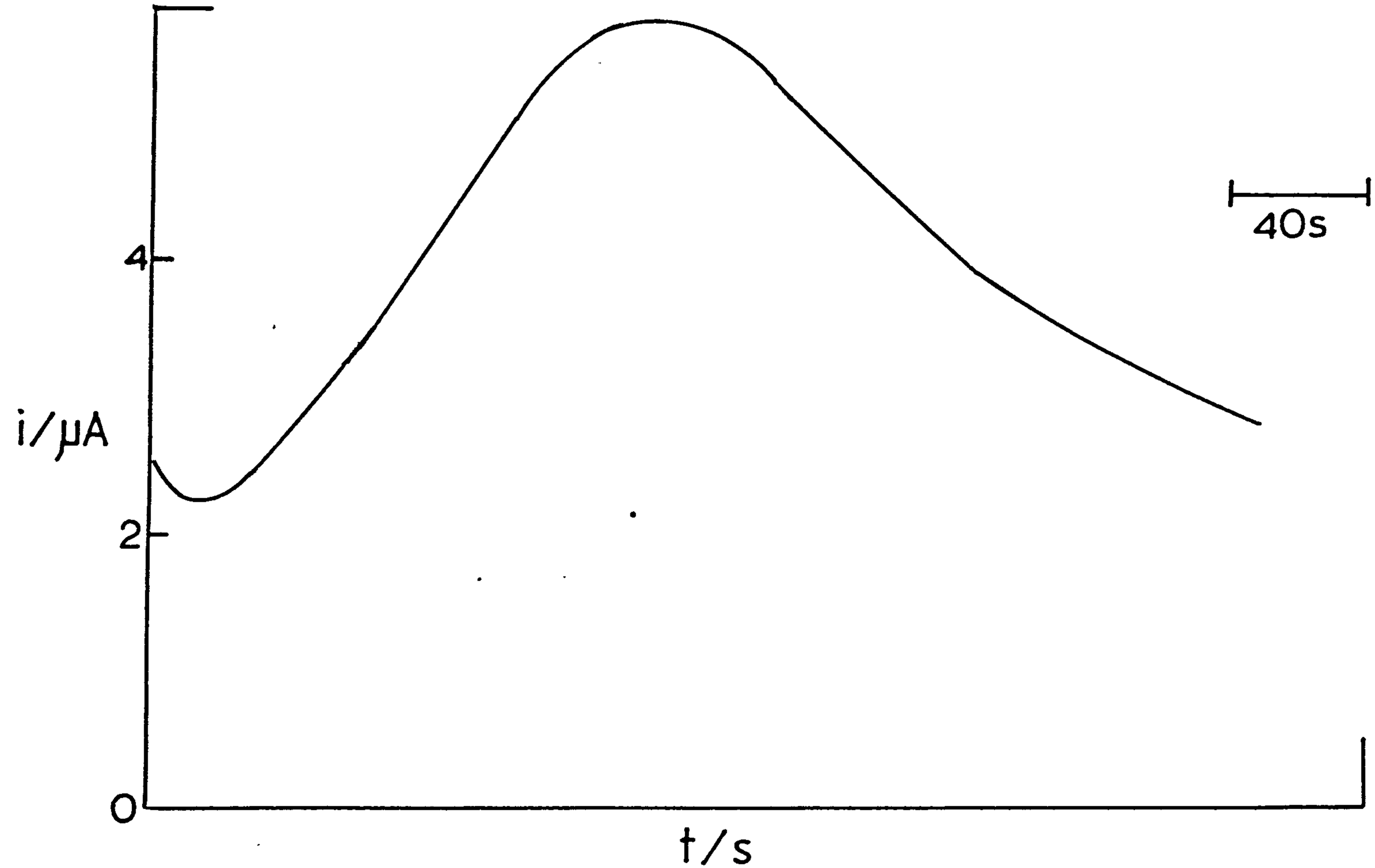

Fig. 6.55 Pb/Ca/Sn

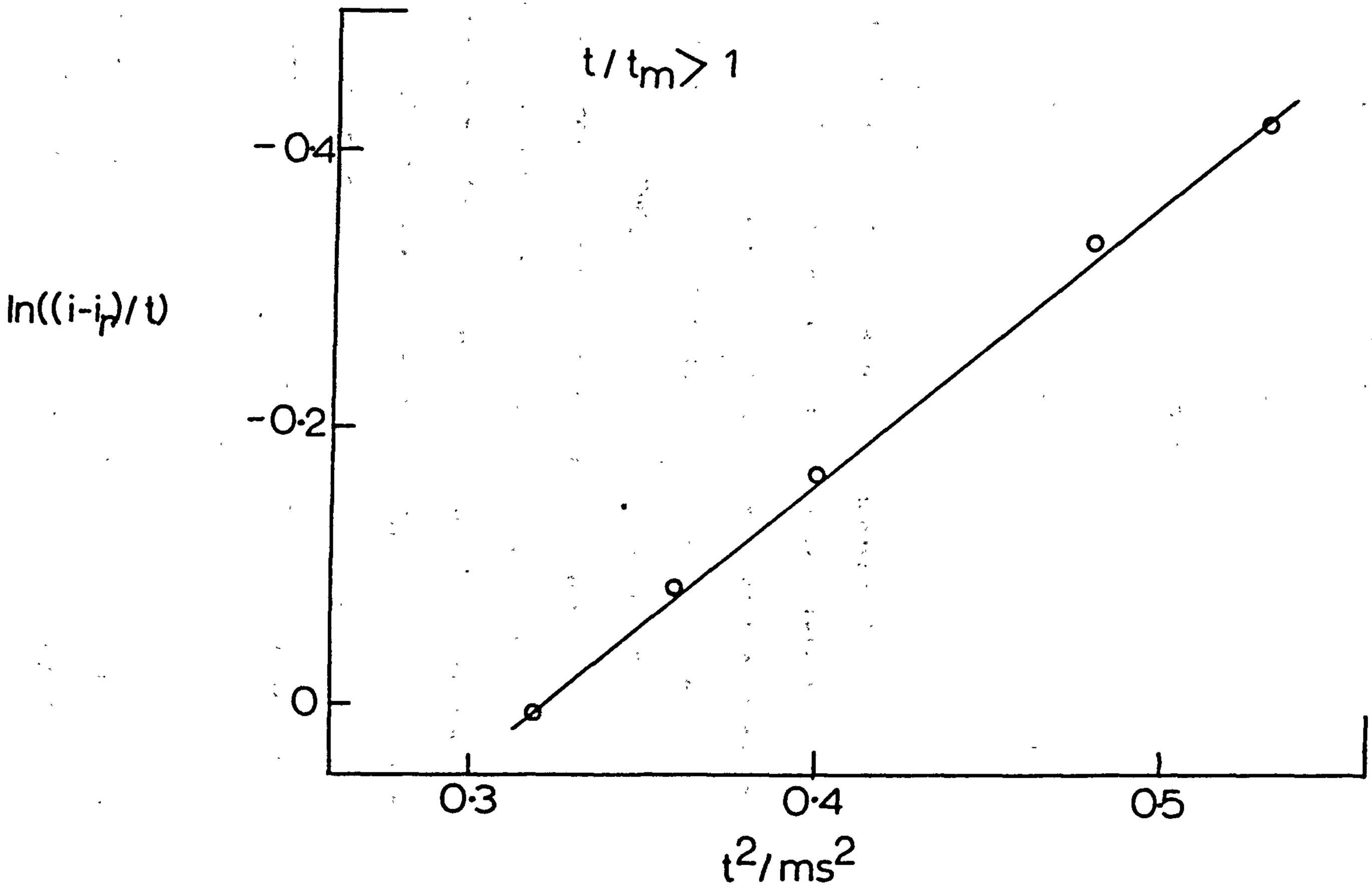

Potentiostatic Pulse Experiments from 400mV to a series of potentials in the PbO_2 region

Pb/Ca/Sn

η (mV)	i_m (μA)	Area under curve ($mCcm^{-2}$)
827	17	12.7
865	23	13.4
873	46	29.7
883	28	14.1
890	27	14.0
895	17	16.3*

*large contribution from oxygen evolution current

As before, the peak current is seen to increase with increasing potential (the reaction is driven deeper into the PbO_2 region) until an optimum i_m value is reached after which the intrusion into the oxygen region is large enough to reduce the effective area available for oxidation to PbO_2 and i_m subsequently falls. This reduction in surface area (Θ) can be attributed to the presence of oxygen bubbles on the alloy surface. Analysis of the i - t plots for the rise in transients for increasing potentials indicates an increase in slope with increasing potential. This is to be expected from the previous chapter on Pb-Bi alloys where we have shown that the rate constant (k) increases with potential. Fig. 6.56 shows this trend for three potentials in the PbO_2 region.

The addition of bismuth to the alloy results in a decrease in i_m values when pulsed to potentials corresponding to those of the

Pb-Ca-Sn alloy in the PbO_2 region. The resulting decrease in oxidisability of the surface over the simple Pb/Ca/Sn alloy is confirmed by calculation of the area under the peaks obtained. The level of bismuth in the alloy is significant; the previous data on the simple Pb-Bi binary system (Chapter 5) has shown a maximum stability concentration of Bi in the range studied here and these data on the Pb/Ca/Sn alloys confirm these findings.

Fig. 6.56

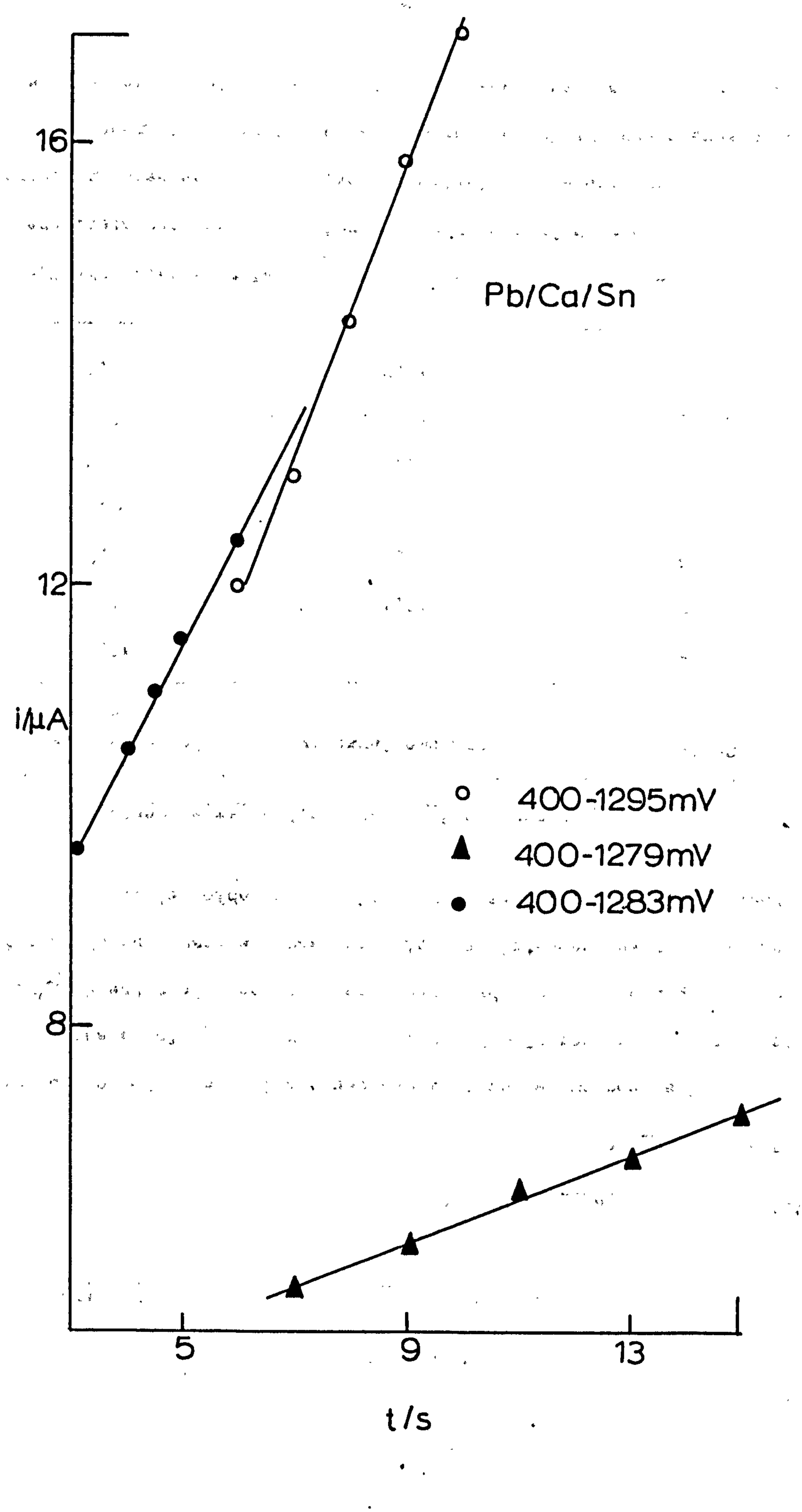

CHAPTER 7

ELECTROCHEMICAL CYCLING OF PASTED LEAD AND ANTIMONIAL-LEAD ELECTRODES ("POSITIVES")

7.1. Results and Discussion

7.1(a) Pure lead

Electrochemical cycling was performed by a series of potential step experiments from 1240mV (PbO_2) to 700mV ($PbSO_4$) for a short reductive period followed by a recharge pulse back into the PbO_2/O_2 region. This was repeated several times and the resulting changes in capacity during cycling are summarised in the table below.

Charge contained in eary cycling experiments

Cycle No.	Discharge Capacity (C)	Recharge Capacity (C)
1	73.0	13.1
2	25.3	12.1
3	26.8	10.8
4	21.8	10.2
5	20.0	9.0
6	18.5	8.0
7	15.7	5.3

There are three interesting features of this data; the first of these is the inability of the electrode to accept recharge, the charge put into the system during the oxidation pulse never matching the charge given out during the corresponding reduction reaction. Secondly, the discharge capacity in the first cycle is much greater

(3-5 orders of magnitude) than during subsequent cycling experiments. Finally the data shown in the previous table exhibits a general trend of decrease in capacity with cycle number. This observation is at first sight rather alarming since previous work on porous lead dioxide electrodes [117] has shown an initial increase in capacity with cycling until a plateau is obtained. A close examination of the experimental conditions, however, soon leads to an explanation for these results. In the experiments reported here, the electrode was subjected to much more severe conditions (with higher discharge rates) than before[117] the potential being instantaneously ($\sim 10\ \mu s$) steeped through 540mV. The decrease in capacity with cycle number can be explained in terms of the formation of "passivated" lead sulphate crystals whose morphology is such that, as a consequence of the severe reduction treatment, they resist oxidation when the electrode is stepped back into the PbO_2 region. As cycling continues, more of the electrode is converted to this "passive" form of $PbSO_4$ leaving less of the matrix available for re-oxidation to lead dioxide. This also explains the inability of the positive electrode to accept recharge and also the very large initial reduction charge as the product lead sulphate is formed.

To confirm these findings, the electrode was then subjected to prolonged reduction in the lead sulphate region (700mV) and cycling experiments were continued as before. The results, summarised in the table below, show the almost total inability of the electrode to accept charge during potentiostatic oxidation following a prolonged reduction period.

Charge/Discharge capacities following prolonged reduction

Cycle No.	Discharge Capacity (C)	Recharge Capacity (C)
8	39.3 (Prolonged Reduction)	0.1
9	12.4	0.1
10	7.9	0.1
11	6.7	0.1
12	5.7	0.1

This data is in good agreement with the "passivated sulphate" theory; prolonged reduction results in almost complete formation of lead sulphate which cannot be oxidised to lead dioxide by the potential step technique.

The electrode was removed from the electrolytic cell and oxidised galvanostatically for several hours in an upward-facing position (25 $mAcm^{-2}$, 0.3M H_2SO_4) with oxygen being freely evolved from the matrix. The final steady state potential under these conditions was 1.250V(vs Hg/Hg_2SO_4) Following equilibration with the cell electrolyte, the electrode was then subjected to the same cycling conditions as before; the results are shown in the table overleaf.

Charge/Discharge Capacities following galvanostatic oxidation

Cycle No.	Discharge Capacity (C)	Recharge Capacity (C)
13	58.8	8.4
14	24.2	6.0
15	18.0	4.8
16	6.5	3.7
17	6.3	3.3

Once again, the same trends are observed, with the reduction charge being very much larger in the first reaction than during subsequent cycles. This shows that the galvanostatic oxidation enables the conversion of "passivated" $PbSO_4$ to PbO_2 which cannot be effected by the potential step technique.

7.1(b) Antimonial-lead

(i) Linear Sweep Cycling

Potentiodynamic cycling experiments were performed between the limits 700mV ($PbSO_4$) and 1250 mV (PbO_2/O_2) at a sweep-speed of 1 mVs^{-1} throughout. Fig. 7.57 shows a series of voltammograms for the early cycle history of the electrode. There are several interesting features of this data; the first of these is the general decrease in peak current ($PbO_2 \rightarrow PbSO_4$ reduction peak) values (ip) with cycling, the difference between ip values for the 1st and 2nd cycles being much greater than during subsequent cycling operations. The table overleaf

Fig. 7.57

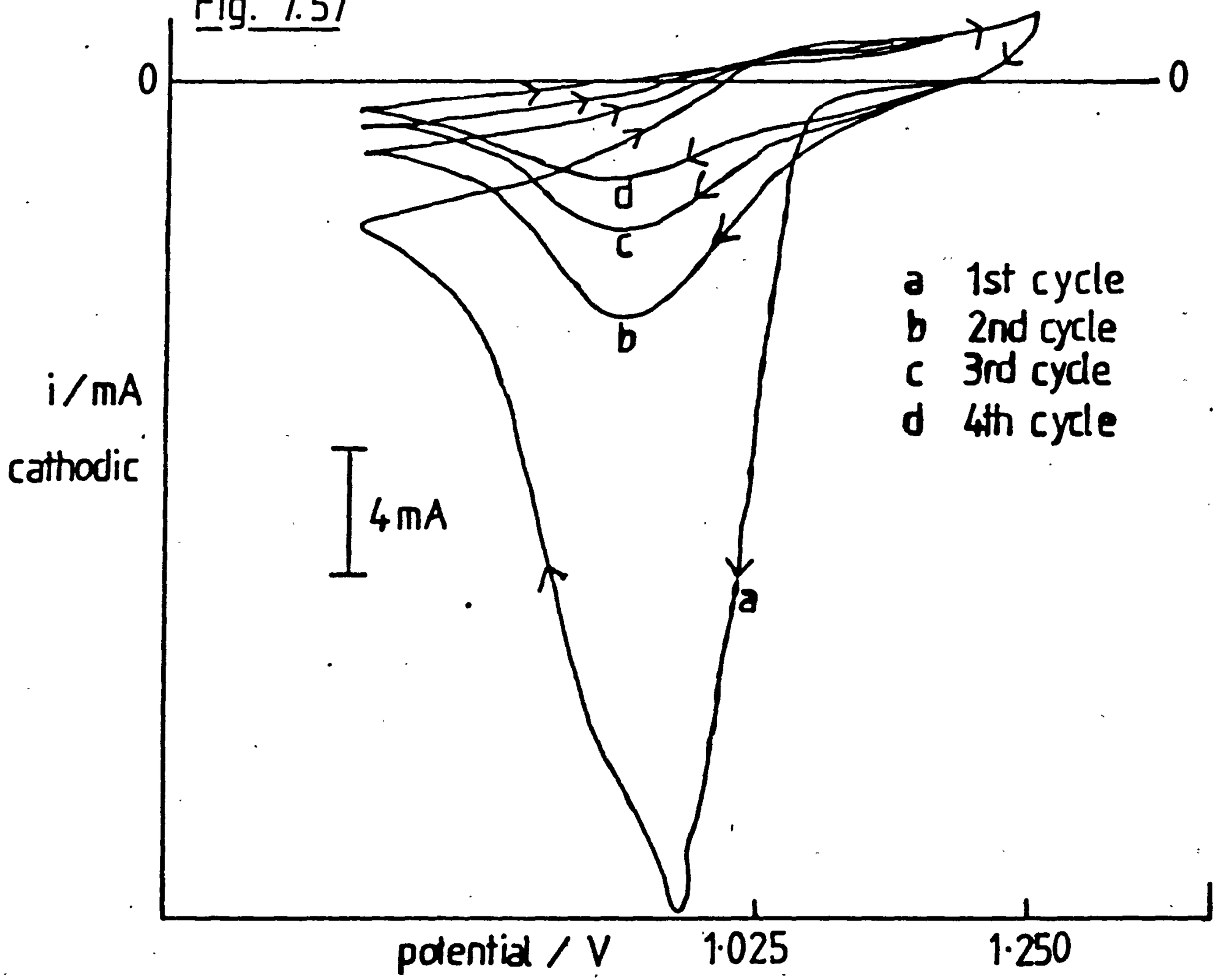
0
0
d
c
b
a
a 1st cycle
b 2nd cycle
c 3rd cycle
d 4th cycle
i / mA
cathodic
4 mA
potential / V
1·025
1·250

summarises these changes in ip with cycle number and gives the potential at which they occur.

Variation of reduction peak current with linear sweep cycling of a porous Pb-Sb electrode (700 - 1250 mV, 1 mVs^{-1})

Cycle No.	Reduction peak current ip mA	Position of ip (Ep) mV
1	17.3	970
2	7.2	935
3	3.9	925
4	2.9	910
5	1.9	895
6	1.5	885
7	1.0	875
8	0.55	872
9	0.35	870
10	0.28	870
11	0.28	870
12	0.28	870

The seemingly-excessive initial reduction current can be explained in terms of the formation of a passivated form of lead sulphate which resists oxidation back to PbO_2 during the anodic potential sweep as in the case of the pure lead electrode. It is impractical to raise the upper sweep limit above 1250mV since this results in the formation of oxygen bubbles in the electrode matrix.

A further interesting feature of the early cycle pattern is the rate of attainment of a constant response after approximately 10 cycles, the ip and Ep values remaining constant regardless of any

subsequent cycling operations. This suggests that the morphology of lead-sulphate reaches an equilibrium form with just a small residual amount of 'un-passivated' $PbSO_4$ present in the ma trix which can be oxidised to PbO_2 and reduced back again to $PbSO_4$ by linear-sweep experiments.

It is interesting to compare this data with that from the work on un-pasted Pb-Sb electrodes (Chapter 4). The major difference can be seen in the much larger currents (and capacities) obtained with the porous electrode; this is to be expected because of the much larger surface area available for reaction in the porous matrix. A second comparison lies with the protuberance of the PbO_2 formation peak; with the flat, unpasted electrode this peak is quite prominent (Fig. 4.2) with the data obtained being typical of that for the development of a single, passivated layer on an electrode surface with no thickening of the deposit occurring. In the case of the porous electrode, however, the absence of a pronounced PbO_2 formation peak can be explained in terms of the layered growth of the product lead-dioxide; this type of oxidation produces many different oxidation peaks which overlap with each other to form a broad band coupled with the oxygen evolution reaction.

A further difference between the flat and the pasted electrodes can be seen in the form of the reduction ($PbO_2 \longrightarrow PbSO_4$) peak. In the case of the pasted electrode a long "reduction tail" is observed; this is characteristic of newly formed porous lead dioxide and shows that the discharge is being driven deep into the porous mass. With the flat electrode, the reduction 'peak' is barely distinguishable.

The lack of rotation speed dependence through these experiments suggests that the conversion here ($PbSO_4 \longrightarrow PbO_2$) proceeds via a solid state process.

ii) Potentiostatic Pulse Experiments

Uncycled electrode

Fig. 7.58 shows the current-time response of a porous Pb-Sb electrode as the potential is instantaneously stepped from the lead-dioxide region (1250mV) to the lead-sulphate region (700mV). An initial current spike, which as before can be attributed mainly to the charging of the double layer at the electrode-electrolyte interphase, is followed by a simple fall in the current flow. The absence of a current peak indicates that sufficient nuclei are present in the lead-dioxide matrix to initiate the electrocrystallisation of lead-sulphate crystals. The corresponding changes in capacity with time are shown in Fig. 7.59; from the graph it can be seen that the electrode is fully discharged, having passed 74C, after a reduction period of 45 minutes. The percentage change in capacity ($^{C}/_{C_{max}} \times 100\%$) as a function of time is shown in Fig. 7.60 from which it can be seen that 50% of the discharge capacity (36C) is reached after only 11% of the total discharge time (5 mins). This very sudden attainment of the discharged state can once again be explained in terms of rapid formation of 'passivated' lead sulphate crystals.

The electrode was considered to be in a fully discharged condition when no further changes in capacity were observed and the electrode was then stepped back into the lead-dioxide region (1250 mV). Fig. 7.61 shows the current-time response as the electrode was subjected to this potentiostatic oxidation. The initial double-layer charging

Fig. 7.58

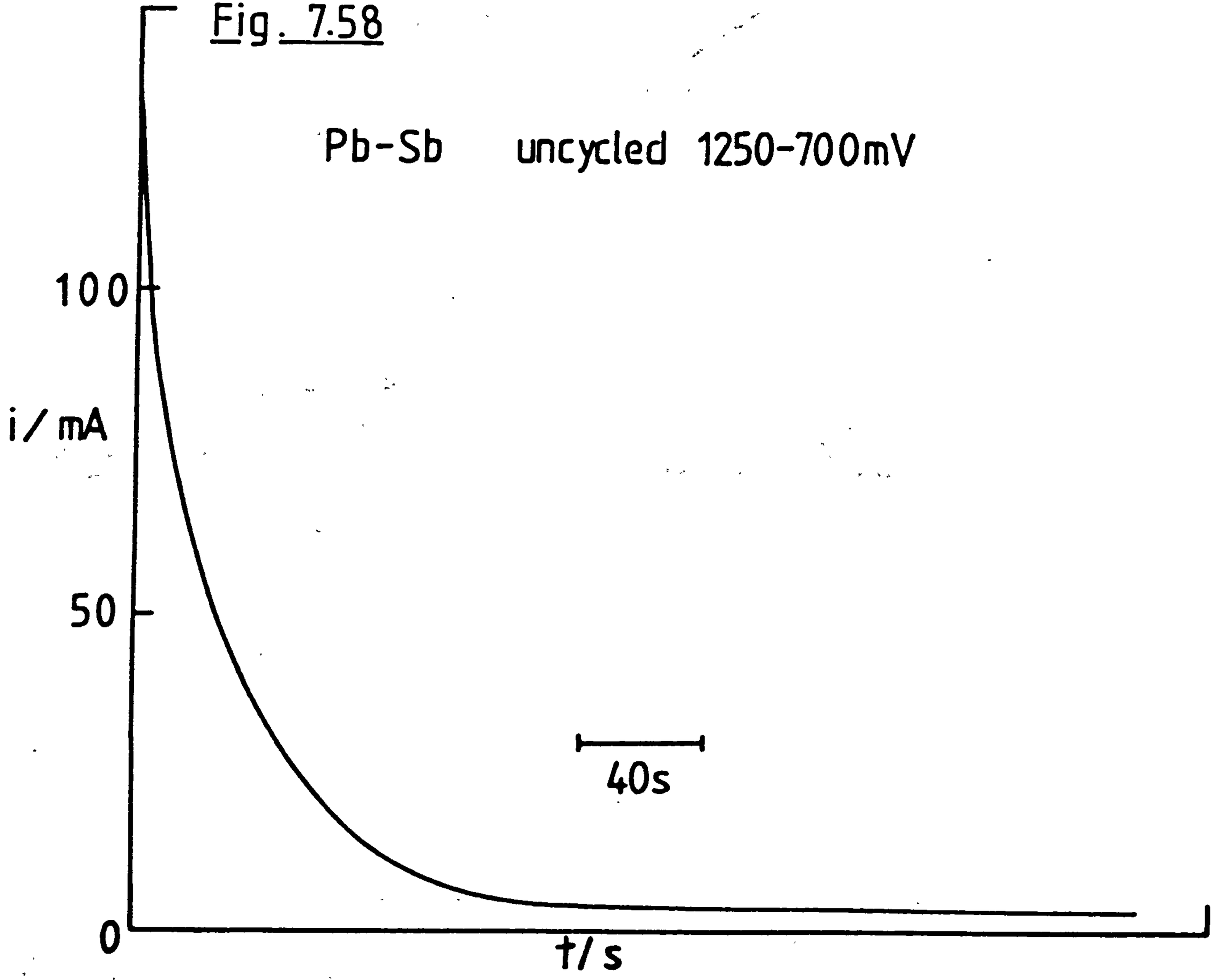

Fig. 7.59

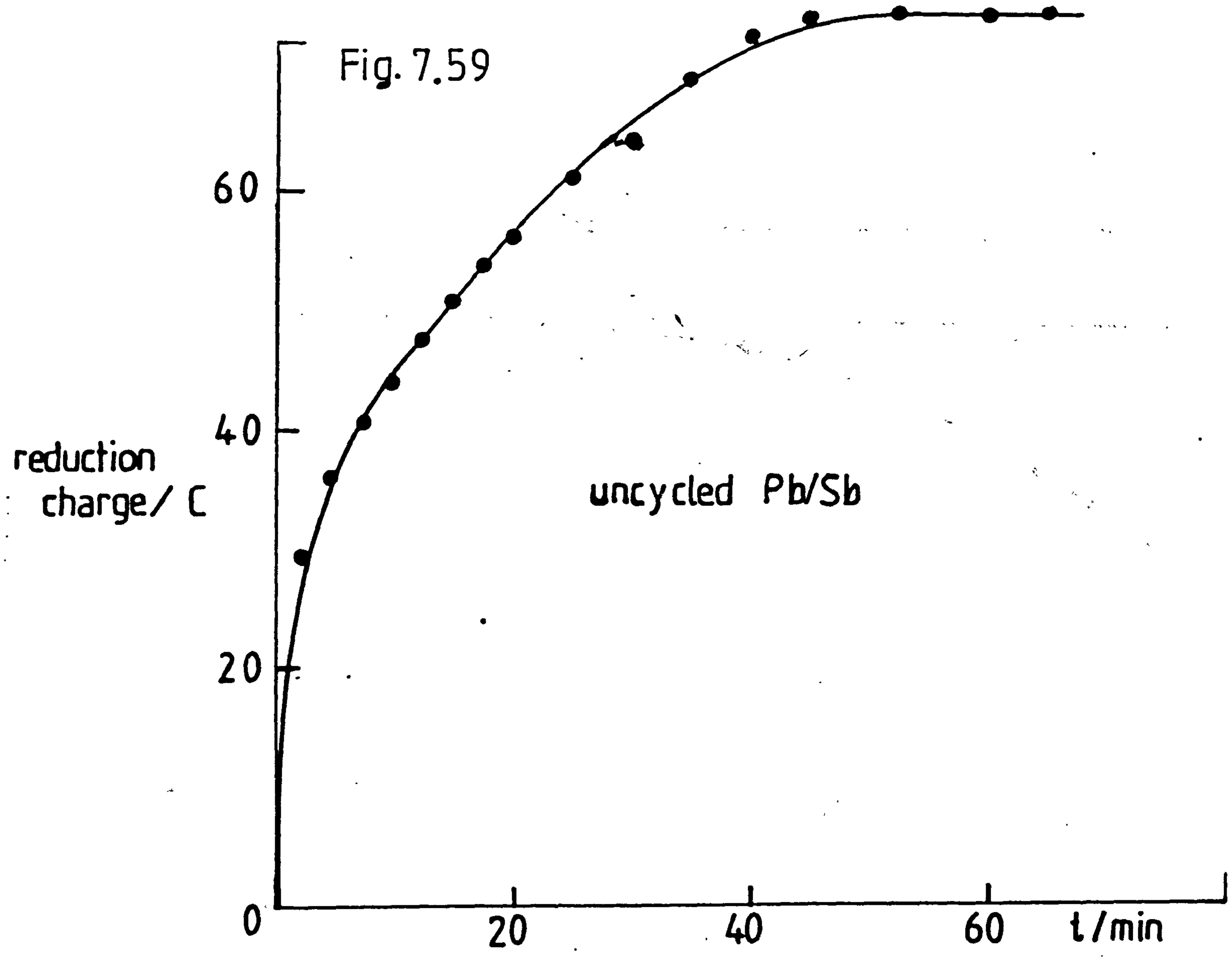

Fig.7.60

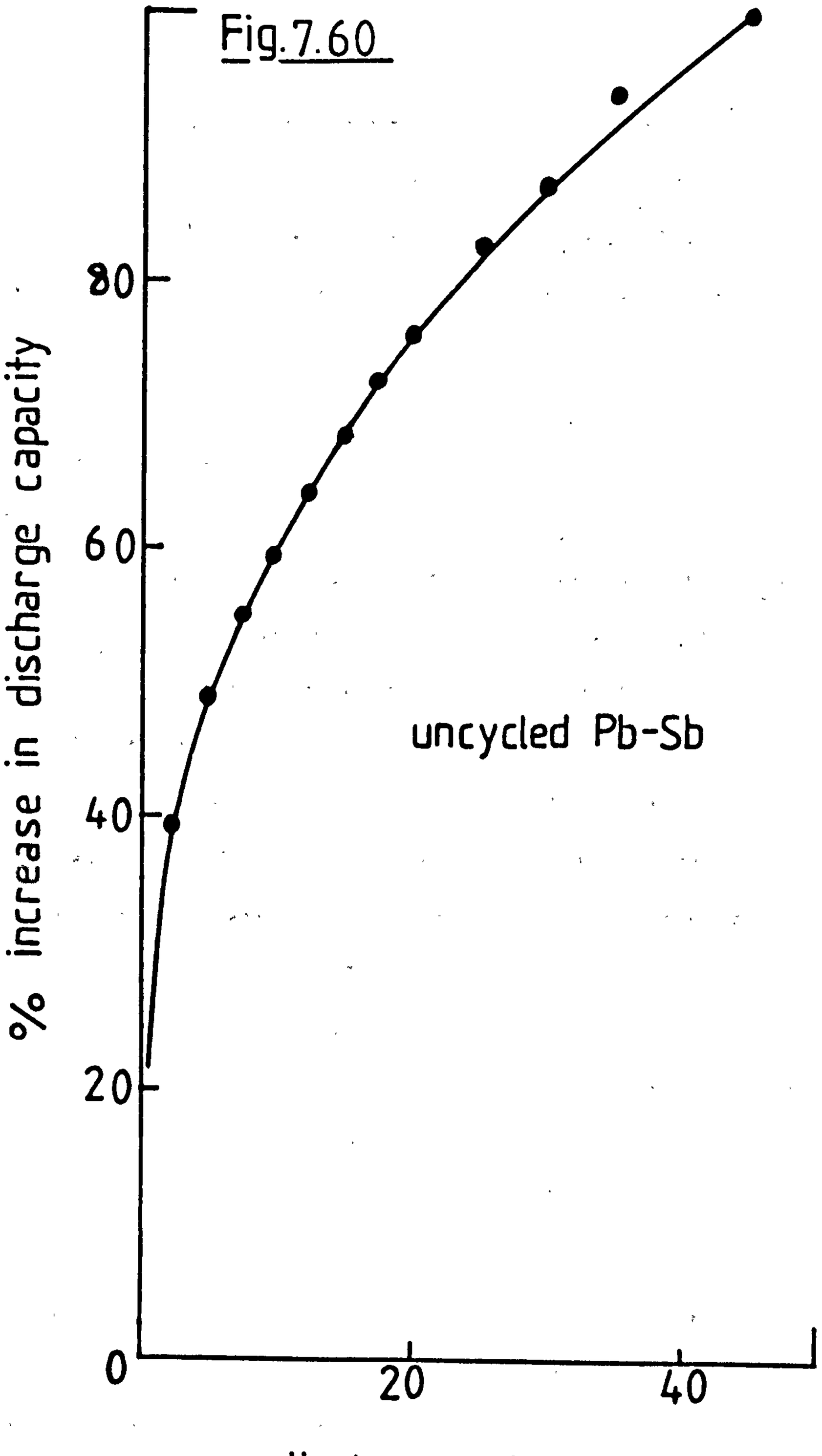
% increase in discharge capacity
80
60
40
20
0
20
40
uncycled Pb-Sb
discharge time / min

spike is followed by an increase in the current due to the formation and growth of nucleation centres for PbO_2 production. Subsequent overlap of these growth centres causes a decrease in current flow with the resultant pattern obtained being that of the current peak shown in Fig. 7.61.

The changes in capacity with time for the potentiostatic oxidation are shown in Fig. 7.62. From this curve we can see that after an oxidation time of over 4 hours, the total charge put back into the porous matrix was only 50 C (i.e. only 68% of the total discharge capacity). This very slow charge acceptance shown by the antimonial lead electrode (and also by pure lead previously) can be explained by the resistance of 'passivated' lead sulphate to oxidise back to lead-dioxide. Eventually, the formation of oxygen bubbles occurs in the porous matrix causing the disruption of the lattice and ensuring the electrode is never fully recharged. To ensure that the electrode was fully charged prior to each experiment it was removed from the cell and oxidised galvanostatically (25 mA/cm^2) in an upwards facing position until a steady potential (1.250 V) was reached (0.3M H_2SO_4).

(b) <u>Cycled Electrodes</u>

Prior to potentiostatic pulse experiments, the electrodes were subjected to a varying number of cycles using linear sweep voltammetry between the limits 700mV and 1250mV. One cycle consisted of a single potential scan between these two extremes and back again with a constant sweep speed of 1 mVs^{-1} throughout. A potentiostatic reduction pulse (1250⟶700 mV) was then performed and the resulting changes in capacity were followed. The variation of discharge capacity

Fig. 7.61

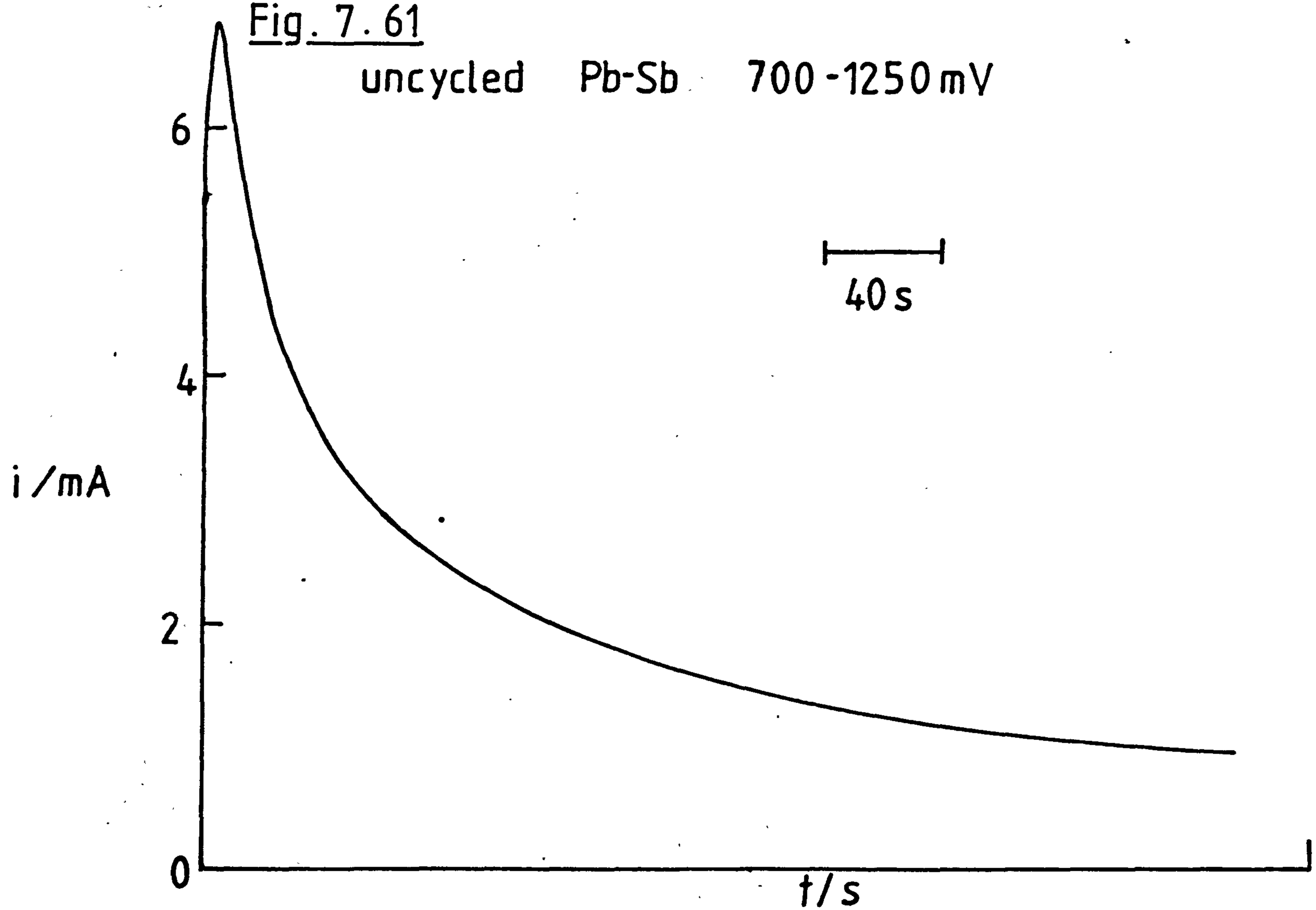

Fig. 7.62

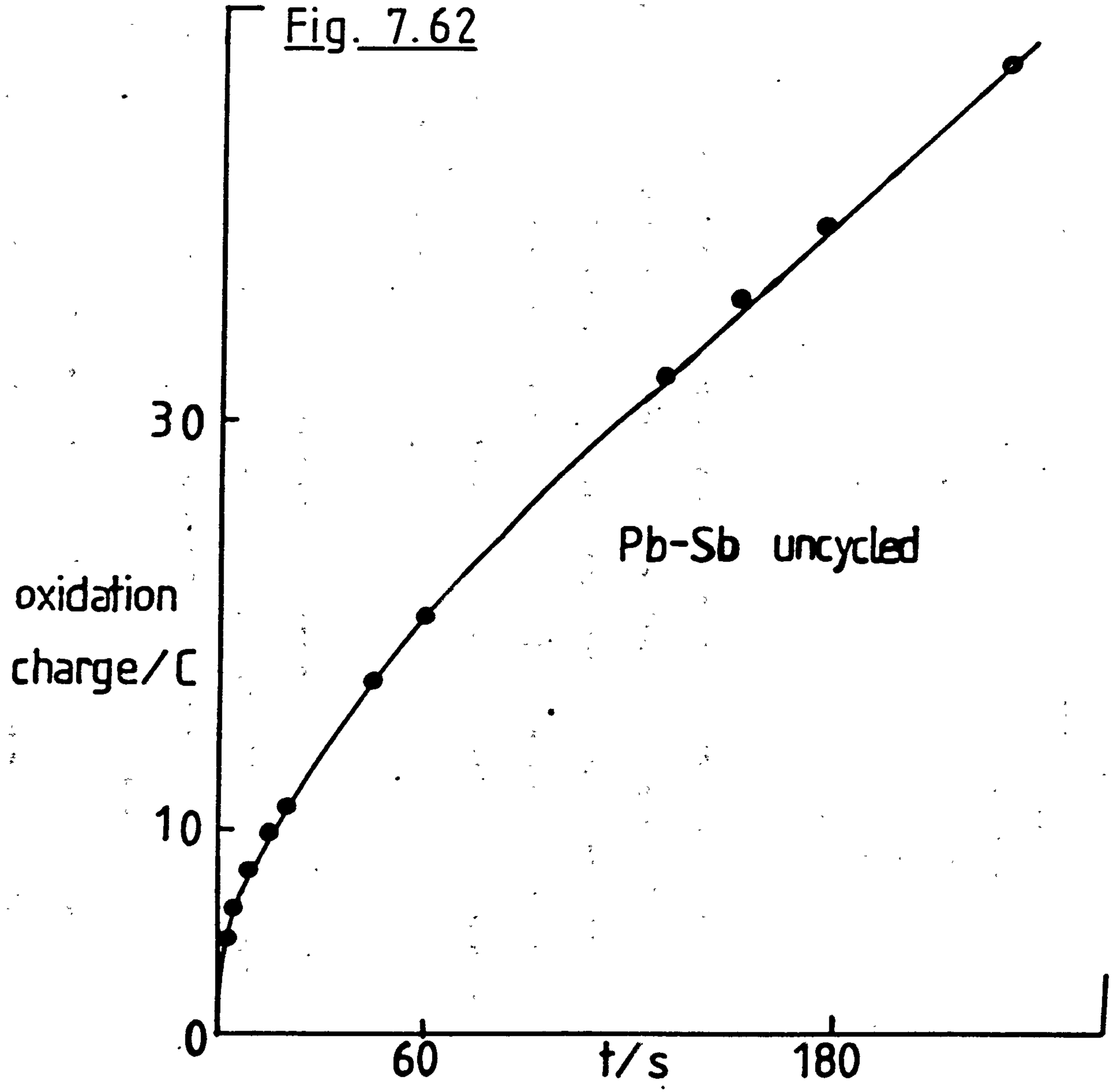

with cycling is shown in the following table together with the time taken to reach the fully discharged state. (To ensure that the electrode was fully recharged prior to each new experiment, galvanostatic oxidation was carried out under the same conditions as before).

Discharge capacities for electrodes subjected to potentiostatic reduction following various cycling conditions (Pb/Sb, porous)

No. of cycles	Discharge Capacity (C)	Time to reach full discharge capacity
0	73.9	45 mins
4	42.3	2 hrs 19 mins
6	13.9	56 mins
11	2.2	12 mins
15	1.8	5 mins
20	1.5	5 mins

The decrease in discharge capacity with cycling can once again be explained in terms of the formation of passivated sulphate during the preparatory linear sweep cycling experiments. These relatively inert sulphate crystals remain unoxidised during the anodic section of the sweep gradually leaving less PbO_2 to be reduced during subsequent potentiostatic pulse reductions.

Fig. 7.63 shows the current-time response of a porous Pb-Sb electrode having been subjected to 20 cycles (L.S.V.)fully discharged by a potentiostatic reduction pulse and finally stepped from the lead sulphate region to the lead-dioxide region. It is interesting to compare the pattern obtained with that for an uncycled electrode (Fig. 7.60); the main difference lies in the much larger currents

observed with an uncycled matrix. In the case of the well-cycled electrode, it has already been shown that the passivated sulphate will have reached an equilibrium morphology so that the only lead-sulphate present in the matrix which can be re-oxidised is the small amount of residual sulphate which never seems to take the passivated form. The fact that two rising and falling in current transients are seen for the cycled electrode brings in the penetration depth concept[118] and indicates that this residual sulphate is not conglomerated into a specific area of the electrode but rather is dispersed throughout the porous mass. The appearance of two distinct current peaks suggest the nucleation and subsequent growth of two fairly distinct layers of lead-dioxide.

Fig. 7.63

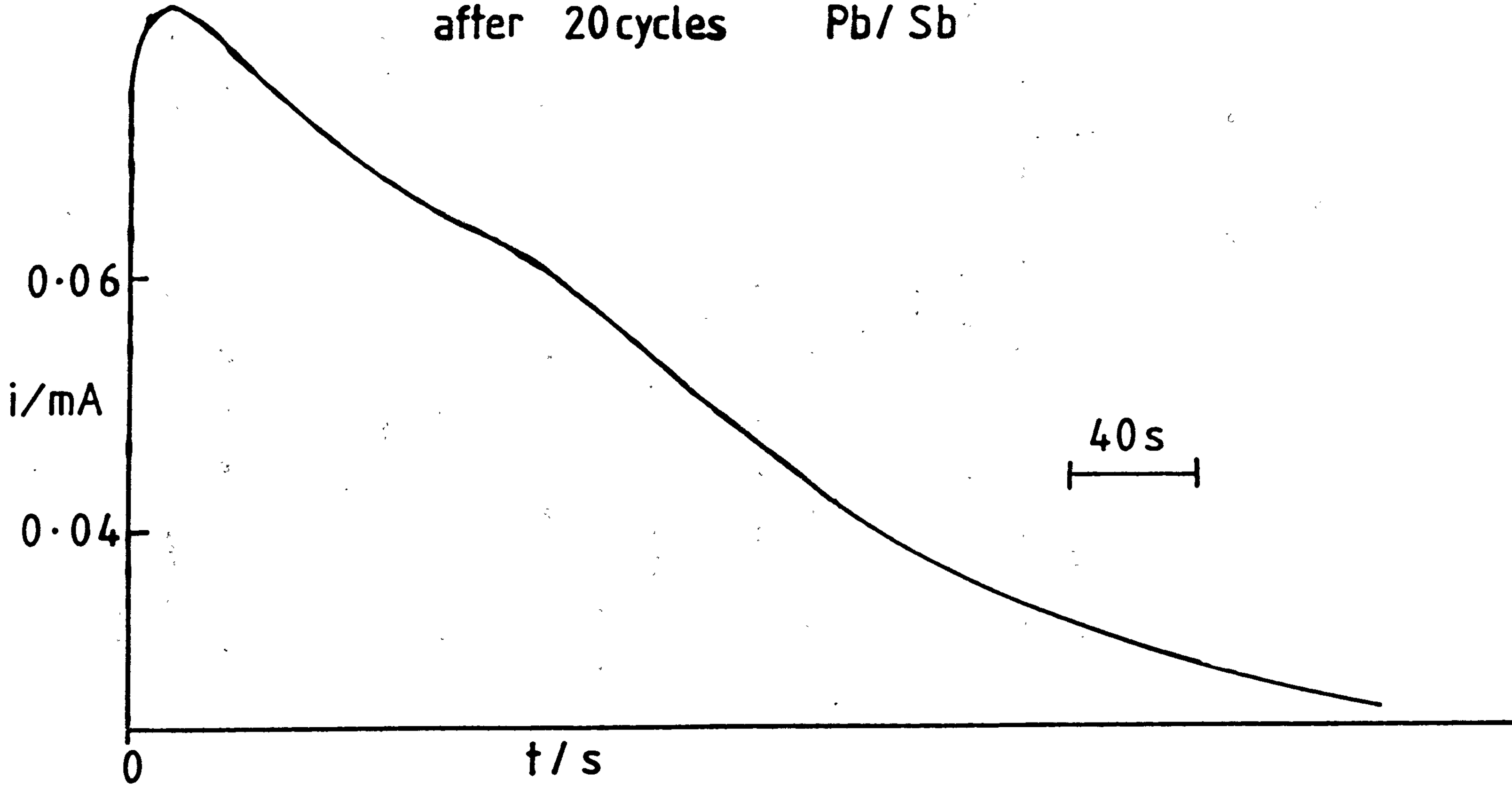

CHAPTER 8

THE EFFECT OF REDUCTION POTENTIAL ON THE RECHARGE CHARACTERISTICS OF POROUS LEAD-BISMUTH ELECTRODES

8.1. Introduction

In the previous chapter it was shown that porous lead and lead-alloy electrodes ("positives") exhibit a reluctance to accept recharge during potentiostatic-pulse cycling experiments. In these experiments the two extreme potentials were kept constant. The most positive potential (1250 mV) cannot be greatly altered; if it is made much more positive, the electrode gradually becomes obscured with bubbles of oxygen. If the oxidation potential is greatly reduced then the product PbO_2 is not produced. The reduction potential can, however, be significantly altered and the effect of varying this potential on the morphology of the $PbSO_4$ crystals can be followed by noting the changes in capacity of the electrode during subsequent recharge experiments. (In general, the larger the $PbSO_4$ crystals the more resistant they will be to oxidation and the lower the recharge capacity during potentiostatic step experiments back into the PbO_2 region.).

This chapter records such a series of experiments performed on a Pb-Bi binary electrode. The level of bismuth chosen was 0.13% since it has been shown (Chapter 5) to be the most useful concentration in the practical automotive battery range.

The surface structure of lead electrodes in the potential range 970mV to -400mV has been studied by many workers and it is well known that the anodic corrosion films formed on lead in sulphuric show a multi-phase structure when formed within a certain potential range[119-123]. Ruetschi[119] has reported that these corrosion films have a layer of $PbSO_4$ against the solution and an interior of tetragonal PbO and/or α-PbO_2 (PbO occurring above -400mV and α-PbO_2 above 500 mV); these limits depend on several factors including sulphuric acid concentration, temperature and the length of the anodizing treatment. The presence of basic lead sulphates has also been reported and the most likely oxide combination is

$$PbO + \alpha\text{-}PbO_2 \quad \text{above 500 mV}$$

$$\alpha\text{-}PbO_2 + \beta\text{-}PbO_2 \quad \text{above 1100 mV}$$

with the β-PbO_2 replacing the $PbSO_4$ at the surface exterior.

The presence of PbO in the interior of corrosion films means that it is protected from the electrolyte by a $PbSO_4$ layer which is practically impermeable to HSO_4^- and SO_4^{2-} species (once the $PbSO_4$ crystals have reached a thickness of at least 1μm). Further corrosion then occurs by dissociation of H_2O beneath the $PbSO_4$ layer.

Pavlov and Dinev[124] looked at potential sweep experiments between -400mV and 960 mV and concluded that the surface structure of the electrode in this region is

$$Pb/PbO \text{ layer}/PbSO_4 \text{ membrane}/H_2SO_4 \text{ solution}$$

while above 960mV the PbO and $PbSO_4$ layers are oxidised to PbO_2. The method of oxidation (potentiostatic or galvanostatic) affects only the ratio of these phases not their presence.

8.2. Results and Discussion

8.2(a) Discharge Experiments

The table given below summarises the total discharge capacity ($PbO_2 \rightarrow PbSO_4$) for a series of potential step experiments from 1250 mV to various potentials in the range -200 mV to 1200 mV and the time taken for these reactions to occur.

Discharge capacities for a series of potential step experiments from 1250 mV on a porous Pb-Bi (0.15%) electrode in 5M H_2SO_4 at 23°C (Nominal surface area = 0.071 cm^2)

Reduction Potential (mV)	Total Discharge Capacity (C)	Time to reach total discharge
1200	zero	-
1100	10.9	92 mins
1050	27.3	106 mins
1000	32.1	63 mins
950	34.7	68 mins
700	37.7	30 mins
400	122.0	47 mins
20	135.6	40 mins
-223	151.6	50 mins

The relationship between discharge capacity and reduction potential is interesting (Fig. 8.64); there appear to be two distinct phases of

Fig. 8.64

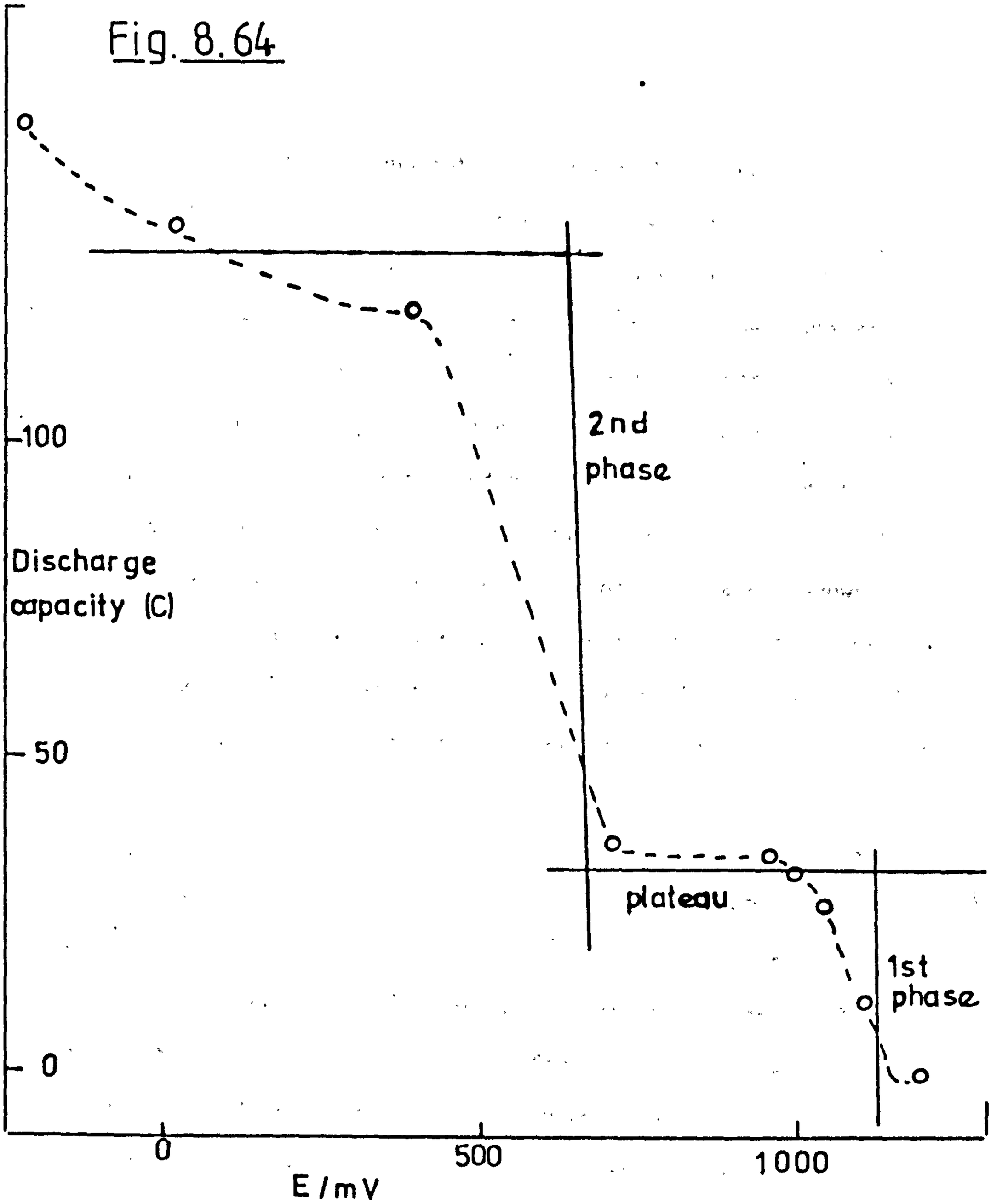
100
50
0
Discharge
capacity (C)
2nd
phase
plateau
1st
phase
0
500
1000
E / mV

PbO_2 reduction within the porous matrix. The first species starts to be reduced at about 1100 mV with the reaction slowing off at approximately 1050 mV. At about 700 mV a second species starts to be reduced with a three-fold increase in capacity output above that of the first species. It is interesting to note that the useful lead-acid battery potential range lies on the plateau between these two phases; this may explain why successful recharge can be carried out with a lead-acid battery positive plate (where the final reduction potential lies only 300 mV below the initial starting potential and lies on the plateau shown in Fig. 8.64 but not with the positive electrodes in the previous experiments (where the reduction potential was 550 mV below the initial potential and lies well within the 2nd reduction phase) described in Chapter 7.

It seems likely that the initial reduction reaction is predominantly $\beta\text{-}PbO_2 \longrightarrow PbSO_4$, although a certain amount of $\alpha\text{-}PbO_2$ is also present at these potentials ( )1100 mV). An explanation for the second reduction phase is rather more searching; it is feasible that it is mainly the reduction of $\alpha\text{-}PbO_2$ to form lead sulphate. The $PbSO_4$ crystals so produced are much larger than normal so accounting for the 3-fold increase in output. It seems likely however, that the situation is more complex than this especially if the presence of tet. PbO in the matrix is also considered. The most exciting observation from these experiments is that comparatively little reduction occurs in the potential range 750 mV to 950 mV so enabling recharge back to PbO_2 to be successfully carried out.

Fig. 8.65 shows a typical current-time transient for a potential step discharge experiment on a porous Pb-Bi electrode. The initial current spike can be attributed mainly to the charging of the double layer at the electrolyte-electrode interphase. The absence of any further increase in the current flow indicates that sufficient nuclei are present in the porous matrix to allow the formation of lead sulphate from lead dioxide. The shape of this transient did not vary with reduction potential, a simple fall in the current was observed. The value of the exponent did vary, however, and the data is summarised in the table below.

The current-time relationship for a series of discharge experiments to various potentials on a Pb-Bi (0.15%) electrode at 23°C in 5M H_2SO_4 (ϕ = 0.071 cm^2)

Reduction Potential (mV)	Relationship
1150	$i \propto t^{-1.5}$
1000	$i \propto t^{-3.5}$
700	$i \propto t^{-4.0}$
400	$i \propto t^{-1.3}$
20	$i \propto t^{-1.7}$
-223	$i \propto t^{-1.8}$

A large increase in the slope of the i-t curves is obtained when the reduction potential lies within one of the reduction phases shown in Fig. 8.64 (700 mV and 1000 mV).

Fig. 8.65

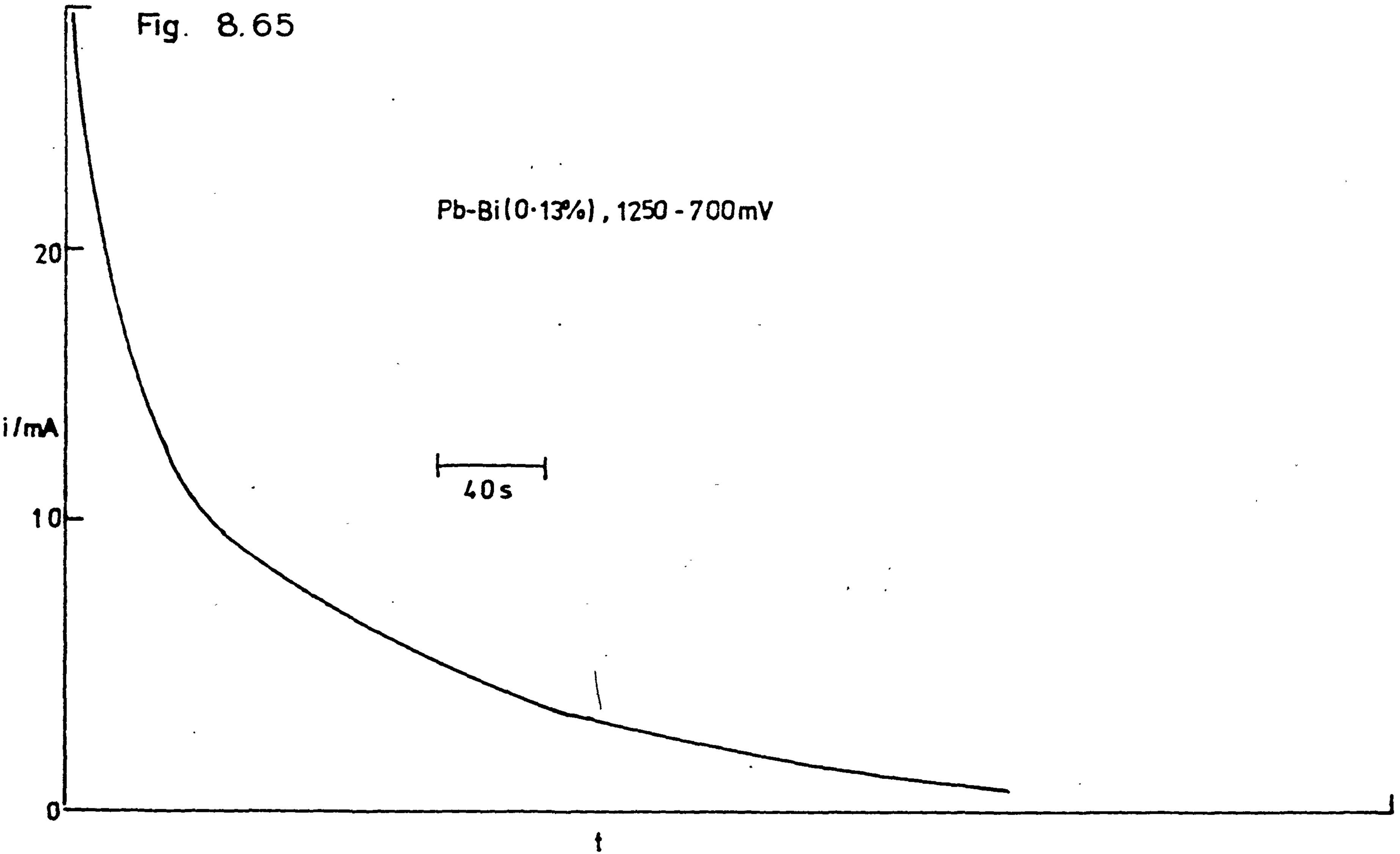

8.2 (b) Recharge Experiments

Figs. 8.66 - 8.69 show the current-time transients for a series of potentiostatic oxidation experiments from various reduction potentials to a set potential in the lead dioxide region (1250 mV). In each of these cases, the initial double-layer charging spike is followed by an increase in the current flow; this can be attributed to the formation and growth of nucleation centres for the production of lead dioxide. The subsequent overlap of these centres results in a decrease in the current flow with the resultant pattern obtained being that of a current peak. The shape of these peaks can be seen to vary with reduction potential suggesting the formation of various types of crystal morphology. At reduction potentials greater than 700 mV, no current peak was observed during the recharge experiment (see e.g. Fig. 8.70) which suggests that sufficient nuclei are already present in the matrix to allow the formation of lead dioxide. It can be concluded from this observation that once the 2nd phase reduction is entered (i.e. the final reduction potential is below about 800mV) the annihilation of nucleation centres for PbO_2 formation occurs and we observe a peak in the i-t oxidation transient.

The ability of porous Pb-Bi electrodes to accept recharge varies with reduction potential and the trend is in good agreement with the explanation of the data presented in Fig. 8.64. The electrode subjected to a reduction potential of 950 mV (i.e. a potential on the plateau between the 2 reduction phases) exhibits a readiness to accept recharge during the corresponding oxidation pulse with over 88% of the total discharge capacity being accepted after only 3 hours of oxidation. When the electrode is subjected, however, to a final

discharge potential which lies within the 2nd reduction phase (e.g. 700 mV) the ability to accept recharge is substantially reduced (only 65% of the total discharge capacity after 3 hours of oxidation).

Fig. 8.66

Pb-Bi (0·13%), -223mV to 1250mV

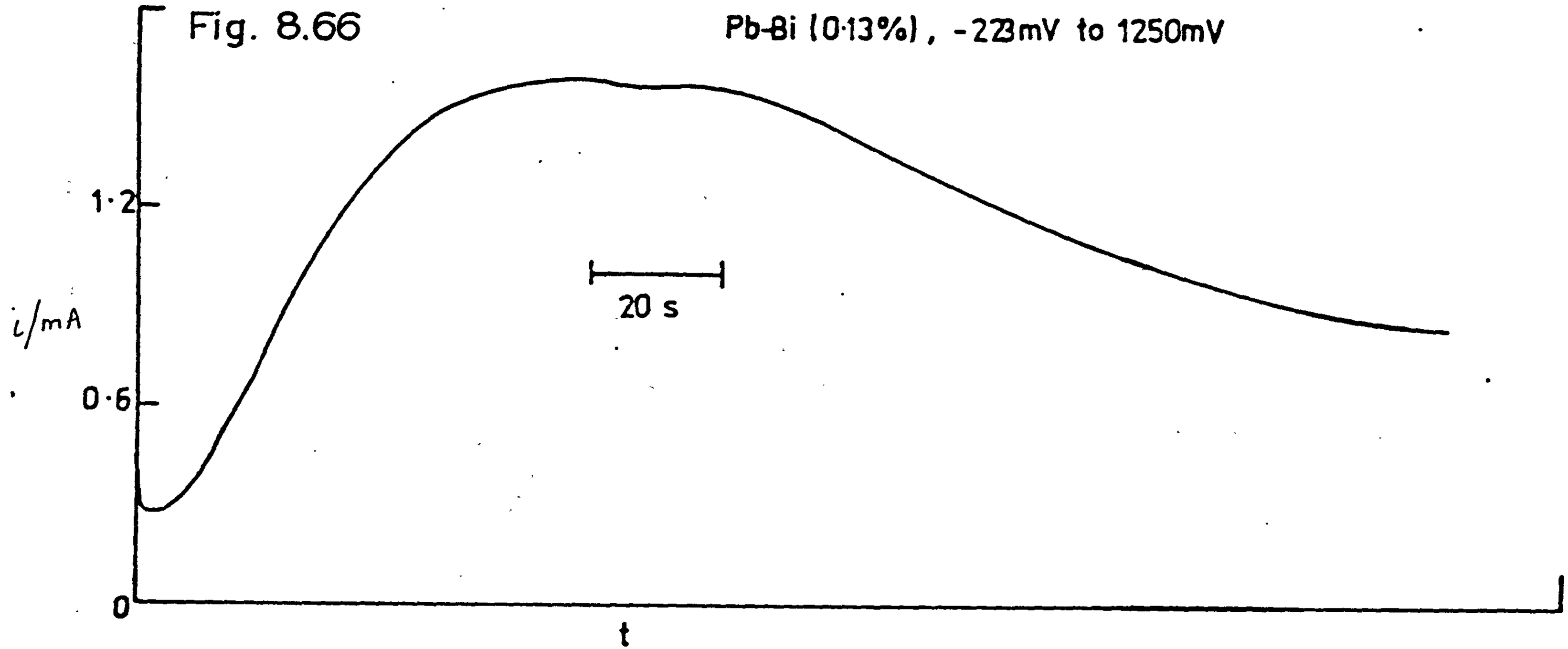

Fig. 8.67

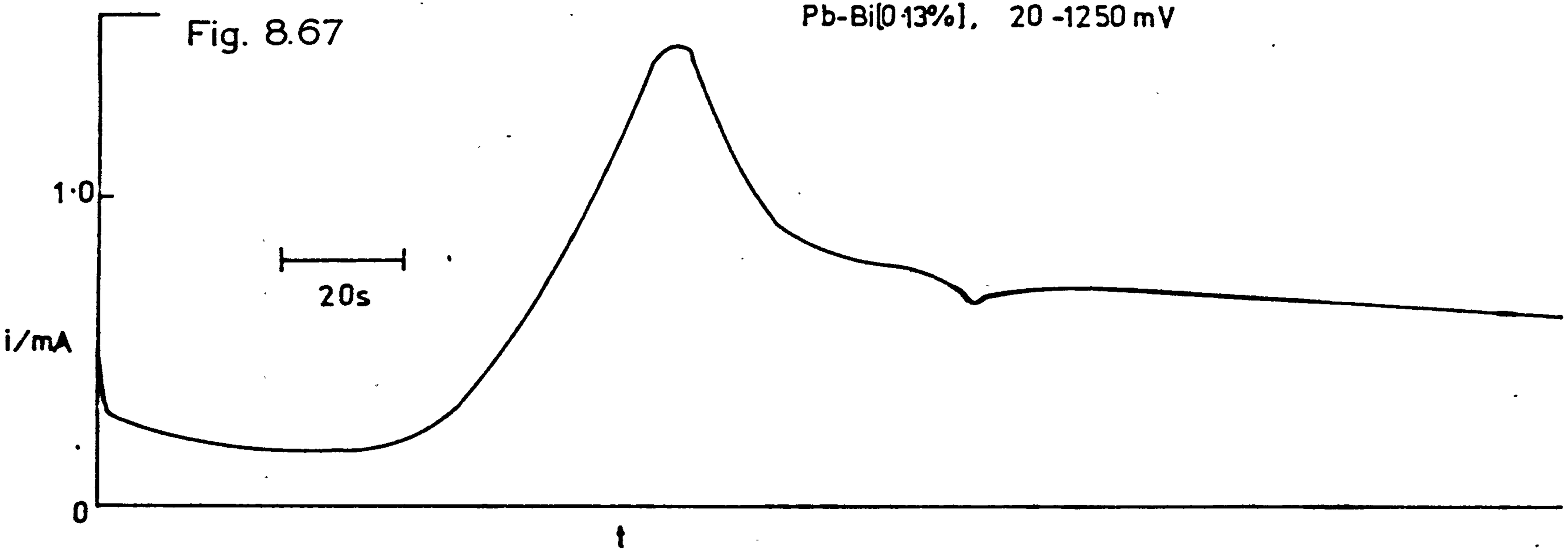

Pb-Bi (0·13%), 400mV-1250mV

Fig. 8.68

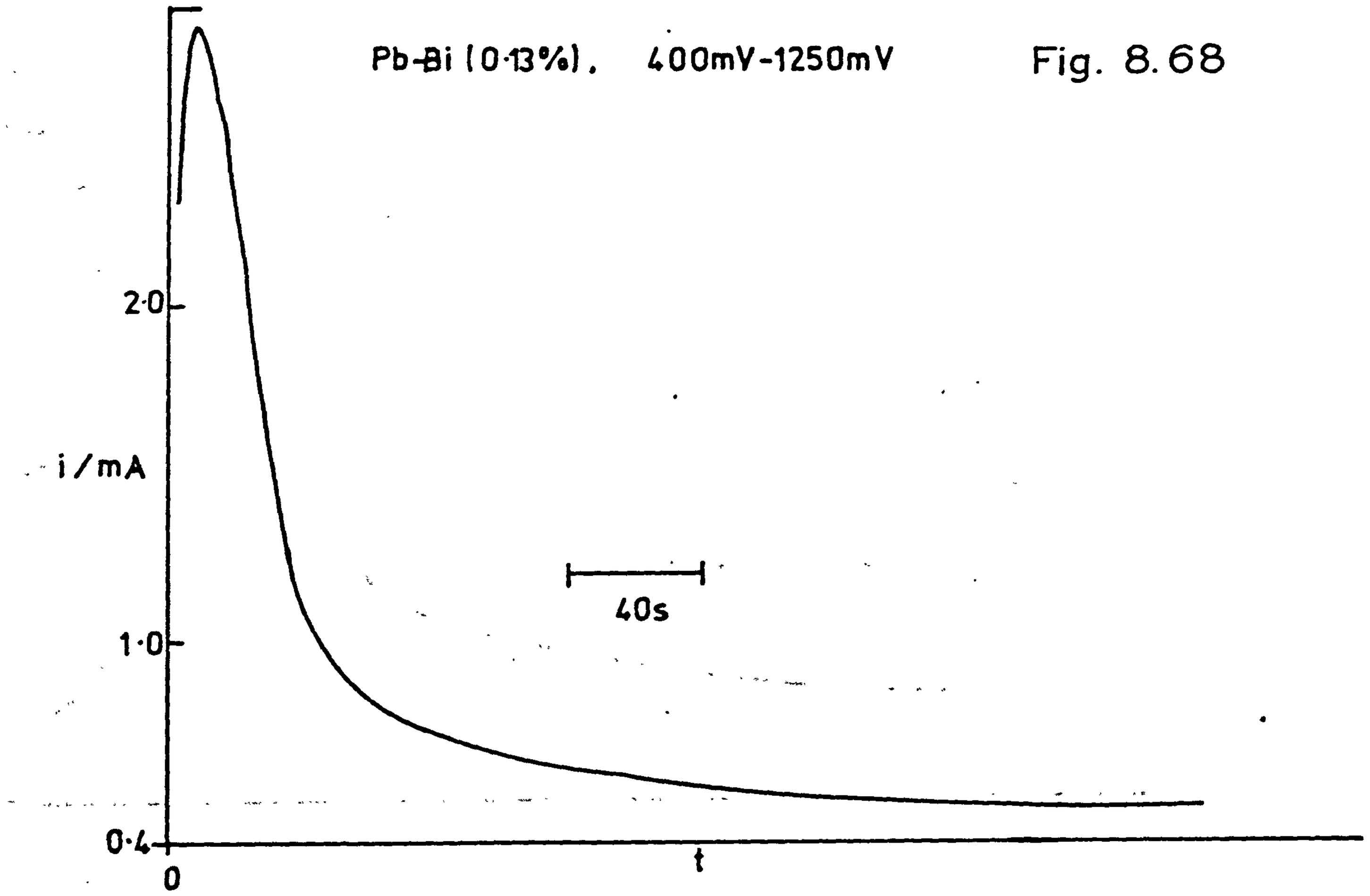

Pb-Bi(0·13%), 700-1250mV Fig. 8.69

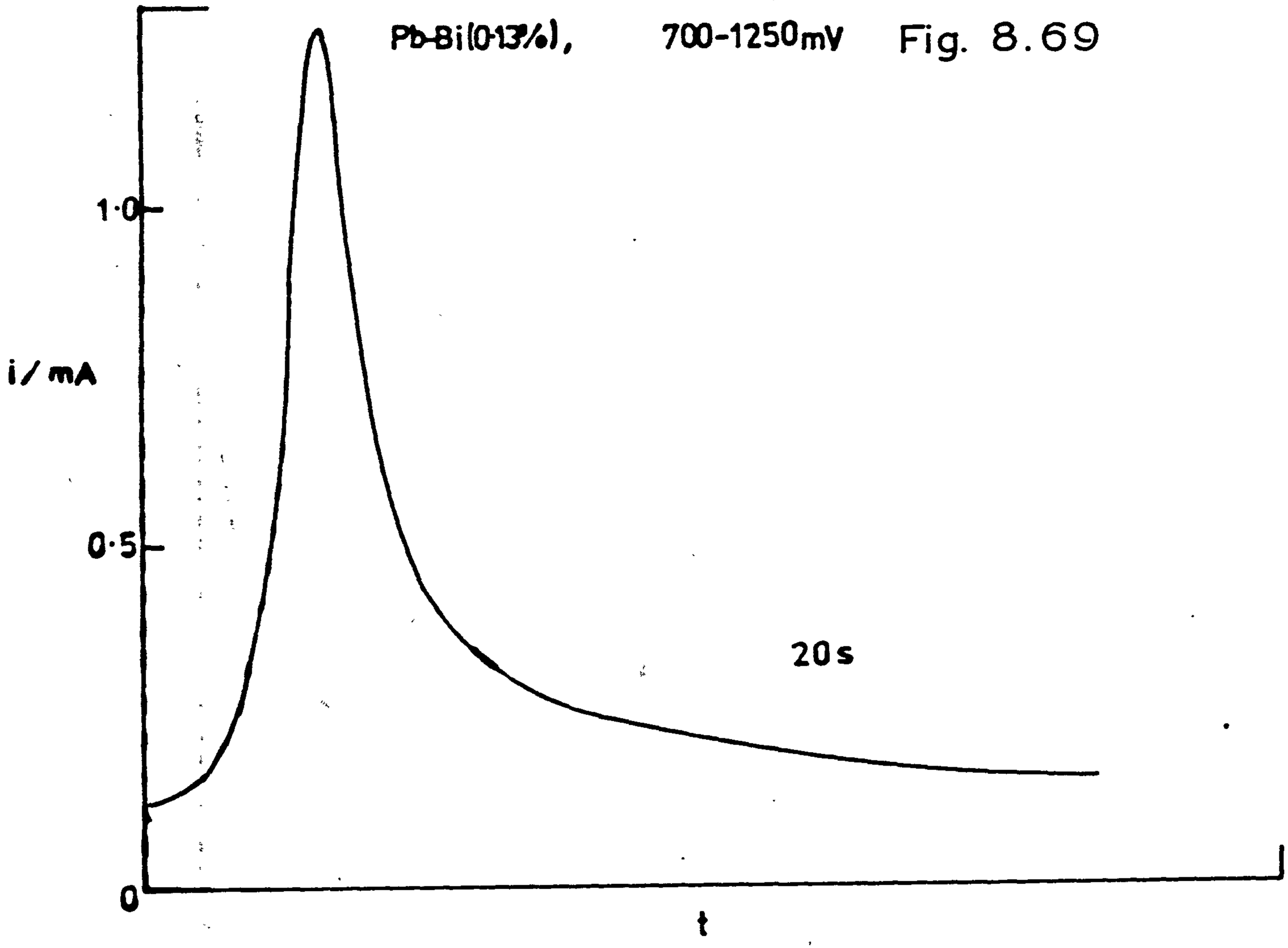

· Pb-Bi (0·13%), 1150-1250 mV Fig. 8.70

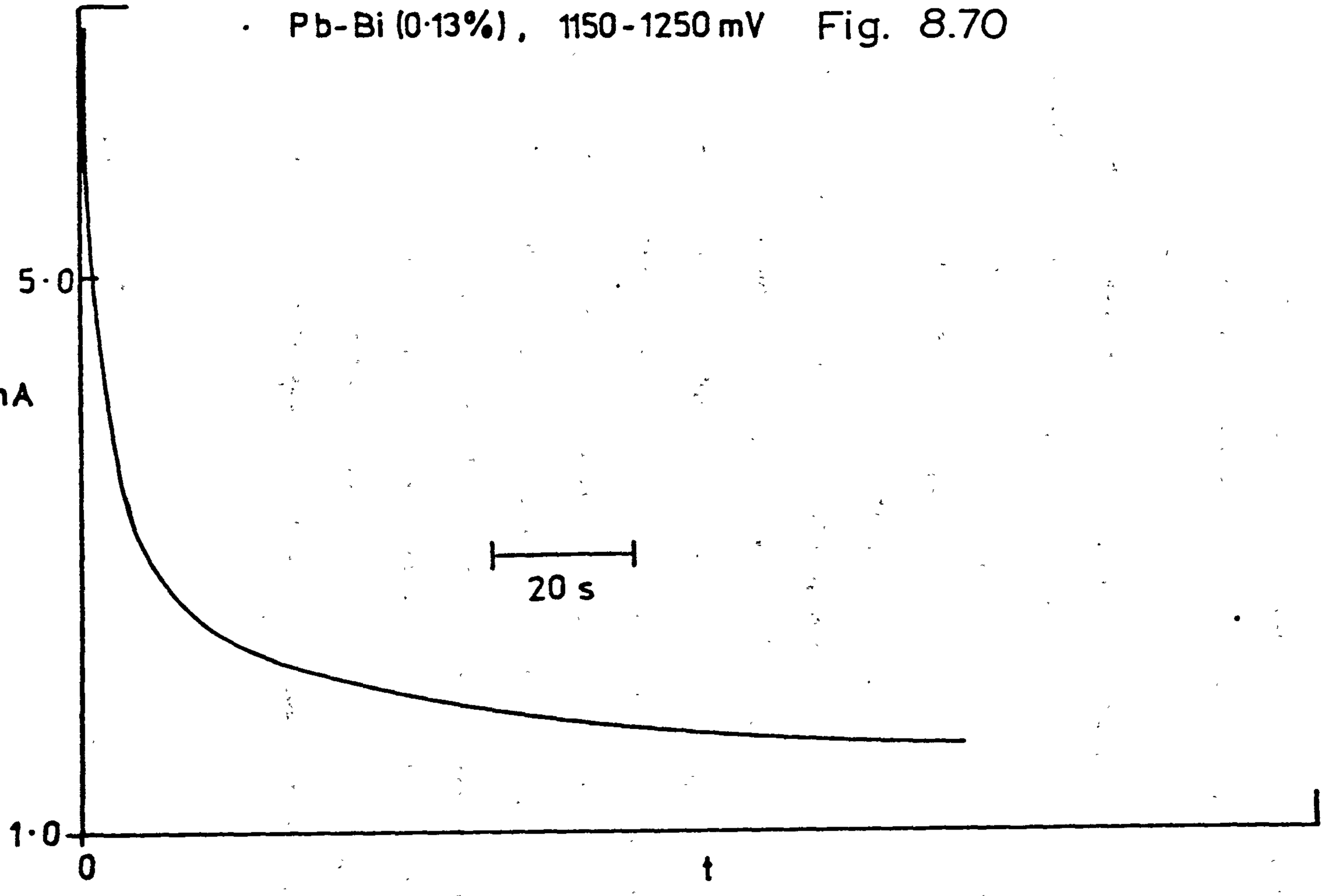

CHAPTER 9

A.C. IMPEDANCE STUDIES ON SMOOTH LEAD/LEAD-ALLOY ELECTRODES IN 5M SULPHURIC ACID

9.1. Introduction

The impedance method for measuring the rates of electrochemical reactions and hence investigating the kinetics is a very powerful technique[125]. Some applications have been made to studying the lead dioxide electrode. The impedance of massive β-PbO_2 films electrodeposited on Pt have been investigated[126,127] and compared with those from simple porous films produced by electrooxidation in sulphuric acid of basic lead sulphate pasted onto lead. It was found possible to obtain some useful kinetic data from the massive β-PbO_2 system. The appearance of a high frequency semicircle in the Sluyters plot observed over a wide range of potential enable the charge transfer resistance θ to be estimated. A plot of log R_{CT} versus E enabled the charge transfer coefficient to be calculated as 0.3 and the exchange current density of 2.4×10^{-5} Acm^{-2} was shown to be quite reasonable for the electrode in 5M H_2SO_4 at 1044 mV. A further interesting feature of these measurements was that the surface of a freshly plated electrode was found to be continuously changing with time. A plot showed this change to result in the charge transfer resistance increasing logarithmically with time. It was argued that this resulted from the progressive thickening of a lead sulphate layer nucleated upon the massive lead dioxide. When the layer is sufficiently thick the diameter of the high frequency semicircle becomes very large and the electrode ultimately becomes insulated from the electrolyte solution. The frequency response of the porous lead dioxide electrode

was quite complex and showed an interesting high frequency region which included an inductive loop. The presence of this inductive loop had also been observed by Keddam et al[128] who studied the lead-acid cell at various stages of discharge. Keddam suggested that geometrical effects were the cause of the inductive loops whereas it seemed to us that the occurrence of the reaction over a distributed region of the electrode as discussed by Darby[129] provided a more realistic explanation.

As the electrode is driven to more negative potentials the Sluyters plot curves over towards the real axis reaching the limit of $\pi/8$ to the real axis. This is what is to be expected for an electrode with semi-infinite pores at right angles to the front of the electrode. This line ultimately degenerates into a more complex shape, however, at these potentials (700 mV) the electrode is largely transformed to lead sulphate. In this region the impedance spectrum was very complicated and discussion of the shapes obtained in the far lead sulphate region were very difficult to interpret. It was decided to attempt to simplify the complex Sluyters plots obtained from the very complex porous (0.05 cm thick) electrode by first investigating the impedance of lead dioxide/lead sulphate films on the base electrode. Current industrial practice uses lead dioxide on a lead-antimony, lead-calcium-tin alloy for the majority of applications of the lead acid cell together with a relative minor interest in the Planté situation where the lead dioxide films are developed on lead. A range of studies were undertaken, therefore, of the simple situation in which films of PbO_2 were formed on pure lead and some alloys of interest, this chapter records the results.

9.2. Experimental

PbO_2 electrodes were formed in 5 M H_2SO_4 solution from lead and lead alloys by momentarily polarising at 2000 mV to start PbO_2 formation and then continued polarisation in the PbO_2 potential region (1250 mV) until the current had fallen to an acceptably low (and constant) level. At the reversible potential in 5 M H_2SO_4 and more positive potentials electrodes were simply poised at the desired potential and the impedances measured in the range 10 kHz to 0.001 Hz. At potentials negative of the reversible potential impedances were measured only when the electrode reduction current had fallen to zero at the potential of interest. In this way the impedances were measured at well-defined pre-electrode states rather than ill-defined ones which are obtained if there is significant electrode reduction current. (It should be noted, however, that if potentials other than the reversible are to be investigated for kinetic data then there is no alternative to the a.c. on d.c. experiment with some uncertainty due to film formation[126,127].

9.3. Results and Discussion

9.3(i) Measurements at the reversible potential

This was determined as the zero current potential and found to be 1.100 mV as the mean value over all the alloy systems investigated Accordingly measurements were made throughout at this potential. The other approach of using a carefully determined E_r for each alloy led to second order differences in the experimental E_r ($\sim$1 mV) which arose apparently from metallurgical effects. It was considered more useful to fix the potential since having a consistent potential (vs Hg_2SO_4/ Hg, 5M H_2SO_4) is a better basis for comparison of impedance data.

Fig. 9.71 shows a Sluyters plot for pure lead to be a rising curve exhibiting neither a well-defined shape nor a Warburg line indicating an interpretable solution process. The Randles plot corresponding to this behaviour is shown in Fig. 9.72. This consists of two diverging lines of which the resistive component line crosses that for the capacitative component. The Figures 9.73-9.79 show impedance loci corresponding to the other alloys investigated. At low frequency the behaviours are very similar and the expected slope of either $\pi/4$ for a planar or $\pi/8$ for a porous electrode was nowhere to be found. It can be concluded from this that the electrode reaction did not involve the free diffusion of species at the electrode. An examination of corresponding Randles plots for the cases shown (Figs. 9.73-9.79) indicate a divergence of the resistive and capacitive lines with cross overs at high frequency. This supports an argument for the reaction occurring completely in the adsorbed state with nothing leaving the electrode. Such a mechanism would fit in with the known adsorprive properties of lead dioxide[130].

At high frequency the impedance data show considerable differences between the alloys and unalloyed lead. The most noticeable feature occurs with the lead-antimony alloy where the presence of a well-developed inductive loop at the highest frequencies is quite distinctive. None of the other alloys exhibit this, however, data reported in the literature[126] for lead dioxide electrodes show that this behaviour occurs with porous lead dioxide electrodes and is confirmed for lead cells by Keddam et al[131]. The occurrence of the high frequency inductive semicircle is a consequence of the porous nature of the electrode and the consequential electrochemistry which occurs over a

Fig. 9.71

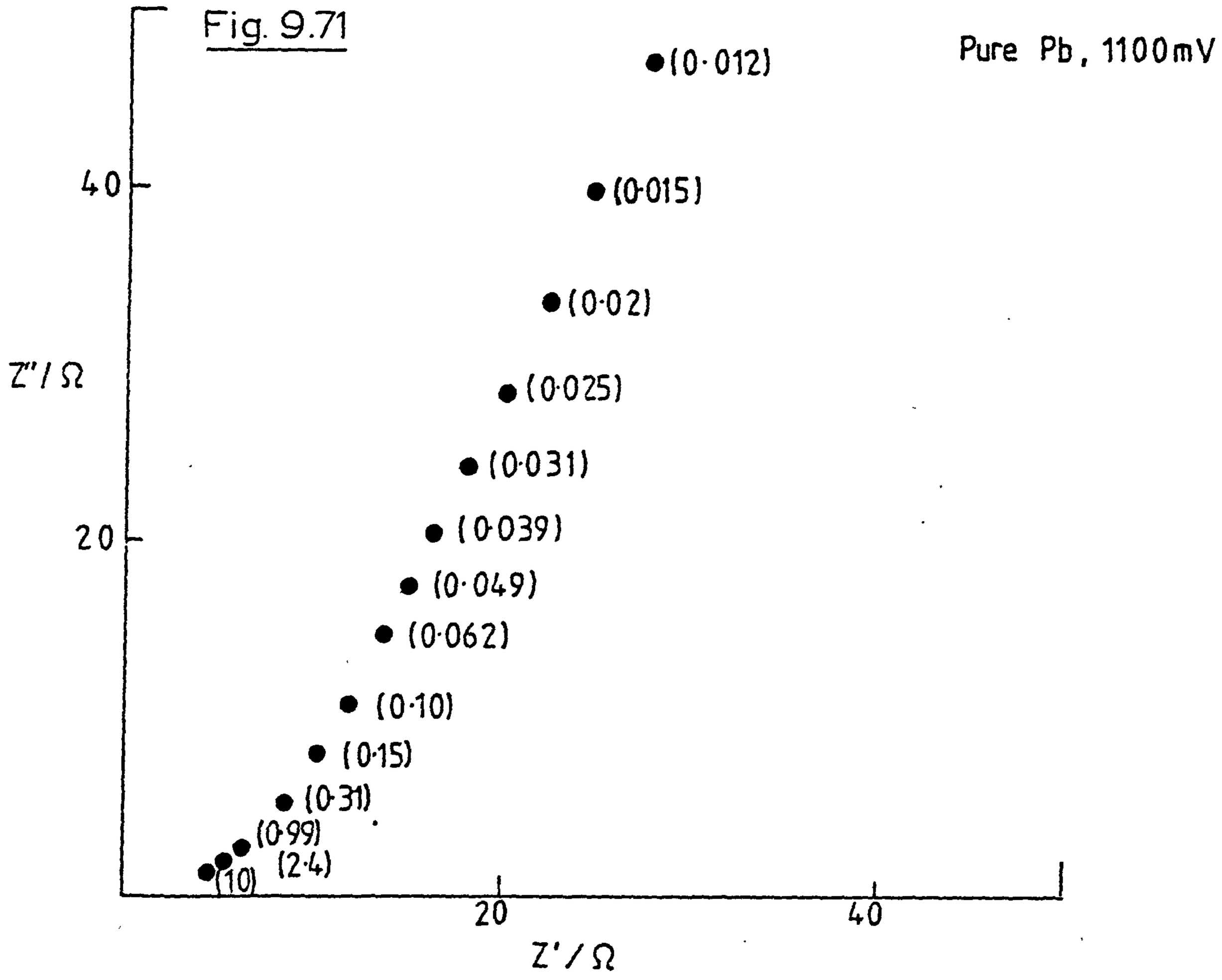
Pure Pb, 1100mV
(0·012)
(0·015)
(0·02)
(0·025)
(0·031)
(0·039)
(0·049)
(0·062)
(0·10)
(0·15)
(0·31)
(0·99)
(2·4)
(10)
40
20
Z''/Ω
20
40
Z'/Ω

distributed region of the electrode. At sufficiently high frequencies the phase angle of the faradaic impedance is negative which arises physically because of a change in reactant concentration with depth in the porous electrode which clearly cannot be with the plane electrode. With the antimonial lead electrode this inductive loop is perfectly developed indicating that the pores are effectively semi-infinite, i.e. about 4 times the characteristic diffusion length $(D/\omega)^{\frac{1}{2}}$ within the frequency range also suggests a more tightly adherent film in accordance with a smaller separation between conductor and dielectric and the flat capacitor theory.

It has been shown previously (Chapter 6) that additions of bismuth to calcium/tin/lead battery alloys cause an increase in the cycle life of the alloy in sulphuric acid. This is confirmed in the present investigation when Figs. 9.77 and 9.78 are compared. It was observed that both the resistance and capacitance of the electrode are decreased with the addition of Bi to Pb-Ca-Sn in agreement with the formation of a layer which is rather less passivating. The outstanding observation at this potential is the lack of any well-defined shapes concerning the electrochemistry. The reason for this must lie in the slowness of the phase formation reactions and the lack of exchange due to this cause. The slope of the low frequency part of the impedance shape is always much greater than the expected Warburg slope of 45^{o} (for a plane electrode) or 22.5^{o} (for a porous electrode). Although there is a little evidence for curvature in this frequency region the electrode is effectively polarisable, the change in slope may simply reflect the porosity.

Pure Pb, 1100 mV

Fig. 9.72

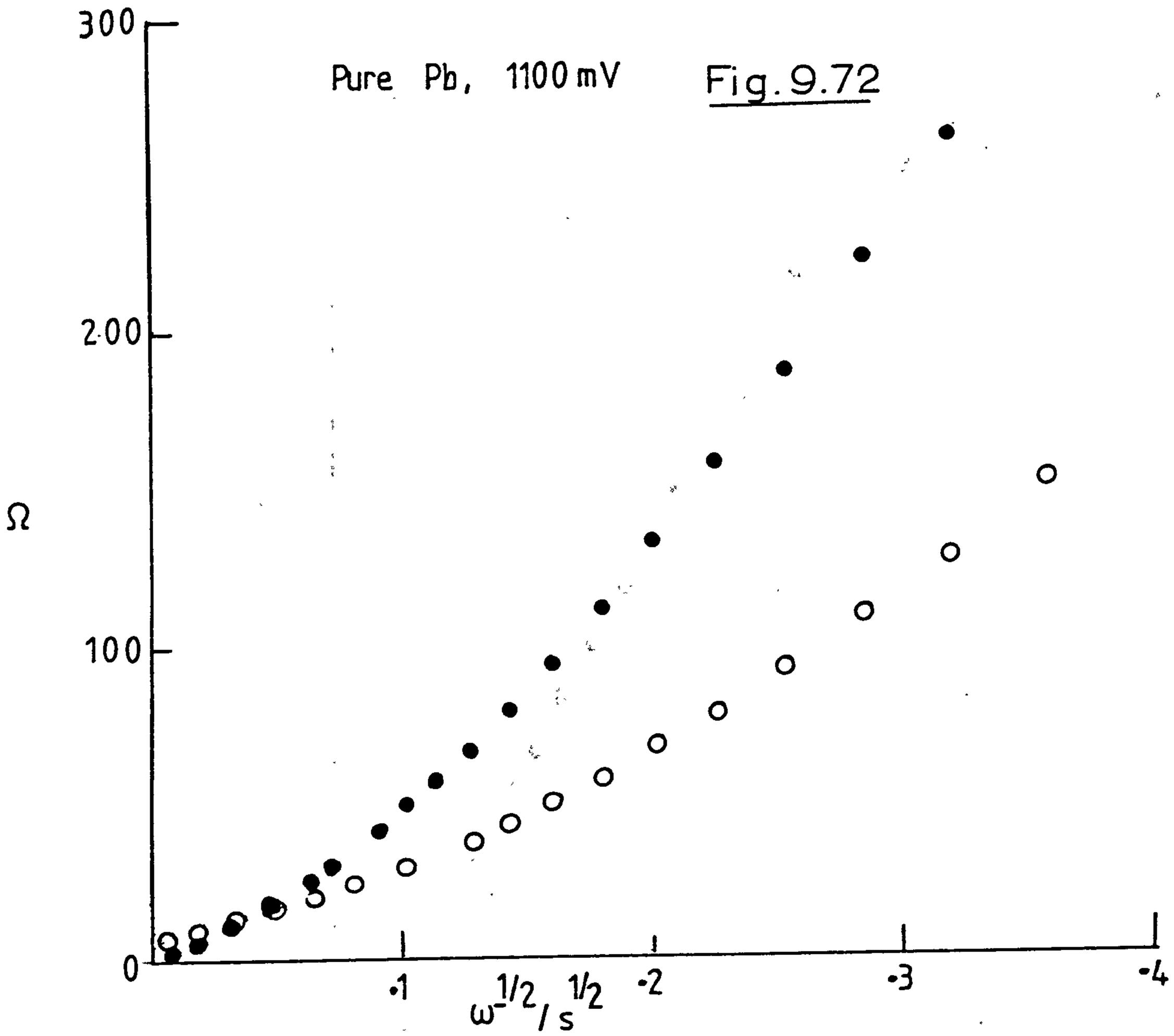

Fig. 9.73

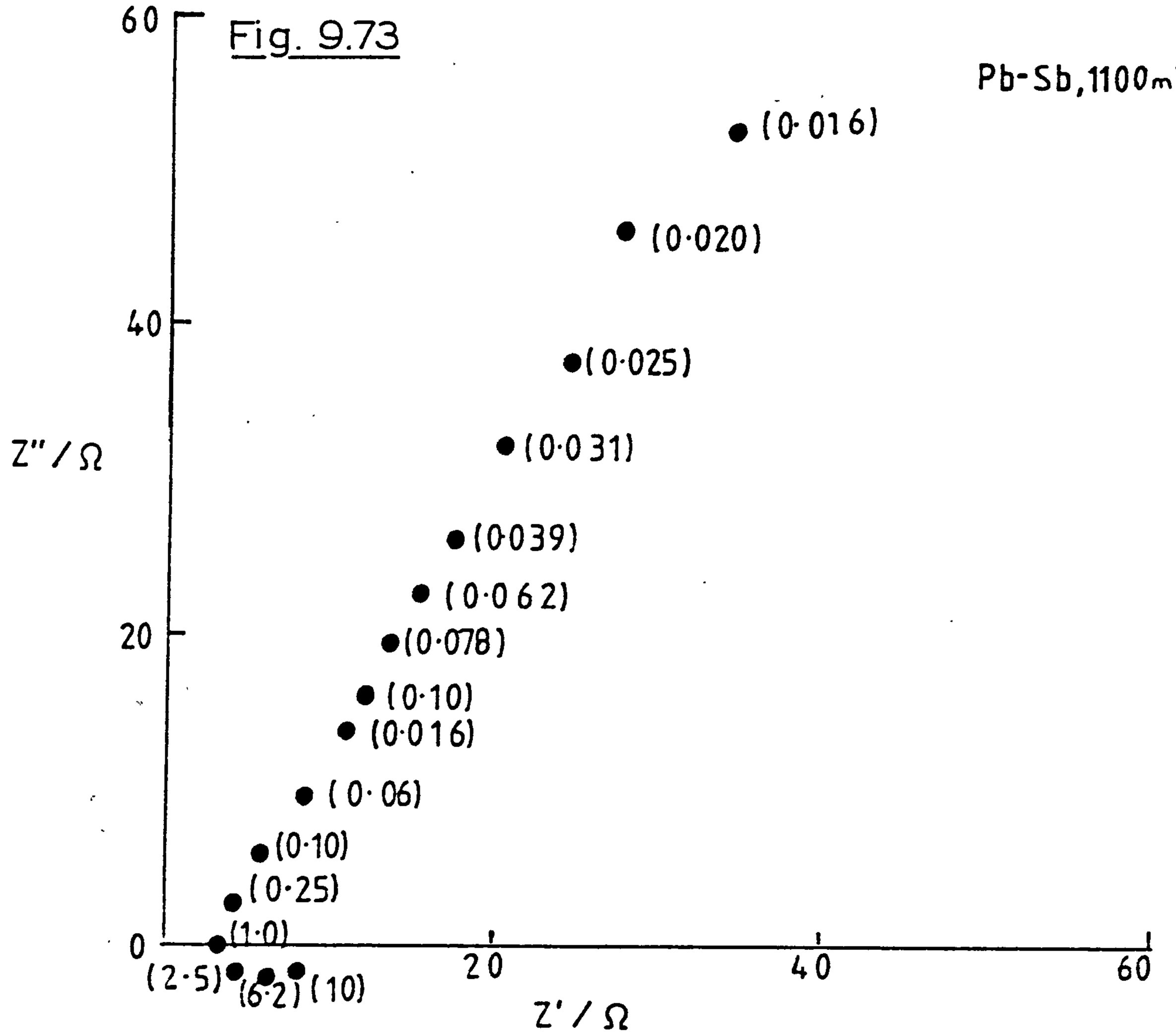
Pb-Sb, 1100mV
(0·016)
(0·020)
(0·025)
(0·031)
(0·039)
(0·062)
(0·078)
(0·10)
(0·016)
(0·06)
(0·10)
(0·25)
(1·0)
(2·5)
(6·2)
(10)
60
40
20
0
20
40
60
Z'' / Ω
Z' / Ω

Fig. 9.74

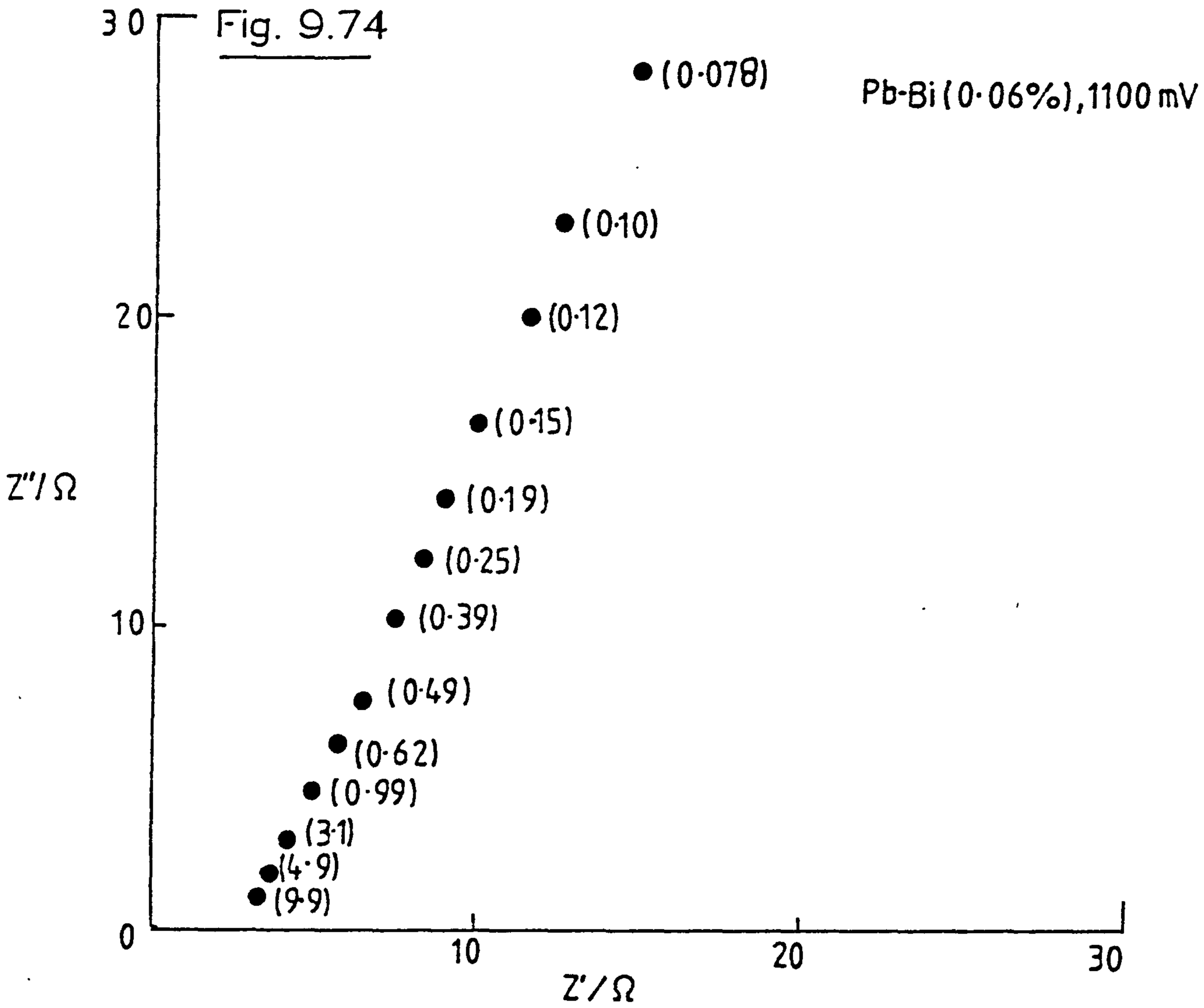
Pb-Bi (0·06%), 1100 mV
(0·078)
(0·10)
(0·12)
(0·15)
(0·19)
(0·25)
(0·39)
(0·49)
(0·62)
(0·99)
(3·1)
(4·9)
(9·9)
Z''/Ω
Z'/Ω
0
10
20
30

Fig. 9.75

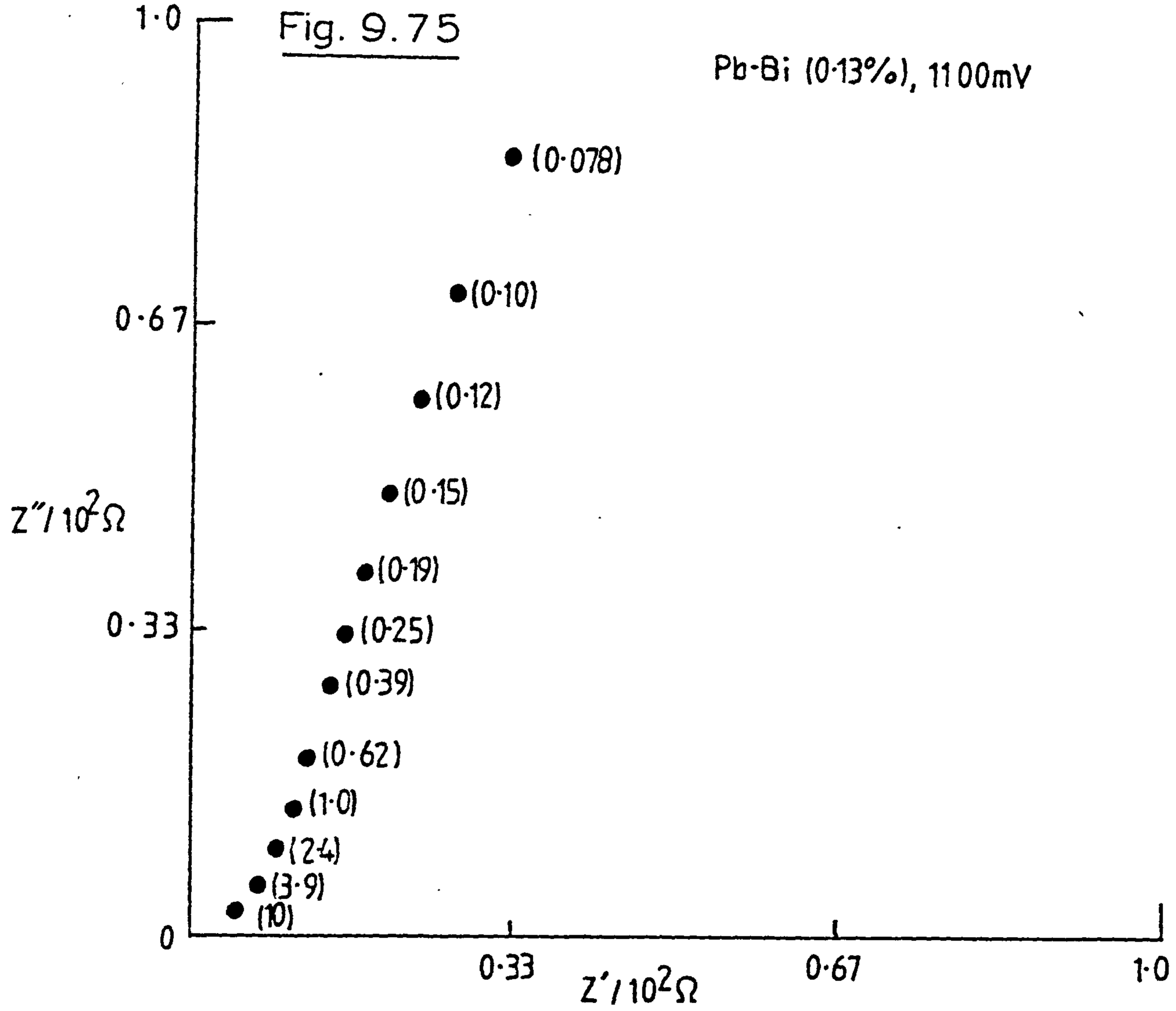
Pb-Bi (0·13%), 1100mV
1·0
0·67
0·33
0
Z″/10²Ω
Z′/10²Ω
0·33
0·67
1·0
(0·078)
(0·10)
(0·12)
(0·15)
(0·19)
(0·25)
(0·39)
(0·62)
(1·0)
(2·4)
(3·9)
(10)

Fig. 9.76

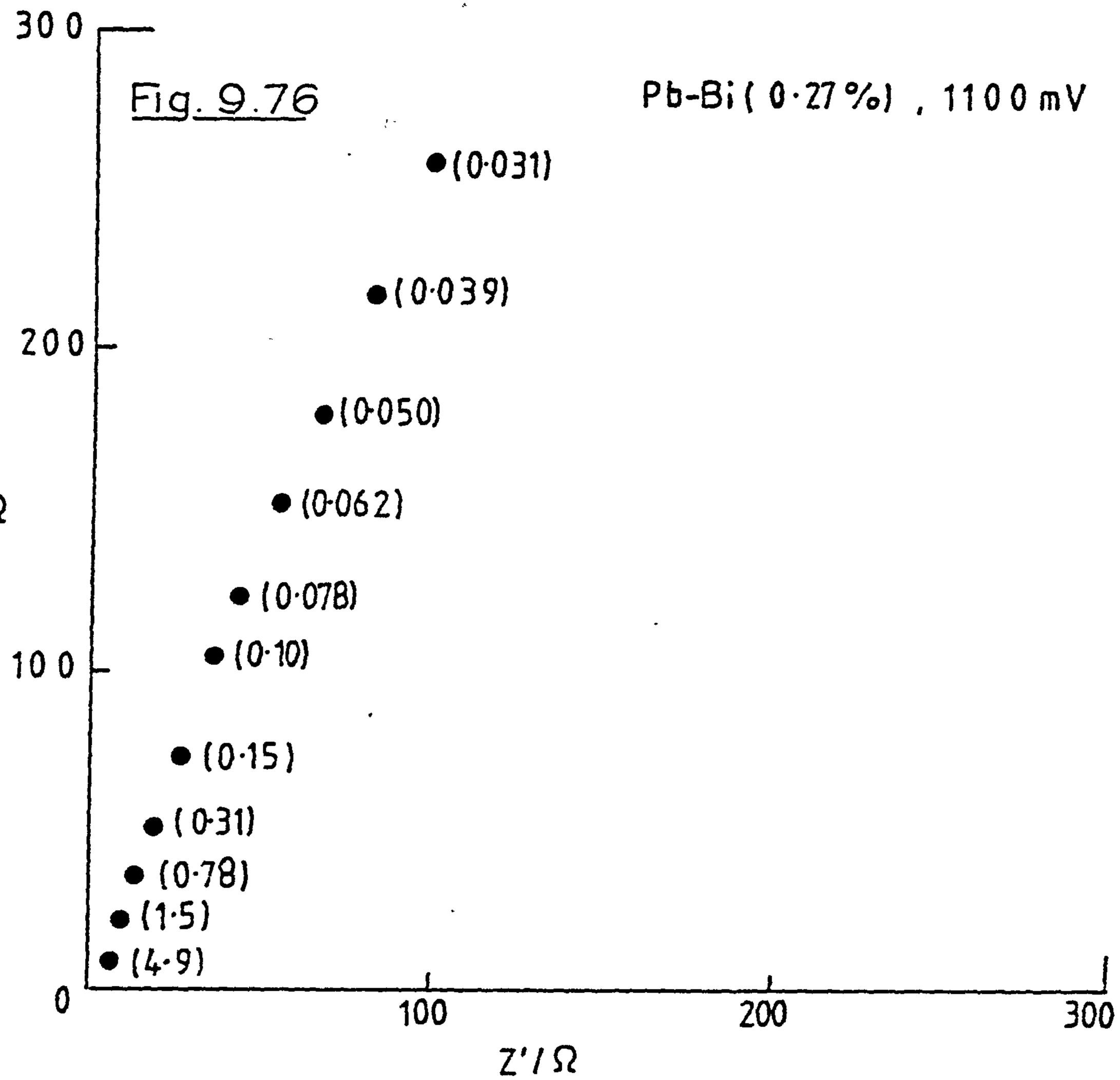
Pb-Bi (0·27 %) , 1100 mV
300
200
100
0
Z'' / Ω
Z' / Ω
100
200
300
(0·031)
(0·039)
(0·050)
(0·062)
(0·078)
(0·10)
(0·15)
(0·31)
(0·78)
(1·5)
(4·9)

Fig. 9.77

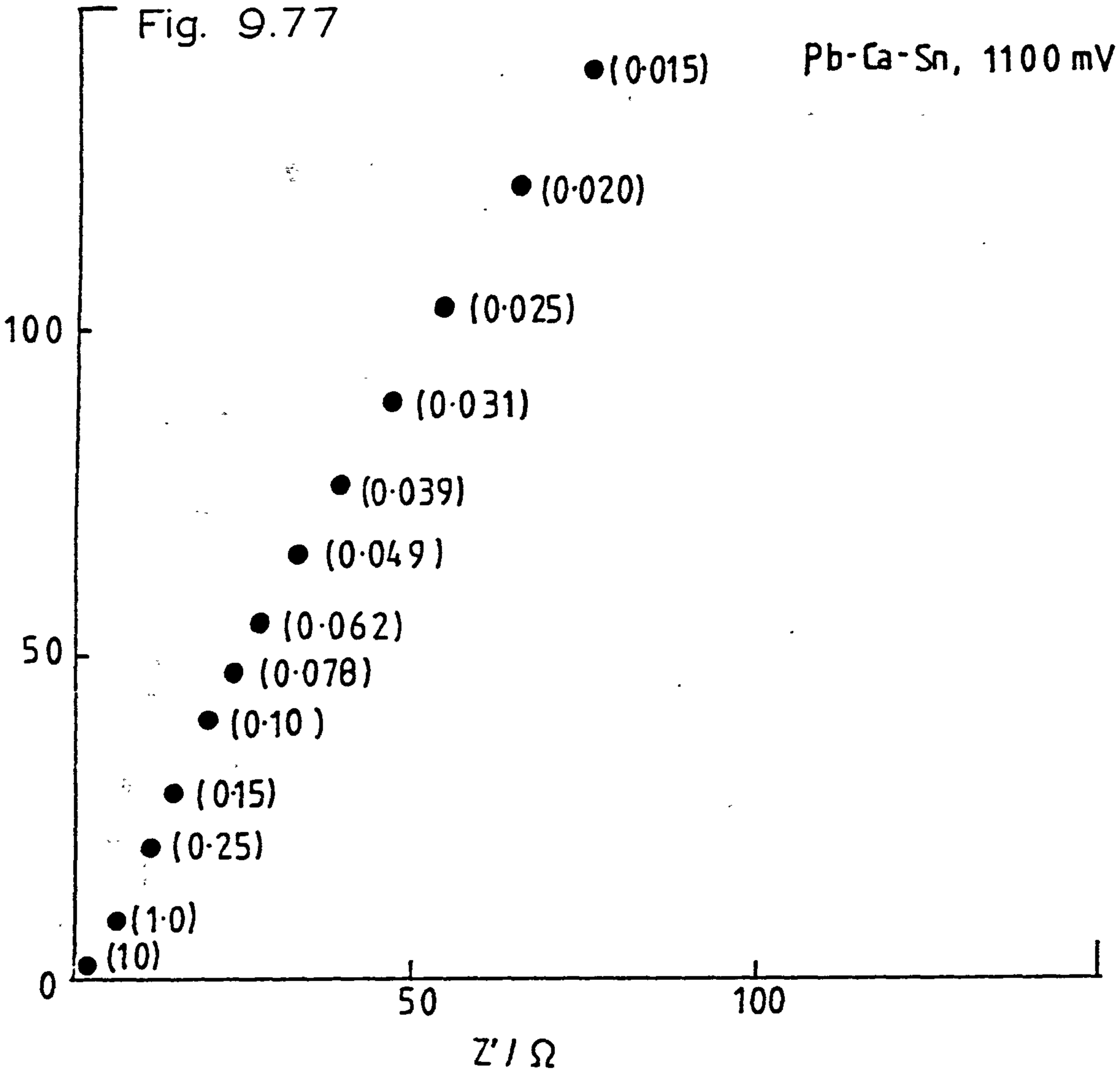
Pb-Ca-Sn, 1100 mV
(0·015)
(0·020)
(0·025)
(0·031)
(0·039)
(0·049)
(0·062)
(0·078)
(0·10)
(0·15)
(0·25)
(1·0)
(10)
100
50
0
50
100
Z'' / Ω
Z' / Ω

Fig. 9.78

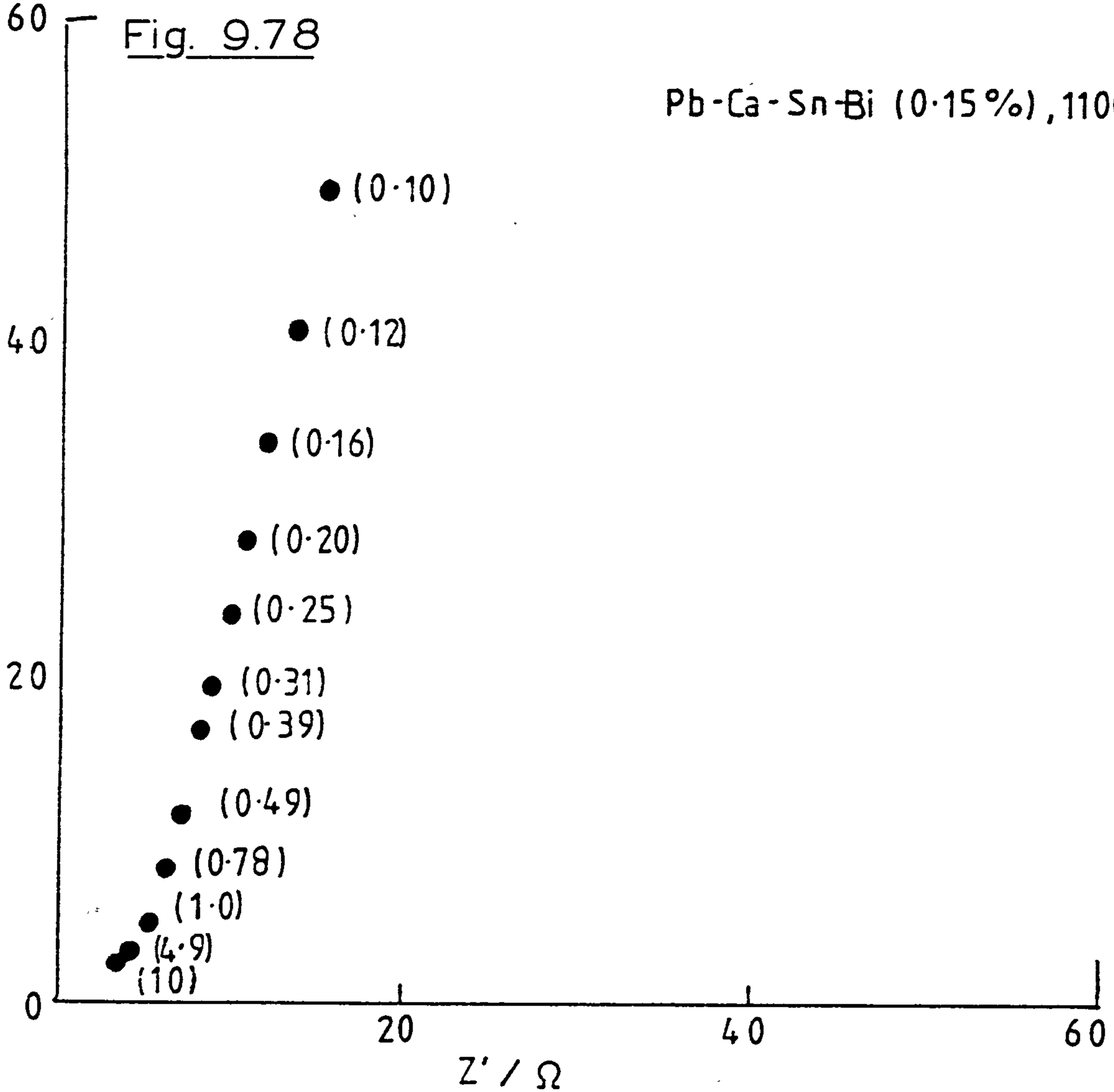
Pb-Ca-Sn-Bi (0·15 %), 1100 mV
(0·10)
(0·12)
(0·16)
(0·20)
(0·25)
(0·31)
(0·39)
(0·49)
(0·78)
(1·0)
(4·9)
(10)
60
40
20
0
20
40
60
Z'' / Ω
Z' / Ω

Fig.9.79

Pb-Ca-Sn-Mg (0·046%), 1100mV

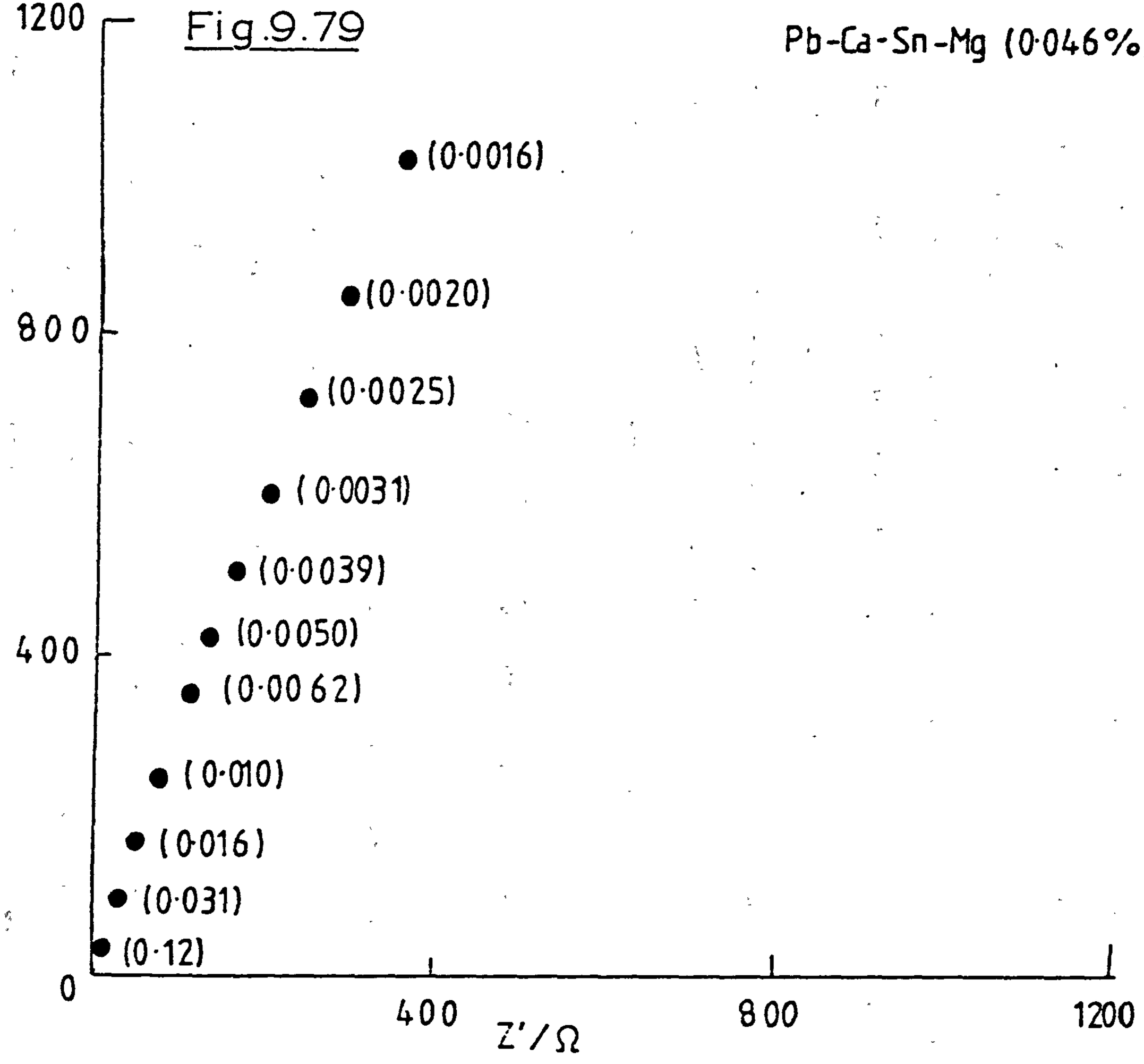

The results on pure lead and the non-antimony containing alloys agree quite well with the impedance shapes reported by Casson et al[127] for electrodeposited β-PbO_2. It can be concluded from this that in the positive region of the equilibrium the deposit on the non-antimonial lead resembles β-PbO_2; however, on the antimony alloy the formation of PbO_2 involves the formation of a pore structure sufficiently well-developed to cause a high frequency inductive shape.

9.3 (ii) Measurements at Polarised Electrodes above 900 mV

a) Pure Lead

When the electrode is forced to potentials positive of the equilibrium potential oxygen gas is produced at the electrode , the bubbles increasingly obscure the electrode and its impedance changes continuously with time. Provided that the potential is not too positive and measurements are made rapidly an "accurate enough" impedance loci can be obtained. Such a one is shown in Fig. 9.80. It consists of an almost vertical straight line approximating to ideal polarisability. It is clear that there is no useful kinetic information to be gathered and it must be concluded that when the potential is sufficiently negative so that the oxygen evolution reaction does not intrude by physical obscurance of the electrode the reaction is so slow as to render the electrode effectively polarisable.

When the electrode potential is shifted to potentials more negative than the equilibrium in the range below 970 mV which is the "operational" potential of PbO_2 electrodes in battery situations the impedance loci becomes that of a system rate controlled by the electrochemistry. A high frequency semicircle is apparent which goes

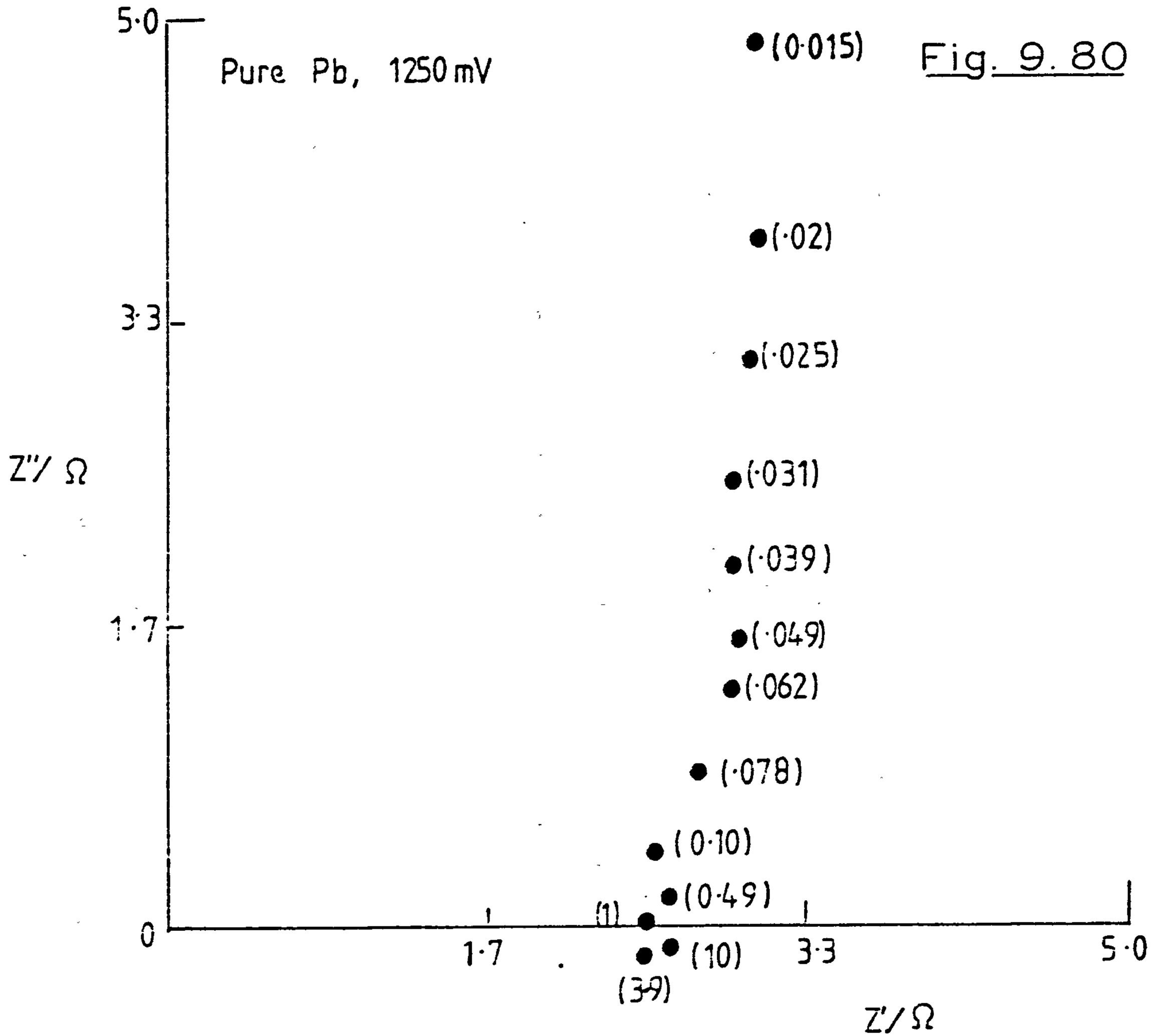
5·0
Pure Pb, 1250 mV
(0·015)
(·02)
3·3
(·025)
Z''/ Ω
(·031)
(·039)
(·049)
1·7
(·062)
(·078)
(0·10)
(0·49)
0
(1)
1·7
(10)
3·3
5·0
(39)
Z'/ Ω

Fig. 9.80

off at lower frequency to form an inclined line. This behaviour is shown by the Figures 9.81 - 9.84 for a series of potentials in the range 970 -930 mV. A feature of the figures is that the dihedral angle of the low frequency tail exceeds $\pi/4$, furthermore this angle increases as frequency is decreased. This cannot be attributed to the PbO_2 or any intermediate phase between the lead base and the PbO_2 and must therefore be attributed to the lead sulphate grown on the lead dioxide as a result of the potential excursion. Although the current flowing across the electrode interfaces had reached effectively zero the sulphate layers did not passivate the electrodes, rather the rate of reaction was throttled down. The electrode behaves therefore as a reaction controlled by charge transfer and diffusion in solution in series with a leaky capacitance representing the sulphate layer. This is convincingly confirmed in Fig. 9.86 in which the analogue shown in Fig. 9.85 is matched to the experimental data. The matching was carried out by writing the complex equations for the cell analogue

$$Z_D = -j/\omega C_L \tag{64}$$

$$Z_F = R_{CT} + \sigma\omega^{-\frac{1}{2}} - j\sigma\omega^{-\frac{1}{2}} \tag{65}$$

for which the impedance is given by

$$Z' = \left[\frac{1}{Z_D} + \frac{1}{Z_F}\right]^{-1} - j/\omega C_X + R_{sol} \tag{66}$$

The equation (66) was decomposed into the real and imaginary parts and each was treated separately by expanding about approximate values (x') of the circuit elements (x) such that

$$x = x' + \Delta x \tag{67}$$

Fig. 9.81

Pure Pb, 970mV

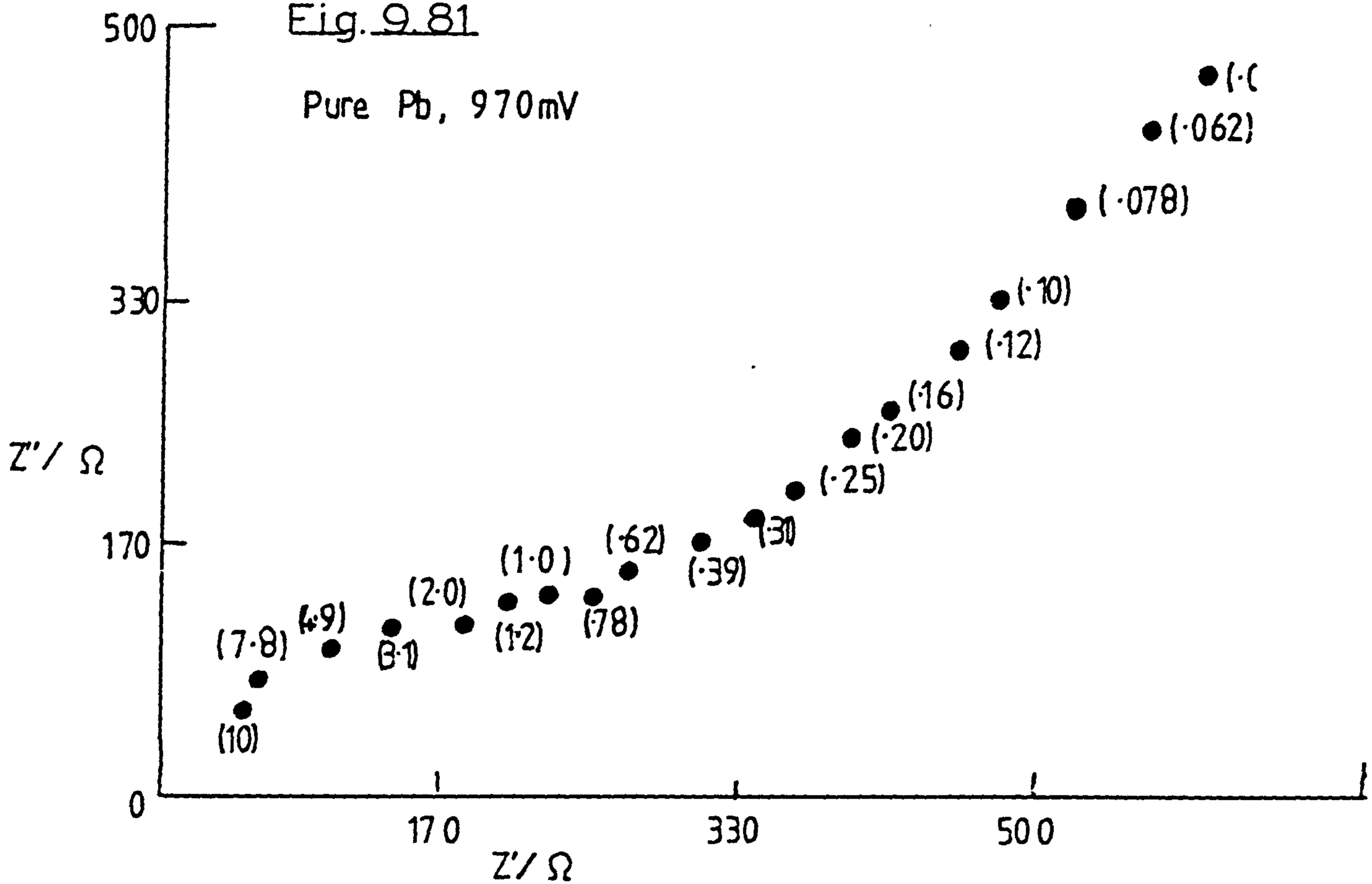

Fig. 9.82

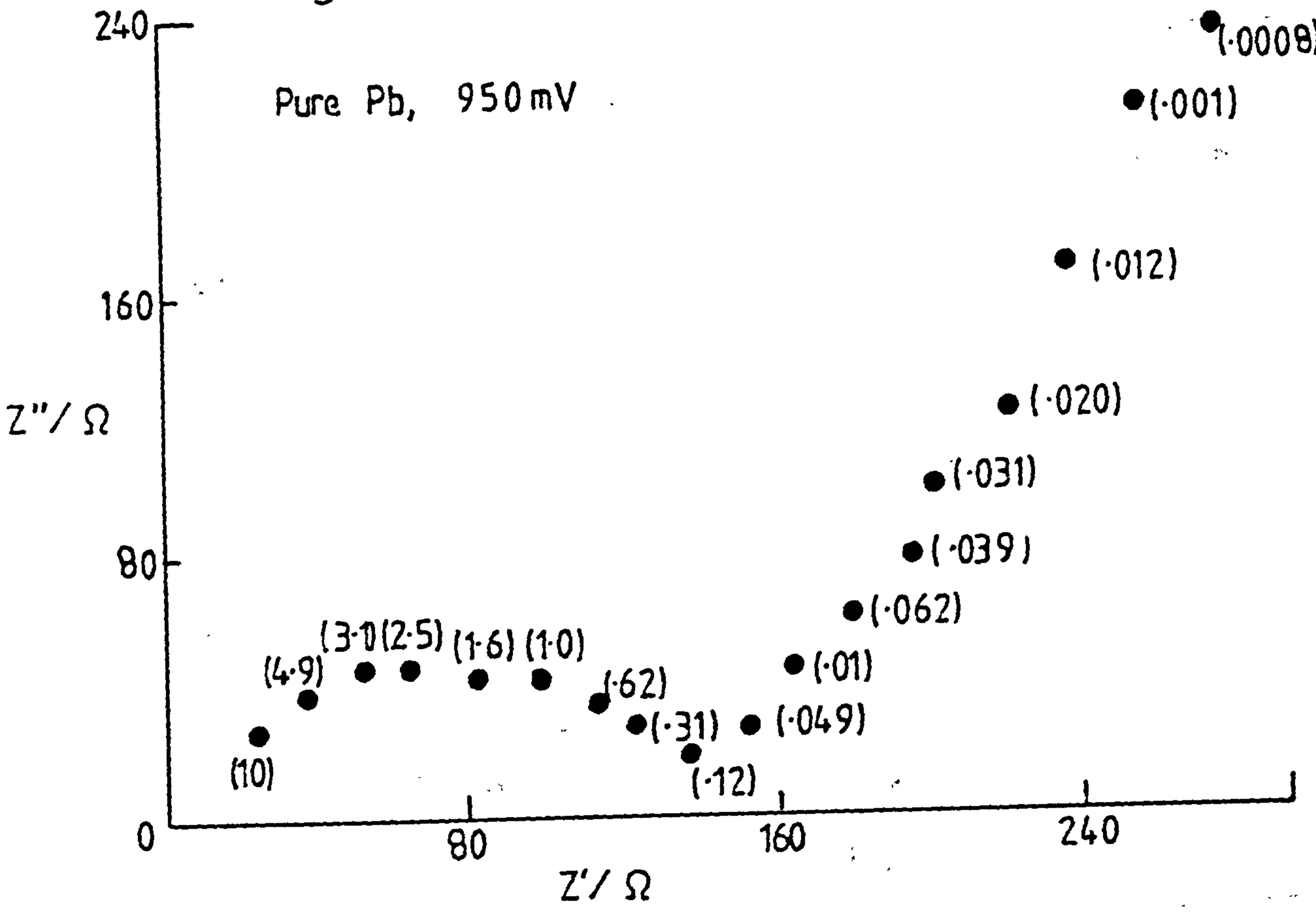
Pure Pb, 950 mV
240
160
80
0
Z''/ Ω
Z'/ Ω
80
160
240
(·0008)
(·001)
(·012)
(·020)
(·031)
(·039)
(·062)
(·01)
(·049)
(·31)
(·12)
(·62)
(4·9)
(3·1)
(2·5)
(1·6)
(1·0)
(10)

Pure Pb, 940mV Fig. 9.83

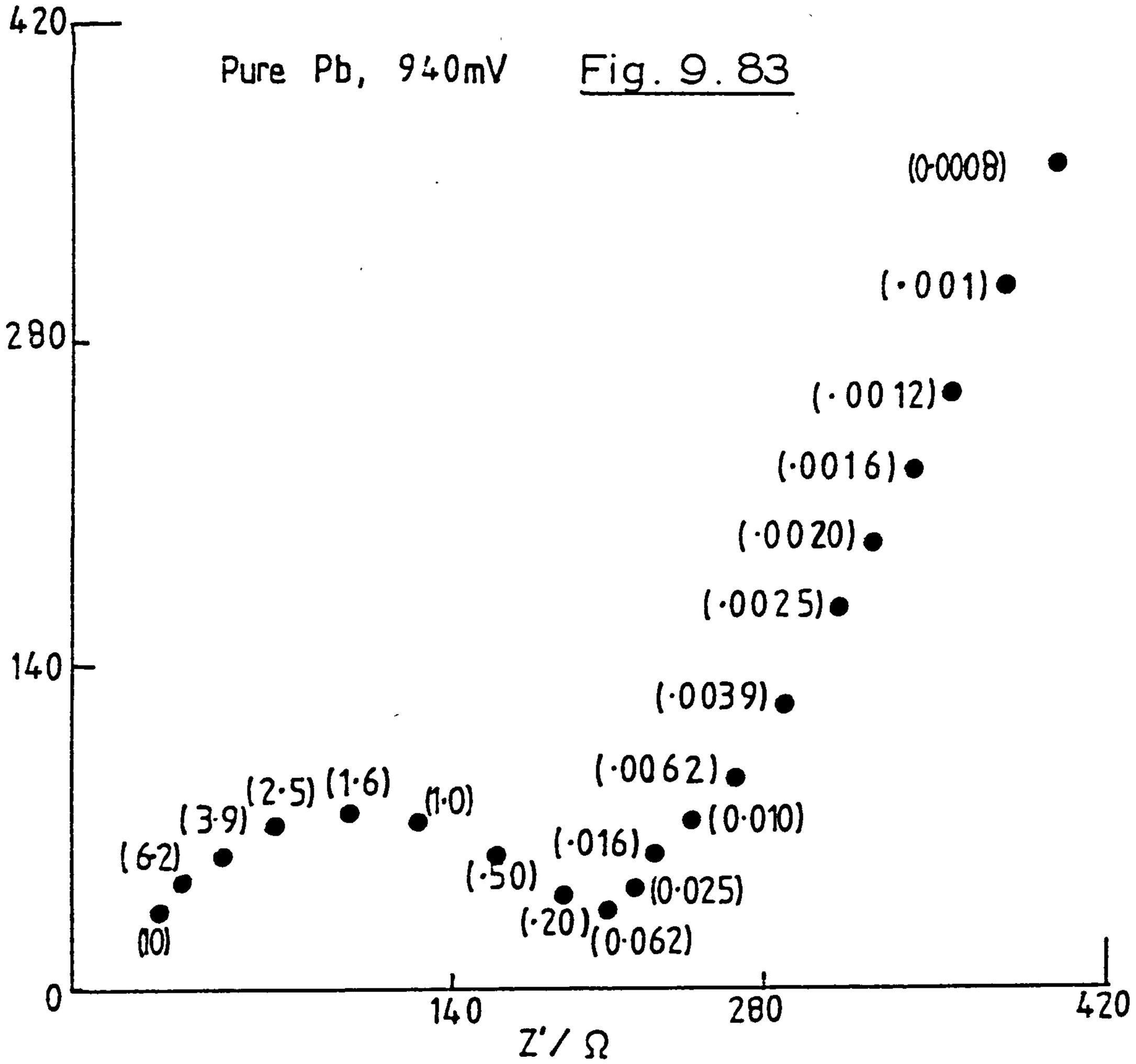

Pure Pb, 930mV Fig. 9.84

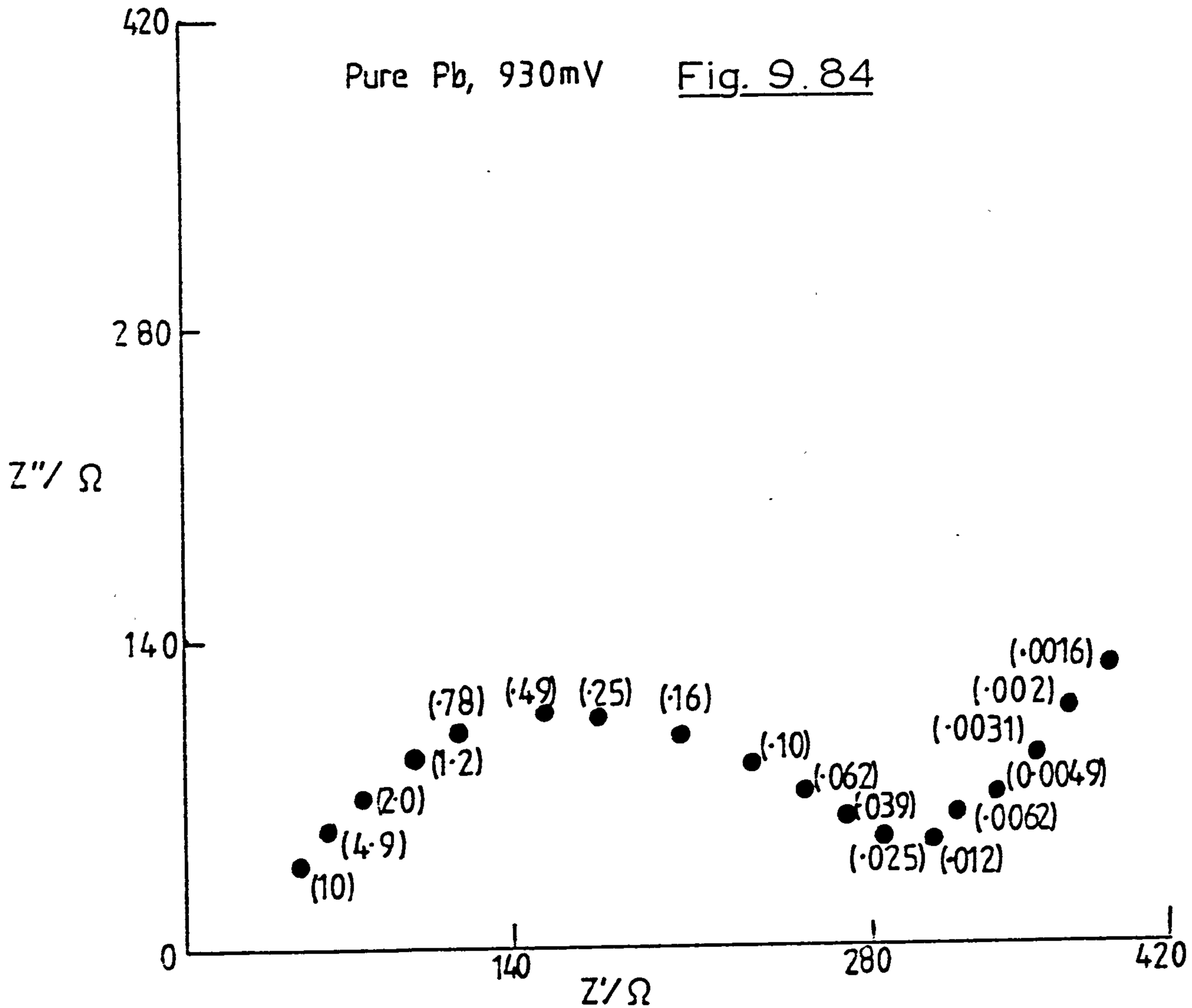

Fig 9.85

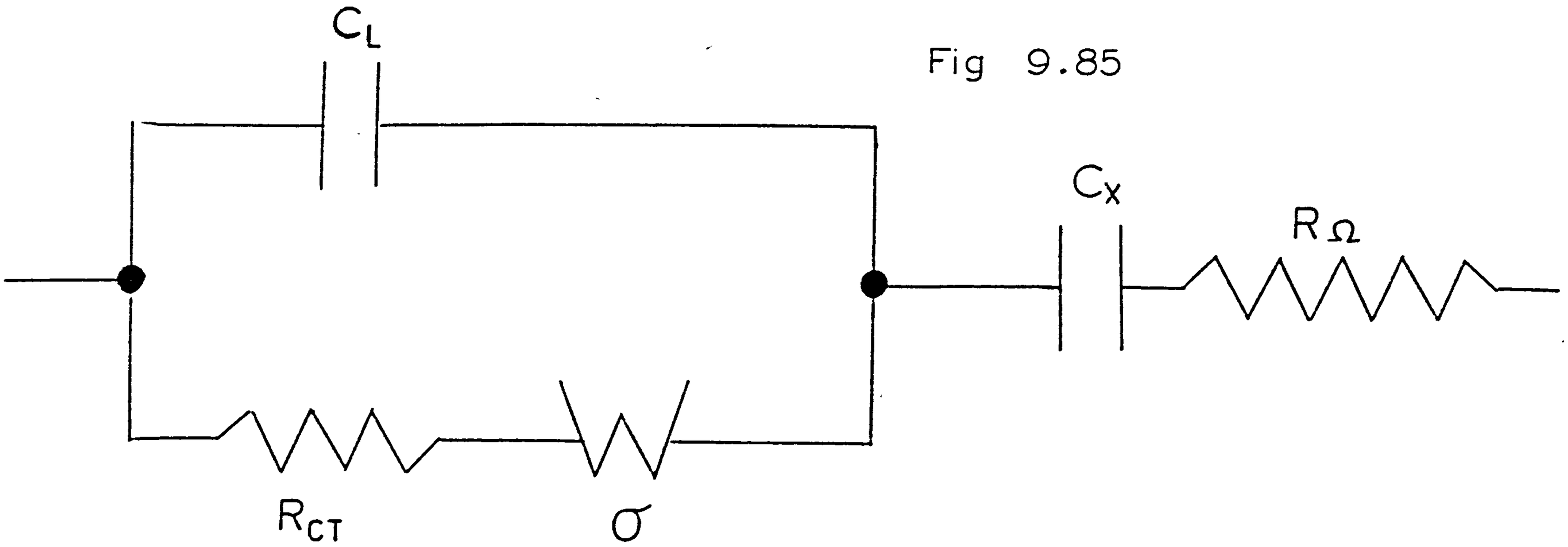

Pure Pb, 940mV

Fig. 9.86

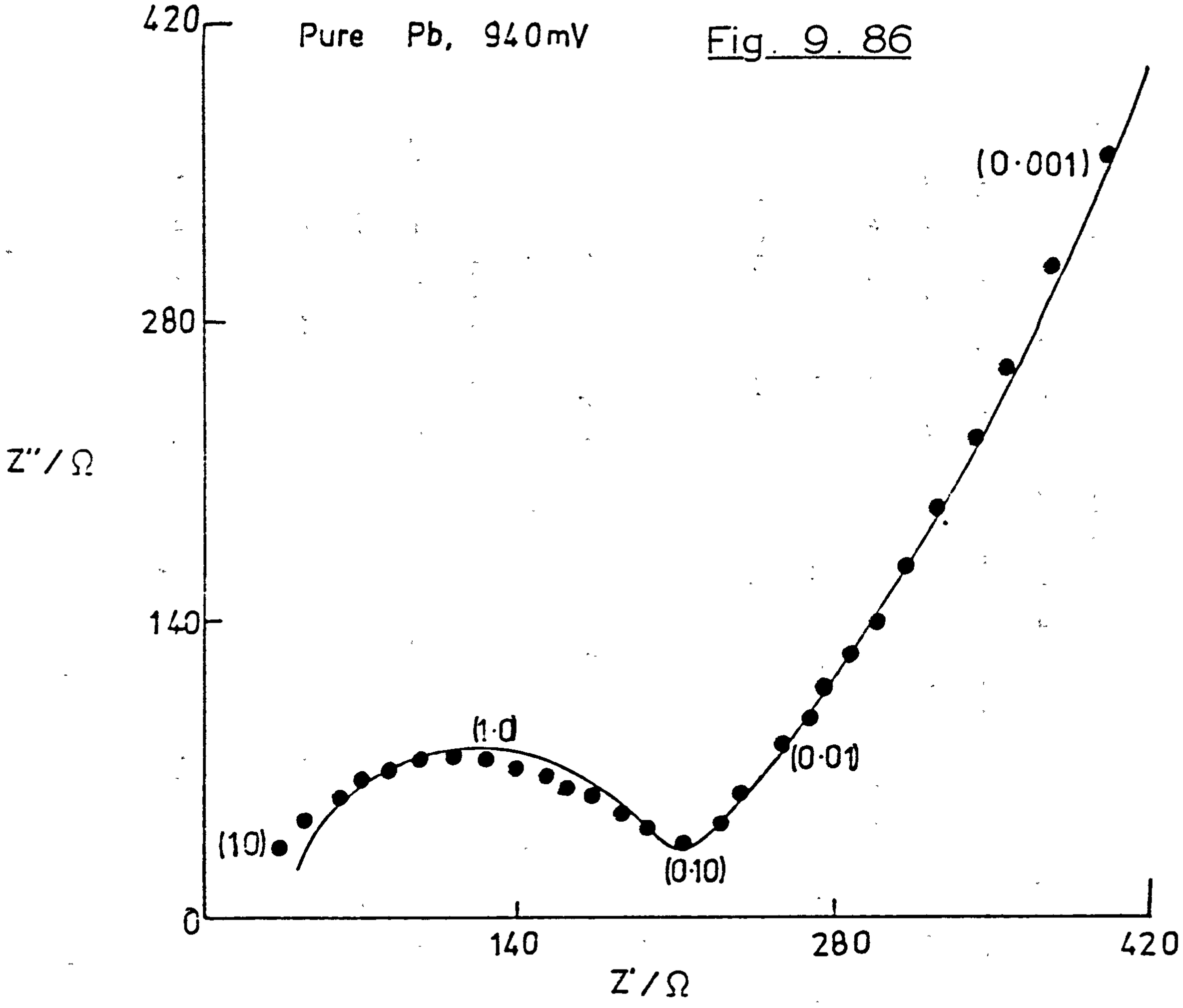

Using Taylor's theorem and neglecting the second and higher order terms to obtain two linear equations

$$R = R' + \sum_c \left[\frac{dR'}{dx}\right]\Delta x \quad \text{and} \quad C = C' + \sum \left[\frac{dC'}{dx}\right] \Delta C \qquad (68(a) \text{ and } (b))$$

In order to calculate values of R' and C' and their differentials approximate values of x are substituted in the expressions for each of the n experimental data points. These n linear equations are reduced by the method of least squares to the C normal equations needed to calculate Δx for each circuit element. The approximate value of x is then corrected by Δx and the process is repeated until Δx is sufficiently small to be neglected.

The calculation and isolation of real and imaginary parts of Z' of the impedance were performed using the complex number handling capability of the computer (PRIME 400). Figure 9.86 confirms that the behaviour especially at low frequency is adequately described by the model of an electrode becoming progressively blocked by a passivating layer of $PbSO_4$ as the potential is driven to more negative potentials. The data from the computer match at the potentials is shown in the table below.

Electrode characteristics obtained from computer match for a pure lead electrode at various potentials

Potential	950 mV	940 mV	930 mV	units
R_Ω	22.17	39.38	57.59	Ω
R_{CT}	100.2	155.9	219.3	Ω
C_L	0.721	0.630	0.602	μF
σ	449.5	414.5	514.2	$\Omega s^{-1/2}$
C_X	1702	1820	7200	μF

The film resistance is effectively R_Ω and this is seen to increase as more $PbSO_4$ is formed on the electrode. The film capacitance increases as potential decreases as more of the surface is covered more effectively with the dielectric. The Warburg coefficient increases with decreasing potential as the diffusing area of the electrode is reduced by the more effectively covering film.

It was not possible to obtain a well defined correlation with potential for either R_Ω, σ, C_L or C_X, however, in the case of R_{CT} a linear relationship was found between log R_{CT} and E. This is shown in Figure 9.87, in which a decade increase in R_{CT} is the result of an 84 mV decrease in potential. This value expresses both the reduction in the effective area of the electrode as a result of the increasing cover passivity and the increase in the reduction rate constant due to the change in potential. Casson[127] found that the Tafel slope for the latter factor was -87 mV per decade so that the passivity factor is 43 mV per decade change in effective area; i.e. a decrease of 43 mV in potential results in a decade decrease in active surface area.

(b) Alloys of Commercial Significance

Figures 9.88-9.93 show typical impedance loci of the series of alloys in the above potential range. Basically the curve is as observed for pure lead, however, the magnitudes of the circuit elements are rather different. The following table shows the salient data.

Electrode characteristics for various alloys; data obtained from computer match (ϕ = 0.071 cm^2)

	Pb-Sb	Pb-Bi (0.06%)	Pb-Bi (0.13%)	Pb-Bi (0.27%)	Pb-Ca-Sn-Bi (0.15%)
970 mV					
R_Ω	32.26	2.65	11.78	30.2	9.22
R_{CT}	22.76	32.91	45.02	113.9	28.36
C_L	0.909	0.89	0.949	0.285	0.860
σ	896	741.8	354	2113	832.6
C_X	167	664	389	157	195
950 mV					
R_Ω	38.48	9.06	17.45	113.4	41.86
R_{CT}	38.07	71.40	105.4	396.9	190.4
C_L	0.925	0.827	0.742	0.248	0.265
σ	1117	634.4	469.8	1909	4290
C_X	297	948	1350	230	74.1
940 mV					
R_Ω	34.3	12.53	26.75	133.2	14.77
R_{CT}	36.4	101.7	164.8	628.8	54.65
C_L	0.740	0.796	0.749	0.227	1.001
σ	1296	5638	389.1	2215	652
C_X	424	1290	1720	251	681
930 mV					
R_Ω	41.17	32.61	28.87	209.1	25.3
R_{CT}	47.92	163.9	241.5	1161	192.2
C_L	0.78	0.783	0.733	0.214	0.742
σ	1362	565.8	416.6	2992	1586
C_X	464	1430	1910	388	448

(units as for previous table)

Pure Pb Fig. 9.87

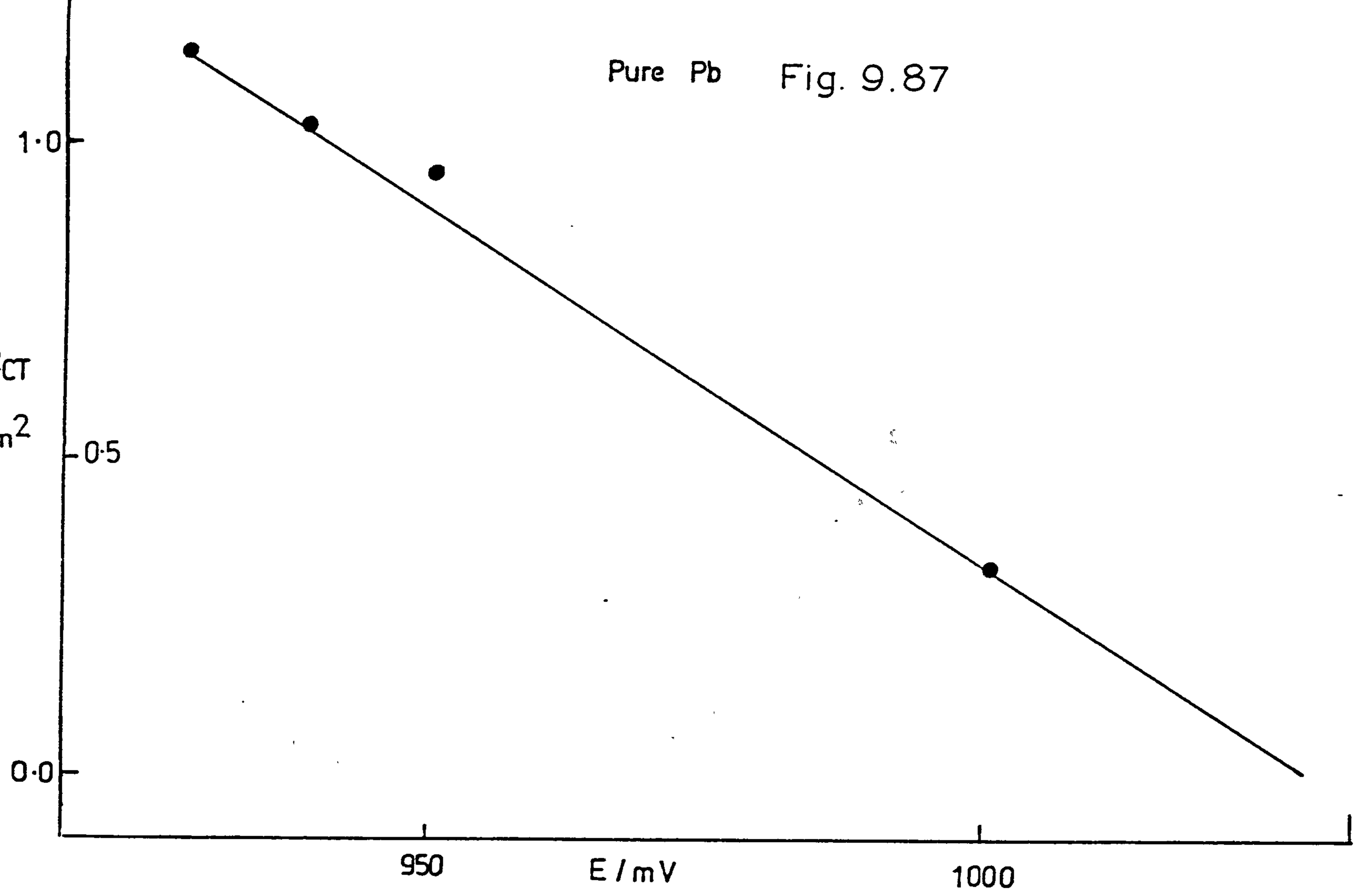

Pb-Sb, 950mV

Fig. 9.88

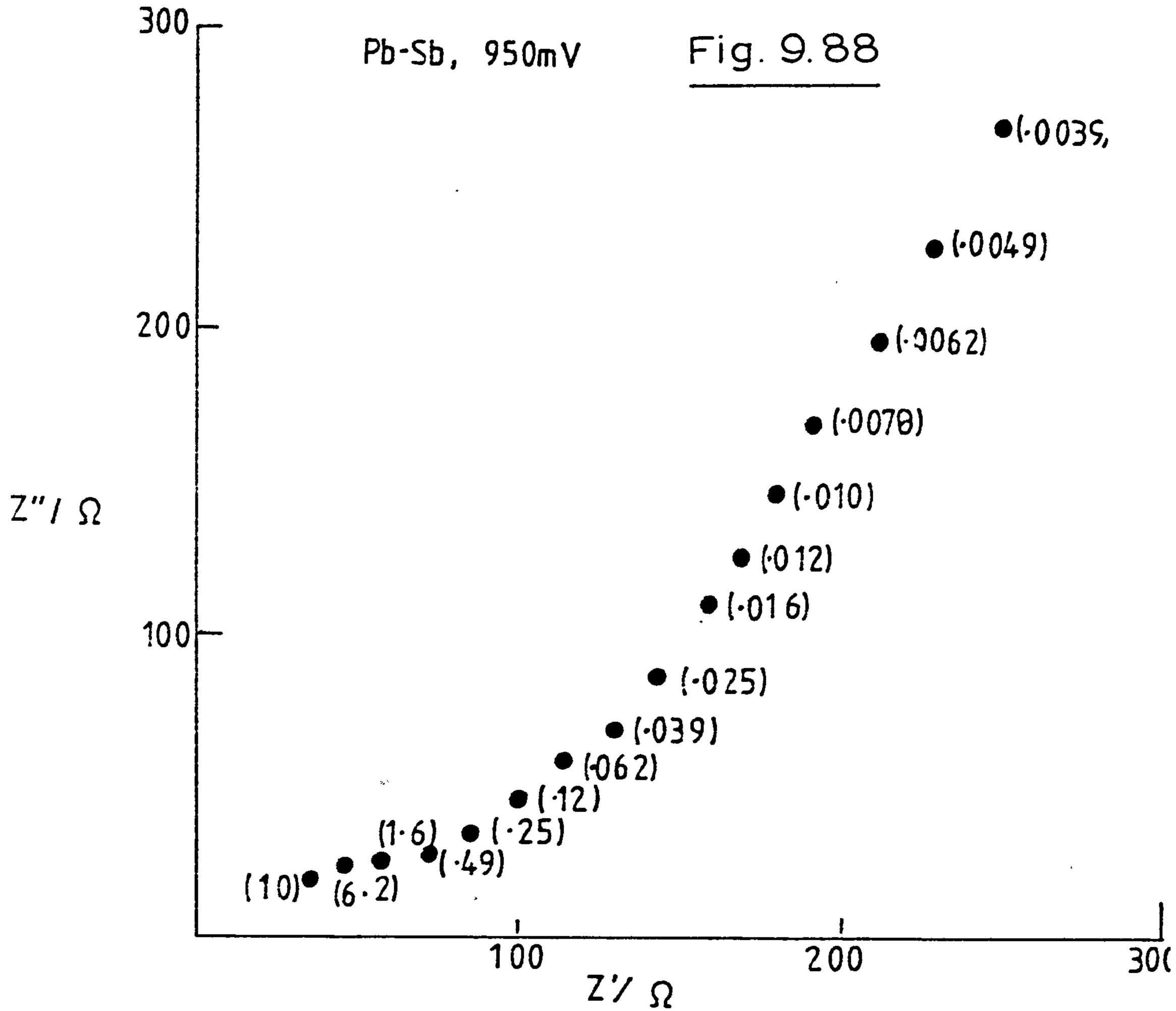

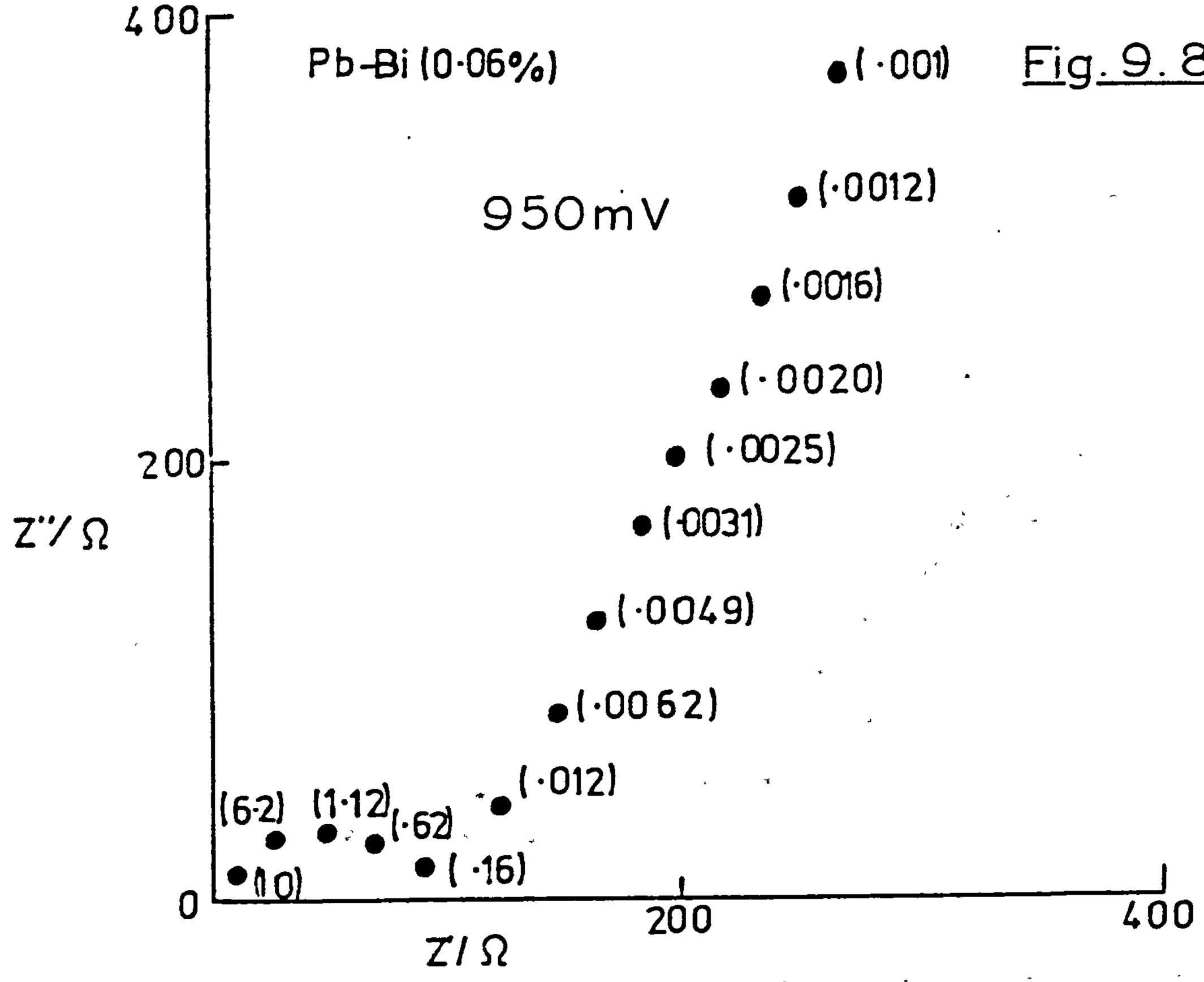
400
200
0
Z''/ Ω
Z'/ Ω
200
400
Pb-Bi (0·06%)
950mV
(·001)
(·0012)
(·0016)
(·0020)
(·0025)
(·0031)
(·0049)
(·0062)
(·012)
(6·2)
(1·12)
(·62)
(·16)
(1·0)

Fig. 9.89

Pb - Bi (0·13%), 950mV

Fig. 9.90

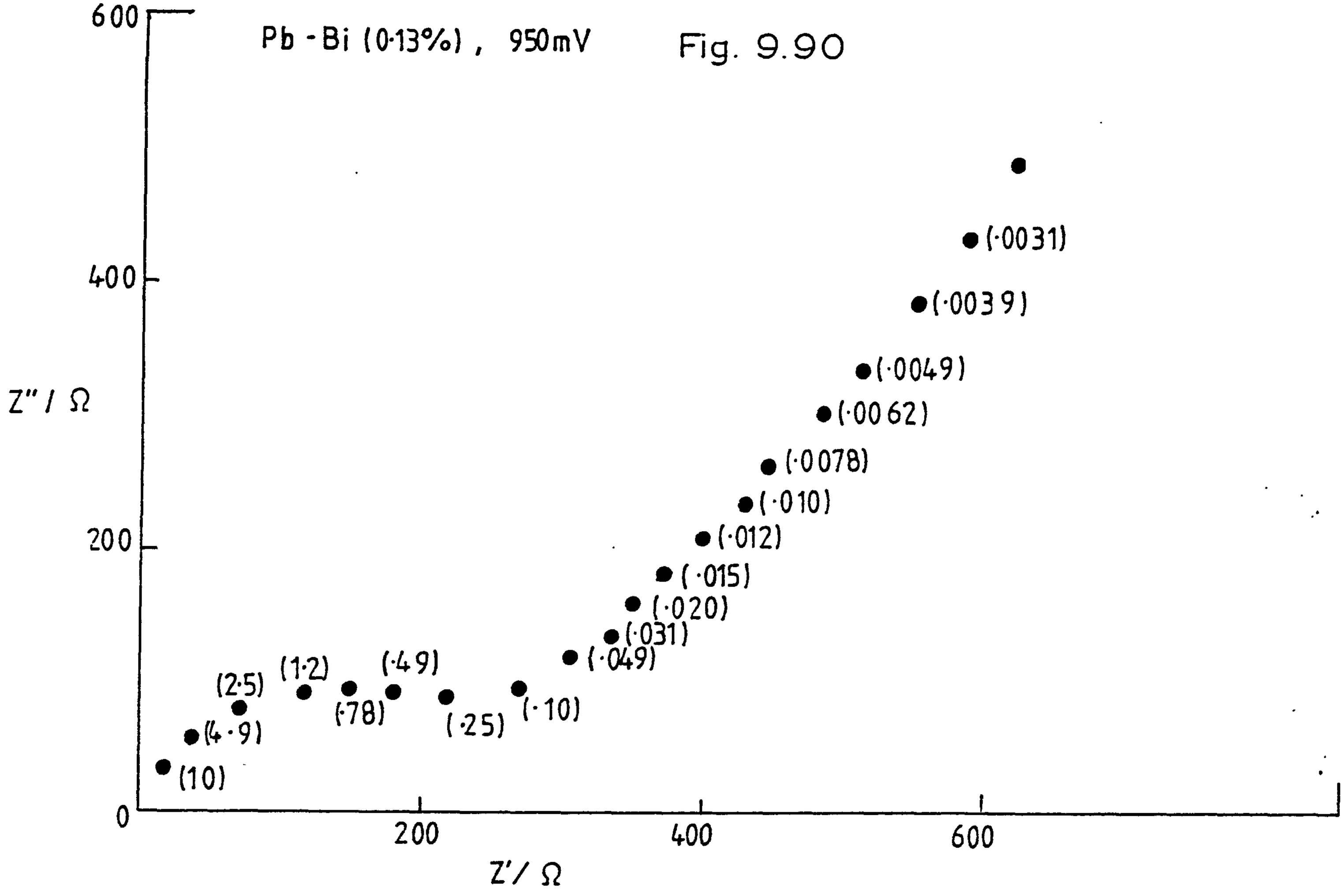

Pb-Bi (0·27%) , 950mV

Fig. 9.91

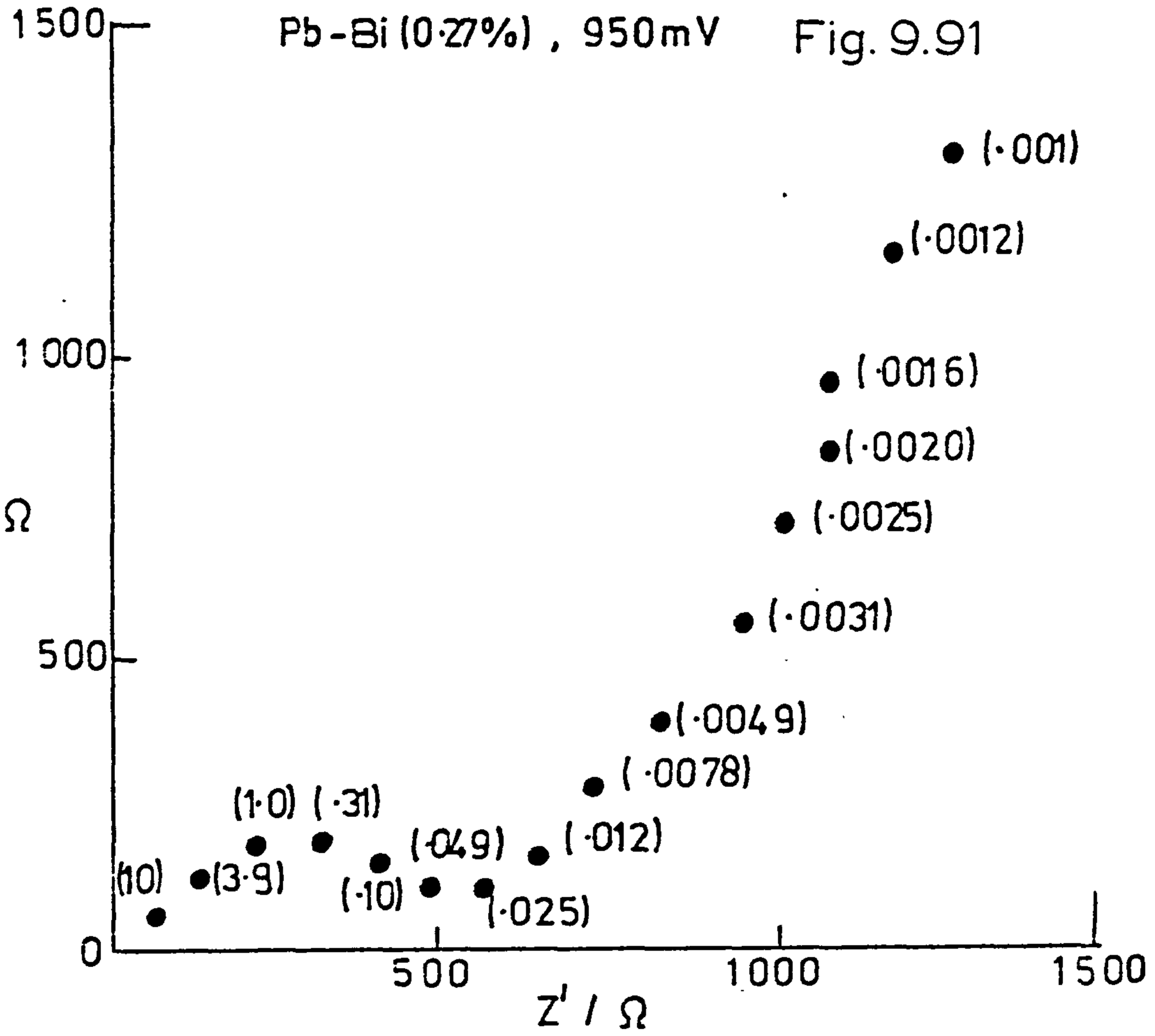

Pb-Ca-Sn, 950mV

Fig. 9.92

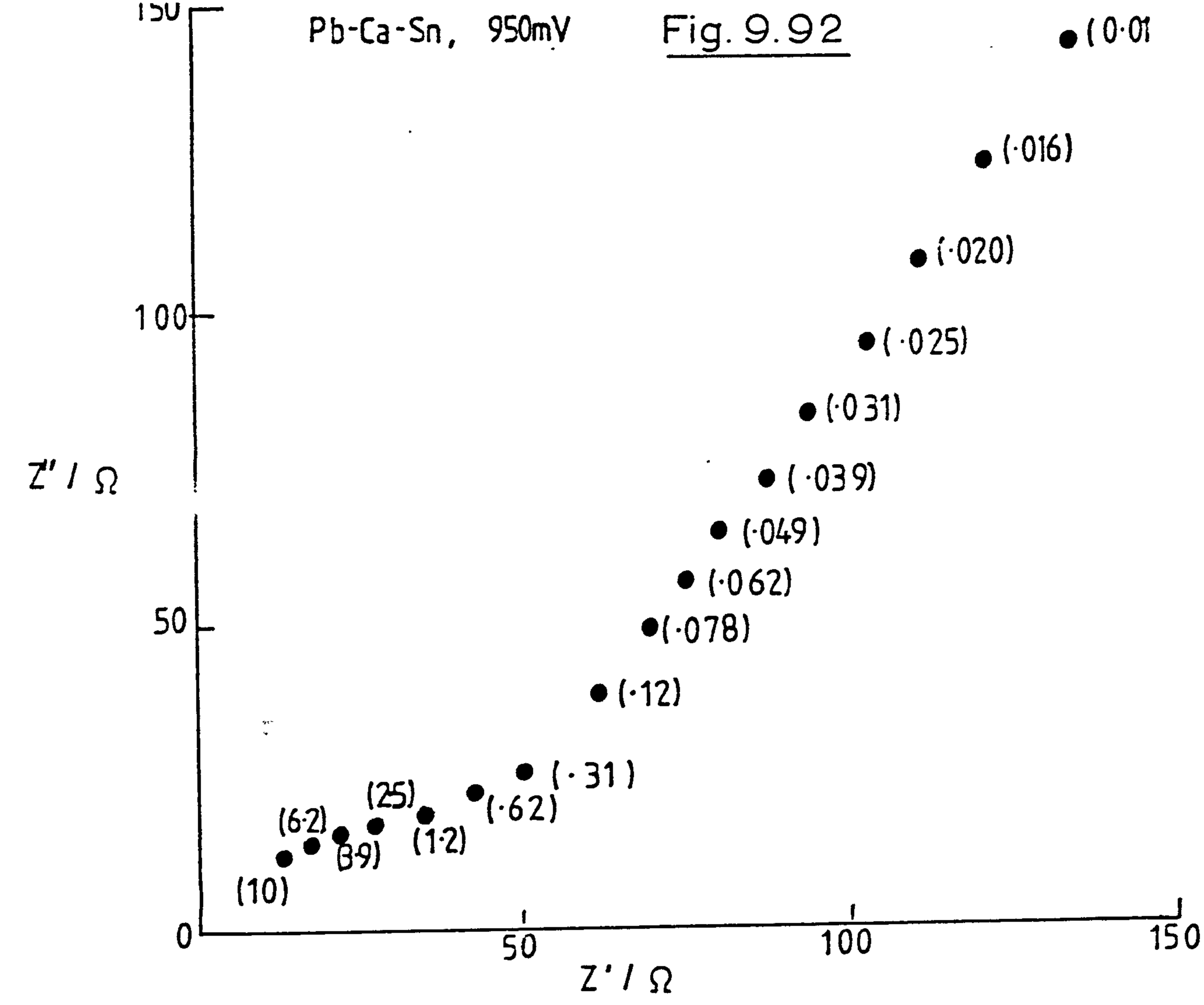

Pb-Ca-Sn-Bi(0·15%), 950 mV

Fig. 9.93

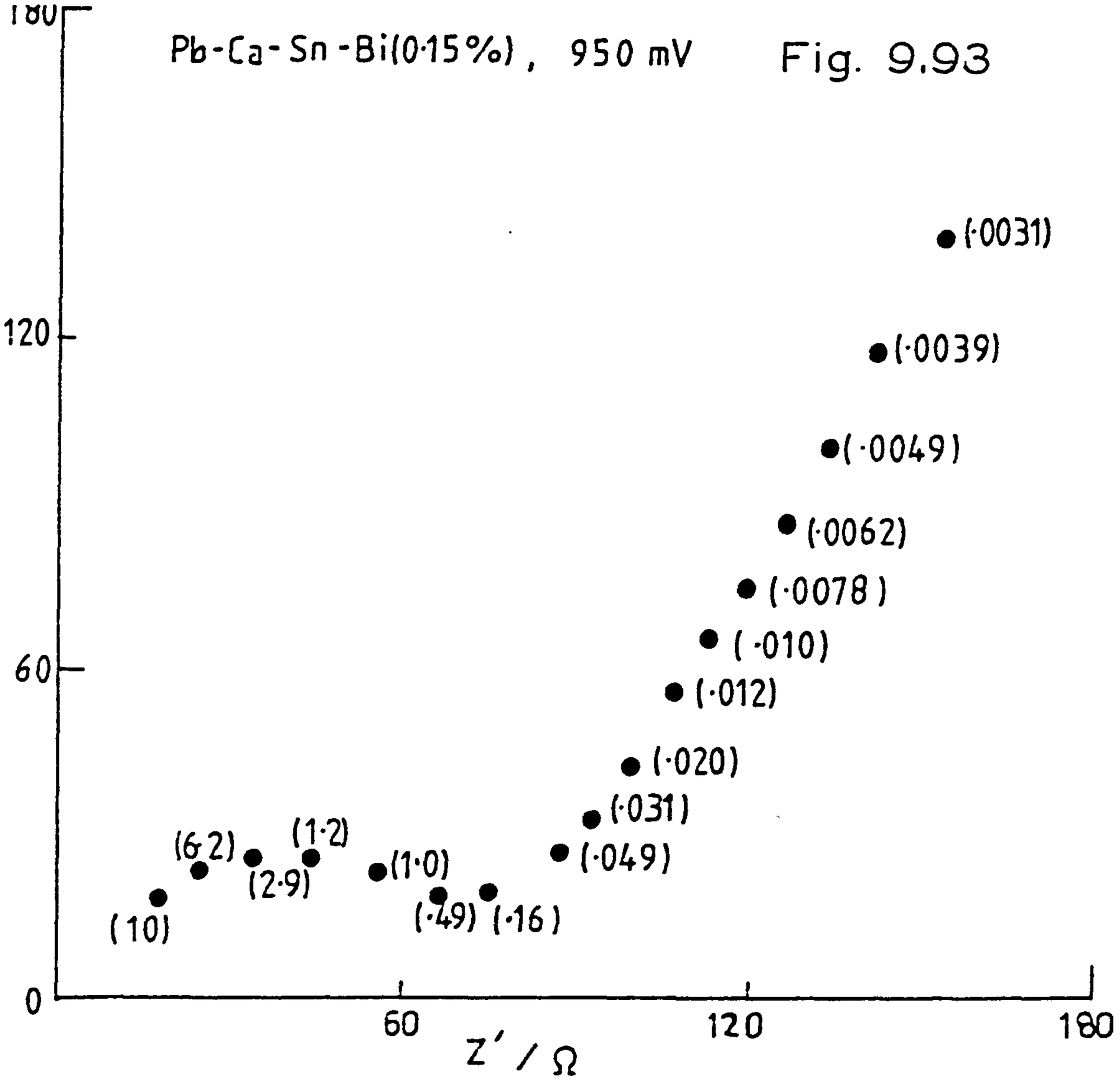

It is clear the effect of the alloying ingredients on the pure lead is to modify all the characteristics of the electrode analogue. Antimony, which may be taken as the optimum alloying ingredient for a pasted plate, has a very marked effect on all the component magnitudes. At all potentials the effective charge-transfer resistances are lower, the double layer capacitance increased, the capacitances of the electrode sulphate layer are very much reduced although similar values of the sulphate film resistance are observed. These observations point to a thicker electrode film produced on the antimonial lead than the antimony free lead. However, the values of the effective Warburg coefficients indicate an effectively larger area available for diffusion in the case of the antimony alloy. These are remarkable and interesting findings for usually a thicker film ingenders better coverage, a higher R_{CT} and a higher σ value. It must be concluded from this that although the film on antimonial lead is thicker than that on pure lead it is more porous and perforated and that even though the charge transfer reaction is able therefore to occur relatively readily, diffusion is difficult resulting in a higher σ value.

Of the few alloys investigated the alloy which produces an effect most like that of Pb/Sb is that produced by the addition of a small amount of bismuth to the Pb/Ca/Sn alloy although the effective film resistance is considerably lower than either the lead or the antimonial lead alloy. This observation strengthens our idea that Bi in the alloy produces a resulting sulphate film which has improved conductivity probably due to the imparting of semiconductor properties by a doping process.

It was shown in Chapter 5 that of the three Bi/Pb alloys investigated the 0.13% Bi alloy represents the best for battery behaviour. This fact is again indicated here for the 0.13% Bi alloy; using the behaviour of the antimonial lead as the optimum this intermediate concentration produced the most antimonial like behaviour.

CONCLUSIONS

1. The appearance of an inductive loop in the impedance loci of PbO_2 layers on Sb/Pb alloy which is absent in the same experimental frequency range with other alloys indicates that the effect of Sb is to produce a more porous deposit.

2. The $PbSO_4$ film on the partially discharged electrode behaves effectively as a capacitor in a series with the faradaic path.

3. The capacitance of the films on Sb alloy is lower than that on other alloys although it is thicker and apparently produces a more restricted diffusional path than other alloys.

4. Bismuth appears to contribute semi-conductor effects to the films developed on the product PbO_2.

9.3 (iii) Measurements at Polarised electrodes below 900 mV

Fig. 9.94 shows the impedance plot for the reduced PbO_2 formed on antimonial Pb at 700 mV to be a distorted semicircle coming off to a rising portion; this is the only system which showed a well-defined high frequency shape. Other systems, for example Fig. 9.95 and 9.96, showed curving high frequency regions but these deteriorated tangentially into rising lines whose dihedral angle generally exceeded 45^{o}. It can be concluded that whereas the film on the other alloys at 700 mV form fairly passive layers that on antimonial lead is not.

Pb-Sb, 700 mV

Fig. 9.94

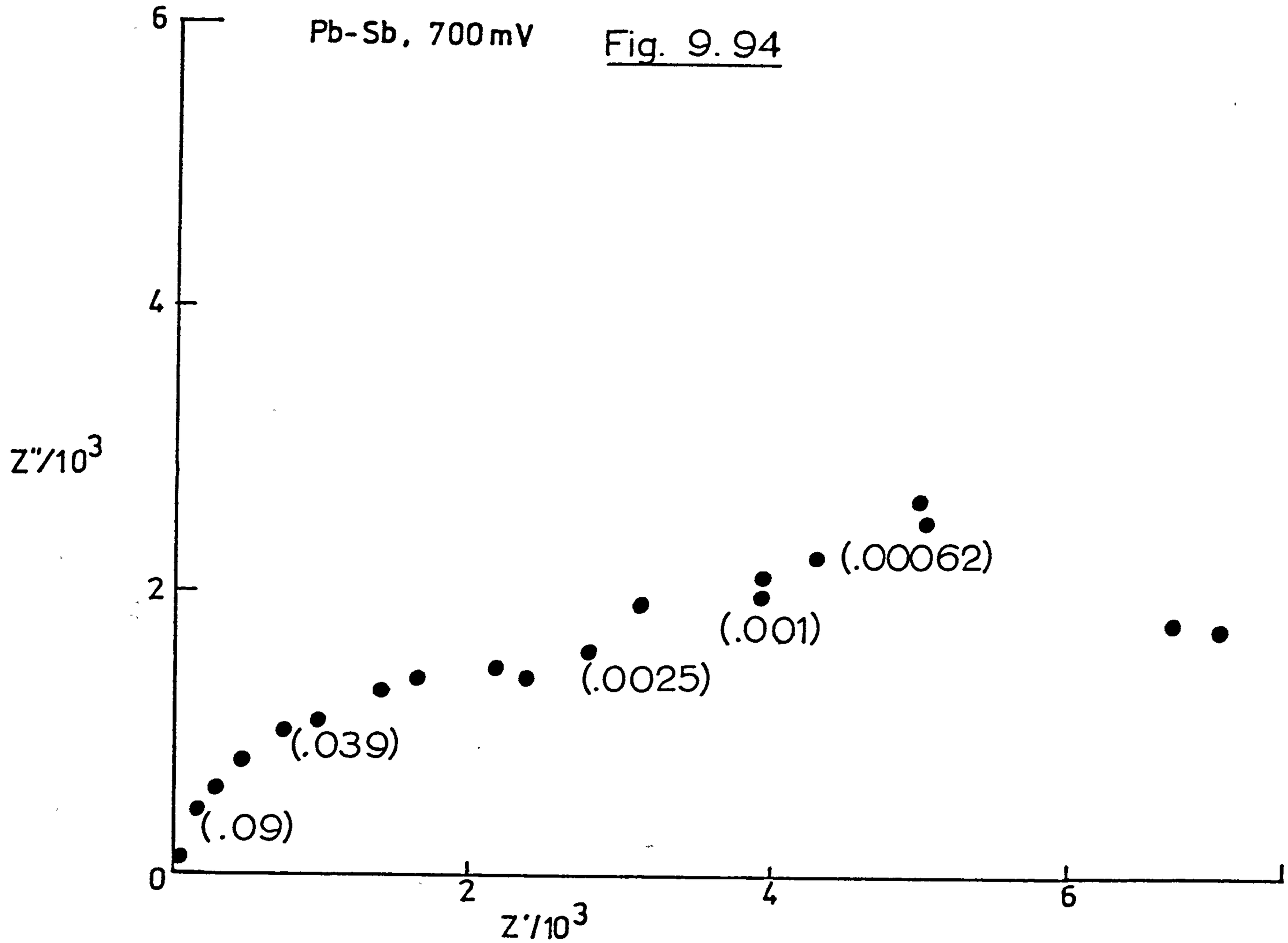

Pb, 700 mV

Fig. 9.95

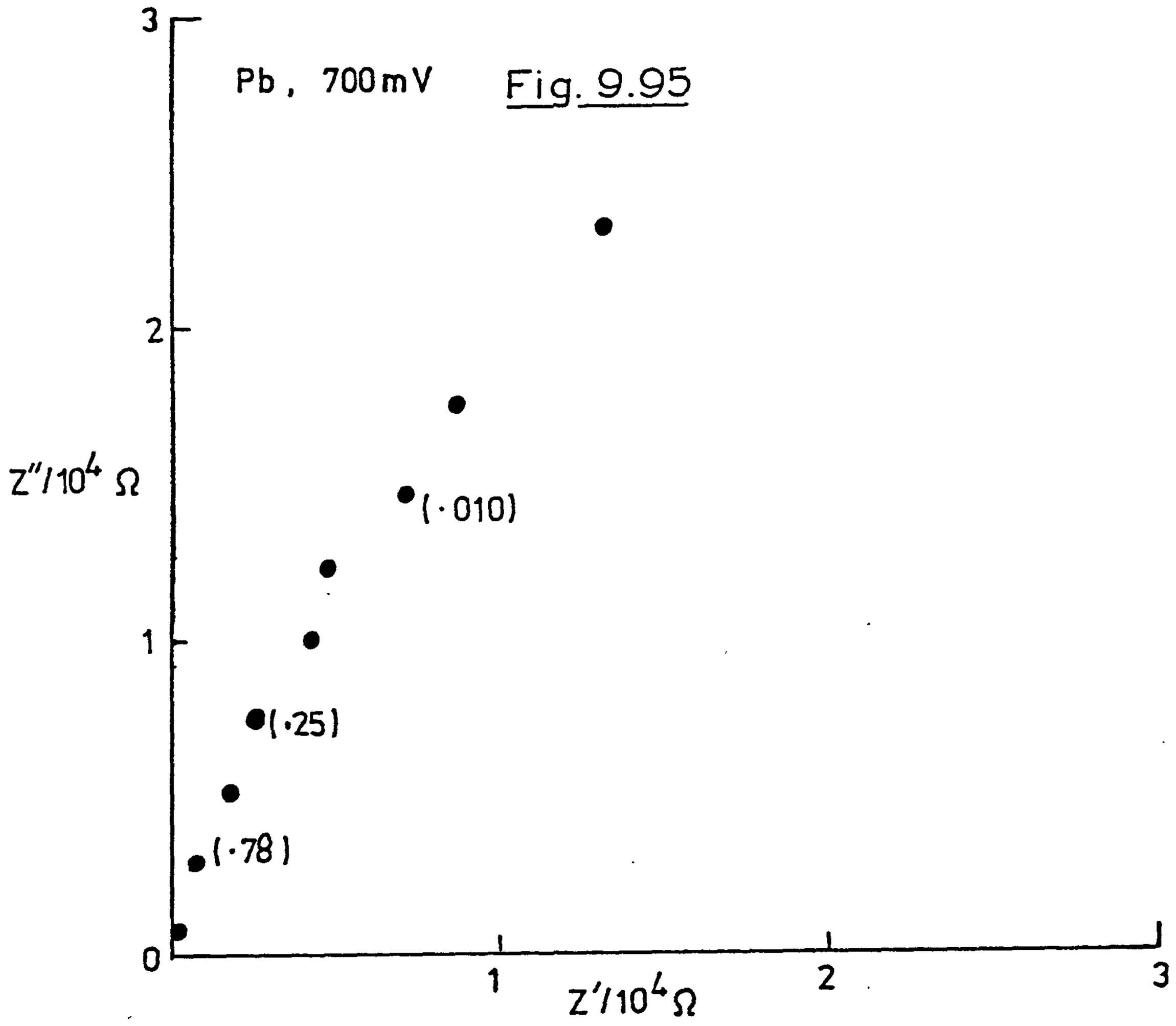

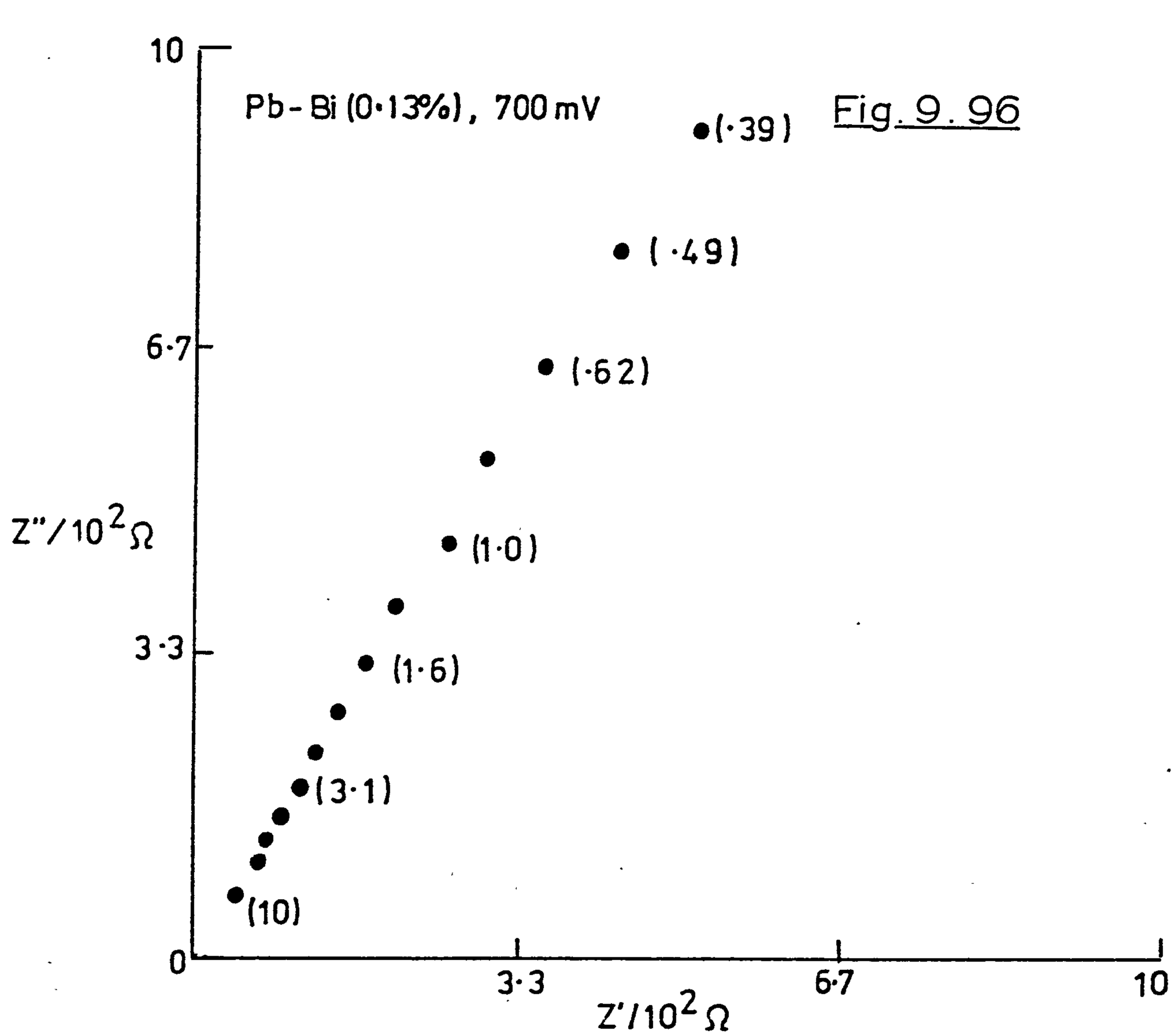

Fig. 9.96

Fig. 9.97 shows that at 400 mV the impedance spectra of the Pb-Sb alloy is a rising line which shows some curvature; this is typical of all the alloys and the most curvature is again observed with the antimonial alloy.

At 0.0 mV the impedance spectra for all alloys are lines, Figs. 9.98 and 9.99, with concavity towards the real axis at the higher frequencies degenerating into a straight line at lower frequency whose slope exceeds 45^{o}. This behaviour indicates that the electrode is passive and relatively polarisable being covered with a layer of $PbSO_4$ which seals off the surface almost completely.

When the electrode is fully reduced the impedance plots are as shown in Figures 9.100-9.103. Here the high frequency semicircle is well defined and comes away from the real axis at the highest frequency at $\sim 90^{o}$ as expected by theory[132]. As the frequency is reduced the complex plane plot begins to be an elongated semicircle, the tail coming away from the resistance axis at approximately 22.5^{o} as required for a porous electrode. In certain alloys (e.g. Bi 0.26%, Pb 99.74%) this was very well developed, however, with pure lead this region was not really observed in the experimental frequency range. The high frequency part moreover rises at 45^{o} from the real axis. This shape can be transformed to the simple charge transfer and diffusion model behaviour by squaring[133]. Furthermore, the Randles Plots for these curves when treated in this manner behave similarly to those already discussed i.e. show the correct variation with frequency. We can conclude from this that the porous nature of the product lead is sufficiently well-developed to cause the electrode to behave

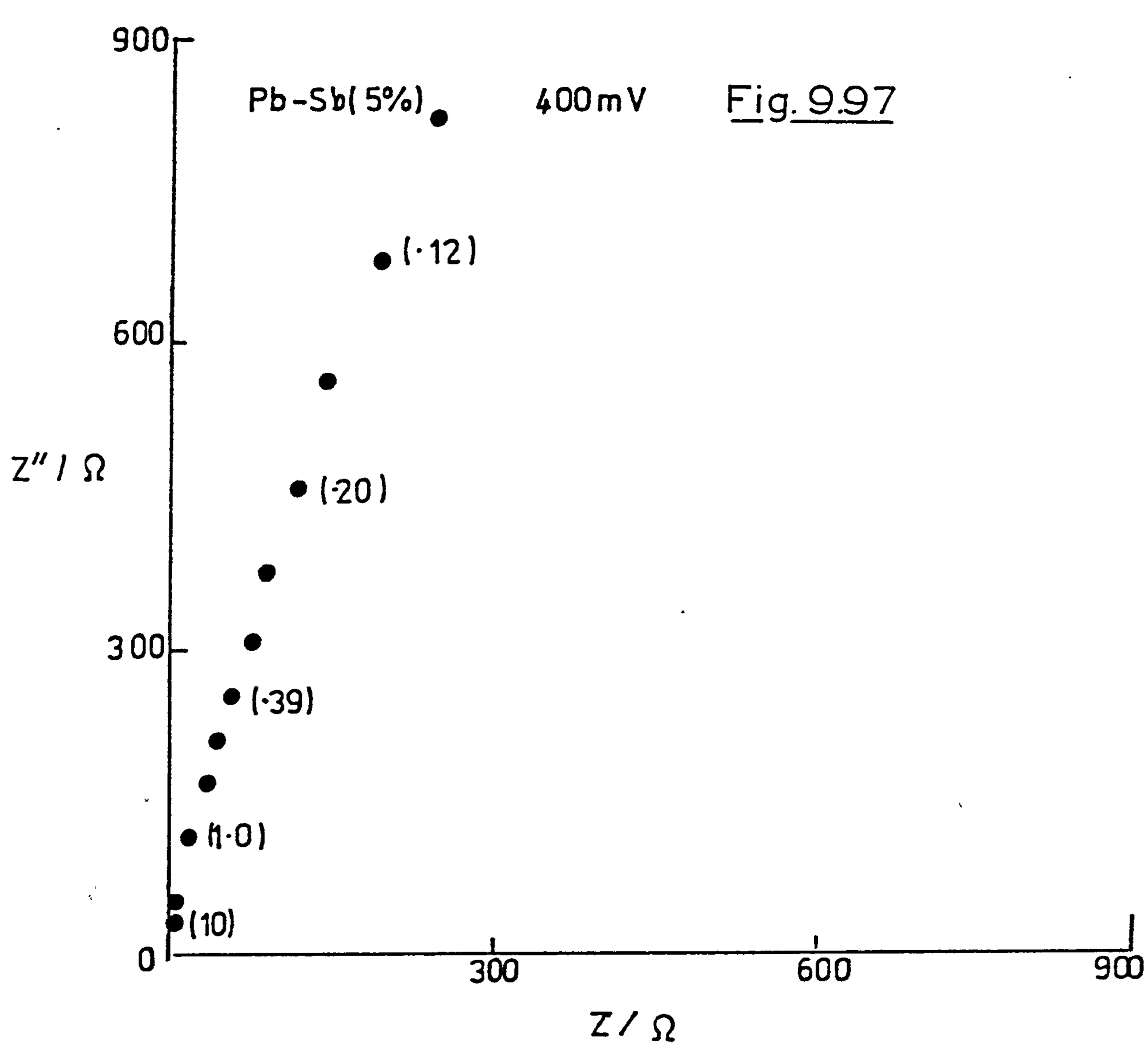

Fig. 9.97

Pb , 0·0 mV

Fig. 9.98

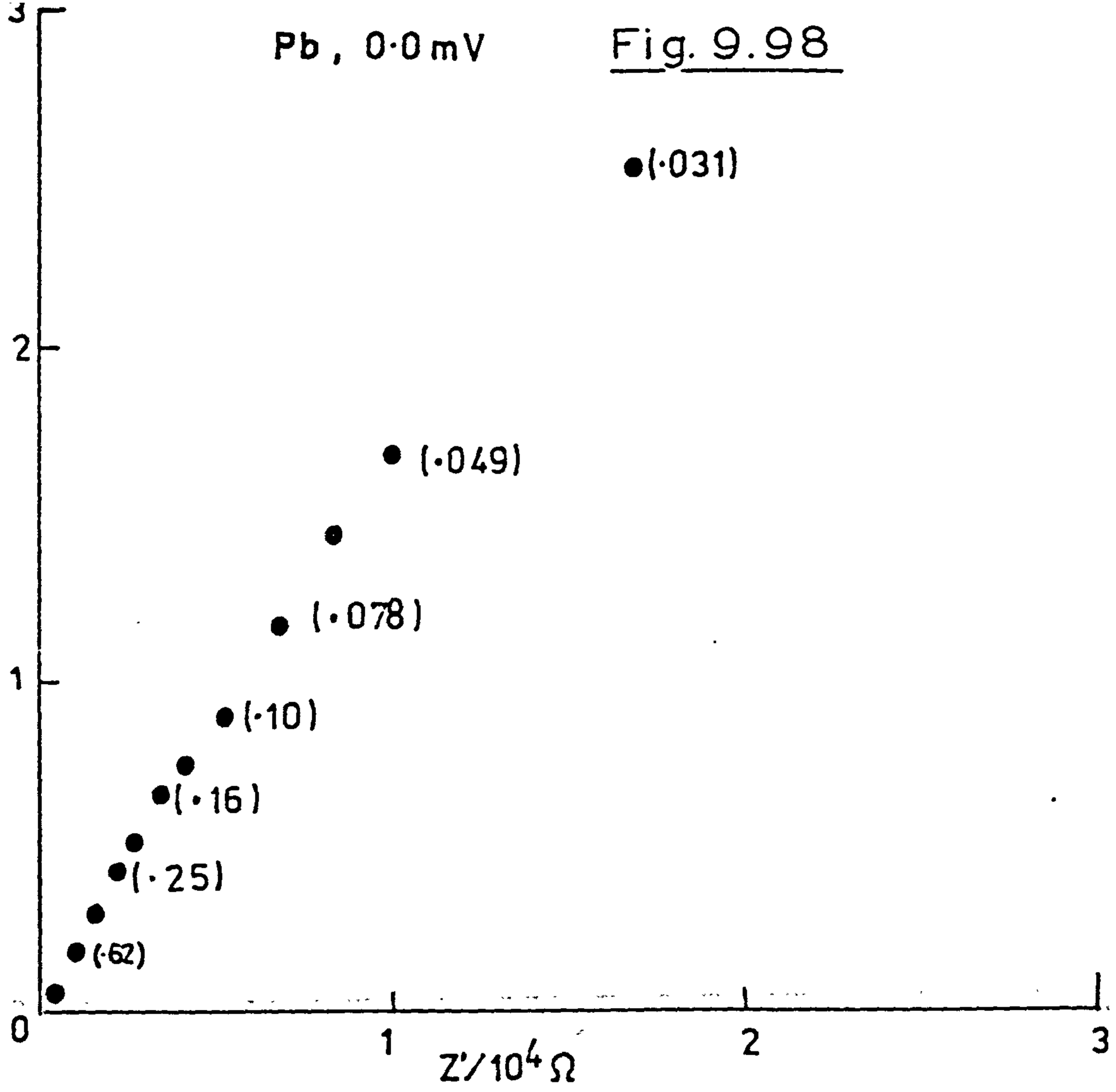

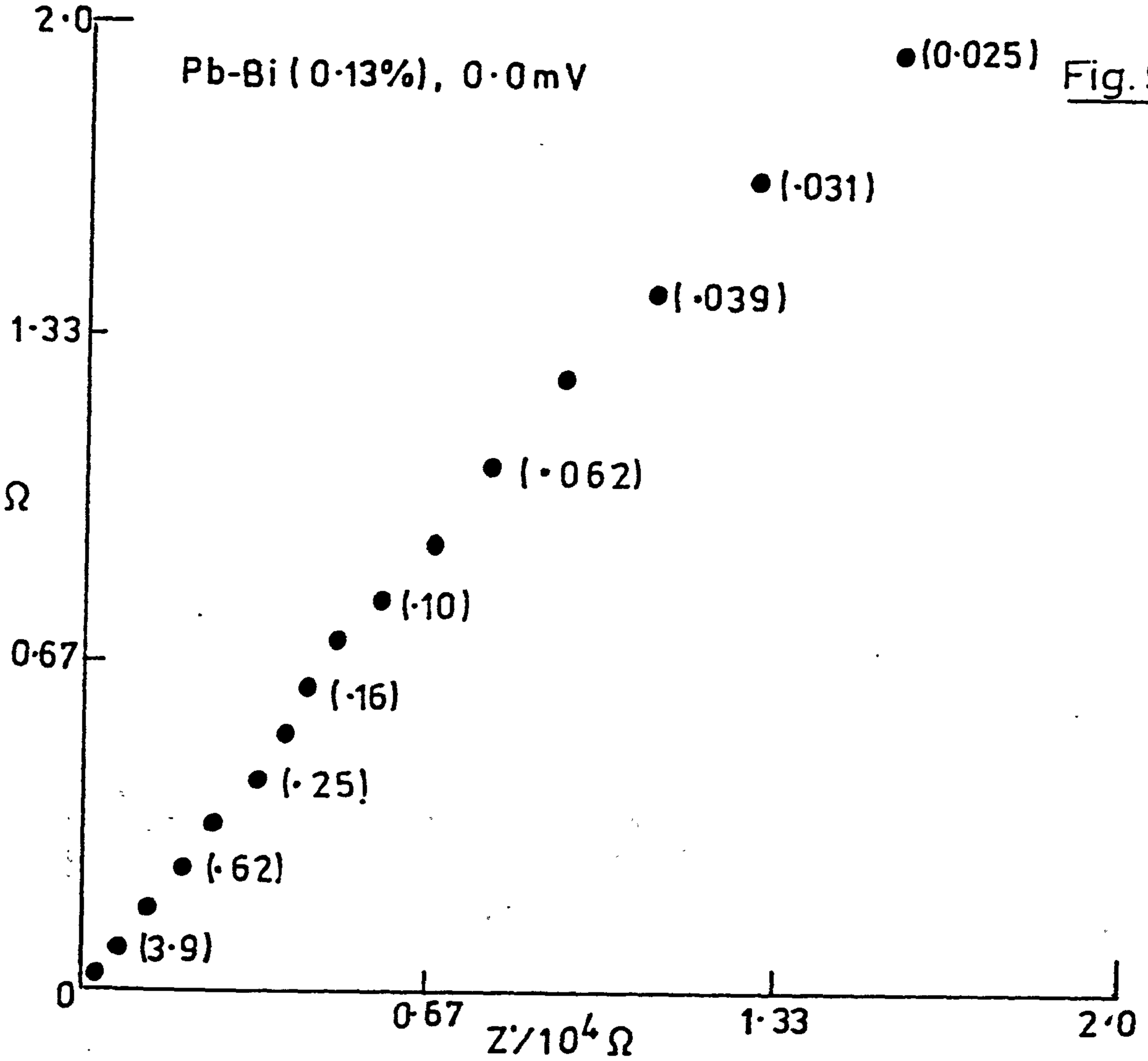
Pb-Bi (0·13%), 0·0 mV
(0·025)
(·031)
(·039)
(·062)
(·10)
(·16)
(·25)
(·62)
(3·9)
2·0
1·33
0·67
0
Z'/10⁴ Ω
0·67
1·33
2·0
Z'/10⁴ Ω

Fig. 9.99

Pure Pb, -970mV Fig. 9.100

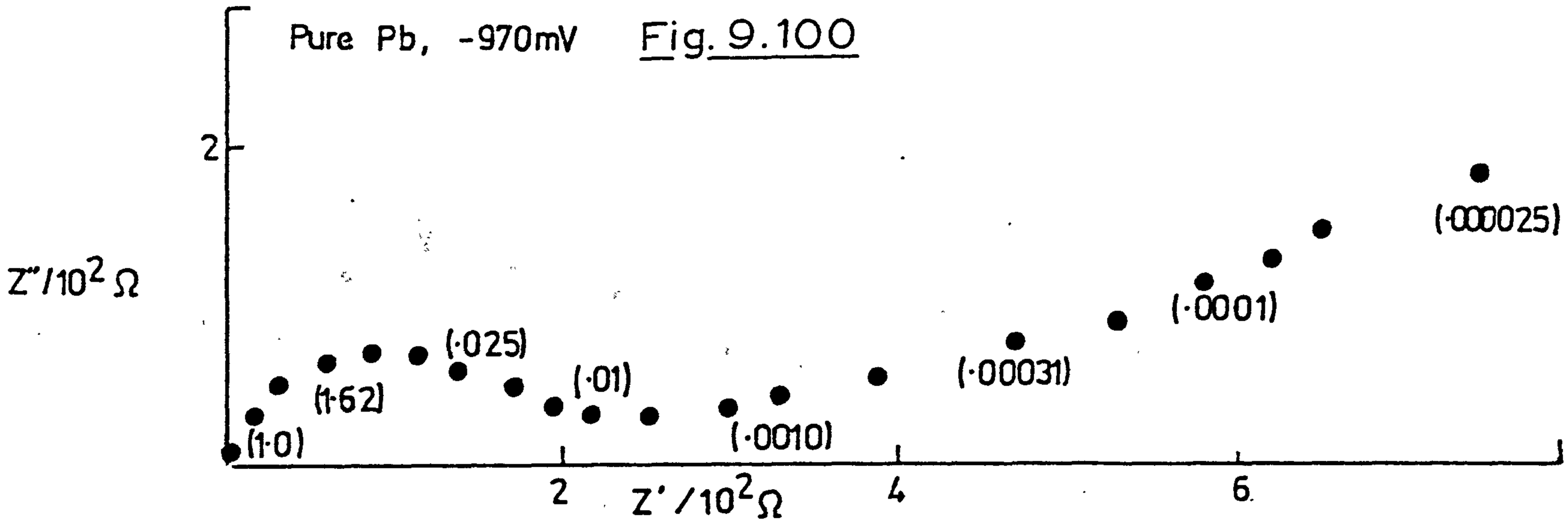

Pb-Sb, -970 mV Fig. 9.101

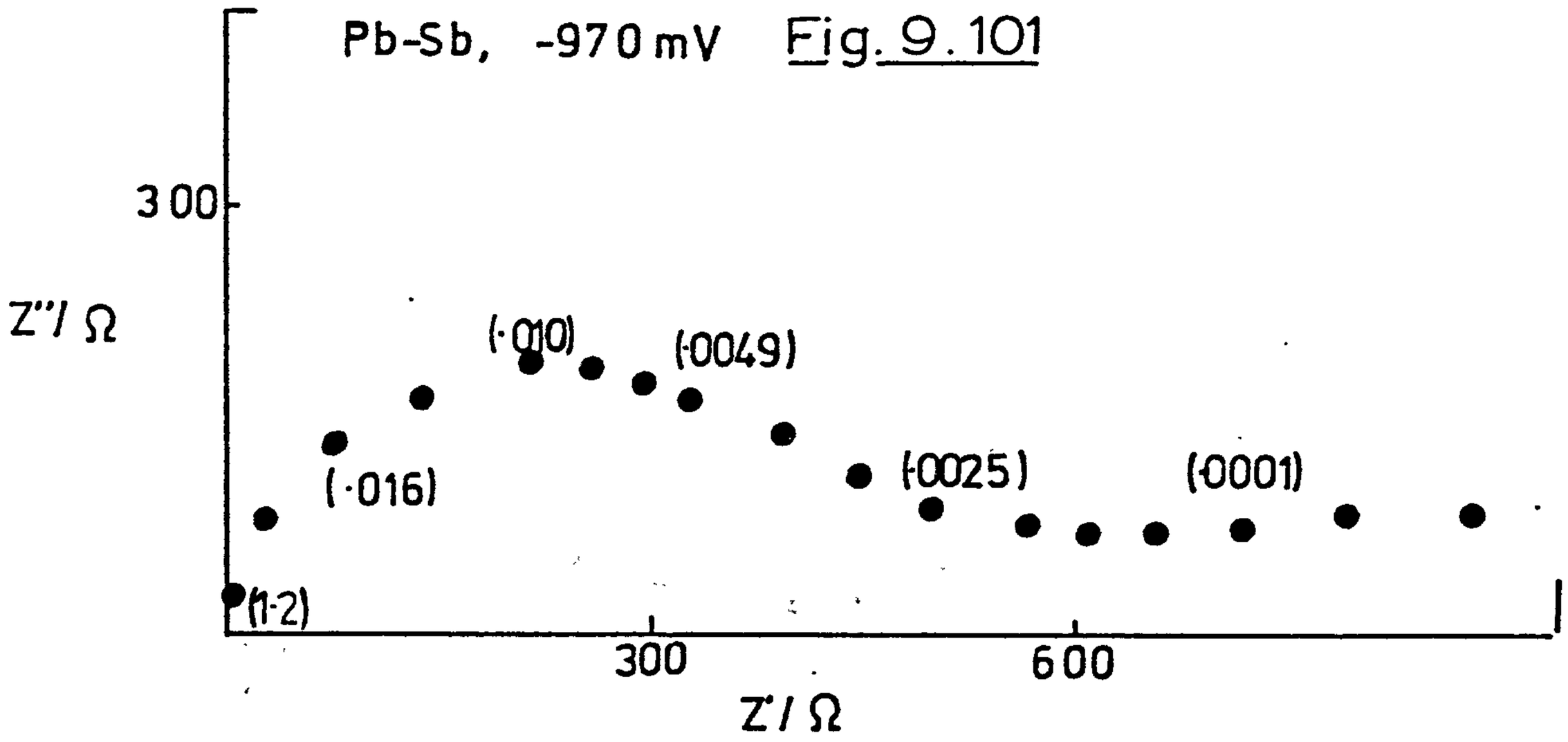

Pb-Bi (0·26%) , -970 mV

Fig. 9.102

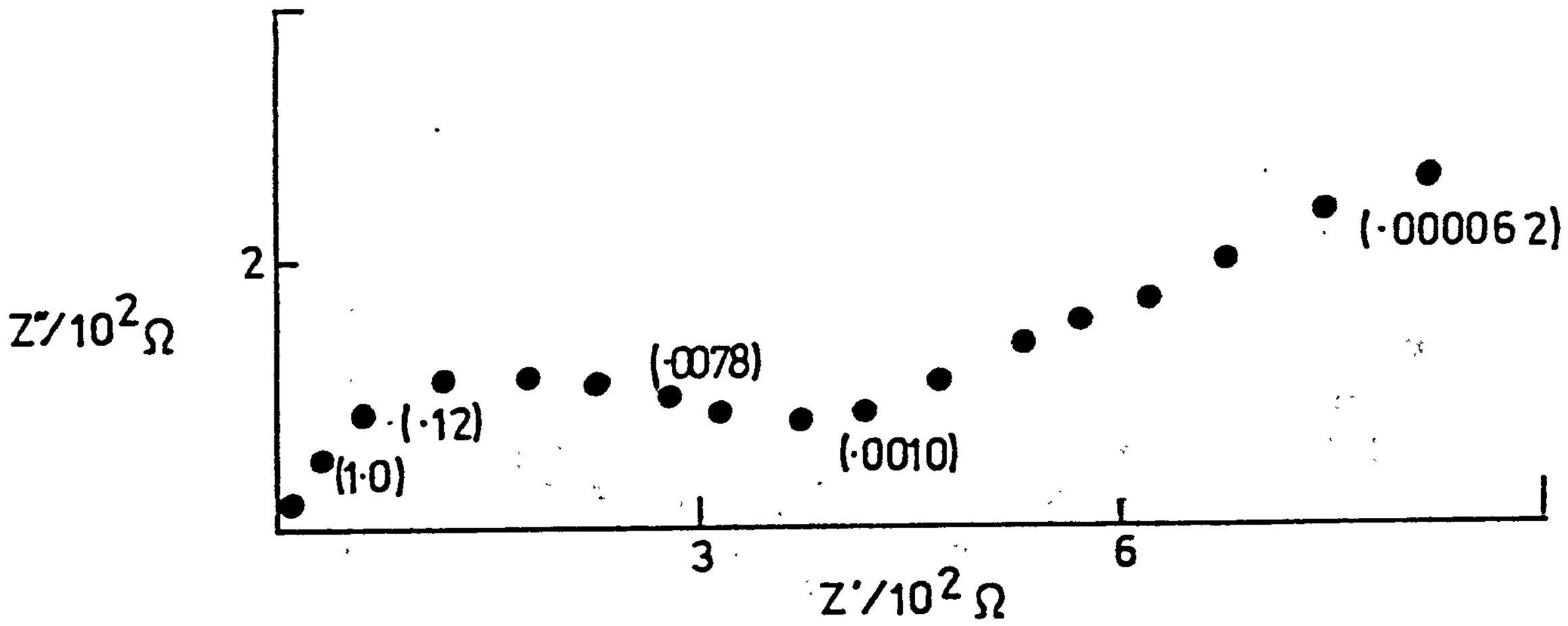

Pb-Ca-Sn-Bi (0·15%). -970 mV

Fig. 9.103

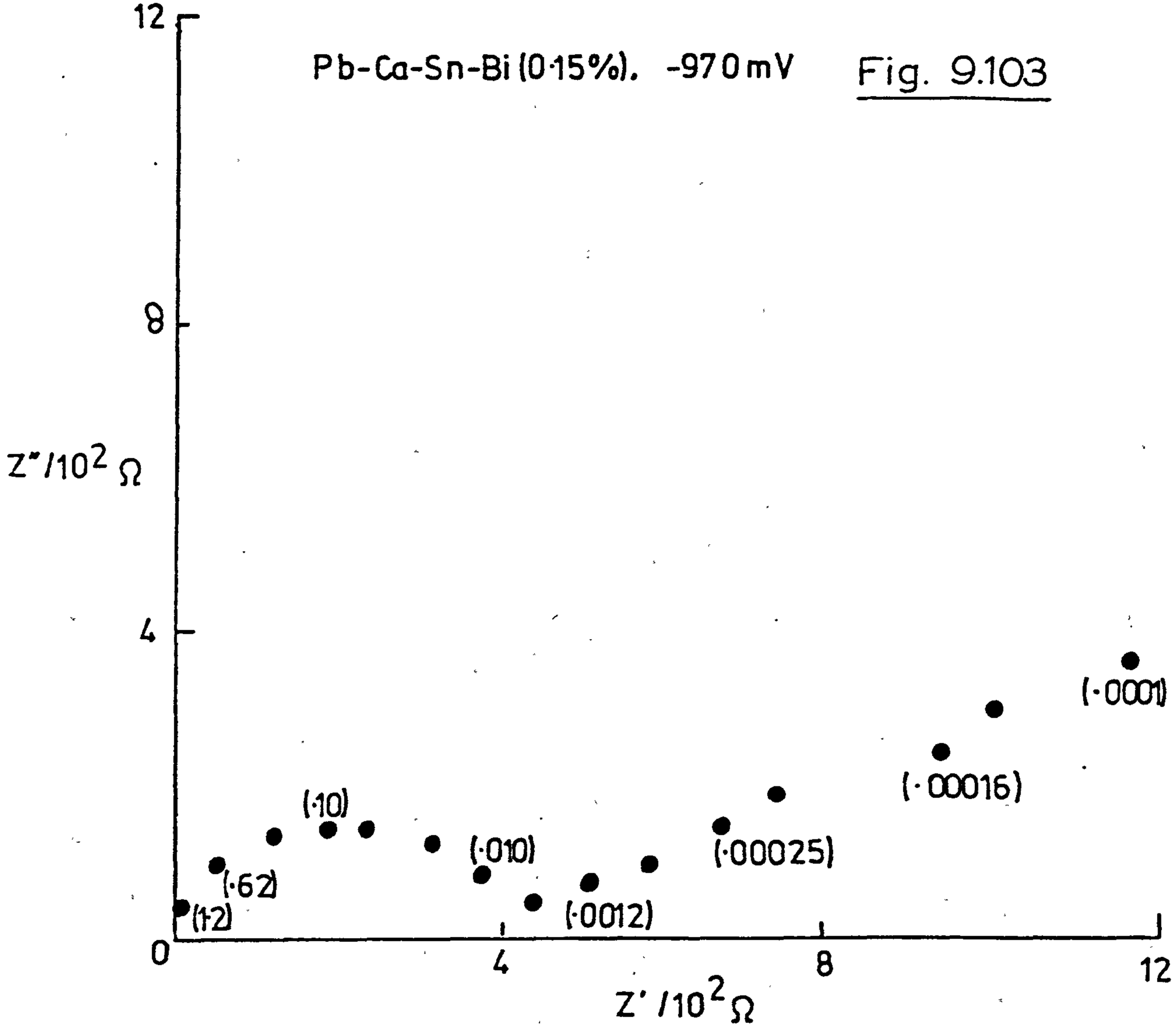

as a porous one at a sufficiently low frequency.

With antimonial lead these features were very obvious and in fact at high frequency a small inductive semicircle indicates that porosity is sufficiently well defined to cause a phase delay due to the porous structure of the electrode. These features were absent in all the other cases except the antimonial alloy.

These results indicate that the nominally porous lead dioxide electrode for which porosity in the sense of de Levie[65] is absent becomes effectively porous in the electrochemical sense when reduced to lead. Thus the 'halving' of the time dependencies observed by Hampson[134] in the case of porous negative electrodes would be expected to be absent in the case of the similarly porous positive electrode produced electrochemically from similar starting materials.

The reason for this lies in the high conductivity and high exchange current for lead in sulphuric acid compared with these same parameters in the case of lead dioxide.

9.3(iv) An alternative model for partially discharged lead-dioxide electrodes

a) Introduction

Using the electrode model as proposed in 9.3(ii) generally gives a satisfactory fit with the experimental data, however, at the most negative potentials the high frequency semicircle was noticeably flattened. This can be considered to be due to surface heterogeniety although an alternative and more likely explanation is that there is a certain

amount of adsorption of reactants and products in the sense of Laitinen and Randles[135]. In the adsorbed state, the electrode reaction

$$PbO_2 + 4H^+ + SO_4^{2-} + 2e \rightleftharpoons PbSO_4 + 2H_2O \qquad (69)$$

occurs giving rise to a further circuit element which shunts the double layer and the reaction. The following experiments describe such a model and the process by which the kinetic parameters were isolated.

b) Experimental

Electrodes were brought to a well defined pre-electrode state by potentiostatting in the region 1100 mV (= E_r) to 930 mV until the current flow fell to zero, this usually took Ca. 1 h. The impedance of the electrodes were than obtained using the automatic technique already described.

c) Results and Discussion

The impedance (Sluyters) plot for the electrode in the potential range of 930 mV consists of a distorted circular shape at high frequencies which goes off into a line at low frequency with an ever increasing slope. The impedance plot for a system under charge-transfer and diffusional control would be expected to be a semicircle going-off into a line with a dihedral angle of 45° at low frequency. The degeneration into a line of dihedral greater than 45° can be explained if the product lead sulphate formed by the potential excursion from E_r to 930 mV is considered to behave as a capacitance in series with the reaction, the resistance of this lead sulphate film simply adding into the so-called solution resistance as shown in Fig. 9.85. The impedance diagram for this model would not give rise to a flattened semicircle

at high frequency but to a perfectly circular shape. The flattening of high frequency semicircles has been discussed in terms of electrode heterogeniety and this is undoubtedly the case in many situations where adsorption does not seem likely. In the present case,however, adsorption of sulphate is probable[130] and since the product and reactants are both insoluble it is to be expected that a parallel reaction in the adsorbed state in the sense of Laitinen and Randles[136] would also be present at the electrode, i.e.

$$PbO_2(s) + HSO_4^- (ads) + 3H^+(ads) + 2e \rightleftharpoons 2H_2O + PbSO_4(s) \quad (70)$$

In addition to the process of Fig. 9.85 the electrode analogue would be as shown in Fig. 9.104.

Experimental data was tested for this behaviour by writing the equations for the real and imaginary parts of the analogue impedance and matching the calculated response to the experimental points. The in-phase (R) and out-of-phase ($1/\omega C$) components of the electrode impedance (Z) are derived from the vector equation for Z' the impedance of the parallel branches of Fig. 9.104,

$$\frac{1}{Z'} = j\omega C_L + \frac{1}{Ry + 1/j\omega C_Y} + \frac{1}{\theta + \sigma\omega^{-1/2} - j\sigma\omega^{-1/2}} \quad (71)$$

together with its two series components

$$Z = Z' + {}^1/_{j\omega C_X} + R_\Omega \quad (72)$$

By separating out the real and imaginary parts we find

$$R = R_\Omega + \frac{A + R_Y C_Y \omega^2 (A + A R_Y + \sigma^2 \omega^{-1})}{D} \quad (73)$$

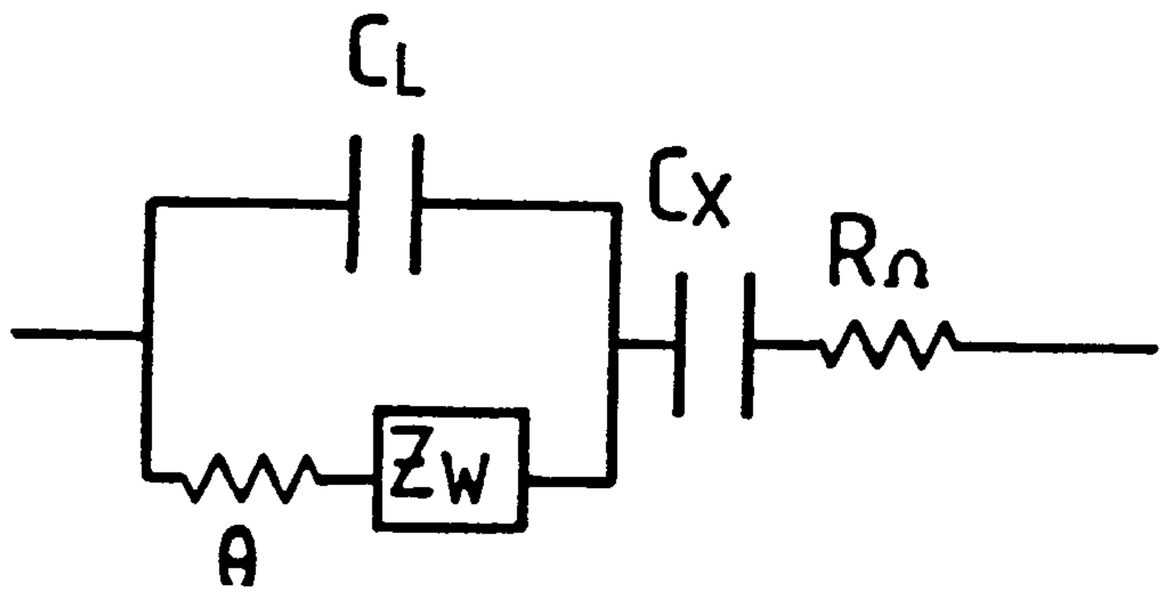

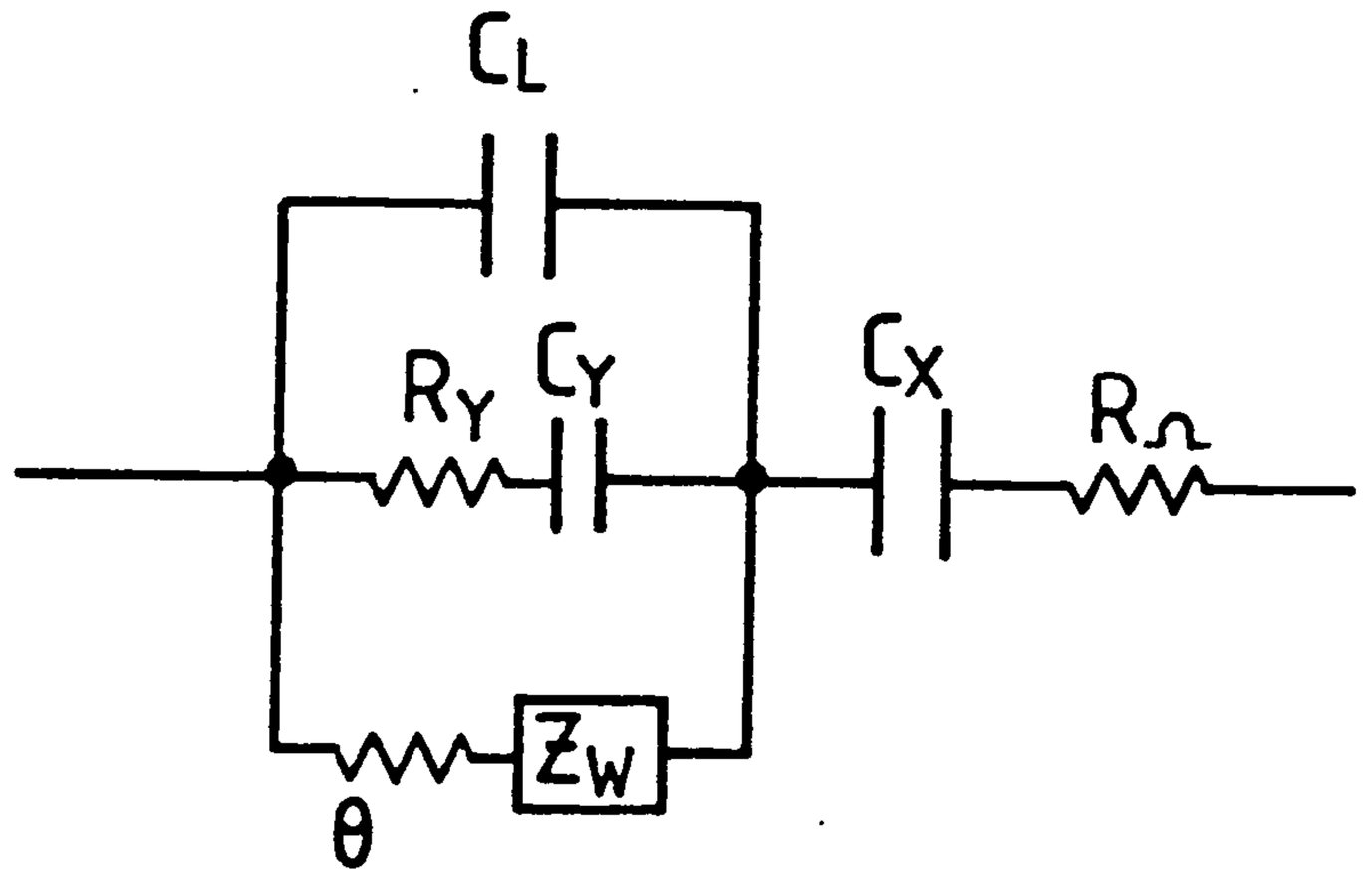

Fig. 9.104

$$\frac{1}{\omega C} = \frac{1}{\omega C_X} + \frac{A^2\left[R_Y^2 . C_Y^2\ \omega^3 C_L + \omega(C_L + C_Y)\right] \quad + B\sigma\omega^{-\frac{1}{2}}\,(1 + (R_Y C_Y \omega)^2 + C_Y \sigma^2)}{D} \tag{74}$$

where $A = \theta + \sigma\omega^{-\frac{1}{2}}$ (75)

$$B = 1 + C_L \sigma \omega^{\frac{1}{2}} \tag{76}$$

$$D = \left[1 + (C_Y + C_L)\sigma\omega^{\frac{1}{2}} - \omega^2 C_L R_Y C_Y A\right] + \left[(C_Y + C_L)\,\omega A + \omega R_Y C_Y B\right]^2 \tag{77}$$

The matching procedure was completed by expanding each of the impedance components about the approximate values using Taylor's theorem and neglecting second and higher orders. The values of the impedance components are then calculated using approximate values for the circuit elements for each of the data points available. A least squares process is used to reduce these equations to the number required to solve for all the circuit elements. The process is repeated until a sufficiently accurate value of each impedance component has been obtained. The calculations were done on the computer (PRIME 400).

Figure 9.105 shows the experimental data compared with the best computer fit corresponding to the model of Fig. 9.85. It is clear from the Figure that although the fit is quite good at low frequency the high frequency semicircle is only matched approximately. The difference although not particularly significant in this case can be in other situations. (The crosses represent the actual experimental data points and the dark lines show the computer fit throughout).

Figure 9.106 shows the correlation of the experimental data to the model shown in Fig. 9.104. Here, the high frequency semicircle is quite considerably elongated but the computed data are a remarkably good fit. Fig. 9.107 shows that a computation similar to the one of Fig. 9.106 but using the capacitance data (out-of-phase component) also provides a good representation. This consistent result is confirmed in Figures 9.108 and 9.109 which show that the R and C data are giving almost identical results. Figure 9.110 shows the data for 950 mV still conforms to the complex model.

It is clear from the Figs. 9.106-9.110 that Fig. 9.104 represents the impedance data to a remarkable degree. This confirms that adsorption at the electrode is significant and must be taken into account. The table given below shows the numerical values obtained from the computations.

$\frac{E}{mV}$	$\frac{C_L}{\mu F}$	$\frac{R_Y}{\Omega}$	$\frac{C_Y}{\mu F}$	$\frac{\theta}{\Omega}$	$\frac{\sigma}{\Omega s^{\frac{1}{2}}}$	$\frac{C_X}{\mu F}$	$\frac{R_\Omega}{\Omega}$
R data							
950	0.431	235	0.210	114	450	-	8.62
940	0.550	774	0.224	168	398	-	30.5
930	0.519	1015	0.232	237	488	-	47.6
C data							
950	0.546	336	0.198	107	448	1696	-
940	0.520	795	0.204	166	404	1750	-
930	0.472	819	0.243	240	445	2320	-

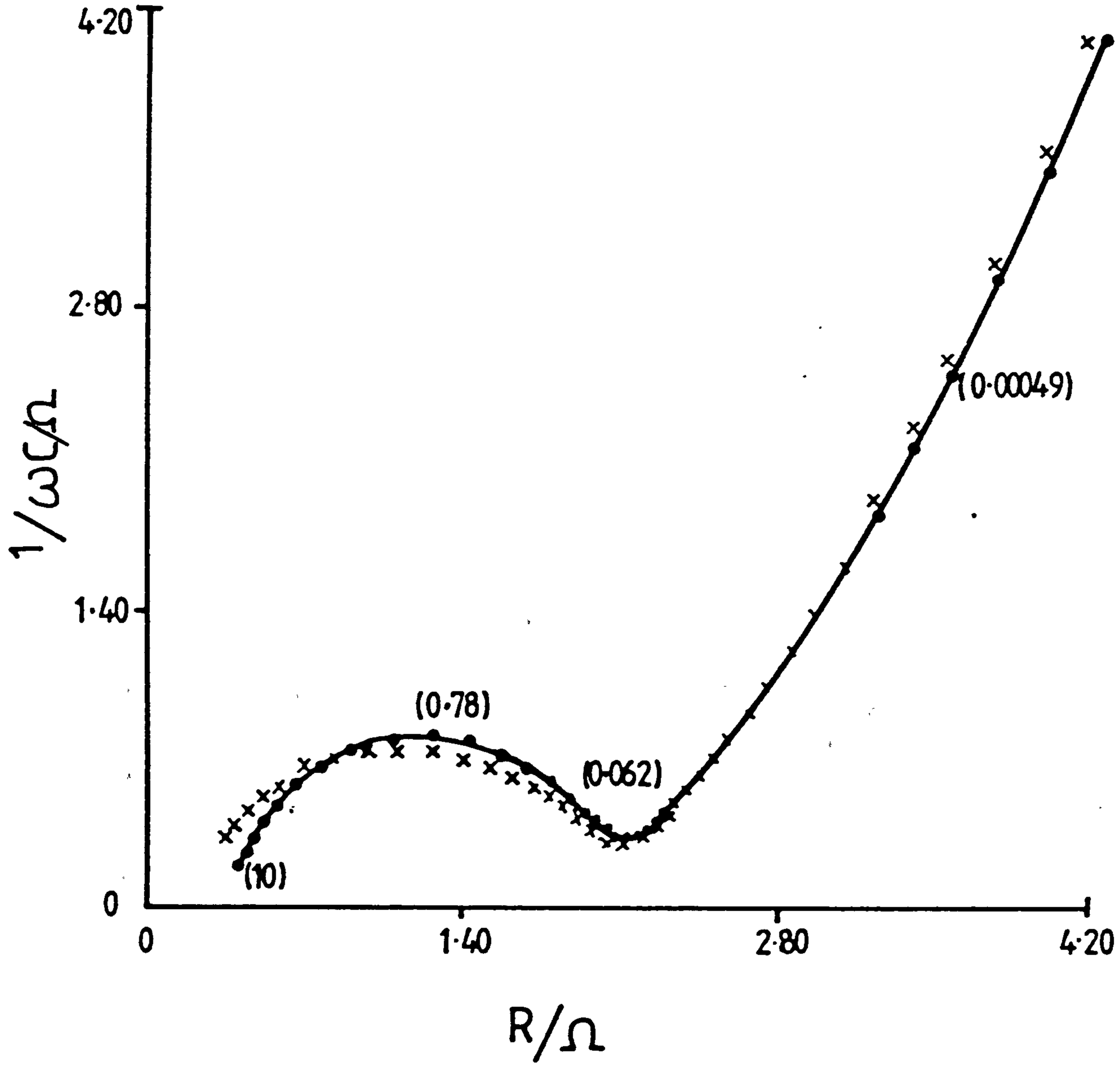

Fig. 9.105

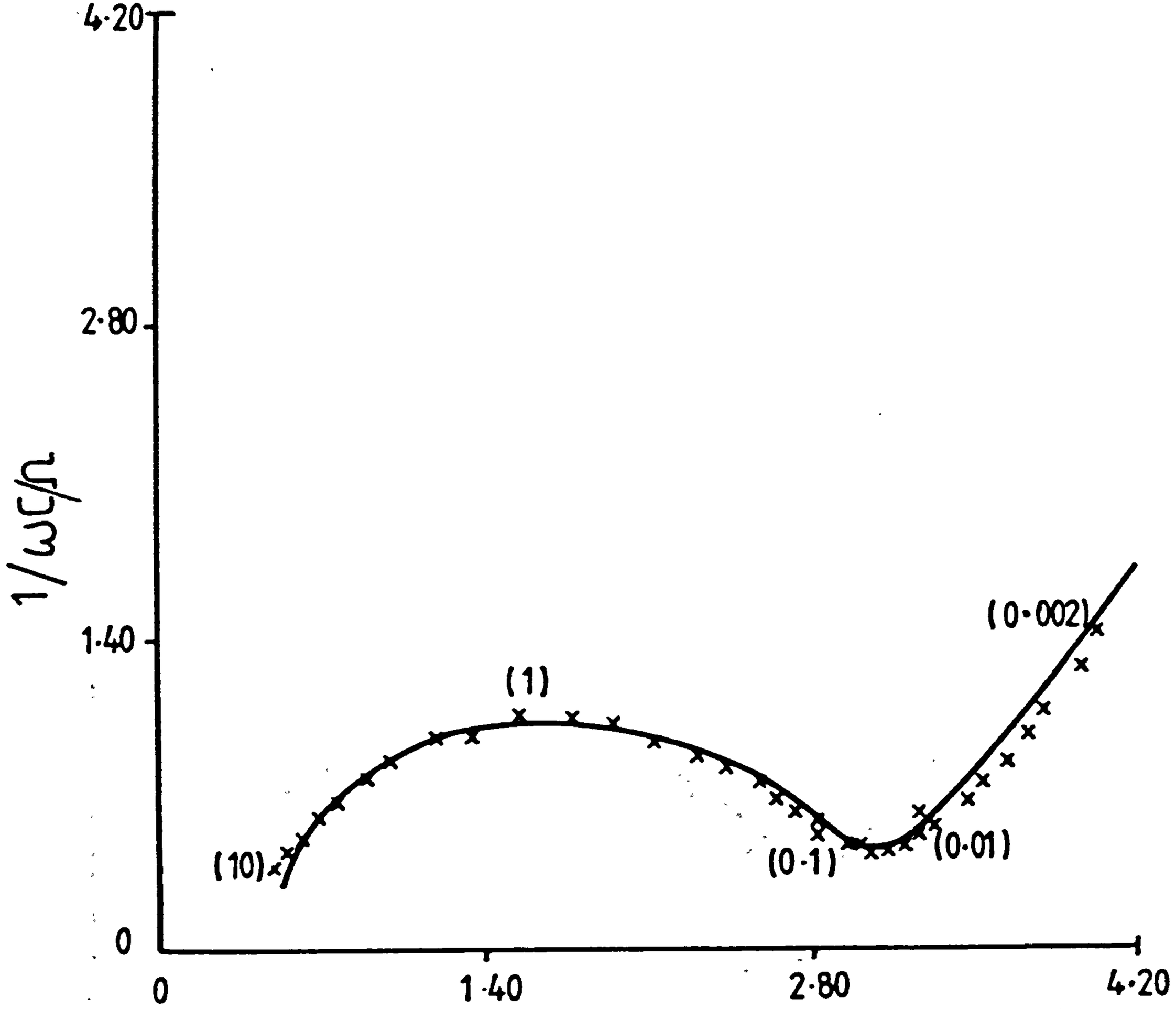

Fig. 9.106

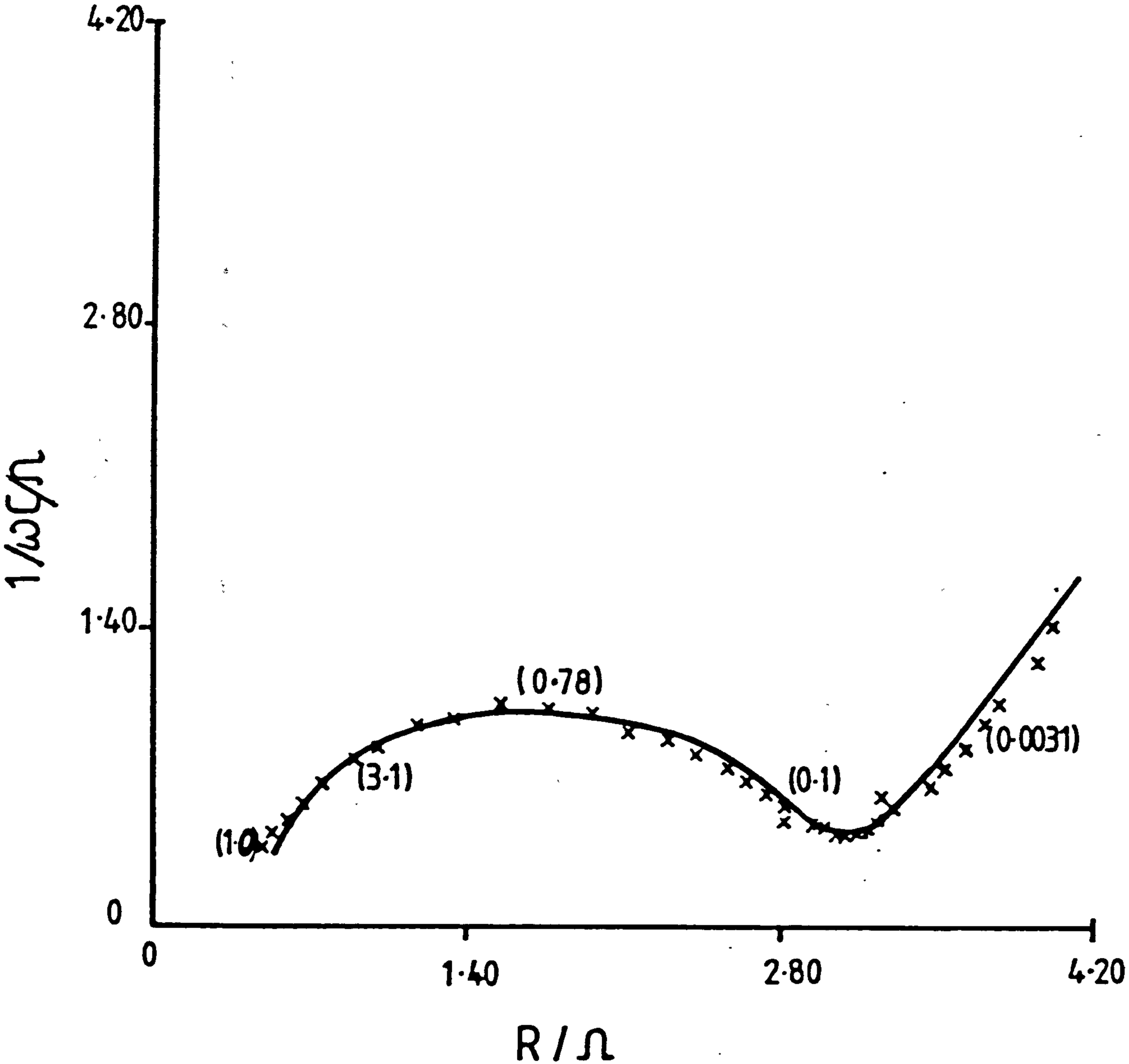

Fig. 9.107

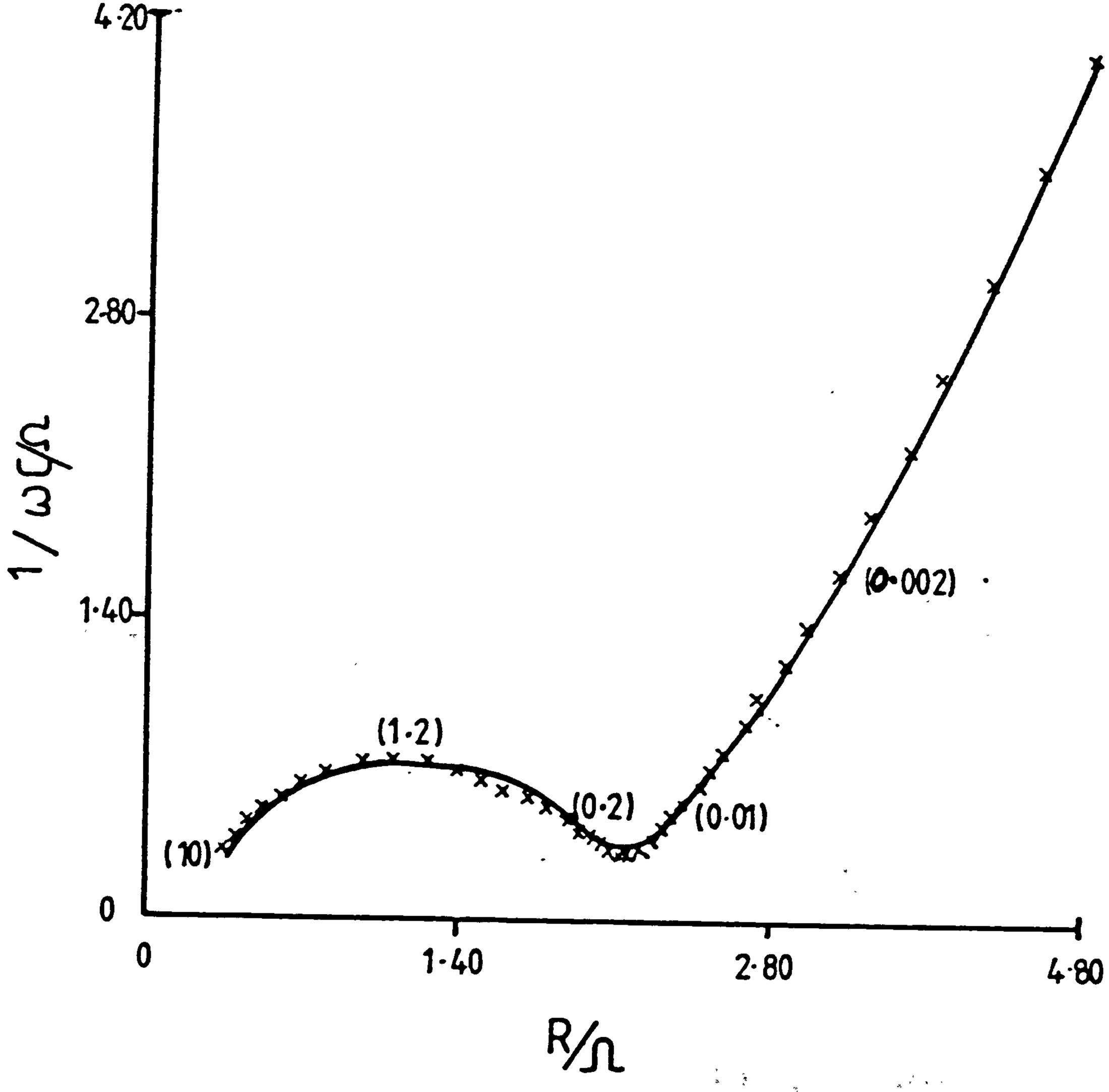

Fig. 9.108

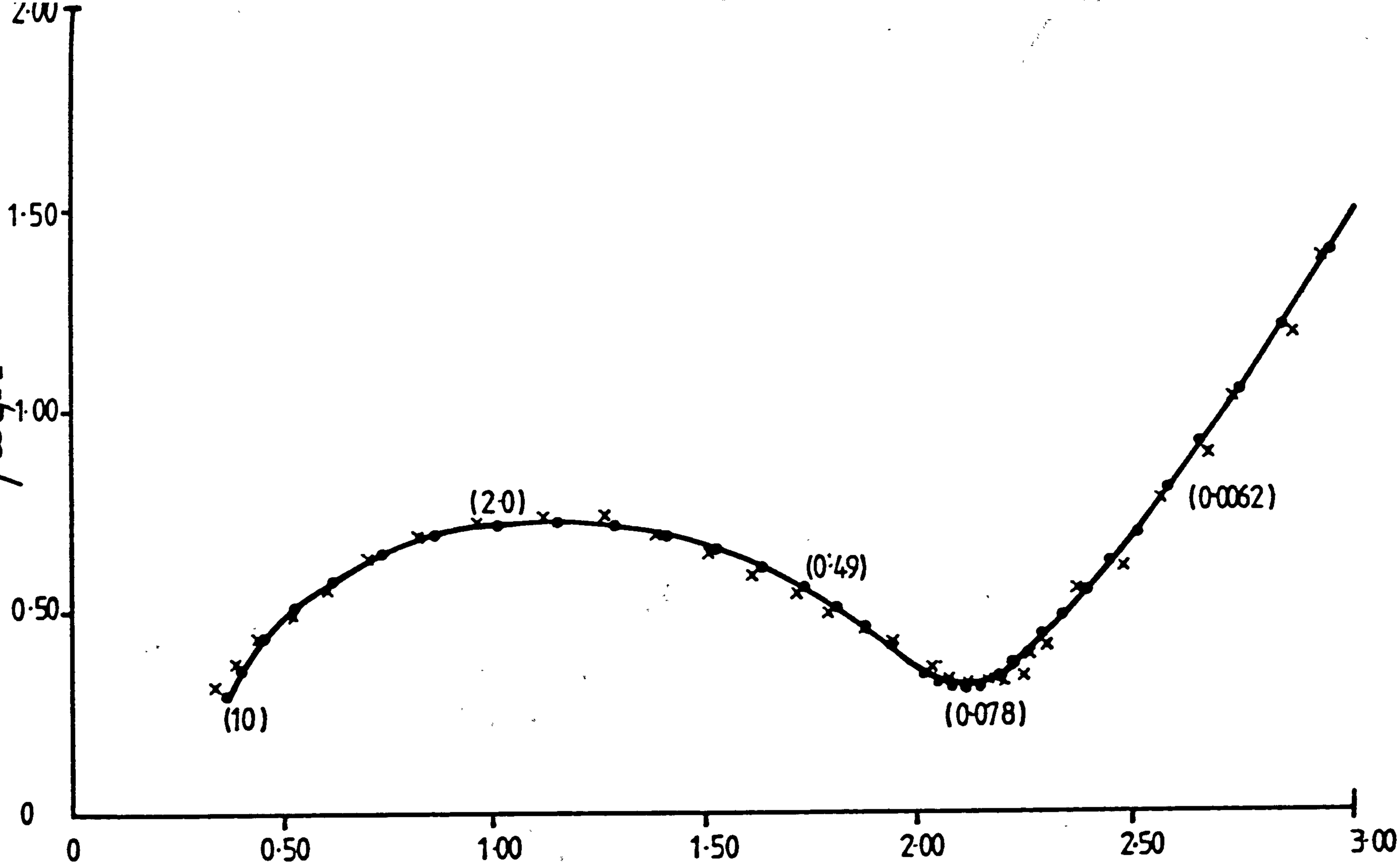
2·00
1·50
1·00
0·50
0
1/ωC/Ω
(2·0)
(0·49)
(0·0062)
(10)
(0·078)
0
0·50
1·00
1·50
2·00
2·50
3·00
R/Ω

Fig. 9.109

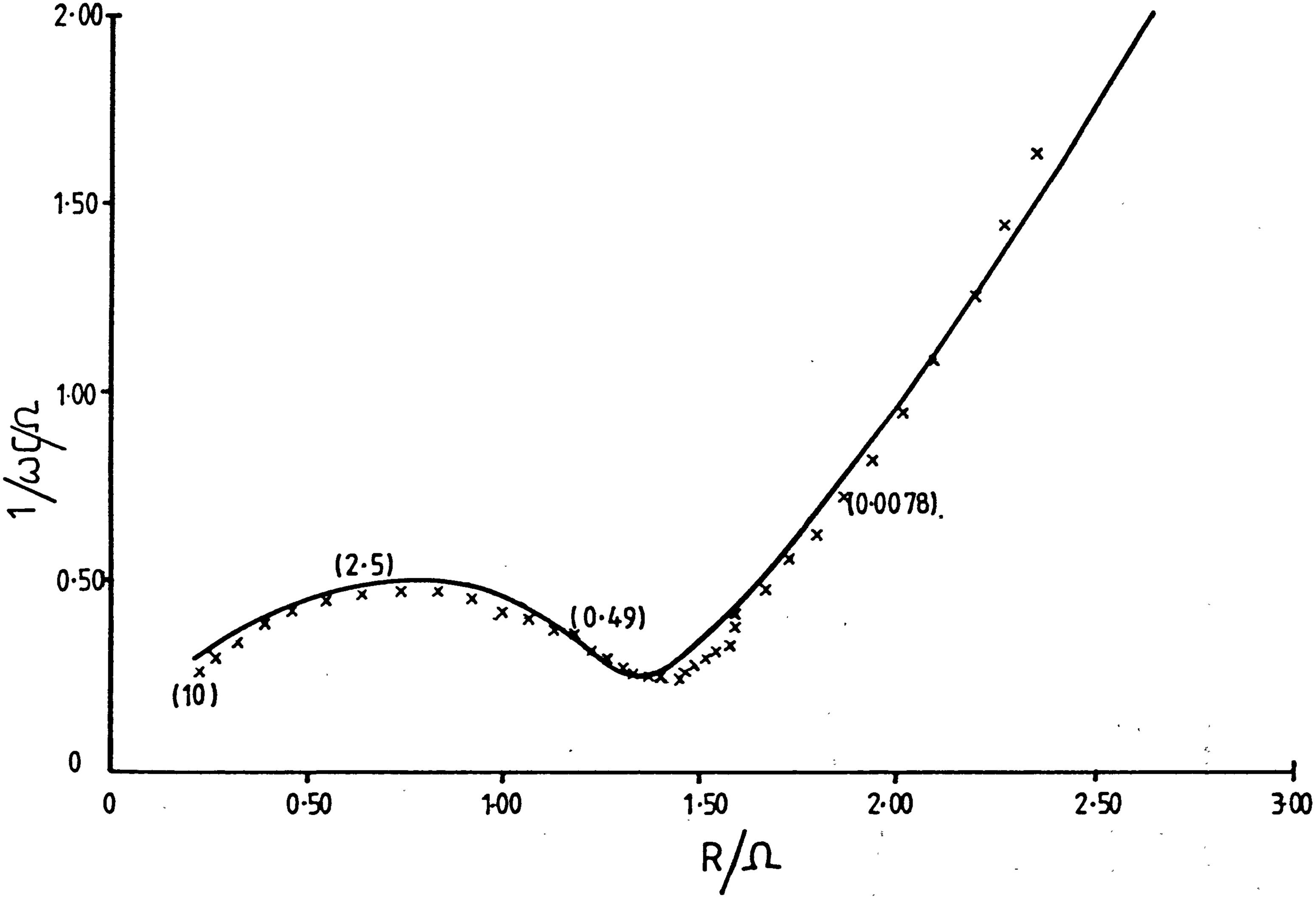
2·00
1·50
1·00
0·50
0
1/ωC/Ω
(10)
(2·5)
(0·49)
(0·0078)
0
0·50
1·00
1·50
2·00
2·50
3·00
R/Ω

Fig. 9.110

found that log θ relates to E linearly and by extrapolating to E_r the exchange current for the system $PbO_2/PbSO_4/H_2SO_4$ at 23°C was found to be 2×10^{-3} Acm^{-2} (in 5M H_2SO_4) from the equation:-

$$i_o = \frac{RT}{2F} \cdot \frac{1}{\theta_{(E-E_r)}} \qquad (79)$$

This is rather higher than obtained by Casson[127] using electrodeposited β-PbO_2. Since the present electrode was formed directly by oxidation of the base lead, it would be expected to be more reactive and have a larger specific surface which would probably play the greatest part in causing the difference.

The development of the series film of $PbSO_4$ is evident through the change of C_χ and R_Ω with decreasing potential. The film components clearly indicate that the film extends over the surface rather than thickening which would cause C_χ to decrease as R_Ω increases. Increases in both shows the extension of a passivating film into the rough electrode surface.

It can be concluded that the complicated model shown in Fig. 9.104 adequately explains the electrode behaviour in the potential region around 940 mV. The flattening of the high frequency semicircle is better explained by adsorption than by surface heterogeniety although surface heterogeniety may explain the small discrepancies observed when the experimental data is treated by two different methods.

Finally it should be emphasised that the "a priori" decomposition

of the electrode impedance into discrete components is only justified operationally since it is successful; in practice this situation is more complex. The double layer capacitance and the film capacitance cannot be independent of each other also C_X must be resistively shunted for d.c. behaviour.

CHAPTER 10

A.C. STUDIES ON POROUS (POSITIVE) LEAD-ALLOY ELECTRODES

10.1. Experimental

The electrical circuitry used was identical to that already described for flat lead and lead-alloy electrodes (Chapter 9). Prior to a.c. impedance measurements, electrodes were oxidised galva nostatically in an upwards facing position (~ 25 mAcm^{-2}, 0.3M H_2SO_4) until a steady potential had been obtained (1.250mV, 0.3M H_2SO_4) and oxygen was freely evolved from the porous matrix. Equilibration in the cell electrolyte (5M H_2SO_4 then followed and the rest potential of the electrode (Er) was determined.

10.2. Results

Fig. 10.111 shows the impedance plot for a fully charged porous (positive) electrode formed on pure lead at the rest potential (1.161 V). The values of the frequency are given in parentheses (Hz). Figs. 10.112-10.114 show the corresponding impedance plots for the formation of $PbSO_4$ from PbO_2 at various potentials (Er-10mV, Er-20mV and Er-40mV).

Similar impedance plots for PbO_2 formed on a Pb-Sb (5.15%) base are shown in Figs. 10.115-10.118 (Er, Er-10mV, Er-20mV, and Er-50mV).

Figs. 10.119-10.121 show the a.c. impedance plots carried

Fig. 10.111

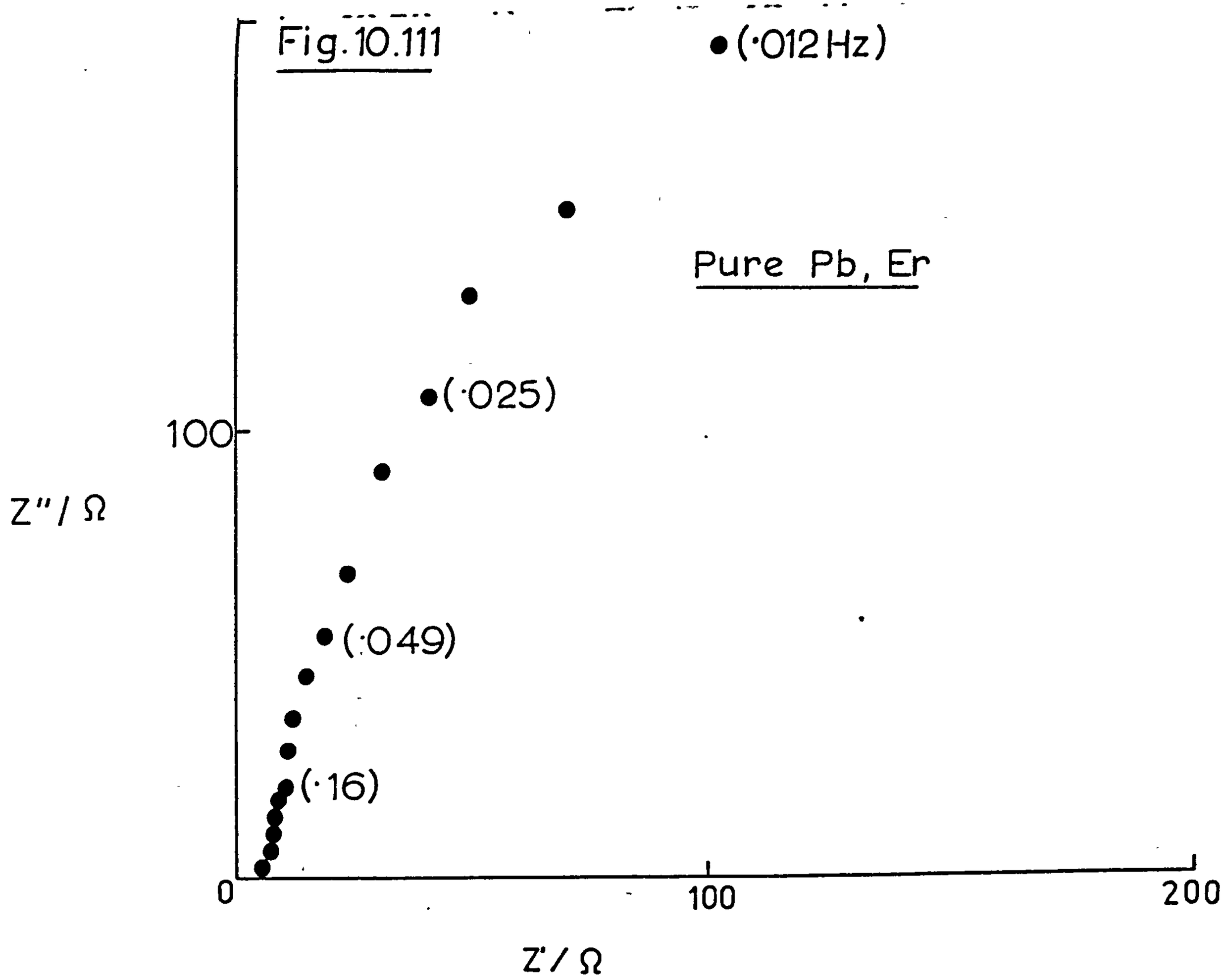

Fig.10.112 Pure Pb, Er -10mV

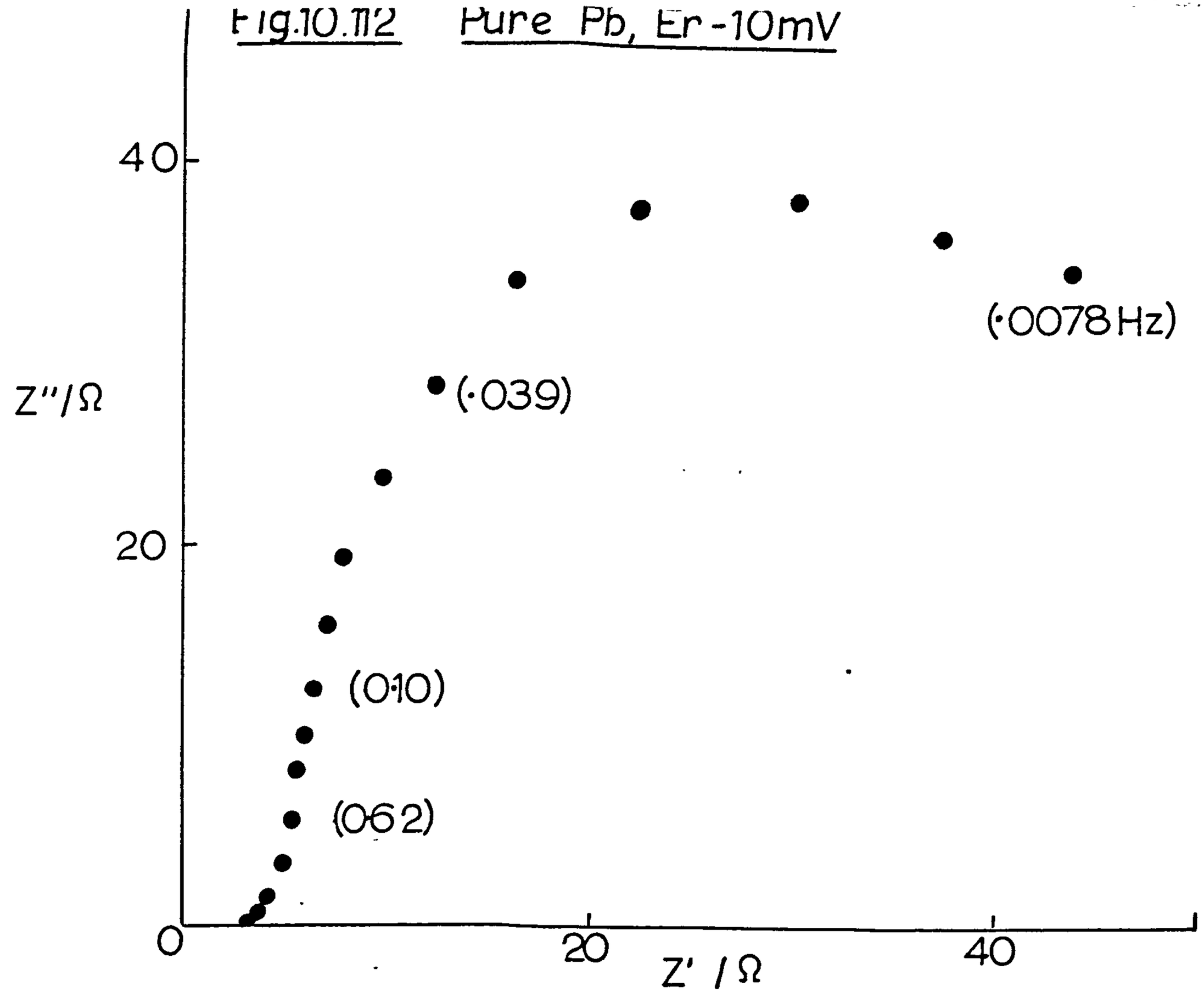

Fig.10.113 Pure Pb, Er-20mV

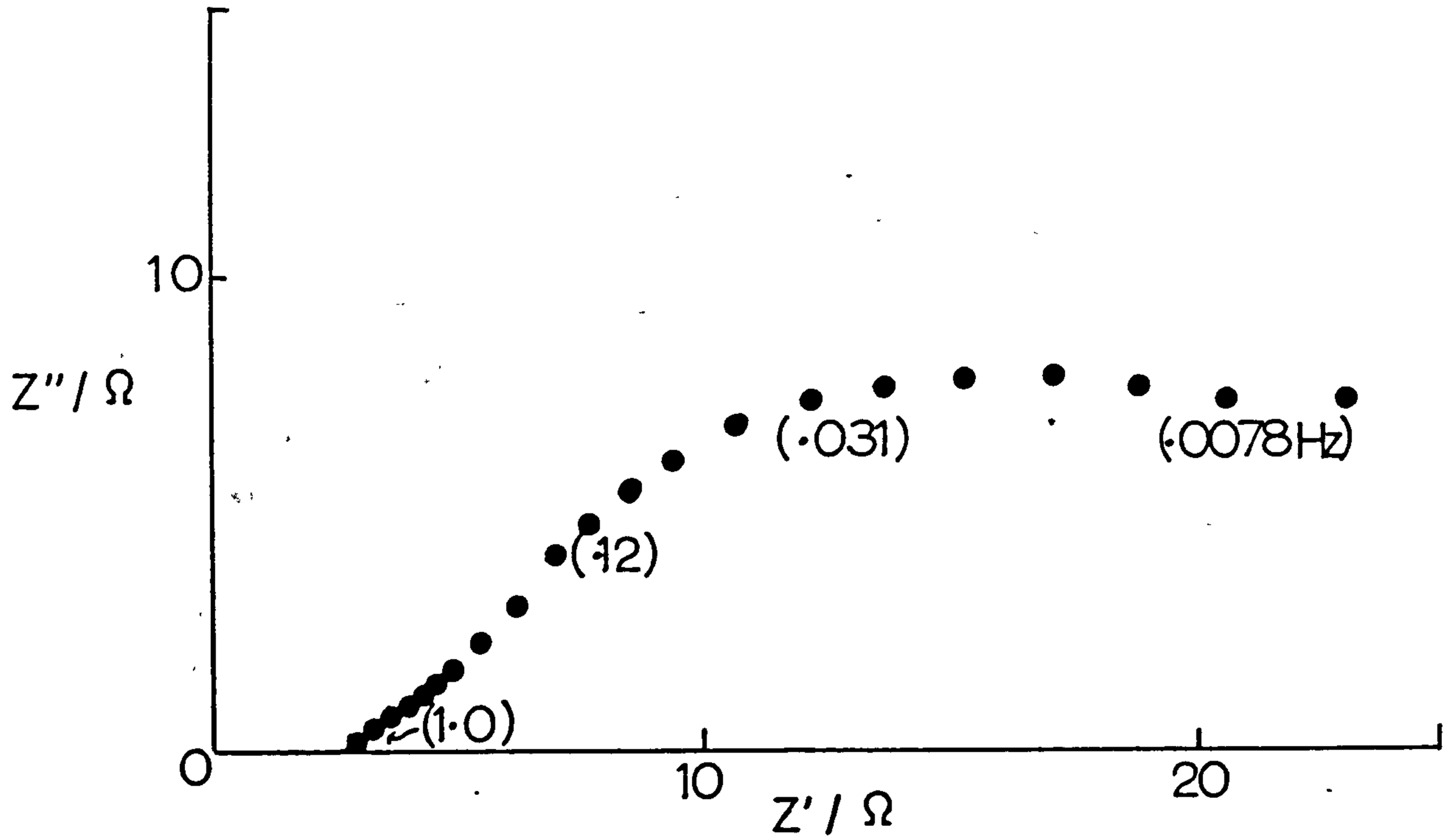

Fig.10.114 Pure Pb, Er-40mV

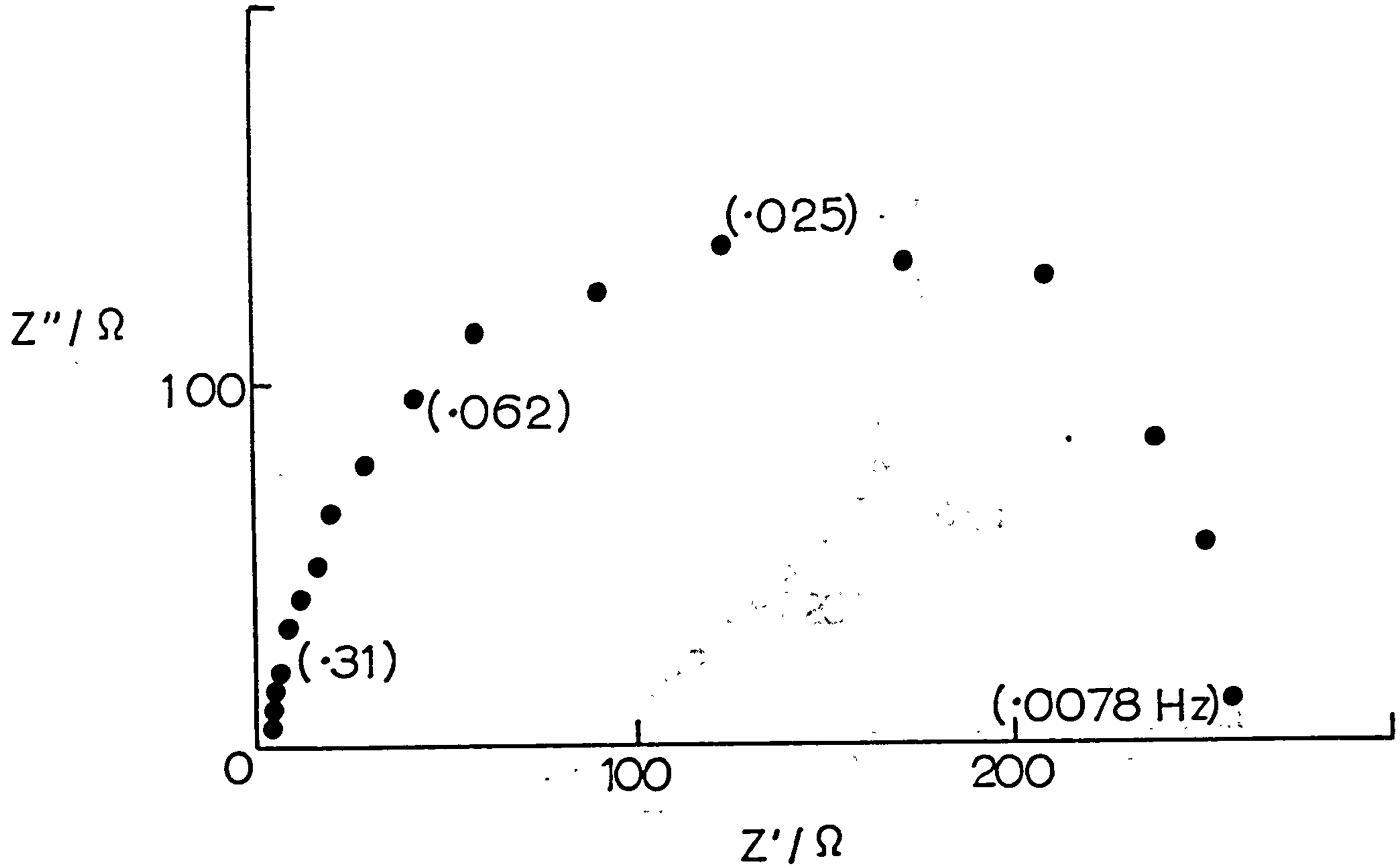

Fig.10.115 Pb / Sb, Er

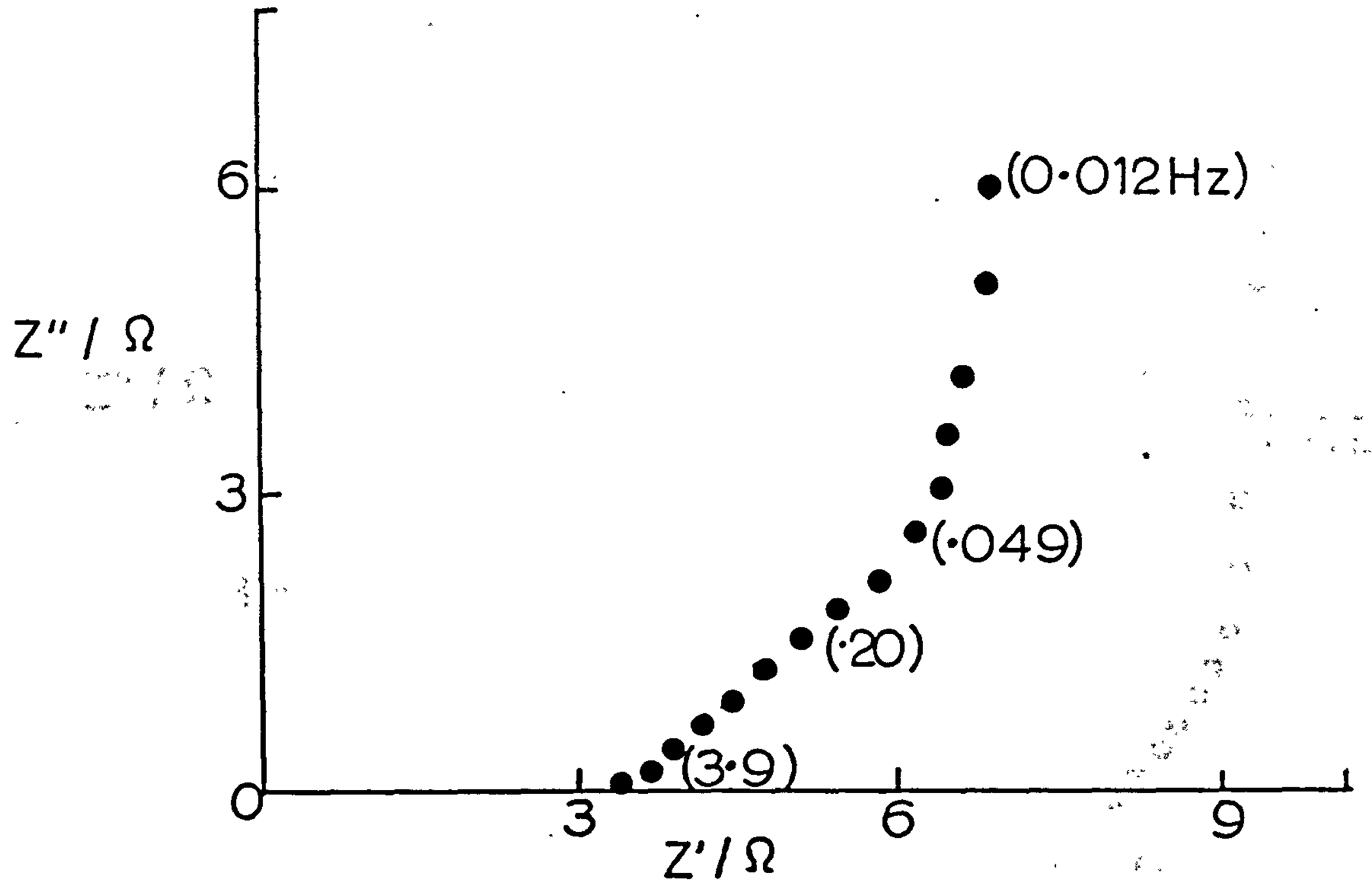

Fig . 10.116

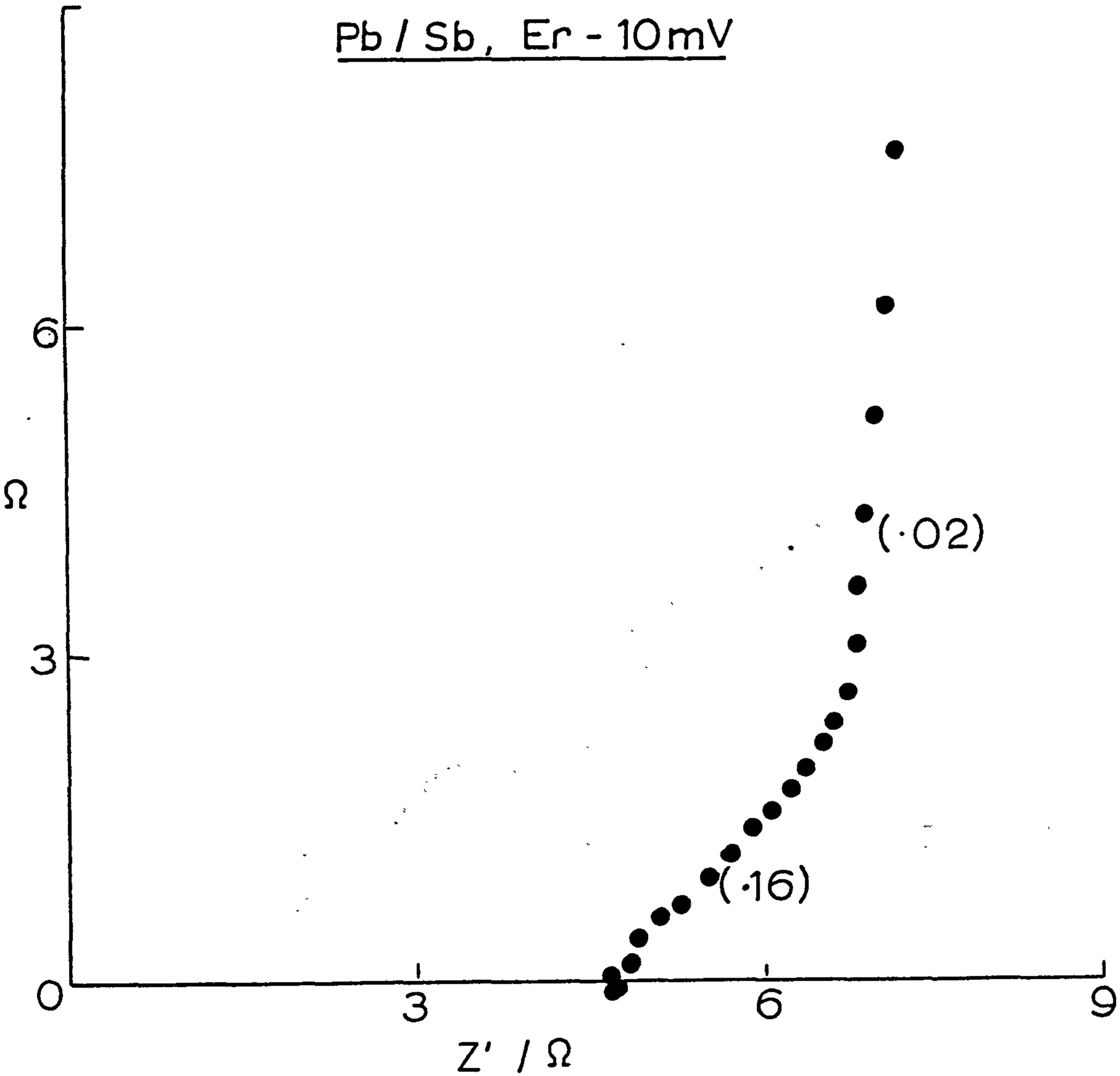

Fig.10.117

Pb / Sb, Er-20mV

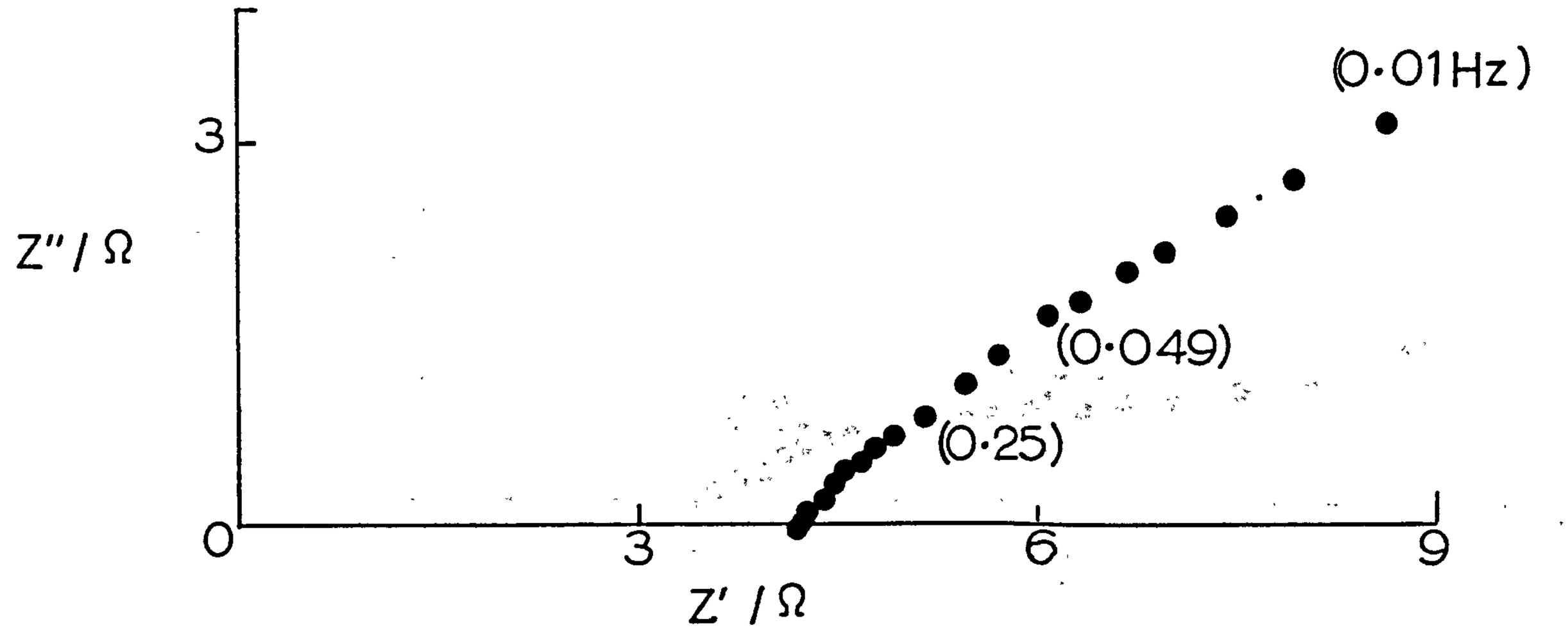

Fig. 10.118

Pb / Sb, Er-50

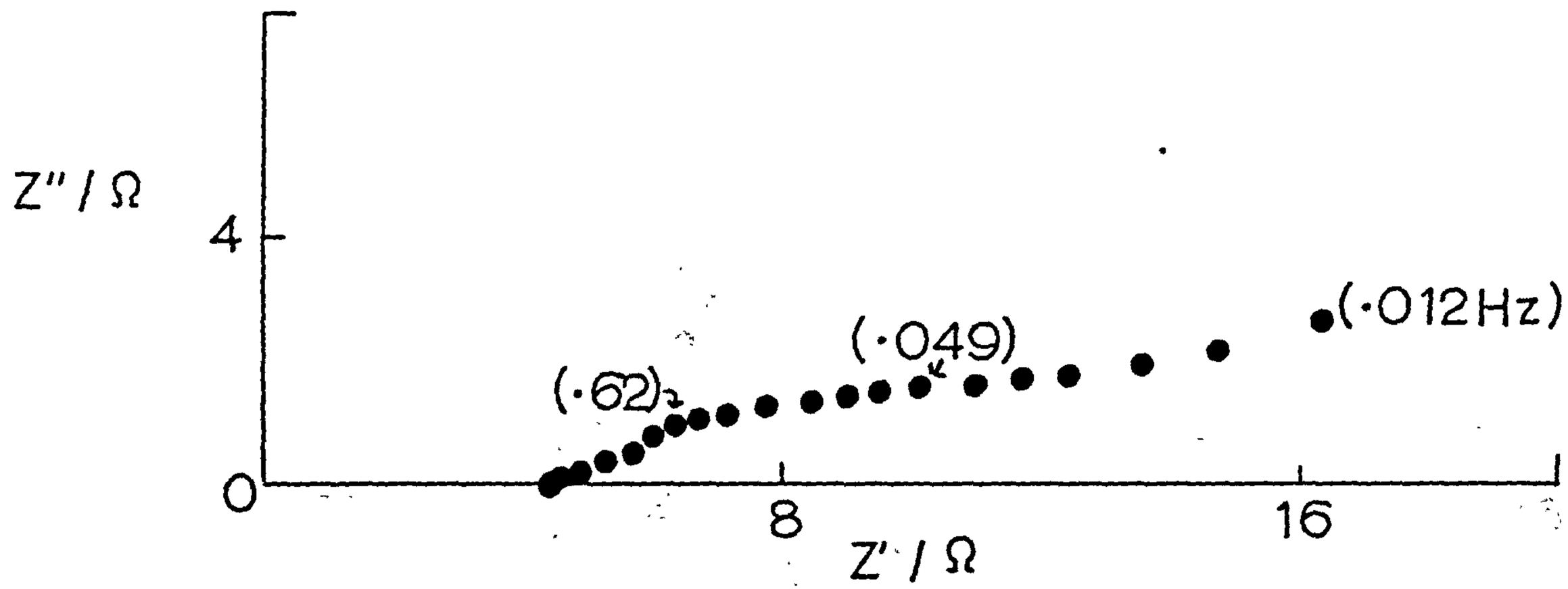

Fig. 10.119

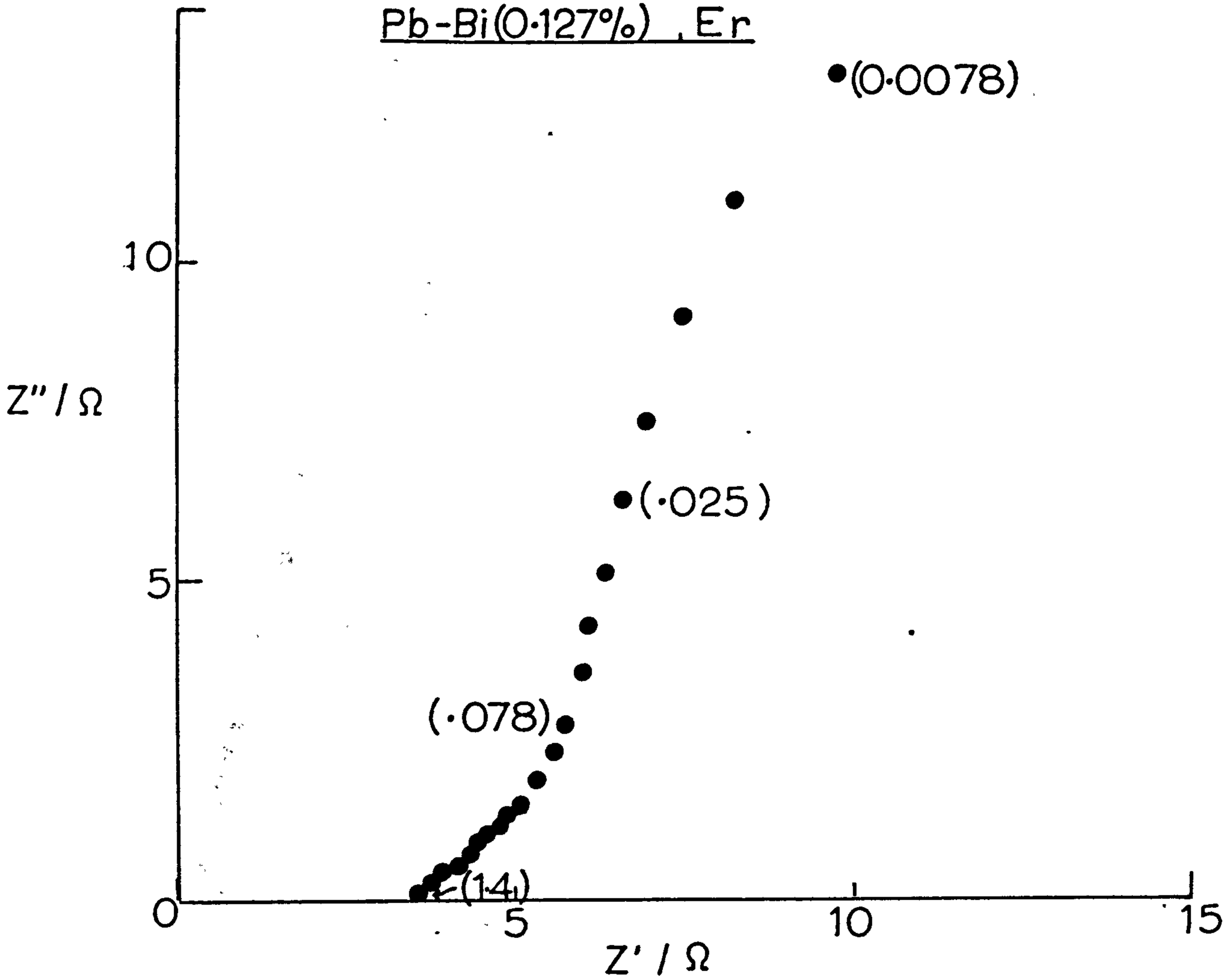

Fig. 10.120

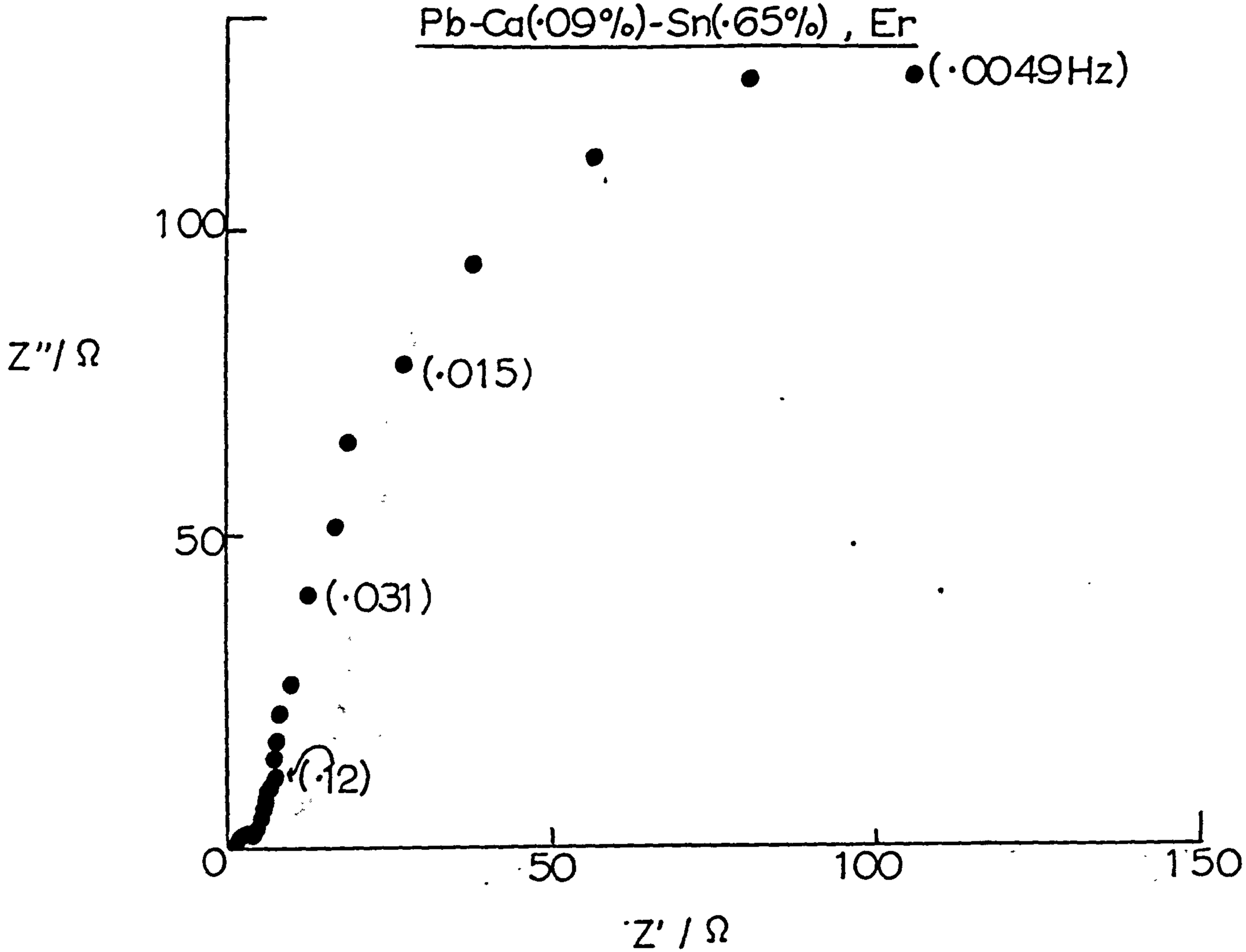

Fig. 10.121

Pb-Ca(·07%)-Sn(·67%)-Mg(·046%), Er

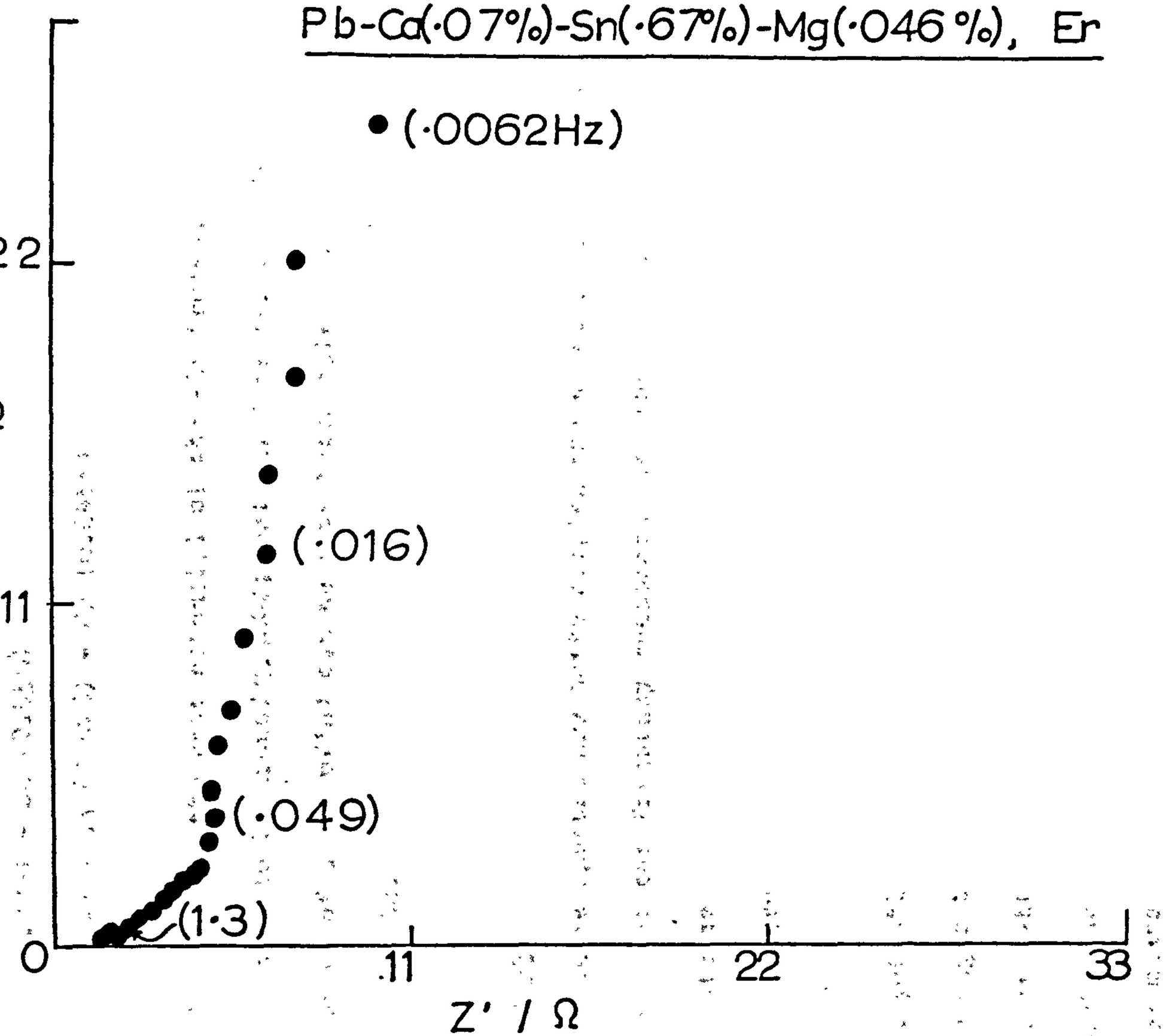

out at the rest potential for PbO_2 formed various lead-alloy bases. The alloys used were:

Pb-Bi (0.127%)

Pb-Ca (0.09%) - Sn (0.65%)

Pb-Ca (0.07%) - Sn (0.67%) - Mg (0.046%)

For each impedance scan, the rest potential of the electrode was determined and found to be around +.160V; small differences in this value(of the order of a few mV's) can be attributed mainly to metallurgical effects.

10.3 Discussion

The impedance spectra are quite complex and a complete discussion and decomposition of the frequency responses into the component processes is outside the scope of the present work, however, a number of qualitative interpretations can be given.

At all potentials the antimonial-lead alloys have the lowest impedances throughout. This suggests that the antimony is acting to form a defect lattice of $PbSO_4$ which is much easier for the charge to pass through. The fact that initially the antimony was only in the base metal means that the mechanism must be via the removal of Sb by corrosion and then the incorporation of antimonial species in the PbO_2 phase. This could be either as Sb(III) or Sb(V); It is clear that the effect of antimony must be considerable since the electrodes have only undergone a small number of cycles and consequently it seems that this involves the removal of Sb species

from the base and deposition on the PbO_2 and the $PbSO_4$.

There is a small but well-defined inductive region of the electrode impedances at the highest frequencies. This agrees with earlier work and is due to retardation of the signal in the pores of the electrode as discussed in Chapter 9.

At high frequencies the line at 45^{o} is due to the diffusion part of the $PbO_2/PbSO_4$ exchange reaction. It might be expected that the line would come off at $22\frac{1}{2}^{o}$ for a porous structure; the fact that it does not may be due to porosity being on a macro scale, however, it is much more likely that the very low conductivity of the electrode results in a considerable penetration depth and that this is not achieved due to the development of solid phase $PbSO_4$ (the reduced species).

At somewhat lower frequencies the transition to control of the current by the oxygen evolution reaction (the potential is well inside the O.E.R. region) is now possible due to the quantity of charge in the a.c. signal. This gives rise to a situation where the impedance locus rises almost vertically before curving over to give a large diameter semicircle.

The Pb-Ca-Sn alloy and the pure lead electrode give very similar results, however, the other alloys all show the antimony effect to some extent. These other alloys are therefore the ones of commercial importance.

As the potential is lowered in the case of Pb and Pb/Sb alloys, changes in the impedance spectra occur. That for the Pb/Sb shows a well-behaved transition to the shape expected for a complex redox reaction followed by a Warburg at low frequency which comes off at $\sim 22\frac{1}{2}^{o}$ for the porous electrode. That for the pure lead shows a diminishing then a growing semi-circle presumably as the charge-transfer semicircle is influenced by the presence of $PbSO_4$ (the reduced species) in the electrode.

It must be emphasised that in this short, qualitative discussion phase formation has been omitted because time did not allow a full investigation of these effects which would only be expected to be found at very low frequency.

CHAPTER 11

FINAL DISCUSSION

11.1. Antimonial Lead

The anodic oxidation products formed on lead and antimonial alloys in sulphuric acid are of interest because of the importance of the lead-acid cell in numerous critical applications, and corrosion of the grid metal in the positive plates limits the life of many cells. Other workers have suggested that the cycle life of the cells, the crystal morphology and even the durability of the positive active material are related to the composition of the grid metal. It has been concluded that antimony nominally used to impart strength to soft lead castings also performs other important functions in positive plate behaviour. There appears to be little question that cells containing antimonial lead grids normally have a longer cycle life than similar cells made with pure lead grids. A very large proportion of the Sb dissolved anodically from the positive grids is retained in the positive active material and serves not only to lower the oxygen overvoltage but also to act as a binding agent between the PbO_2 particles. The recent trend towards development of maintenance-free lead-acid cells means that these advantages of having Sb present in the positive grid must be carefully weighed against the disadvantages, not least of these being the deleterious effect on of Sb on the self-discharge reaction.

In an electrochemical investigation of possible replacements for Sb as the grid alloying ingredient in the lead-acid battery it

was considered necessary to first attempt to isolate a specific 'antimony effect'. This was achieved using potentiostatic pulse measurements (Ch. 4). The production of a double-peak in the current-time transient for the reaction $PbSO_4 \longrightarrow PbO_2$ was shown to be due to the presence of antimony in the base lead. The interpretation of this effect was given in terms of the formation of a duplex layer of PbO_2 on the alloy base. A study of the crystal morphology of the product lead-dioxide (Ch. 4) together with an investigation of the charge contained in these two oxidation peaks revealed that the primary layer formed on Pb-Sb is analagous to the single oxidation layer formed on pure lead. Other workers have shown that the oxide film formed on Pb-Sb has a major presence of β -PbO_2 in the outer layer. The absence of a firmly-bound secondary layer of β-PbO_2 on the pure lead surface was explained in terms of the ability of the Sb to act as a nucleating agent for the β-PbO_2 in the primary corrosion layer.

11.2 Other grid alloying ingredients

The simple lead-bismuth binary alloy was studied using three concentrations of bismuth in the range 0.06% - 0.27% bismuth. The susceptibility of the alloy to anodic attack was shown not to be linear but rather a parabolic relationship was established with the intermediate bismuth level being the most stable. This observation is of importance to lead-acid battery manufacturers since this provides the optimum level of Bi for use as a grid alloying ingredient.

The effect of adding bismuth to lead-calcium-tin was to increase the cycle-life of the alloy which was attributed mainly to a decrease in the oxidisability of the alloy surface. This improvement in the cycle-life of the positive electrode is of significance to battery manufacturers and certainly much more work is needed before the question of replacing Sb with Pb-Ca-Sn-Bi (in the positive grid of the lead-acid battery) can really be answered. These results serve to show that effort must be concentrated around levels of bismuth of approx. 0.127 wt.%. The addition of bismuth (an impurity in some primary lead sources) to Pb-Ca-Sn alloys does not appear to be detrimental to the maintenance-free characteristics of calcium alloys at the levels of addition tested[136]; The effect of bismuth on gassing rates has been reported to be minimal and much less significant than that caused by antimony[137-140].

REFERENCES

1. G.W. Vinal, Storage Batteries, 4th Edn. (Wiley), New York, 1955, P.15.

2. W. Hofmann, "Lead and Lead Alloys", Ind.ed., p.196, Springer-Verlag, New York (1970).

3. P. Casson, N.A. Hampson and K. Peters, Unpublished Work

4. J. Greenwood, Metall.Rev., 23, 279 (1961).

5. M. Dasoyan, Dokl.Akad.Nauk., 107, 863 (1956).

6. N.L. Parr, A. Muscott and A.J. Crocker, J.Inst.Met., 87, 321 (1957).

7. G. Kostorz and S. Mihailovich, Inst.Conf.Strength and Metal Alloys Conf.Proc., 1, 304 (1970).

8. E. Hoehne, Metallwirtschaft, 23, 60 (1944).

9. H. Helmholtz, Wied Ann., 7 (1879) 377

10. A. Gouy, J.Phys., 9 (1910) 457.

11. D.L. Chapman, Phil.Mag., 25 (1913) 475.

12. O. Stern, Z.Electrochem., 30 (1924) 508

13. D.C. Grahame, Chem.Rev., 41 (1947) 441

14. M.A.V. Devanathan, J.O'M Bockins and K. Müller, Proc.Roy.Soc., London, A274 (1963) 55.

15. S. Levine, G.M. Bell and A.L. Smith, J.Phys.Chem., 75 (1969) 3534.

16. B.B. Damaskin and A.N. Frumkin, Electrochimica Acta, 19 (1974) 173.

17. R. Parsons, J.Electroanal.Chem. 59 (1975) 229.

18. I.L. Cooper and J.A. Harrison, J.Electroanal Chem. 66 (1975) 85

19. I.L. Cooper and J.A. Harrison, Electrochimica Acta, 22 (1979) 519

20. I.L. Cooper and J.A. Harrison, Electrochimica Acta, 22, (1977) 1361

21. I.L. Cooper and J.A. Harrison, Electrochimica Acta, 22 (1977) 1365.

22. I.L. Cooper and J.A. Harrison, Electrochimica Acta, 23 (1978) 545.

23. A.N. Frumkin, Svensk.Kemish, Tidskrift, 77 (1965) 300

24. A.N. Frumkin, J.Res.Inst.Catalysis, Hokkaido Univ., 15 (1967) 61

25. W.A. Caspari, Z.Physik.Chem., 30 (1899) 89

26. T. Erdey-Gruz and M. Volmer, Z.Physik.Chem., 105A, (1930) 203

27. K.J. Vetter, Z.Physik.Chem., 194 (1950) 284

28. K.J. Vetter, Z.Elektrochem., 56 (1952) 931

29. J. Tafel, Z.Physik.Chem., 50 (1905) 641

30. J.A.V. Butler, Proc.Roy.Soc., 157A (1936) 423

31. T.Berzins and P. Delahay, J.Amer.Chem.Soc., 77 (1955) 6448

32. J.E.B. Randles, Trans.Farad.Soc., 48 (1952) 828

33. V.V. Losev, "Modern Aspects of Electrochemistry", Vol. 7, Ed. B.E. Conway and J.O'M. Bockris, Butterworths (1972) 314

34. V.G. Levich, Advan.Electrochem.Eng., 4 (1966)249

35. R.A. Marcus, Electrochim.Acta, 13(1968) 995

36. R.R. Dogonadze, "Reactions of molecules at electrodes", Wiley (1971) 135

37. V.G. Levich, "Physico-Chemical Hydrodynamics", Prentice Hall, Englewood Cliffs, 1962.

38. J.E.B. Randles, Disc.Farad.Soc., 1 (1947) 11

39. J.E.B. Randles, Trans.Farad.Soc., 48 (1952) 951

40. E. Warburg, Ann.Physik., 67 (1899) 493; 6 (1901) 125.

41. M. Sluyters-Rebach, D.J. Kooijam and J.H. Sluyters, "Polarography", Ed. G.J. Hills, Macmillan Press (1964) 143

42. P. Delahay and T.J. Adams, J.Amer.Chem.Soc., 74 (1952) 5740.

43. H. Gerischer, Z.Physik.Chem., 202 (1953) 302

44. K.J. Vetter, Z.Physik.Chem., 199 (1952) 285.

45. J.H. Sluyters, Rec.Trav.Chim., 79 (1960) 1093.

46. P.Delahay, "New Instrumental Methods in Electrochemistry", Interscience Publishers Inc., New York (1966) Chapter 6.

47. D.C. Grahame, J.Electrochem.Soc., 99 (1952) 370C.

48. M. Sluyters-Rehback and J.H. Sluyters, in "Electroanalytical Chem", Vol. 4 (edit.by A.J. Bard) Dekker, New York (1970) p.1.

49. H.A. Laitinen and J.E.B. Randles, Trans.Faraday.Soc., 51 (1955) 54.

50. R.D. Armstrong and A.A. Metcalfe, J.Electroanalyt.Chem. 71 (1976) 5.

51. N.A. Hampson, S.A.G.R. Karunathilaka and R. Leek, J.Appl.Electrochem., 10 (1980) 3.

52. R.S. Nicholson and J. Shain, Anal.Chem., 36 (1964) 706.

53. W.M. Schwarz and J. Shain, J.Phys.Chem., 69 (1965) 30.

54. A. Sevcik, Coll.Czech.Chem.Comm., 13 (1948) 349

55. W. Kemula and Z. Kublik, Anal.Chim.Acta., 18 (1958) 104.

56. H. Matsuda and Y. Ayabe, Z.Elektrochem., 59 (1955) 494.

57. J.E.B. Randles, Trans.Farad.Soc., 44 (1948) 322,327

58. M. Fleischmann and H.R. Thirsk, Advan.Electrochem. and Electrochem.Eng., 3 (1963) 123.

59. J.A. Harrison and H.R. Thirsk, Electroanalytical Chemistry, Vol.5 (Ed. A.J. Bard), Marcel Dekker, New York (1971).

60. M. Avrami, J.Chem.Phys., 7 (1939) 103; 8 (1940) 212; 9 (1941) 177.

61. R.D. Armstrong and J.A. Harrison, J.Electrochem.Soc., 116 (1969) 328.

62. M. Fleischmann, J.A. Harrison and H.R. Thirsk, Trans.Faraday.Soc., 61 (1965) 2742.

63. F C. Frank, Proc.Roy.Soc., A201 (1950) 586

64. R.D. Armstrong, M.Fleischmann and H.R. Thirsk, J.Electroanal.Chem., 19 (1968) 325.

65. R. de Levie, in P.Delahay (Ed.) Advan.Electrochem.Electrochem.Eng., 6 (1967) 329.

66. J. O'M Bockris and S. Srinivasan, "Fuel Cells: Their Chemistry", Chap.V, McGraw-Hill, New York (1969).

67. F.A. Grens 11, Electrochim.Acta, 15(1970) 1047.

68. J. Newman and W. Tiedmann, Am.Inst.Chem.Eng.J., 21 (1975) 25.

69. D. Simonsson, Thesis, Inst.Kemist.Technologi, Kungl, Tekniska, Hongkolan, Stockholm, 1973.

70. A. Winsel, Z.Elektrochem., 66 (1962) 287.

71. O.S. Ksenzhek and V.V. Stender, Dokl.Akad.Nauk.SSSR, 107 (1956) 280.

72. H. Bode, "Lead-Acid Batteries", Wiley-Interscience, New York (1977).

73. J. Euler and W. Nonnenmacher, Electrochim.Acta, 2 (1960) 268

74. J. Euler, Electrochim.Acta, 8 (1963) 409.

75. J.S. Newman and C.W. Tobias, J.Electrochem.Soc., 109 (1962) 1183

76. R.C. Alkire, E.A. Grens 11 and C.W. Tobias, J.Electrochem.Soc., 116(1969) 1328.

77. R.C. Alkire and B. Place, J.Electrochem.Soc., 119 (1972) 1678.

78. J.S. Dunning, D.M. Bennion and J. Newman, J.Electrochem.Soc., 118 (1971) 1251.

79. J.S. Dunning & D.N. Bennion, Proc.Advances in Battery Technology Symposium, The Electrochemical Soc., Inc., Southern California-Nevada Section, Vol. 5, 1969.

80. K. Micka and I. Rousar, Electrochim.Acta, 19 (1974) 499

81. K. Micka and I. Rousar, Electrochim.Acta, 18 (1973) 629.

82. K. Micka and I. Rousar, Electrochim.Acta., 21 (1976) 599.

83. D. Simonsson, J.Electrochem.Soc., 120 (1973) 151.

84. D. Simonsson, J.Appl.Electrochem., 3 (1973) 261.

85. D. Simonsson, J.Appl.Electrochem., 4 (1974) 109.

86. M. Risberg, P.Sahlestrom and D. Simonsson, Report TRITHA-KTE-1003, Royal Inst.Technol., Stockholm, 1973.

87. J. Lehning, Elektrotech.Z., 93A (1972) 62

88. W. Runge, Elektrotech.Z., 93A (1972) 67

89. A.D. Turner, A.E.R.E. Report No. R8931, 1978.

90. A.C. Riddeford, Advan.Electrochem.Electrochem.Eng., 4 (1966) 167.

91. M.A. Hampson and M.J. Willars, Surf.Technol., 7 (1978) 247.

92. R.D. Armstrong, M.F. Bell & A.A. Metcalfe, J.Electroanal.Chem., 77 (1977) 287.

93. M. Fleischmann and H.R. Thirsk, Trans.Faraday.Soc., 51 (1955) 71

94. H.S. Pancsar in 'Power Sources', Vol. 3, edited by D.H. Collins, Oriel Press, Newcastle-upon-Tyne (1971).

95. J.G. Sunderland, J.Electroanalyt.Chem., 71 (1976)341.

96. K. Elbs and J. Forsell, Z.Elektrochem. 8 (1902) 760.

97. W. Feirknecht, J.Appl.Electrochem., 62 (1958) 795.

98. P. Rüetschi, R.T. Angstadt and B.D. Cahan, J.Electrochem.Soc., 106 (1959) 547.

99. P. Casson, N.A. Hampson and K. Peters, J.Appl.Electrochem., 124 (1977) 1655.

100. S.G. Canagaratna, P.Casson, N.A. Hampson and K. Peters, J.Electroanalyt.Chem., 79 (1977) 273.

101. P. Casson, N.A. Hampson and K. Peters, J.Electroanalyt.Chem., 83 (1977) 87.

102. P. Casson, N.A. Hampson and K. Peters, J.Electroanalyt.Chem., 92 (1978) 191.

103. J. Burbank, NRL Report 7256, May 1971.

104. J. Burbank, J.Electrochem.Soc., 104 (1957) 693.

105. T.F. Sharpe, J.Appl.Electrochem., 124 (1977) 168.

106. J.L. Dawson, M.I. Gillibrand and J. Wilkinson, Power Sources 3 (1970) 1

107. J.L. Dawson, J. Wilkinson and M.I. Gillibrand, J.Inorg.Nucl.Chem., 32 (1970) 501.

108. F. Arifuku, M. Yoneyama and H. Tamura, J.Appl.Electrochem., 9 (1979) 629.

109. F. Arifuku, M. Yoneyama and H. Tamura, J.Appl.Electrochem., 9 (1979) 635.

110. J. Burbank, J.Electrochem.Soc., 111 (1964) 1112.

111. E.J. Ritchie and J. Burbank, J.Electrochem.Soc., 117 (1970) 229.

112. C. Zener, Acta Metall., 6 147 (1948).

113. V.J. Bryntseva, V.G. Bundzhe, Yu.D. Dunaev, G.Z. Kiryakov and L.A. Tskhe, Zasch.Metall, 3, 504 (1967).

114. J.A. Gonzalcs, M. Rvejula and S. Felui, Rev.Met (Madrid), 7, 105 (1971).

115. D.D. McDonald, "Transient Techniques in Electrochemistry", P. 281, Plenum Press, New York (1977).

116. J.L. Devitt and M. Myers, J.Electrochem.Soc., 123, 1769 (1976).

117. G. Smith, "Storage Batteries", Pitman Publishing, London (1971) P.40.

118. P. Casson, Ph.D. Thesis, Loughborough University (1978).

119. P. Rüetschi, J.Electrochem.Soc., 120 (1973) 3, 331

120. J.J. Lander, J.Electrochem.Soc., 98, 213 (1951); 103, 1 (1956)

121. J. Burbank, J.Electrochem.Soc., 103, 87, (1956).

122. P. Rüetschi and R.T. Angstadt, J.Electrochem.Soc., 111, 1323, (1964).

123. E. Sato & T. Shiina, J.Electrochem.Soc.Japan, 32, 148 (1964).

124. D. Pavlov & Z.Dinev, J.Electrochem.Soc., 127 (1980) 4, 855

125. M. Sluyters-Rehbach and J.H. Sluyters, Chapter 1, in Advances in Electroanalytical Chem., Ed. A.J. Bard, Marcel Dekker, New York, (1967).

126. S.G. Canagaratna and N.A. Hampson, Surface Technology, 5 (1977) 163

127. P. Casson, N.A. Hanpson and M.J. Willars, J.Electroanal.Chem., 97 (1979) 21.

128. M. Keddam, Z. Stognov and J.C. Lestrade, J.Appl.Electrochem., 7 (1977) 539.

129. R. Darby, J.Electrochem.Soc., 116 (1966) 392, 496.

130. J.P. Carr, N.A. Hampson and R. Taylor, J.Electroanal.Chem., 27 (1970) 201.

131. M. Keddam, S. Stymar and H. Takenoute, J.Appl.Electrochem. 7 (1977) 539.

132. M. Sluyters-Rehbeck & J.H. Sluyters, Electroanal.Chem., Vol.4 (Ed. A.J. Bard) Dekker, New York (1970) P.17

133. S.A.G.R. Karurathilaka, N.A. Hampson, R. Leek & T. Sinclair, J.Appl.Electrochem, 10 (1980) 603.

134. N.A. Hampson & J.B. Lakeman, J.Electroanal.Chem., 107 (1980) 107.

135. H.A. Laitinen and J.E.B. Randles, Trans.Faraday.Soc., 51, 54 (1955).

136. I.K. Gibson, Chloride Technical Ltd (CTL) Project Report No. 4280, 1981.

137. U.S. Sokolov, T.M. Caldwell and E.R. Stein, Abstract 35, Fall Meeting, Electrochem.Soc., 1973.

138. G. Ashworth, C.T.L. Report No. 2386, May 1976.

139. G.W. Vinal and G.N. Schramm, J.Amer.Inst.Electrical Engineer, 44, 128, 1925.

140. J.R. Pierson, C.F. Weinlein and C.F. Wright, Power Sources 5 (Edit. D.H.Collins), Academic Press, London, (1975) P. 97.